INVESTIGATION OF CATALYTIC SORBENTS FOR CAPTURE AND CONVERSION OF CO_2 TO METHANE

A Dissertation
Presented to
The Academic Faculty

by

Sang Jae Park

In Partial Fulfillment
of the Requirements for the Degree
Doctor of Philosophy in the
School of Chemical & Biomolecular Engineering

Georgia Institute of Technology
December 2021

INVESTIGATION OF CATALYTIC SORBENTS FOR CAPTURE AND CONVERSION OF CO_2 TO METHANE

Approved by:

Dr. Christopher W. Jones, Advisor
School of Chemical & Biomolecular Engineering
Georgia Institute of Technology

Dr. Andrew J. Medford
School of Chemical & Biomolecular Engineering
Georgia Institute of Technology

Dr. Ryan P. Lively
School of Chemical & Biomolecular Engineering
Georgia Institute of Technology

Dr. Andrei G. Fedorov
School of Mechanical Engineering
Georgia Institute of Technology

Dr. Krista S. Walton
School of Chemical & Biomolecular Engineering
Georgia Institute of Technology

Date Approved: [August 18, 2021]

ACKNOWLEDGEMENTS

I would first like to thank my parents, Hye Kyung Kim and Jin Won Park, my sister Minah Park, and my brother-in-law Yong Ha Kwon for all their love and support. I am the third Ph.D. in my family, and my father and sister gave me so much advice regarding not only how to become a good researcher, but also about how to stay calm amidst all challenges and to overcome such difficulties. Furthermore, everyone in my family gave me so much encouragement and positivity throughout my Ph.D. Without all their love and support I would not be where I am today.

I must thank my advisor Dr. Christopher Jones for all his guidance. I believe I had a slow start to my Ph.D., but he still gave me much freedom to practice my creativity, while giving me perfect advice at the perfect time. Furthermore, he consistently encouraged and supported me, while teaching me how to think critically. He was wonderful advisor, a wise mentor, and a good friend. It was a true blessing to have him as my Ph.D. advisor.

I would also like to acknowledge my friends and colleagues for making my time at Georgia Tech one of the best chapters in my life. Frederick B. Chung, my roommate for 5 years, for being a wonderful roommate and a wonderful brother; Youngkyu Jeon, Dongjune Kim, Brian Lee, Geonhwa Jeong, Gyutae Nam, Sungtaek Choi, Seungwan Jung, Ryan M. Choi, Jay Lee for being great friends and for making me a better basketball player; Nima Ronaghi, for listening to all my scientific challenges that I faced for every project that I did, while constantly encouraging me; Simon Pang, for training me on so many devices and in chemical synthesis when I initially joined the group; Michele Sarazen, for teaching me how to brainstorm and think about catalysis projects; Chunjae Yoo for all the

insightful discussions about my project; Byunghyun Min and Akshay Korde for consistently encouraging me and telling me that I will get it done; Hyun June Moon, Youn Ji Min, and Mingyu Song for all their discussions about why we are lucky to be in the Jones group and how we can improve our group culture.

Finally, I would like to attribute all my glory to God.

TABLE OF CONTENTS

LIST OF TABLES

LIST OF FIGURES

SUMMARY

The atmospheric CO_2 concentration has increased throughout the last century, and this fact has been reported to be a major contributor to global climate change. To reduce the amount of CO_2 emissions, CO_2 capture from either point sources or from the atmosphere, followed by geological sequestration or conversion of the captured CO_2 into value added products, have been studied in the past. Currently, CO_2 capture processes and CO_2 conversion steps are performed as separate processes, which can contribute significant energy costs related to the temperature swing step, capital costs associated with two separate process units, and transportation and storage costs for the desorbed CO_2.

Recently, dual function materials (DFMs) and catalytic sorbents have been reported as potential materials that could help resolve such drawbacks. Such materials were reported to be capable of capturing CO_2 and converting it into methane, which can be used as fuel source, in one reactor system under an isothermal condition, thereby removing the temperature swing step and (potentially) the CO_2 storage or transportation steps. DFMs have more than one functionality, such as CO_2 sorption and catalytic sites in a single grain, while catalytic sorbents have adsorptive sites and catalytic sites on separate grains. The capture and conversion process is done in 2 steps. The first step is the CO_2 capture step, where the DFM or catalytic sorbent adsorbs CO_2 under CO_2 flow, and the second step is the conversion step, where adsorbed CO_2 is converted into methane under renewable H_2 flow. However, the study of combined capture and conversion of CO_2 into methane is still in its infancy. Only a few materials have been tested as DFMs and catalytic sorbents for combined capture and conversion, and very little has been done regarding their capture and

methanation mechanisms. The aim of proposed work here is to synthesize a catalytic sorbent with higher methanation capacity and to begin developing a better understanding of the CO_2 methanation mechanism on the synthesized material.

In the first section of this thesis, $NaNO_3$ promoted MgO was synthesized and its performance as a sorbent material to sorb CO_2 at concentrations relevant to flue gas CO_2 capture at intermediate temperature, which is reported be a favorable reaction condition for CO_2 methanation, was evaluated. The effects of $NaNO_3$ loading and sorption temperature on CO_2 sorption capacity and kinetics were investigated through thermogravimetric analysis (TGA). The mechanism of CO_2 sorption by $NaNO_3$ promoted MgO was studied using *in situ* X-ray diffraction (XRD) analysis and *in situ* Fourier-transform infrared spectroscopy (FTIR). Furthermore, it was found that partially desorbed sorbents showed much improved sorption kinetics compared to fresh sorbents, and can be used to perform isothermal sorption and desorption cycles by switching the inlet gas from CO_2 gas to inert gas.

Secondly, catalytic sorbents were synthesized through physically mixing $NaNO_3$/MgO sorbent and Ru/Al_2O_3 catalyst, and its performance as a catalytic sorbent was evaluated by measuring CO_2 sorption and methane production capacities in a combined capture and methanation cycle. Two different methods were used to prepare the catalytic sorbent : i) packing the two components, $NaNO_3$/MgO and Ru/Al_2O_3, in two separate beds and ii) first mixing and pelletizing the two components together, then packing as a single bed. It was found that packing as two separate beds showed higher sorption and methane production capacities, while packing as a single bed after thorough mixing caused a drastic decrease in the CO_2 sorption capacity of the $NaNO_3$/MgO. Furthermore, CO_2 methanation

reaction pathways were studied over 1% Ru/Al_2O_3 and 5% $NaNO_3$/1%Ru/Al_2O_3 catalysts through CO_2 and H_2 reaction order measurements and *in situ* FTIR spectroscopy.

As the last part of this thesis, an in-depth investigation of CO_2 methanation pathways over four types of catalysts, 1%Ru/Al_2O_3, 5% Ru/Al_2O_3, 5% $NaNO_3$/1%Ru/Al_2O_3, and 5% $NaNO_3$/1%Ru/Al_2O_3, was performed. Transmission electron microscopy (TEM), X-ray photoelectron spectroscopy (XPS), XRD, and CO chemisorption were performed to characterize the synthesized catalysts. CO_2 and H_2 reaction order measurements, activation energy measurements, *in situ* FTIR spectroscopy, and steady state isotopic transient kinetic analysis were done to gain insight regarding reaction pathways over different catalysts. It was found that bicarbonate and linear carbonyl species were true reaction intermediates over both Ru/Al_2O_3, while formate species behaved as spectator species. For $NaNO_3/Ru/Al_2O_3$ catalysts, it was found that carbonate, formate, and linear carbonyl were reaction intermediates for methanation reaction. Based on spectroscopic observation and results from kinetic study, reaction pathways were proposed for Ru/Al_2O_3 and $NaNO_3/Ru/Al_2O_3$. Rate laws corresponding to each reaction pathway were derived, and experimental data obtained were fitted to the derived rate law to obtain kinetic constants as well.

Overall, this thesis shows that catalytic sorbents synthesized through physical mixing of $NaNO_3$/MgO and Ru/Al_2O_3 show a high sorption capacity and methane production in the combined capture and methanation cycle, and therefore may be a promising material for such applications. It was found that $NaNO_3$ has a promotional effect on CO_2 sorption for MgO, but also has a promotional effect on methane production over Ru/Al_2O_3 catalysts. However, the kinetics of CO_2 sorption are still slow and the MgO

support tended to sinter over multiple cycles of capture and methanation, and therefore further studies to improve CO_2 sorption kinetics and MgO support stability are suggested as future directions for this line of research.

CHAPTER 1. INTRODUCTION

1.1 Introduction

Currently, energy generation in the world heavily depends on combustion of fossil fuels, and future energy consumption is expected to increase. The continuous increase in use of fossil fuels has led to a drastic increase in CO_2 emissions to atmosphere, and these emissions have been the major contributor to climate change over the past century.[1] As a result, numerous studies have been done in the past several decades to find an efficient way to reduce CO_2 emissions.

1.1.1 CO_2 Capture

Post combustion CO_2 capture is one field that has been deeply investigated.[2–6] In this process, CO_2 is captured from the source of CO_2 emission, typically a large point source, often in the form of flue gas. The most commonly used CO_2 capture process in industry is absorption by aqueous amine solutions.[7] In this process, an aqueous amine, such as monoethanolamine (MEA) or diglycolamine (DGA), is used to capture CO_2. Captured CO_2 is stripped from the amine solution at elevated temperatures (100 – 140°C), and the CO_2-free amine solution is then used again for CO_2 capture in the next cycle. Although this technology is commonly deployed at scale for CO_2 removal from streams with high value (e.g. methane contaminated with CO_2), it is often deemed too expensive for environmental clean-up applications.[8] Several reasons for the relatively high costs are that (i) the amine solution is slowly lost as the temperature is elevated for stripping CO_2,

(ii) corrosion of devices due to the basic amine solutions, and (iii) the energy intensive CO_2 stripping process that requires heating large volumes of water to high temperatures.

Separation of CO_2 using solid adsorbents has been studied as an alternative that can potentially reduce the cost of the CO_2 capture process.[6,8,9] Various materials such as zeolites,[10,11] supported amines,[12–16] metal organic frameworks (MOFs),[17–19] and alkali or alkali earth based metal adsorbents[20–23] have been studied in the past. Alkali earth metal oxides, such as calcium oxide or magnesium oxide, are the cheapest materials among those listed above. These materials show high CO_2 sorption capacity at high temperature, typically above 600°C. Barker et al. showed that the CO_2 sorption capacity of CaO with 10 μm particle size was 13.4 mmol/g in a pure CO_2 stream at 1139 K.[24] A downside is that CaO is well known for its fast degradation of capacity over multiple cycles due to sintering. Nonetheless, it was shown that such a drawback could be improved by controlling the particle size of the sorbents. In another work by Barker, he showed that the capacity of 10 nm particle size CaO was 16.6 mmol/g in a pure CO_2 stream at 850 K, and 93% of the initial capacity was retained after 30 cycles.[21] Farrauto et al. also tested CaO loaded γ-Al_2O_3 as a CO_2 sorbent at an intermediate temperature of 300°C, and showed that it can sorb CO_2 up to 0.22 mmol CO_2/g sorbent under such conditions, while having much better regenerability than bulk CaO.[20]

1.1.2 CO_2 Hydrogenation

Utilization of CO_2 to produce value added products through catalytic conversion is another field that has been considered for reduction of CO_2 emissions. For example, many researchers have explored the hydrogenation of CO_2 with renewable hydrogen as a way to

produce valuable products such as methane, methanol, alkanes and olefins.[25–29] Especially methanation of CO_2 is reported to be advantageous, because production of methane from CO_2 is directly linked to production of synthetic natural gas (SNG), which can be used again as a fuel source. Indeed, this has been demonstrated on an industrial scale by Audi's "e-gas" facility in Germany. This facility currently produces 1000 metric tons/year of SNG from concentrated CO_2, while capturing 2800 metric tons of CO_2.[30]

The product species formed from hydrogenation of CO_2 depends on both the reaction temperature and pressure. To understand the selectivity to different product species via hydrogenation of CO_2, thermodynamic calculations were done for several possible products of CO_2 hydrogenation, including methane, carbon monoxide, methanol, and ethane (selected as an example of longer hydrocarbons). Equations (1) – (4) each represent a chemical reaction of CO_2 hydrogenation into different products, and the Gibbs free energy was calculated for each reaction at atmospheric pressure and varying temperature. The calculated Gibbs free energy for each reaction is plotted in Figure 1.1.

$$CO_2 + H_2 \rightarrow CO + H_2O \quad (1)$$

$$CO_2 + 4H_2 \rightarrow CH_4 + 2H_2O \quad (2)$$

$$CO_2 + 3H_2 \rightarrow CH_3OH + H_2O \quad (3)$$

$$2CO_2 + 7H_2 \rightarrow C_2H_6 + 4H_2O \quad (4)$$

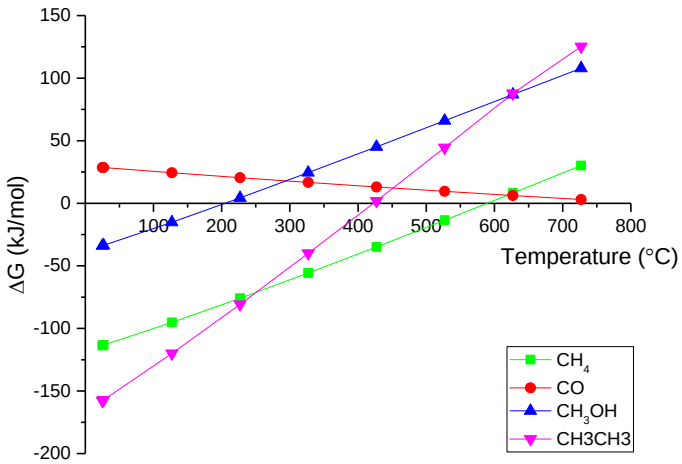

Figure 1.1 - Gibbs free energy for different reactions of CO_2 hydrogenation.

The trends in Figure 1.1 show that at atmospheric pressure, methane is the most favorable product of CO_2 hydrogenation in the temperature range of 250 °C to 600 °C. As temperature is increased above 600 °C, CO became a more favorable product. This observation corresponds to past work regarding methanation of CO_2. At atmospheric pressure, CH_4 is known to be the primary product in the temperature range between 300 °C and 500 °C, [31–33] while selectivity towards CO is known to increase as temperature nears or increases above 600 °C.[34–37] Ruthenium and nickel are the most commonly used catalysts for CO_2 methanation, while copper is commonly used when carbon monoxide is preferred.

Figure 1.1 also shows that methanol is an unfavored product at atmospheric pressure. Ethane, an example used to represent longer hydrocarbons, is favored only at temperatures below 250 °C, but the reaction of CO_2 hydrogenation is kinetically limited at such low temperatures, thereby making hydrocarbons difficult products to obtain at atmospheric pressure. This also corresponds with the general notion that synthesis of higher

hydrocarbons and methanol require both high temperature and pressure.[38–44] Copper catalysts are used in the pressure range between 2MPa and 8MPa, along with temperatures of 200 °C or above, to produce methanol. Like methanol, high pressures, above 1 MPa, and temperatures above 300 °C, are required to synthesize higher hydrocarbons. Iron catalysts are most frequently used to synthesize longer hydrocarbons, but the selectivity towards hydrocarbons can be low, and promoters such as potassium or manganese are often added to improve the selectivity.[43,44]

1.1.3 CO_2 Methanation Mechanism

Various possible CO_2 methanation mechanisms have been proposed for a range of catalysts in the past, but, in general, they can be categorized to two mechanisms : an associative scheme and a dissociative scheme.[45] A figure that represents the two mechanisms is shown below.

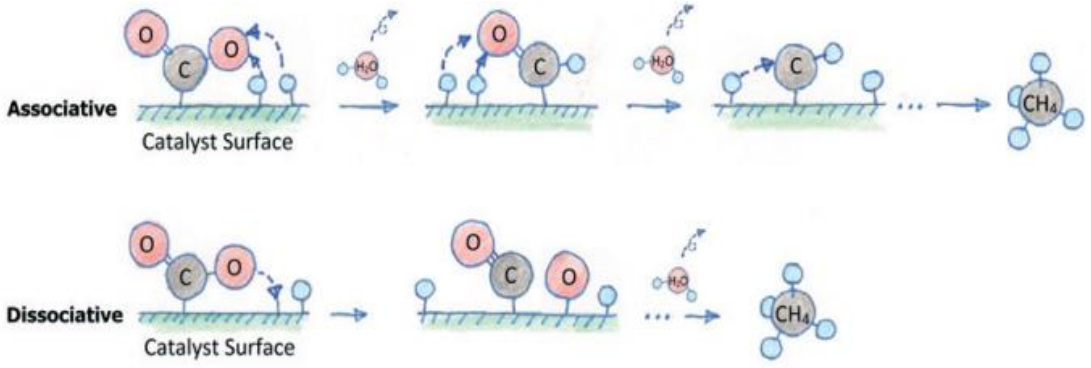

Figure 1.2 - Two proposed mechanisms for CO_2 methanation. Reproduced with permission from ref 45. Copyright Royal Society of Chemistry.

The associative methanation mechanism suggests that CO_2 associatively adsorbs on the catalyst surface, and forms oxygenate intermediates with adsorbed H_2, which subsequently hydrogenates the carbon species into CH_4. This kind of behavior was reported

in multiple works. Aldana et al. reported that in their study of CO_2 methanation over a Ni-ceria-zirconia catalyst that adsorbed carbonate groups (CO_3) were observed initially at a temperature of 150 °C, which eventually hydrogenated to bicarbonate (HCO_3) and formate (HCOO) species as the temperature increased.[46] Similar findings were observed by Upham et al. in their work regarding Ru-ceria catalysts.[47] They reported that introducing CO_2 before H_2 to the catalyst produced CO and methane as products. However, when H_2 was introduced before CO_2, ceria was reduced by H_2, which reduced CO_2 to CO, but did not produce methane as a product, thereby supporting the associative CO_2 methanation mechanism.

The dissociative methanation pathway suggests that CO_2 directly dissociates to CO and O as intermediates during the methanation process. By performing *in situ* diffuse reflectance infrared Fourier transform spectroscopy (DRIFTS) measurements, and employing steady state isotope transient kinetic analysis (SSITKA), Eckle et al. asserted that CO_2 methanation occurs through a dissociative mechanism over a Ru/Al_2O_3 catalyst. Although both carbonyl groups and formate groups were observed on the metal surface, when the reactant CO_2 was switched to an isotopic form, the CO band was reduced quickly, while the formate group showed a slow response. From such observations, they concluded that the formate species are unlikely to be the reaction intermediates in the methanation reaction. Although it is believed that many factors, including temperature, pressure, the ratio of H_2 to CO_2, and type of catalyst used can affect the mechanism of CO_2 methanation, further study is still needed to understand through which mechanism(s) the reaction occurs over different catalysts.

1.2 Combining CO_2 Capture and Conversion

Typically, schemes that combine both CO_2 capture and CO_2 conversion require CO_2 to be separated from the point source, then be stripped from the sorbent, and transported to another vessel for subsequent reaction. In other words, the separation and reaction unit operations are done separately. In particular, the repeated heating and cooling processes for adsorption and desorption steps in the separation are energy intensive processes. As an alternative to use of separate unit operations, Farrauto et al. proposed CO_2 capture and conversion into methane using dual function materials (DFMs) as a possible solution to overcome these challenges. DFMs contain both catalytic and adsorptive sites on a single support. By having both catalyst and adsorbent together, Farrauto asserted that capture and conversion of CO_2 could be done in a single vessel at isothermal conditions, thereby removing both the CO_2 desorption step and CO_2 transportation step. Furthermore, methane, which can be used as fuel source, is produced as the product of this process. Figure 1.3 is a modified schematic from a reference that summarizes the usage of DFMs in a carbon-looping process stream.[48]

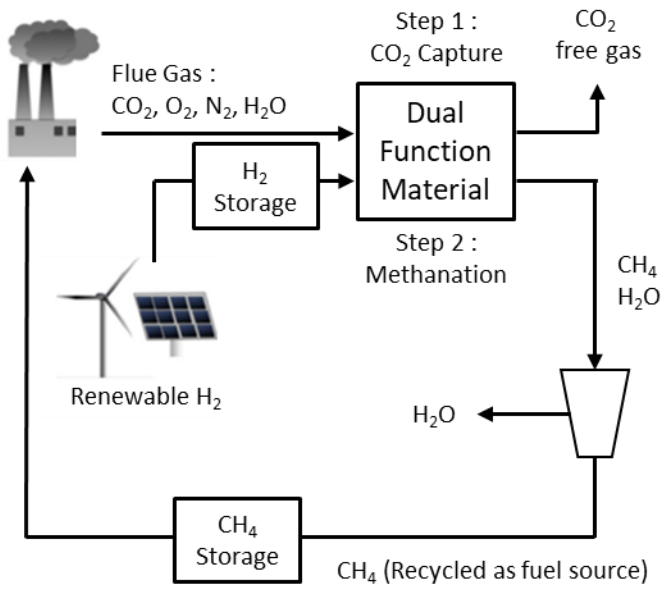

Figure 1.3 - Schematics summarizing capture and conversion of CO_2 to methane. Reproduced with permission from ref 49. Copyright Elesevier.

The proposed DFM application is composed of two steps. First is the capture of CO_2 from flue gas. In this step, CO_2 is captured by the adsorbent sites on the DFM, and the (relatively) CO_2 free flue gas is released to atmosphere. The second step is conversion of CO_2 into CH_4. In this step, the captured CO_2 bound to the sorbent sites of the DFM reacts with hydrogen, which was assumed to be produced from renewable sources, and is converted to methane by catalytic reaction. Then the converted methane is stored and recycled in the energy generation process as a fuel source. This approach can be envisioned as a way for facilities with existing methane combustion equipment to continue to operate the equipment while minimizing CO_2 emissions, in the limit even approaching emission free operation. It also is a way to store electrical energy when it is low cost, by using electrical energy to make hydrogen from electrolysis of water, and making CO_2 into methane.[50]

In his recent works regarding DFMs, Farrauto et al. tested various loadings of ruthenium and nickel, providing catalytic sites, and calcium oxide and sodium oxides, providing CO_2 sorption sites, supported on γ-Al_2O_3. The performance of each DFM was measured by the methanation capacity, which is the mols of methane produced per kg of DFM. The CO_2 capture step was conducted in 10% CO_2/N_2 (30 mL/min) for 30 minutes, and the methanation step was performed in 4% H_2/N_2 (26 mL/min) for 2 h. Both steps were performed at an isothermal temperature of 320 °C. The best performing material was 5% Ru 10% CaO/ γ-Al_2O_3, which showed a methanation capacity of 0.50 mol CH_4/kg DFM. In addition to DFMs listed in Table 1.1, other DFMs or catalytic sorbents composed of Na_2CO_3,[51] K_2CO_3,[52] and MgO[53,54] as adsorptive sites, and Ni[55–57] and Rh[49] as catalytic, hydrogenation sites have been reported as well. It should be noted that catalytic sorbents are different from DFMs in that they are usually synthesized through physical mixing of a sorbent and a catalyst , and unlike DFMs, have adsorptive sites and catalytic sites in mostly separate grains.

Table 1.1 - Methane turnover and methanation capacity during 1 cycle of CO_2 capture and conversion step from literature. Reproduced with permission from ref 48. Copyright Elesevier.

Sample	g-mol CH_4/kg DFM
γ-Al_2O_3	0.00
10% Ru/γ-Al_2O_3	0.10
1% CaO 10%Ru/γ-Al_2O_3	0.19
5% CaO 10%Ru/γ-Al_2O_3	0.27
10% CaO 10%Ru/γ-Al_2O_3	0.30
1.1% Ru 10%CaO/γ-Al_2O_3	0.27
2% Ru 10%CaO/γ-Al_2O_3	0.35
5% Ru 10%CaO/γ-Al_2O_3	0.50
6.8% Ru 10%CaO/γ-Al_2O_3	0.44
10.6% Ru 10%CaO/γ-Al_2O_3	0.46
10% Ru/γ-Al_2O_3 + 10%CaO/γ-Al_2O_3	0.12
10% Ni 6% Na_2O/γ-Al_2O_3	0.27

1.3 Outlook and Scope

There are only a few studies of DFMs and catalytic sorbents, as the study of CO_2 recycling via combined capture and methanation is still in its infancy. Both the CO_2 sorption capacities and methane production capacities are modest, with materials using CaO or $NaCO_3$ as sorptive sites showing CO_2 sorption capacities in range of 0.3 ~ 0.7 mmol CO_2/g, and those using Ru or Ni as catalytic sites showing methane production capacities in range of 0.2 ~ 0.6 mmol CH_4/g. However, because there have been many studies done in the field of CO_2 capture and CO_2 methanation separately, there are many promising materials and synthesis methods that can potentially be combined to reach higher methanation capacities, and thus synthesize catalytic sorbents with higher methanation capacities. Furthermore, within the DFM/catalytic sorbents studied up to date, the mechanism(s) of CO_2 capture and methanation are still not well-developed. To this end, this dissertation focuses on development of new catalytic sorbents with higher CO_2 sorption and methane production capacities than previously studied materials, in simulated flue gas conditions, and on understanding the CO_2 sorption and methanation mechanism(s) over the synthesized catalytic sorbents. Chapter 2 investigates alkali metal promoted MgO for CO_2 capture at concentrations relevant to simulated flue gas (~10% CO_2) at intermediate temperatures (250 °C ~ 300 °C). Chapter 3 focuses on applying the sorbent material investigated in chapter 2 to synthesize catalytic sorbents comprised of $NaNO_3$/MgO + Ru/Al_2O_3, and evaluates the performance of the synthesized material in combined capture and methanation cycles. Chapter 4 focuses on revealing the methanation mechanism over the catalyst materials used in combined capture and methanation cycles. Lastly, chapter 5 outlines current challenges in the field and proposes a future path forward.

1.4 Reference

(1) Solomon, S.; Qin, D.; Manning, M.; Marquis, M.; Averyt, K.; Tignor, M.; Miller, H. *Climate Change 2007: The Physical Science Basis: Contribution of Working Group I to the Fourth Assessment Report of the Intergovernmental Panel on Climate Change*; Cambridge Univ. Press, 2007.

(2) Yu, C.-H.; Huang, C.-H.; Tan, C.-S. A Review of CO_2 Capture by Absorption and Adsorption. *Aerosol Air Qual. Res.* **2012**, *12* (5), 745–769.

(3) Wang, M.; Lawal, A.; Stephenson, P.; Sidders, J.; Ramshaw, C. Post-Combustion CO_2 Capture with Chemical Absorption: A State-of-the-Art Review. *Chem. Eng. Res. Des.* **2011**, *89* (9), 1609–1624.

(4) Mondal, M. K.; Balsora, H. K.; Varshney, P. Progress and Trends in CO_2 Capture/Separation Technologies: A Review. *Energy* **2012**, *46* (1), 431–441.

(5) Yang, H.; Xu, Z.; Fan, M.; Gupta, R.; Slimane, R. B.; Bland, A. E.; Wright, I. Progress in Carbon Dioxide Separation and Capture: A Review. *J. Environ. Sci.* **2008**, *20* (1), 14–27.

(6) Choi, S.; Drese, J. H.; Jones, C. W. Adsorbent Materials for Carbon Dioxide Capture from Large Anthropogenic Point Sources. *ChemSusChem* **2009**, *2* (9), 796–854.

(7) Bailey, D. W.; Feron, P. H. M. Post-Combustion Decarbonisation Processes. *Oil Gas Sci. Technol.* **2005**, *60* (3), 461–474.

(8) Samanta, A.; Zhao, A.; Shimizu, G. K. H.; Sarkar, P.; Gupta, R. Post-Combustion

CO_2 Capture Using Solid Sorbents: A Review. *Ind. Eng. Chem. Res.* **2012**, *51* (4), 1438–1463.

(9) Bollini, P.; Didas, S. A.; Jones, C. W. Amine-Oxide Hybrid Materials for Acid Gas Separations. *J. Mater. Chem.* **2011**, *21* (39), 15100–15120.

(10) Cavenati, S.; Grande, C. A.; Rodrigues, A. E. Adsorption Equilibrium of Methane, Carbon Dioxide, and Nitrogen on Zeolite 13X at High Pressures. *J. Chem. Eng. Data* **2004**, *49* (4), 1095–1101.

(11) Harlick, P. J. E.; Tezel, F. H. An Experimental Adsorbent Screening Study for CO_2 Removal from N2. *Microporous Mesoporous Mater.* **2004**, *76* (1–3), 71–79.

(12) Franchi, R. S.; Harlick, P. J. E.; Sayari, A. Applications of Pore-Expanded Mesoporous Silica. 2. Development of a High-Capacity, Water-Tolerant Adsorbent for CO_2. *Ind. Eng. Chem. Res.* **2005**, *44* (21), 8007–8013.

(13) Chaikittisilp, W.; Khunsupat, R.; Chen, T. T.; Jones, C. W. Poly(Allylamine)–Mesoporous Silica Composite Materials for CO_2 Capture from Simulated Flue Gas or Ambient Air. *Ind. Eng. Chem. Res.* **2011**, *50* (24), 14203–14210.

(14) Yue, M. B.; Sun, L. B.; Cao, Y.; Wang, Y.; Wang, Z. J.; Zhu, J. H. Efficient CO_2 Capturer Derived from As-Synthesized MCM-41 Modified with Amine. *Chem. - A Eur. J.* **2008**, *14* (11), 3442–3451.

(15) Yue, M. B.; Chun, Y.; Cao, Y.; Dong, X.; Zhu, J. H. CO_2 Capture by As-Prepared SBA-15 with an Occluded Organic Template. *Adv. Funct. Mater.* **2006**, *16* (13),

1717–1722.

(16) Xu, X.; Song, C.; Andresen, J. M.; Miller, B. G.; Scaroni, A. W. Novel Polyethylenimine-Modified Mesoporous Molecular Sieve of MCM-41 Type as High-Capacity Adsorbent for CO_2 Capture. *Energy and Fuels* **2002**, *16* (6), 1463–1469.

(17) Eddaoudi, M.; Kim, J.; Rosi, N.; Vodak, D.; Wachter, J.; Keeffe, M. O.; Yaghi, O. M. Systematic Design of Pore Size and Functionality in Isoreticular MOFs and Their Application in Methane Storage. *Science (80-.).* **2002**, *295* (5554), 469–472.

(18) Millward, A. R.; Yaghi, O. M. Metal-Organic Frameworks with Exceptionally High Capacity for Storage of Carbon Dioxide at Room Temperature. *J. Am. Chem. Soc.* **2005**, *127* (51), 17998–17999.

(19) Arstad, B.; Fjellvåg, H.; Kongshaug, K. O.; Swang, O.; Blom, R. Amine Functionalised Metal Organic Frameworks (MOFs) as Adsorbents for Carbon Dioxide. *Adsorption* **2008**, *14* (6), 755–762.

(20) Gruene, P.; Belova, A. G.; Yegulalp, T. M.; Farrauto, R. J.; Castaldi, M. J. Dispersed Calcium Oxide as a Reversible and Efficient CO_2 Sorbent at Intermediate Temperatures. *Ind. Eng. Chem. Res.* **2011**, *50* (7), 4042–4049.

(21) Barker, R. The Reactivity of Calcium Oxide towards Carbon Dioxide and Its Use for Energy Storage. *J. Appl. Chem. Biotechnol.* **1974**, *24*, 221–227.

(22) Bhatia, S.; Perlmutter, D. Effect of the Product Layer on the Kinetics of the CO_2

Lime Reaction. *AIChE J.* **1983**, *29* (1), 79–86.

(23) Lee, S. C.; Choi, B. Y.; Lee, T. J.; Ryu, C. K.; Ahn, Y. S.; Kim, J. C. CO_2 Absorption and Regeneration of Alkali Metal-Based Solid Sorbents. *Catal. Today* **2006**, *111* (3–4), 385–390.

(24) Barker, R. The Reversibility of the Reaction $CaCO_3 \rightleftarrows CaO+CO_2$. *J. Appl. Chem. Biotechnol.* **2007**, *23* (10), 733–742.

(25) Porosoff, M. D.; Yan, B.; Chen, J. G. Catalytic Reduction of CO_2 by H_2 for Synthesis of CO, Methanol and Hydrocarbons: Challenges and Opportunities. *Energy Environ. Sci.* **2016**, *9* (1), 62–73.

(26) Wang, W.; Wang, S.; Ma, X.; Gong, J. Recent Advances in Catalytic Hydrogenation of Carbon Dioxide. *Chem. Soc. Rev.* **2011**, *40* (7), 3703–3727.

(27) Centi, G.; Quadrelli, E. A.; Perathoner, S. Catalysis for CO_2 Conversion: A Key Technology for Rapid Introduction of Renewable Energy in the Value Chain of Chemical Industries. *Energy Environ. Sci.* **2013**, *6* (6), 1711.

(28) Su, X.; Xu, J.; Liang, B.; Duan, H.; Hou, B.; Huang, Y. Catalytic Carbon Dioxide Hydrogenation to Methane: A Review of Recent Studies. *J. Energy Chem.* **2016**, *25* (4), 553–565.

(29) Rönsch, S.; Schneider, J.; Matthischke, S.; Schlüter, M.; Götz, M.; Lefebvre, J.; Prabhakaran, P.; Bajohr, S. Review on Methanation - From Fundamentals to Current Projects. *Fuel* **2016**, *166*, 276–296.

(30) Wellnitz, J.; Subic, A.; Trufin, R. *Sustainable Automotive Technologies 2013*; Springer, 2012.

(31) Garbarino, G.; Bellotti, D.; Riani, P.; Magistri, L.; Busca, G. Methanation of Carbon Dioxide on Ru/Al_2O_3 and Ni/Al_2O_3 Catalysts at Atmospheric Pressure: Catalysts Activation, Behaviour and Stability. *Int. J. Hydrogen Energy* **2015**, *40* (30), 9171–9182.

(32) Garbarino, G.; Riani, P.; Magistri, L.; Busca, G. A Study of the Methanation of Carbon Dioxide on Ni/Al_2O_3catalysts at Atmospheric Pressure. *Int. J. Hydrogen Energy* **2014**, *39* (22), 11557–11565.

(33) Riani, P.; Garbarino, G.; Lucchini, M. A.; Canepa, F.; Busca, G. Unsupported versus Alumina-Supported Ni Nanoparticles as Catalysts for Steam/Ethanol Conversion and CO_2 Methanation. *J. Mol. Catal. A Chem.* **2014**, *383–384*, 10–16.

(34) Stone, F. S.; Waller, D. Cu-ZnO and $Cu-ZnO/Al_2O_3$ catalysts for the Reverse Water-Gas Shift Reaction. The Effect of the Cu/Zn Ratio on Precursor Characteristics and on the Activity of the Derived Catalysts. *Top. Catal.* **2003**, *22* (3–4), 305–318.

(35) Liu, Y.; Liu, D. Study of Bimetallic $Cu-Ni/\gamma-Al_2O_3$ Catalysts for Carbon Dioxide Hydrogenation. *Int. J. Hydrogen Energy* **1999**, *24* (4), 351–354.

(36) Chen, C. S.; Cheng, W. H.; Lin, S. S. Study of Reverse Water Gas Shift Reaction by TPD, TPR and CO_2 Hydrogenation over Potassium-Promoted Cu/SiO_2 Catalyst. *Appl. Catal. A Gen.* **2002**, *238* (1), 55–67.

(37) Chen, C. S.; Cheng, W. H.; Lin, S. S. Study of Iron-Promoted Cu/SiO_2 catalyst on High Temperature Reverse Water Gas Shift Reaction. *Appl. Catal. A Gen.* **2004**, *257* (1), 97–106.

(38) Toyir, J.; Ramírez De La Piscina, P.; Fierro, J. L. G.; Homs, N. Highly Effective Conversion of CO_2 to Methanol Over Supported and Promoted Copper-Based Catalysts: Influence of Support and Promoter. *Appl. Catal. B Environ.* **2001**, *29* (3), 207–215.

(39) Toyir, J.; De la Piscina, P. R.; Fierro, J. L. G.; Homs, N. Catalytic Performance for CO_2 Conversion to Methanol of Gallium-Promoted Copper-Based Catalysts: Influence of Metallic Precursors. *Appl. Catal. B Environ.* **2001**, *34* (4), 255–266.

(40) Liu, J.; Shi, J.; He, D.; Zhang, Q.; Wu, X.; Liang, Y.; Zhu, Q. Surface Active Structure of Ultra-Fine Cu/ZrO_2 Catalysts Used for the CO_2+H_2 to Methanol Reaction. *Appl. Catal. A Gen.* **2001**, *218* (1–2), 113–119.

(41) Guo, X.; Mao, D.; Lu, G.; Wang, S.; Wu, G. Glycine-Nitrate Combustion Synthesis of CuO-ZnO-ZrO_2 Catalysts for Methanol Synthesis from CO_2 Hydrogenation. *J. Catal.* **2010**, *271* (2), 178–185.

(42) Słoczyński, J.; Grabowski, R.; Kozłowska, A.; Olszewski, P.; Stoch, J.; Skrzypek, J.; Lachowska, M. Catalytic Activity of the M/($3ZnO{\cdot}ZrO_2$) System (M = Cu, Ag, Au) in the Hydrogenation of CO_2 to Methanol. *Appl. Catal. A Gen.* **2004**, *278* (1), 11–23.

(43) Riedel, T.; Claeys, M.; Schulz, H.; Schaub, G.; Nam, S.-S.; Jun, K.-W.; Choi, M.-

J.; Kishan, G.; Lee, K.-W. Comparative Study of Fischer–Tropsch Synthesis with H_2/CO and H_2/CO_2 Syngas Using Fe- and Co-Based Catalysts. *Appl. Catal. A Gen.* **1999**, *186* (1–2), 201–213.

(44) Dorner, R. W.; Hardy, D. R.; Williams, F. W.; Willauer, H. D. K and Mn Doped Iron-Based CO_2 Hydrogenation Catalysts: Detection of $KAlH_4$ as Part of the Catalyst's Active Phase. *Appl. Catal. A Gen.* **2010**, *373* (1–2), 112–121.

(45) Miao, B.; Ma, S. S. K.; Wang, X.; Su, H.; Chan, S. H. Catalysis Mechanisms of CO_2 and CO Methanation. *Catal. Sci. Technol.* **2016**, *6* (12), 4048–4058.

(46) Aldana, P. A. U.; Ocampo, F.; Kobl, K.; Louis, B.; Thibault-Starzyk, F.; Daturi, M.; Bazin, P.; Thomas, S.; Roger, A. C. Catalytic CO_2 Valorization into CH_4 on Ni-Based Ceria-Zirconia. Reaction Mechanism by Operando IR Spectroscopy. *Catal. Today* **2013**, *215*, 201–207.

(47) Upham, D. C.; Derk, A. R.; Sharma, S.; Metiu, H.; McFarland, E. W. CO_2 Methanation by Ru-Doped Ceria: The Role of the Oxidation State of the Surface. *Catal. Sci. Technol.* **2015**, *5* (3), 1783–1791.

(48) Duyar, M. S.; Treviño, M. A. A.; Farrauto, R. J. Dual Function Materials for CO_2 Capture and Conversion Using Renewable H_2. *Appl. Catal. B Environ.* **2015**, *168–169*, 370–376.

(49) Duyar, M. S.; Wang, S.; Arellano-Treviño, M. A.; Farrauto, R. J. CO_2 Utilization with a Novel Dual Function Material (DFM) for Capture and Catalytic Conversion to Synthetic Natural Gas: An Update. *J. CO_2 Util.* **2016**, *15*, 65–71.

(50) Rosa, R. The Role of Synthetic Fuels for a Carbon Neutral Economy. *C - J. Carbon Res.* **2017**, *3* (2).

(51) Bermejo-López, A.; Pereda-Ayo, B.; González-Marcos, J. A.; González-Velasco, J. R. Mechanism of the CO_2 Storage and in Situ Hydrogenation to CH_4. Temperature and Adsorbent Loading Effects over Ru-CaO/Al_2O_3 and Ru-Na_2CO_3/Al_2O_3 Catalysts. *Appl. Catal. B Environ.* **2019**, *256*, 117845.

(52) Omodolor, I. S.; Otor, H. O.; Andonegui, J. A.; Allen, B. J.; Alba-Rubio, A. C. Dual-Function Materials for CO_2 Capture and Conversion : A Review. *Ind. Eng. Chem. Res.* **2020**, *59*, 17612–17631.

(53) Hu, Y.; Guo, Y.; Sun, J.; Li, H.; Liu, W. Progress in MgO Sorbents for Cyclic CO_2 Capture : Review. *J. Mater. Chem. A* **2019**, *7*, 20103–20120.

(54) Sun, H.; Zhang, Y.; Guan, S.; Huang, J.; Wu, C. Direct and Highly Selective Conversion of Captured CO_2 into Methane through Integrated Carbon Capture and Utilization over Dual Functional Materials. *J. CO_2 Util.* **2020**, *38*, 262–272.

(55) Arellano-Treviño, M. A.; He, Z.; Libby, M. C.; Farrauto, R. J. Catalysts and Adsorbents for CO_2 Capture and Conversion with Dual Function Materials : Limitations of Ni-Containing DFMs for Flue Gas Applications. *J. CO_2 Util.* **2019**, *31*, 143–151.

(56) Proaño, L.; Arellano-treviño, M. A.; Farrauto, R. J.; Figueredo, M.; Jeong-Potter, C. W.; Cobo, M. Mechanistic Assessment of Dual Function Materials, Composed of Ru-Ni , Na_2O/Al_2O_3 and Pt-Ni , Na_2O/Al_2O_3 , for CO_2 Capture and Methanation by

in-Situ DRIFTS. *Appl. Surf. Sci.* **2020**, *533*, 147469.

(57) Bermejo-López, A.; Pereda-Ayo, B.; González-Marcos, J. A.; González-Velasco, J. R. Ni Loading Effects on Dual Function Materials for Capture and In-Situ Conversion of CO_2 to CH_4 Using CaO or Na_2CO_3. *J. CO_2 Util.* **2019**, *34*, 576–587.

CHAPTER 2. $NANO_3$ -PROMOTED MESOPOROUS MGO FOR HIGH-CAPACITY CO_2 CAPTURE FROM SIMULATED FLUE GAS WITH ISOTHERMAL REGENERATION

Parts of this chapter are adapted from 'Park, S. J.; Kim, Y.; Jones, C. W., $NaNO_3$ -Promoted Mesoporous MgO for High-Capacity CO_2 Capture from Simulated Flue Gas with Isothermal Regeneration. *ChemSusChem* **2020**, 13 (11), 2988-2995' with permission from Wiley and Sons.

2.1 Introduction

Among many solid materials, magnesium oxide is a promising sorbent material due to its wide range of operating temperatures for CO_2 sorption, high theoretical CO_2 sorption capacity, low cost, and lower energy requirement for regeneration relative to related metal oxide materials, such as calcium oxide or lithium zirconate.[1–5] Its potential as a promising candidate for CO_2 sorption grew even further following a report that porous MgO promoted by molten alkaline metals enabled higher CO_2 adsorption capacity and faster uptake kinetics in an intermediate temperature range (250–400 °C) than a bare MgO sorbent.[6–8] As a result, there has been a growing interest in using such molten alkaline metal promoted MgO for CO_2 capture in such an intermediate temperature range.[21-42] Zhang et al showed that a CO_2 adsorption capacity of 15 mmol CO_2/g could be obtained by $NaNO_3$ promoted MgO,[6] while Zhao et al reported that MgO promoted by an $NaNO_3$ and $NaNO_2$ binary mixture showed an adsorption capacity of 18.9 mmol CO_2/g.[25] Harada et al. also synthesized (Li-Na-K)NO_3 coated MgO particles that showed a adsorption capacity as high as 15.7 mmol CO_2/g.[9]

However, most prior work has focused on sorbing concentrated CO_2, typically with a molar concentration of 85% and above, targeting pre-combustion CO_2 capture applications. In contrast, little work has been done focused on sorption using CO_2 concentrations relevant to flue gas separations or other applications. Pre-combustion CO_2 capture is typically performed in modern integrated gasification combined cycle (IGCC) plants, but is not well-suited for pulverized coal or gas-fired power plants, which comprise most currently existing plants.[32] To explore if alkaline metal promoted MgO materials may be more widely applicable than simply for pre-combustion capture, one must explore CO_2 capture using flue gas compositions relevant to post-combustion capture.

In this chapter, $NaNO_3$ promoted mesoporous MgO was used to evaluate how effective such materials can be for capture of CO_2 under conditions relevant to flue gas capture (10% CO_2 at ~1 bar total pressure). In parallel, we sought to further understand the role of the sodium promoters in the adsorption of CO_2. Additionally, isothermal regeneration of the sorbent over multiple cycles is shown using a partially desorbed $NaNO_3$ promoted MgO material, which suggests the potential for concentration swing applications in the absence of a thermal input. Such a process could reduce complexity as well as energy use, providing significant advantage.

2.2 Experimental Section

2.2.1 Chemicals and Materials

All chemical reagents used for synthesis of sorbents, including urea (ACS reagent, 99%), magnesium acetate tetrahydrate (ReagentPlus, 99%), ammonium solution (2 M in methanol), and sodium nitrate were obtained from Sigma Aldrich. 10% CO_2/He, N_2, and He cylinders were obtained from Airgas.

2.2.2 Synthesis of Mesoporous MgO and Impregnation of $NaNO_3$

Mesoporous MgO was synthesized through a modified method described in the literature.[25] First, 28.83 g of urea and 34.31 g of magnesium acetate tetrahydrate were added to 100 mL of distilled water and stirred for 1 h to ensure all salts were completely dissolved. Then 0.2 mL of ammonia solution was added to the mixture and stirred for an additional 30 min. The solution was then equally distributed to 4 different 45 mL Teflon autoclaves, and heated at 180 °C for 5 h. After cooling to room temperature, white precipitates were recovered by filtration and washed with 2 L of distilled water followed by 2 L of ethanol. The white powder was then calcined in static air at 600 °C for 5 h.

To synthesize $NaNO_3$ promoted MgO sorbents, different amounts of $NaNO_3$ were dissolved in distilled water to obtain stock solutions of different $NaNO_3$ concentrations. Then, solutions of different $NaNO_3$ concentration were loaded onto the synthesized mesoporous MgO support through incipient wetness impregnation to obtain different loadings of $NaNO_3$ within the sorbents. $NaNO_3$ impregnated sorbents were then calcined at 350 °C in static air for 30 min.

2.2.3 Material Characterization

N_2 physisorption was performed using a Micromeritics Tristar II 3020 at 77K. Approximately 150 mg of sorbents were used for each measurement and all sorbents were degassed at 110 °C for 6 h prior to N_2 physisorption measurements. Scanning electronic microscopy (SEM) was performed using a Hitachi 8230. X-ray diffraction (XRD) was performed on an Empyrean PANalytical diffractometer using Cu Kα radiation operated at

40kV and 40mA. XRD patterns were obtained in the range from 25 ° to 80° 2θ angle using a 0.013° step size.

2.2.4 In-situ XRD measurements

For in-situ XRD under nitrogen flow, XRD patterns were obtained from 230 °C to 320 °C at a 10 °C interval, while the temperature was increased in between target temperatures at a 5°C/min ramp. For in-situ XRD under CO_2 flow, samples were pretreated under 90 mL/min of N_2 flow at 350 °C for 2 h. Samples were then cooled to 260°C, followed by exposure to 90 mL/min of 10%/He flow. XRD patterns were obtained in the range from 25 ° to 80° 2θ angle using a 0.026° step size.

2.2.5 In-situ FTIR spectroscopy

A Thermo Nicolet iS10 IR spectrometer with a mercury cadmium telluride (MCT) detector was used for in-situ FTIR spectroscopy measurements. Samples were pressed at 1000 psi into a wafer, which was then placed in a Harrick transmission flow cell equipped with a BaF_2 window. The sample in wafer form was pretreated under He flow of 50 mL/min at a temperature of 325 °C for 2 h. Then the temperature was cooled to 260 °C, and once the temperature stabilized at 260 °C, 10% CO_2/N_2 was flowed into the cell at 50 mL/min.

2.2.6 CO_2 sorption studies

A TA instrument Q500 TGA was used to measure sorption capacities of the sorbents. Approximately 30 mg of sorbent was loaded on a platinum sample pan. The sample was heated to 350 °C at a rate of 10 °C/min under a helium flow of 90 mL/min. The sample was pretreated at 350 °C for 2 h under helium flow to desorb sorbed humidity

or CO_2 from the sample. Then the temperature was cooled to the temperature of interest and equilibrated to the set temperature in 15 min. The gas was then switched from helium to 10% CO_2/He at 90 mL/min, and the sample was exposed to 10% CO_2/He flow for 12 h. The mass change was measured, and the sorption capacity was calculated based on the mass increase.

For sorption capacity measurements of the partially desorbed sample, the selected sorbent was exposed to CO_2/He flow for 12 h at 260 °C after the standard degassing pretreatment. Then, the gas was switched to helium flow and the temperature was increased to 350 °C at 10 °C/min. The sorbent was heated at 350 °C for 15 min, and temperature was cooled to the temperature of interest and equilibrated to the set temperature in 5 min. The gas was then switched to 10% CO_2/He flowing at 90 mL/min and the sorbents were exposed to the CO_2 flow for 3 h.

2.2.7 Induction period calculation

The length of the induction periods was calculated based on data presented in Figure 2.3, Figure 2.4, Figure 2.8, and Figure A.5. For induction period calculations using data from Figure 2.3 and Figure 2.4, data points every 8 minutes were selected, and second derivative was taken using a numerical method. For Figure 2.8 and Figure A.5, data points every 3 min were selected, and again the second derivative was taken using a numerical method. For all cases, the time point where the second derivative had the highest value was selected as the length of the induction period for CO_2 sorption with the given sorbent sample and employed experimental conditions.

2.3 Results and Discussion

Sorbents were prepared by impregnating different loadings of $NaNO_3$ salts onto lab-synthesized mesoporous MgO through incipient wetness impregnation. The sorbents were labeled with the following naming scheme: MgO_$NaNO_3$_x, where x represents the molar ratio between the $NaNO_3$ promoter and the MgO support. The porosity of the synthesized sorbents was studied through nitrogen physisorption experiments (Figure 2.1). All samples showed type IV isotherms, as commonly observed for different mesoporous materials.[33,34] The fact that almost no uptake was observed in the lower relative pressure regime indicates that minimal micropores exist in the sorbents and the hysteresis curve observed between relative pressures of 0.8 and 1.0 indicates the presence of a large amount of mesopores. Increased $NaNO_3$ loading resulted in decreased N_2 uptake, likely due to the presence of $NaNO_3$ promoters contained within the mesopores of the MgO. The isotherm data were analyzed to calculate key physical characteristics such as the BET surface area and pore volume, which are shown in Table 2.1.

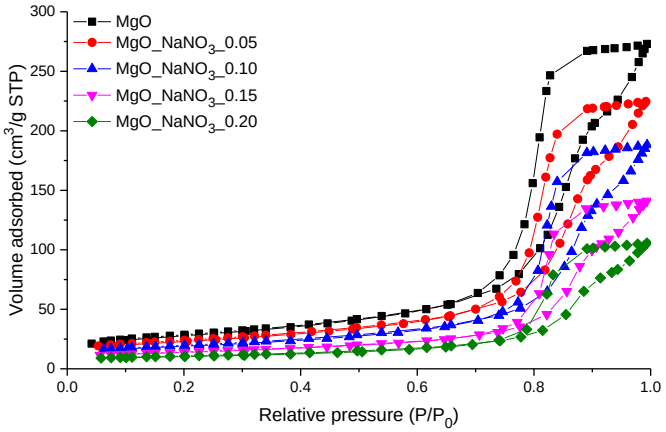

Figure 2.1 - Nitrogen physisorption isotherms of mesoporous MgO promoted by different loadings of $NaNO_3$.

Table 2.1. Textural properties of $NaNO_3$ promoted MgO sorbents

	BET surface area (m^2/g)	Pore Volume (cm^3/g)
Bare MgO	99	0.42
MgO_$NaNO_3$_0.05	82	0.35
MgO_$NaNO_3$_0.10	67	0.29
MgO_$NaNO_3$_0.15	48	0.22
MgO_$NaNO_3$_0.20	36	0.16

The crystalline structure of the sorbents was also investigated using X-ray diffraction (XRD), as shown in Figure 2.2. The XRD patterns showed that a crystalline MgO support was synthesized and confirmed the presence of crystalline $NaNO_3$ within the synthesized sorbent, although it should be noted that at the working temperatures for CO_2 capture, the promoters may not remain crystalline (vide infra).

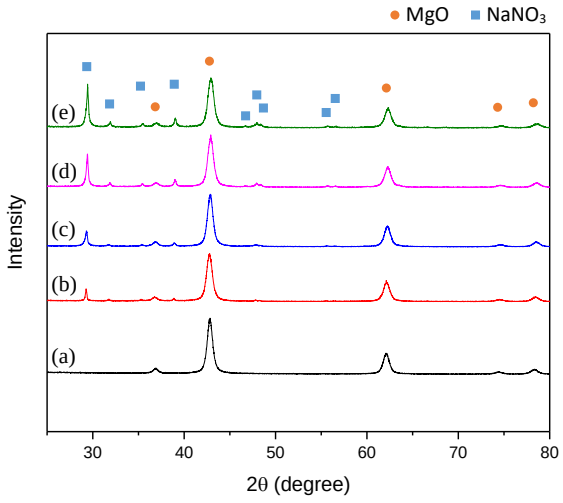

Figure 2.2. XRD patterns of (a) bare MgO support, (b) MgO_$NaNO_3$_0.05, (c) MgO_$NaNO_3$_ 0.10, (d) MgO_$NaNO_3$_0.15, (e) MgO_$NaNO_3$_0.20, taken at ambient temperature.

The CO_2 sorption capacity of the materials was measured gravimetrically using a TA Instruments Q500 TGA. CO_2 sorption was performed at 250 °C for 12 h with 10% CO_2 balanced by helium, and the sorption capacity is shown in Figure 2.3. Bare MgO showed a very small 12 h sorption capacity of only 0.13 mmol CO_2/g. A small amount of CO_2 was sorbed immediately upon exposure to CO_2 and the sorption capacity remained essentially constant for the remainder of 12 h. An increase in the sorption capacity was observed as the molar ratio between $NaNO_3$ and MgO increased to 0.10, yielding an sorption capacity of 4.66 mmol CO_2/g and 9.32 mmol CO_2/g at a molar ratio of 0.05 and 0.10, respectively. However, with a further increase in the ratio above 0.10, a decrease in in the sorption capacity was observed, showing 8.27 mmol CO_2/g and 7.33 mmol CO_2/g at molar ratios of 0.15 and 0.20, respectively. These observations indicate that an ideal loading of $NaNO_3$ promoter exists for this support, which gives the highest sorption capacity for this family of materials.

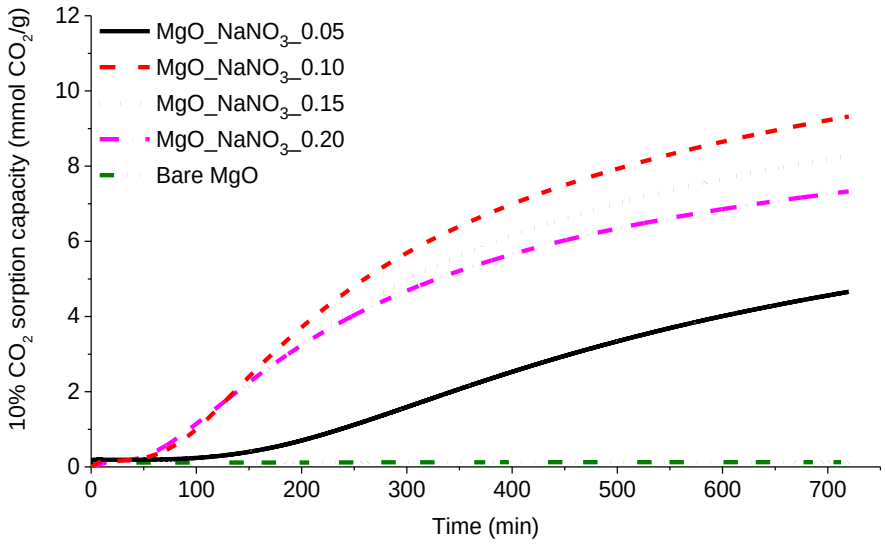

Figure 2.3. CO_2 sorption capacities measured at 250 °C under simulated, dry flue gas conditions for mesoporous MgO promoted by different loadings of $NaNO_3$.

MgO_$NaNO_3$_0.10, which showed the highest sorption capacity at 250 °C, was selected for further study at varying temperatures. Similar adsorption experiments were performed for 12 h CO_2 exposures at temperatures between 230 °C and 280 °C, and the sorption uptake curves at each temperature are shown in Figure 2.4. The 12 h sorption capacity increased with an increase in temperature from 230 °C to 260 °C, showing the highest sorption capacity of 11.2 mmol CO_2/g at 260 °C. However, with further increase in temperature above 260 °C, the sorption capacity decreased. At 280 °C, the sorption demonstrated a prolonged induction period throughout the entire 12 h of CO_2 exposure, showing only 0.18 mmol CO_2/g uptake, and never quite showing a significant increase in uptake rate that was observed at the other temperatures tested. Such results differed from previous studies that were performed at high concentrations of CO_2 (above molar concentration of 85% CO_2) in that similar materials studied by others typically showed the highest CO_2 capacity in the temperature range between 300 °C and 350 °C. [6,7,9,12,14,16,24–26,35,36]

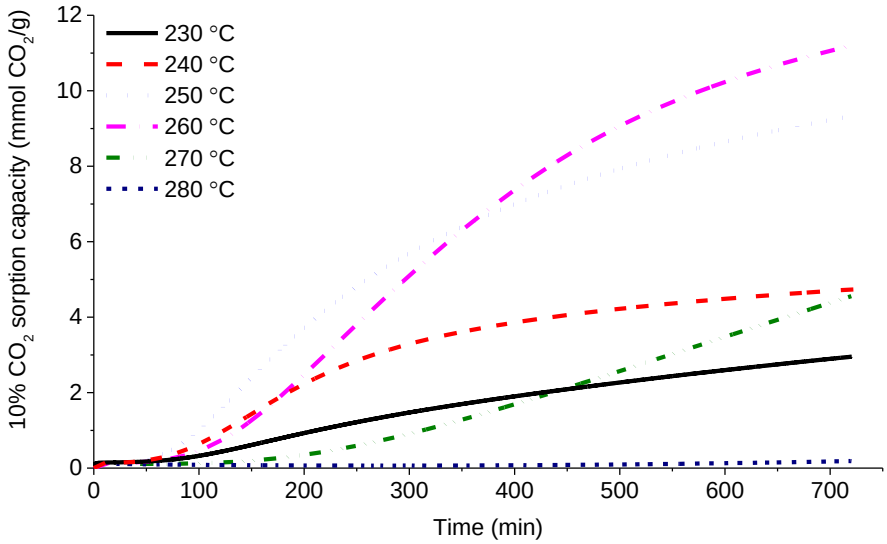

Figure 2.4. CO_2 sorption capacity measured at different temperatures between 230 °C and 280 °C under simulated flue gas for 12 h for the MgO_$NaNO_3$_0.10 sample.

It should be noted that for all loadings of $NaNO_3$ and for all the temperatures tested, the sorption curves showed a similar shape, where a slow induction period was observed initially upon exposure to CO_2, then followed by a faster uptake, yielding an S-shaped curve. Harada et al hypothesized that the sorption curve could be divided into three stages: (i) the initial sorption of CO_2 on the exposed MgO surface, (ii) a rapid increase in uptake rate caused by nucleation and nuclei growth of $MgCO_3$, and (iii) a slowing of CO_2 uptake rate due to diffusion limitations experienced by CO_2, caused by formation of carbonate layers.[7] Although the reason for the induction period at the initial stage of CO_2 sorption remained unclear, they hypothesized that the CO_2 initially dissolved in the molten $NaNO_3$ medium, and then interacted with oxide ions (O^{2-}) within the nitrate medium to form carbonate ions (CO_3^{2-}). The formed carbonate ions have improved contact with MgO than when no nitrate medium was present (e.g. in Na free materials) and readily reacts with MgO and initiates nucleation of $MgCO_3$.[7,26]

In general, our CO_2 sorption capacity measurements for different loadings of $NaNO_3$ on MgO and under different temperatures were in good agreement with such a hypothesis. Figure A.1 shows that increasing the $NaNO_3$ loading could shorten the induction period in the initial stage of CO_2 sorption. However, as observed in Figure 2.3, despite shorter induction periods, the CO_2 uptake for samples of higher $NaNO_3$ loading tended to slow down faster than the MgO_$NaNO_3$_0.10 sample. All three compositions with a $NaNO_3$:MgO ratio of 0.10, 0.15, 0.20 had similar uptake until the 150 min exposure point. However, as the sorption time exceeded 150 min, the increase in uptake tended to slow as the $NaNO_3$ loading increased, consistent with higher diffusion limitations experienced by CO_2 as the $NaNO_3$ loading increased.

Sorption capacity measurements at different temperatures corresponded quite well with the working hypothesis of Harada et al. as well. Under the given hypothesis, the solubility of CO_2 in molten sodium nitrate medium plays a crucial role in determining the length of the induction period. Since the solubility of a gas within a liquid medium tends to decrease at higher temperatures, the induction period should increase as the temperature increases, which corresponds well with our data, as shown in Figure A.2. However, in the following stage after the induction period, the growth phase of the $MgCO_3$ nuclei, carbonation would occur more rapidly at higher temperature, due to increased reaction kinetics. The competing effect between these two factors may be the reason why the highest 12 h sorption capacity was observed at a temperature of 260 °C. Although the induction period increased as the temperature increased, at temperatures below 260 °C, enough CO_2 was likely dissolved in the molten sodium nitrate medium so that when the temperature increased, the rate of nuclei growth increased as well. However, the rate of nuclei growth

would be affected not only by temperature, but also by the concentration of CO_2 within the molten medium. Thus, as temperature increased above 260 °C, the solubility effect may become more significant than the kinetic effect, thereby causing a decrease in the 12 h sorption capacity. At 280 °C, it is likely that so little CO_2 was dissolved within the molten salt medium that the increase in uptake rate was never observed. It should also be noted that at temperatures between 230 °C and 250 °C, the decrease in the induction period was much lower (Figure A.2) than over the temperature range from 250 °C to 280 °C, where a more pronounced reduction was evident.

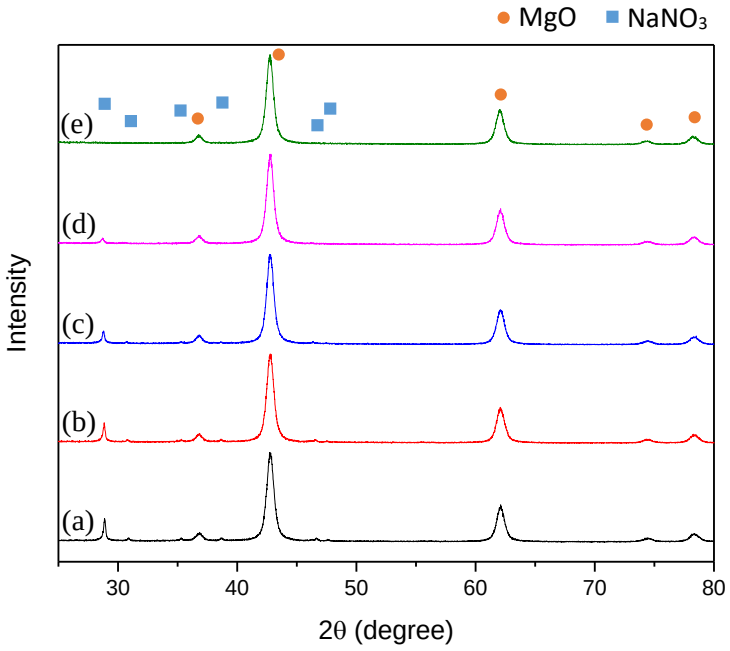

Figure 2.5. XRD patterns of MgO_$NaNO_3$_0.10 taken at (a) 30 °C, (b) 230 °C, (c) 240 °C, (d) 250 °C, (e) 260 °C under a nitrogen purge.

As observed in Figure 2.5, XRD peaks indicative of the crystalline structure of $NaNO_3$ were still observed at temperatures between 230 °C and 260 °C. The intensity of such characteristic peaks decreased as the temperature increased, and completely

disappeared at a temperature of 260 °C. Thus, it is hypothesized that in the temperature range between 230 °C and 260 °C, $NaNO_3$ was in a partially molten state, and more molten sodium nitrate medium became available to dissolve CO_2 as the temperature increased.

This interpretation of our data also corresponds with previous reports showing the highest sorption capacity observed at temperatures between 300 °C and 325 °C when testing with higher partial pressures of CO_2. Even with lower solubility of CO_2 in $NaNO_3$ due to increased temperature, at a higher partial pressure of CO_2, more CO_2 could be dissolved in the molten sodium nitrate medium. To test such a hypothesis, similar sorption experiment were run under pure CO_2 at 280 °C, as shown in Figure A.5. While a low sorption capacity of 0.18 mmol CO_2/g was obtained at 280 °C under 10% CO_2/He, a much improved sorption capacity of 16.7 mmol CO_2/g was observed using pure CO_2 (Figure A.5 (a)). In these experiments, while the CO_2 concentration was increased 10 fold, the sorption capacity was >90 times higher for the pure CO_2 case. Also, while the sorption was in the induction phase throughout the entire 12 h during exposure to 10% CO_2/He, a much shortened induction period of 12 minutes (Figure A.5 (b)) was observed using pure CO_2. Such observations further support the notion that the concentration of CO_2 in the molten alkali medium is an important factor that affects the length of induction period.

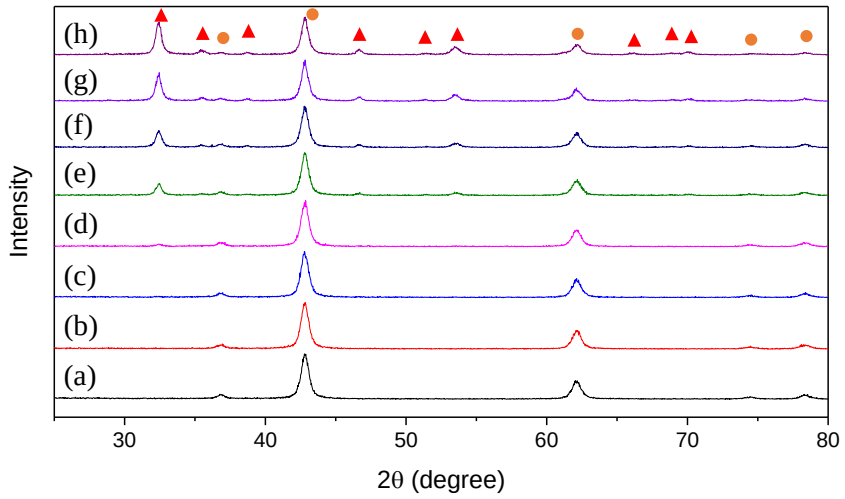

Figure 2.6. In-situ XRD patterns of MgO_$NaNO_3$_0.10 taken (a) 0 min, (b) 30 min, (c) 60 min, (d) 90 min, (e) 120 min, (f) 180 min, (g) 360 min, (h) 720 min after exposure to 10% CO2/He flow at 260 °C.

To observe the crystalline structure of $NaNO_3$ promoted MgO during CO_2 sorption, in-situ XRD patterns of MgO_$NaNO_3$_0.10 were taken at different times during exposure to a flow of 10% CO_2/He at 260 °C, as shown in Figure 2.6. It should be noted that peaks indicating crystalline $NaNO_3$ were not observed in any of the patterns. As previously mentioned, $NaNO_3$ likely becomes completely molten by a temperature of 260 °C, thereby losing its crystalline structure. XRD patterns taken in the first 60 min of exposure to 10% CO_2/He flow showed that essentially no change in crystalline structure was observed in the first hour of CO_2 sorption. However, the pattern taken after 90 min showed a small peak at 32.4°, and the intensity of this peak continued to increase for the rest of the 12 h experiment. The identification of the newly formed peaks after 12 h of CO_2 sorption showed that $MgCO_3$ was formed as a result of carbonation of MgO.[6,7] The XRD patterns indicate that nucleation of $MgCO_3$ occurred between 60 min and 90 min after CO_2 sorption, which also corresponded well with the calculated 72 min induction period (Figure A.2) for the same

sample in the TGA at the same temperature. Such observation indicate that the induction period in the initial period of CO_2 sorption is likely occurring due to the time needed for the nucleation of $MgCO_3$.

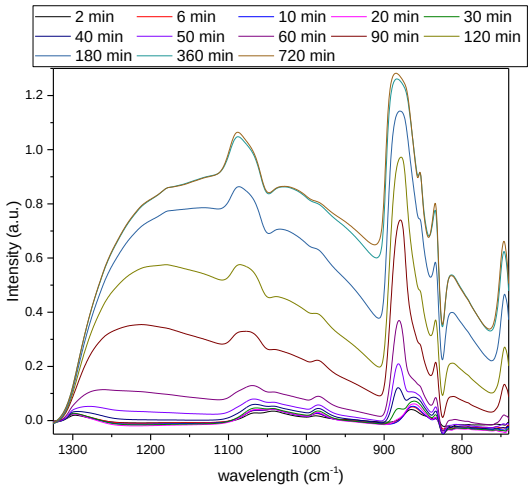

Figure 2.7. In-situ FTIR spectra of MgO_$NaNO_3$_0.10 taken during exposure to 10% CO_2/He at 260 °C.

CO_2 sorption by the MgO_$NaNO_3$_0.10 sample was further probed at 260 °C through in-situ transmission IR spectroscopy, to better understand the formation of different CO_2 species during CO_2 sorption. The time-resolved FTIR spectra during CO_2 sorption are shown in Figure 2.7. Bands at 865 cm^{-1} and 1296 cm^{-1} are immediately observed, likely representing surface unidentate carbonates formed upon CO_2 exposure.[35,37] Peaks at 1088 cm^{-1}, 884 cm^{-1} and 746 cm^{-1} were assigned to ν_1, ν_2, ν_4 modes of bulk carbonate ions.[7,26,35,37,38] These three bands were not clearly observable until approximately 50 min after CO_2 exposure, indicating that some time was needed until a bulk carbonate was formed. Once the carbonate peaks were formed at the 50 min mark, the intensity of such bands rapidly increased until 6 h, upon which the increase in peak intensity

slowed. Combining observations made from FTIR and XRD indicate that bulk $MgCO_3$ was forming during CO_2 sorption, which was enabled by the presence of $NaNO_3$. There was a time period that was needed for nucleation of $MgCO_3$ to start, which is the likely reason for the induction period.[7,10]

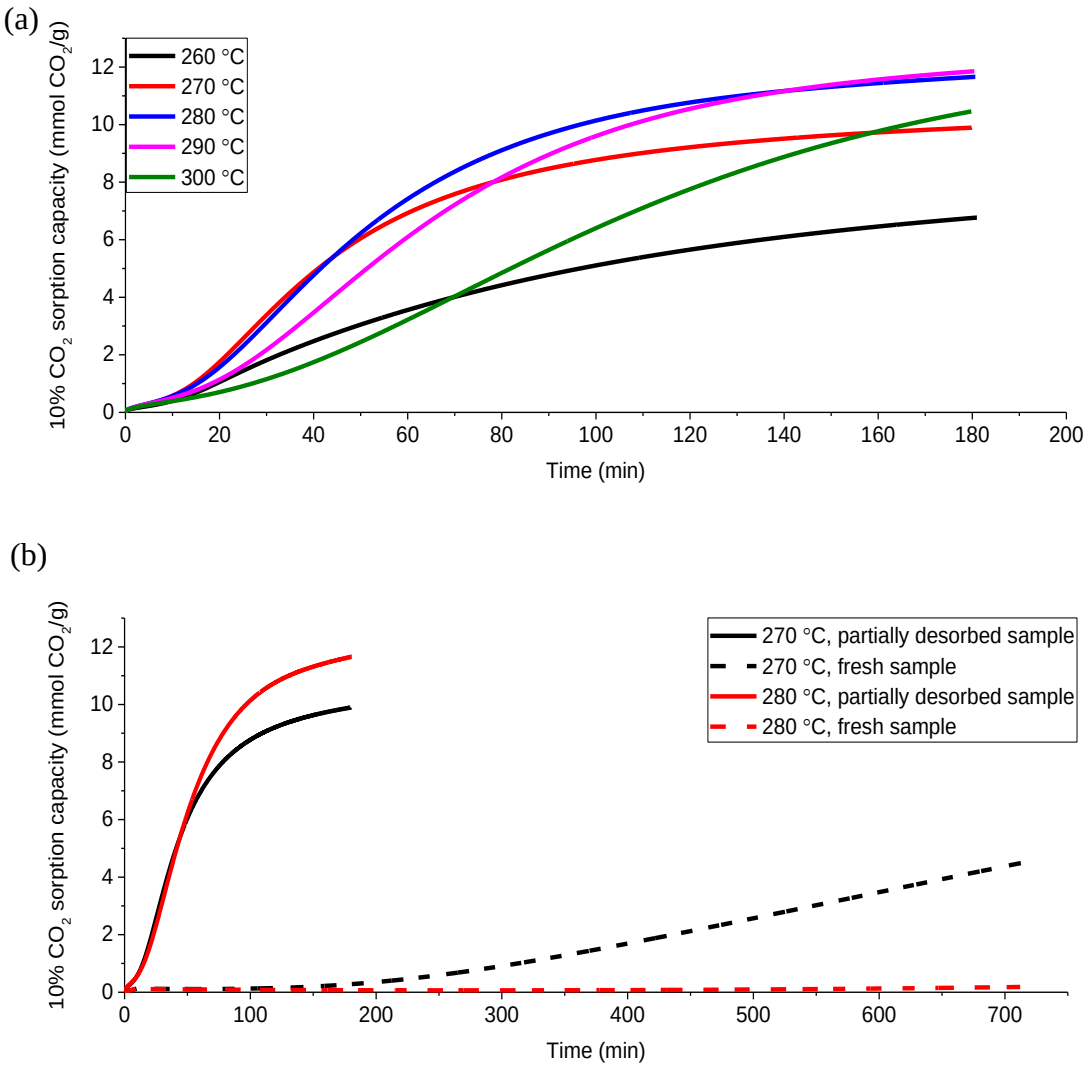

Figure 2.8. (a) CO_2 sorption capacity measured over 3 h at different temperatures between 260 °C and 300 °C under simulated flue gas for a 94% desorbed MgO_$NaNO_3$_0.10 sample after initial CO_2 sorption over 12 h. (b) Comparison of sorption uptake kinetics of partially desorbed MgO_$NaNO_3$_0.10 and fresh MgO_$NaNO_3$_0.10 at 270 °C and 280 °C.

For $NaNO_3$ promoted MgO, Zhang et al. also showed that a partially desorbed sample after an initial, full sorption cycle tended to show increased uptake kinetics in the following cycle of CO_2 sorption.[6,35] This previous study, like most others, was done in pure CO_2, so a similar experiment was performed using 10% CO_2 to observe if an improved sorption capacity could be observed. To perform such an experiment, MgO_$NaNO_3$_0.10 was initially exposed to 10% CO_2/He gas for 12 h at 260 °C. Then, the temperature was increased to 350 °C at a 10 °C/min rate, and the sorbent was heated at 350 °C for 15 minutes under helium flow to desorb approximately 94% of the CO_2 that was sorbed in the initial CO_2 exposure period. The temperature was then decreased to the temperature of interest and the gas was switched from helium to 10% CO_2/He, and the sorption capacity was measured for 3 h.

As shown in Figure 2.8, the partially desorbed sample showed much improved sorption kinetics. In just 3 h of sorption, an uptake capacity of 6.77 mmol CO_2/g was obtained at a temperature of 260 °C. Considering only 1.97 mmol CO_2/g was obtained in 3 h of sorption (Figure 2.4) during the initial cycle at 260 °C, a significant improvement in uptake kinetics was observed. To ensure such an improvement was due to the prior CO_2 uptake and partial desorption, a similar experiment was performed after fully desorbing the sample after the initial 12 h CO_2 sorption period. As shown in Figure A.4, a much lower sorption capacity of 0.84 mmol CO_2/g was observed in 3 h of sorption in this case, indicating that the improved kinetics were due to the partial desorption of CO_2, not simply due to cycling the sorbent. Also, as shown in Figure 2.8 (b), while a very low sorption capacity of 0.18 mmol CO_2/g was observed in the first 12 h of sorption at 280 °C for fresh sorbent, a much improved sorption capacity of 11.7 mmol CO_2/g was observed in just 3 h

of sorption for the partially desorbed sorbent. Indeed, the sorption capacity remained high even at temperatures as high as 300 °C after partial desorption. Induction period calculations at different temperatures (Figure A.5) showed that the induction periods were much shorter for partially desorbed samples, showing induction periods less than 20 minutes at a temperature range between 260 °C and 300 °C. At a temperature of 260 °C, the induction period was shortened from 100 minutes for the initial cycle to 9 minutes for the partially desorbed sample, indicating an order of magnitude decrease in the induction time.

Observations from in-situ XRD data indicate that a drastic increase in uptake was initiated by nucleation of $MgCO_3$. Based on this correlation of uptake rate from the TGA with formation of $MgCO_3$ in the XRD patterns it was hypothesized that the unique behavior observed from the partially desorbed sample is likely due to differences between primary nucleation and secondary nucleation events. In primary nucleation, a nucleation of crystalline material occurs in the absence of any crystalline material, while in secondary nucleation, a crystalline phase is already present from the beginning of the crystallization process.[39–41] In primary nucleation, longer induction periods are commonly observed due to the time needed for a stable nucleus to form. However, in secondary nucleation, due to the presence of a crystalline phase, such time is drastically reduced, thereby showing much reduced induction periods. Furthermore, in-situ XRD (Figure A.6) and in-situ FTIR (Figure A.7) data of the partially desorbed sample did not indicate any major differences in the species formed during CO_2 sorption for the fresh and partially desorbed samples, further supporting this hypothesis.

The different, advantageous behavior observed from the partially desorbed sample also led to our re-examination of the hypotheses about the nature of the rate limiting step in the CO_2 sorption using molten alkaline promoted MgO sorbents. Until now, the two most supported suggestions regarding the regarding rate limiting step in CO_2 sorption were that: 1) dissolution of MgO in the $NaNO_3$ medium to form $[Mg^{2+}\cdots O^{2-}]$ ionic pairs or 2) formation of carbonate ions in the molten medium, owing to high solubility of O^{2-} ions in $NaNO_3$ medium.[6,7,26,27] As previously observed in Figure A.5, a significantly shortened induction period was observed for CO_2 sorption under exposure to pure CO_2 than under 10% CO_2/He. If formation of $[Mg^{2+}\cdots O^{2-}]$ ionic pears through dissolution of MgO was the rate limiting step, the induction period would not have shown such drastic decrease, indicating that this step is unlikely to be the rate limiting step under our sorption conditions. Formation of carbonate ions is also unlikely to be the rate limiting step, since such a drastic change in the induction period would not have been observed between a partially desorbed sorbent and the fully desorbed sorbent. Thus, collective observations from our data set suggest an alternate hypothesis is needed to explain the observations under our conditions. We suggest that the rate limiting step in the experiments performed here is associated with the time needed for primary nucleation of $MgCO_3$ to occur and that this time could be shortened by partially desorbing the sample to initiate secondary nucleation.

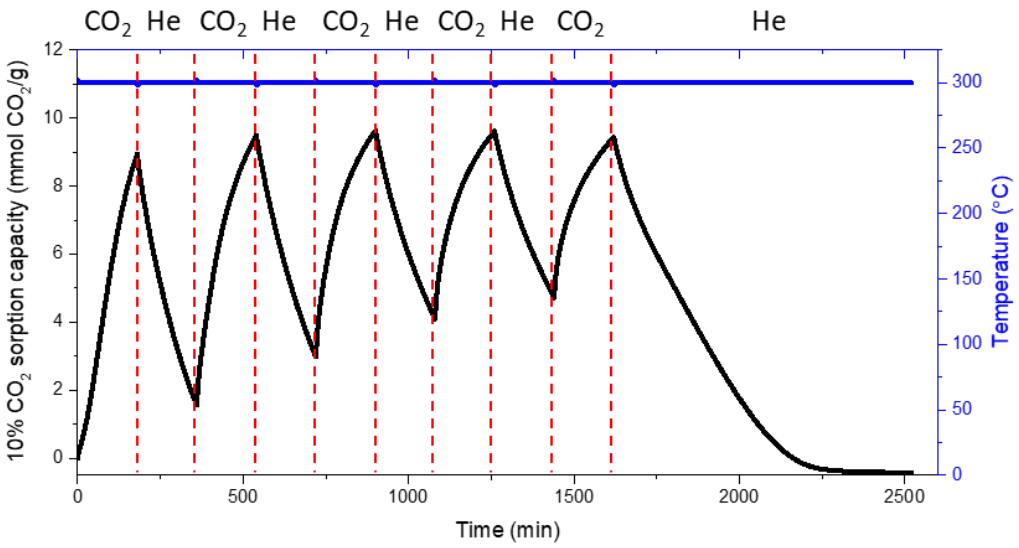

Figure 2.9. Sorption and desorption cycles performed isothermally at 300 °C using 94% desorbed MgO_$NaNO_3$_0.10 sample under 10% CO_2/He and helium purge flow.

Lastly, based on the increased uptake rate observed for the partially desorbed MgO_$NaNO_3$_0.10, 5 cycles of isothermal sorption and desorption were performed isothermally at 300 °C (Figure 2.9). Throughout the first 5 cycles, the material maintained a high sorption capacity above 4 mmol CO_2/g. However, as shown in Table 2.2, a continuous decrease in both sorption and desorption capacity was observed after each cycle, showing a decrease from 8.95 mmol CO_2/g to 4.72 mmol CO_2/g of sorption capacity after 5 cycles. After the 5 cycles of sorption and desorption, the sorbent was heated under a helium purge at 300 °C for 15 h to desorb CO_2 completely (Figure 2.9). N_2 physisorption was performed on the MgO_$NaNO_3$_0.10 after different pretreatments to observe how the textural properties changed after each stage, as shown in Table 2.3. While as synthesized MgO_$NaNO_3$_0.10 had a BET surface area 67 m^2/g (Table 2.1), it showed a much lower surface area of 17 m^2/g after 12 h of sorption at 260 °C and 30 min of desorption at 350 °C. After 5 cycles of isothermal cycling, a minimal surface area of 4 m^2/g was observed,

which indicates that at such a temperature range, $NaNO_3$ promoted MgO sorbents experience sintering after each cycle of sorption and regeneration.

Table 2.2. Sorption and desorption capacity of partially desorbed MgO_$NaNO_3$_0.10 at each cycle during 5 isothermal regeneration at 300 °C.

Number of Cycles	1	2	3	4	5
Sorption capacity (mmol CO_2/g)	8.95	7.94	6.65	5.52	4.72
Desorption capacity (mmol CO_2/g)	7.40	6.51	5.54	4.89	-

Table 2.3. Textural properties of MgO_$NaNO_3$_0.10 after different pretreatments.

	BET surface area (m^2/g)	Pore Volume (cm^3/g)
MgO_$NaNO_3$_0.10 – fully desorbed after 12 h of CO_2 sorption	17	0.12
MgO_$NaNO_3$_0.10 – fully desorbed isothermally after 5 cycles of isothermal cycle	4	0.02

To observe how the ratio between $NaNO_3$ and MgO changes, SEM-EDS mapping was performed on the MgO_$NaNO_3$_0.10 material after different pretreatments, as shown in Figure A.8, Figure A.9, and Figure A.10. It should be noted that a sorbent-rich portion of the SEM image was selected to exclude the background carbon tape for accurate composition analysis. While as synthesized MgO_$NaNO_3$_0.10 had a Na wt%/Mg wt% ratio of 0.16 (Figure A.8 (g)), this ratio decreased to 0.11 (Figure A.9 (g)) after 1 cycle of CO_2 sorption for 12 h and desorption for 30 min, and further decreased to 0.047 (Figure A.10 (g)) after 5 isothermal cycles of sorption and regeneration. Such data imply that both a decrease in surface area of the sorbent due to sintering of MgO and a loss of $NaNO_3$

promoters after multiple cycles of sorption and regeneration could be contributing to the decrease in sorption capacity after each cycle of isothermal regeneration. The isothermal cycling of the partially desorbed $NaNO_3$ promoted MgO sorbents under a flue gas composition of CO_2 has been observed in this work for the first time, to best of our knowledge. Although further study will be needed to improve the cyclic stability of such sorbents and limit sintering, considering the significant amount of energy required in temperature swing processes for regeneration of sorbents, we believe that the potential for isothermal cycling may present some processing advantages.

2.4 Conclusion

In summary, $NaNO_3$ promoted mesoporous MgO was found to be effective in capturing CO_2 in simulated flue gas conditions at intermediate temperature. The concentration of CO_2 within the molten $NaNO_3$ medium is shown to have significant impact on the length of the induction period that leads to nucleation of $MgCO_3$, which is followed by rapid uptake of CO_2. It was also found that a previously CO_2-loaded, partially desorbed $NaNO_3$ promoted MgO showed a much shorter induction period and improved kinetics in capturing CO_2 under simulated flue gas conditions compared to the fresh sorbent. Such a material was also capable of adsorbing and desorbing significant amounts of CO_2 by simply switching gases between simulated flue gas and inert gas, allowing for isothermal sorbent regeneration by concentration swing.

2.5 Reference

(1) Wang, J.; Huang, L.; Yang, R.; Zhang, Z.; Wu, J.; Gao, Y.; Wang, Q.; O'Hare, D.; Zhong, Z. Recent Advances in Solid Sorbents for CO2 Capture and New Development Trends. *Energy Environ. Sci.* **2014**, *7*, 3478–3518.

(2) Feng, B.; An, H.; Tan, E. Screening of CO2 Adsorbing Materials for Zero Emission Power Generation Systems. *Energy & Fuels* **2007**, *21*, 426–434.

(3) Cao, C.; Qu, J.; Wei, F.; Liu, H.; Song, W. Superb Adsorption Capacity and Mechanism of Flowerlike Magnesium Oxide Nanostructures for Lead and Cadmium Ions. *ACS Appl. Mater. Interfaces* **2012**, *4*, 4283–4287.

(4) Kim, Y.; Anh, V.; Park, M.; Lee, C. Sulfur Removal from Municipal Gas Using Magnesium Oxides and a Magnesium Oxide/Silicon Dioxide Composite. *Microporous Mesoporous Mater.* **2014**, *197*, 299–307.

(5) Choi, S.; Drese, J. H.; Jones, C. W. Adsorbent Materials for Carbon Dioxide Capture from Large Anthropogenic Point Sources. *ChemSusChem* **2009**, *2* (9), 796–854.

(6) Zhang, K.; Li, X. S.; Li, W.; Rohatgi, A.; Duan, Y.; Singh, P.; Li, L.; King, D. L. Phase Transfer-Catalyzed Fast CO2 Absorption by MgO-Based Absorbents with High Cycling Capacity. *Adv. Mater. Interfaces* **2014**, *1*, 1400030.

(7) Harada, T.; Simeon, F.; Hamad, E. Z.; Hatton, T. A. Alkali Metal Nitrate-Promoted High-Capacity MgO Adsorbents for Regenerable CO2 Capture at Moderate Temperatures. *Chem. Mater.* **2015**, *27*, 1943–1949.

(8) Xiao, G.; Singh, R.; Chaffee, A.; Webley, P. Advanced Adsorbents Based on MgO

and K2CO3 for Capture of CO2 at Elevated Temperatures. *Int. J. Greenh. Gas Control* **2011**, *5* (4), 634–639.

(9) Harada, T.; Hatton, T. A. Colloidal Nanoclusters of MgO Coated with Alkali Metal Nitrates/Nitrites for Rapid, High Capacity CO2 Capture at Moderate Temperature. *Chem. Mater.* **2015**, *27*, 8153–8161.

(10) Jo, S.; An, Y.; Kim, K.; Choi, S.; Kwak, J.; Oh, K.; Kwon, Y. Mechanisms of Absorption and Desorption of CO2 by Molten NaNO3-Promoted MgO. *Phys. Chem. Chem. Phys.* **2017**, *19*, 6224–6232.

(11) Kim, K.; Han, J. W.; Lee, K. S.; Lee, W. B. Promoting Alkali and Alkaline-Earth Metals on MgO for Enhancing CO2 Capture by First-Principles Calculations. *Phys. Chem. Chem. Phys.* **2014**, *16*, 24818–24823.

(12) Vu, A. T.; Park, Y.; Jeon, P. R.; Lee, C. H. Mesoporous MgO Sorbent Promoted with KNO3 for CO2 Capture at Intermediate Temperatures. *Chem. Eng. J.* **2014**, *258*, 254–264.

(13) Lee, S. C.; Cha, S. H.; Kwon, Y. M.; Park, M. G.; Hwang, B. W.; Park, Y. K.; Seo, H. M.; Kim, J. C. Effects of Alkali-Metal Carbonates and Nitrates on the CO2 Sorption and Regeneration of MgO-Based Sorbents at Intermediate Temperatures. *Korean J. Chem. Eng.* **2016**, *33* (12), 3448–3455.

(14) Qiao, Y.; Wang, J.; Zhang, Y.; Gao, W.; Harada, T.; Huang, L.; Hatton, T. A.; Wang, Q. Alkali Nitrates Molten Salt Modified Commercial MgO for Intermediate-Temperature CO2 Capture : Optimization of the Li/Na/K Ratio. *Ind. Eng. Chem.*

Res. **2017**, *56*, 1509–1517.

(15) Wook, B.; Hwan, J.; Jin, H.; Ryu, H.; Lee, D.; Beom, J.; Kim, H.; Chool, S.; Chang, J. CO2 Capture and Regeneration Properties of MgO-Based Sorbents Promoted with Alkali Metal Nitrates at High Pressure for the Sorption Enhanced Water Gas Shift Process. *Process Saf. Environ. Prot.* **2018**, *116*, 219–227.

(16) Cui, H.; Zhang, Q.; Hu, Y.; Peng, C.; Fang, X.; Cheng, Z.; Galvita, V. V; Zhou, Z. Ultrafast and Stable CO2 Capture Using Alkali Metal Salt-Promoted MgO-CaCO3 Sorbents. *ACS Appl. Mater. Interfaces* **2018**, *10*, 20611–20620.

(17) Kwak, J.; Kim, K.; Yoon, J. W.; Oh, K.; Kwon, Y. Interfacial Interactions Govern the Mechanisms of CO2 Absorption and Desorption on A2CO3-Promoted MgO (A=Na, K,Rb, and Cs) Absorbents. *J. Phys. Chem. C* **2018**, *122*, 20289–20300.

(18) Harada, T.; Brown, P.; Hatton, T. A. Nonvolatile Colloidal Dispersion of MgO Nanoparticles in Molten Salts for Continuous CO2 Capture at Intermediate Temperatures. *ACS Sustain. Chem. Eng.* **2019**, *7*, 7979–7986.

(19) Hiremath, V.; Trivino, M. L. T.; Seo, J. G. Eutectic Mixture Promoted CO2 Sorption on MgO-TiO2 Composite at Elevated Temperature. *J. Environ. Sci.* **2018**, *76*, 80–88.

(20) Kwak, J.; Kim, K.; Oh, K.; Kwon, Y. Performance Enhancement of All-Solid CO2 Absorbent Based on Na2CO3 - Promoted MgO by Using ZrO2 Dispersant. *Int. J. Greenh. Gas Control* **2019**, *81* (September 2018), 38–43.

(21) Wang, K.; Zhao, Y.; Clough, P. T.; Zhao, P.; Anthony, E. J. Structural and Kinetic Analysis of CO2 Sorption on NaNO2-Promoted MgO at Moderate Temperatures. *Chem. Eng. J.* **2019**, *372*, 886–895.

(22) Hu, Y.; Guo, Y.; Sun, J.; Li, H.; Liu, W. Progress in MgO Sorbents for Cyclic CO2 Capture : Review. *J. Mater. Chem. A* **2019**, *7*, 20103–20120.

(23) Yang, X.; Zhao, L.; Li, X.; Xiao, Y. Magnesium Oxide-Based Absorbents for CO2 Capture at Medium Temperature. *Curr. Pollut. Reports* **2018**, No. 4, 13–22.

(24) Vu, A. T.; Ho, K.; Jin, S.; Lee, C. H. Double Sodium Salt-Promoted Mesoporous MgO Sorbent with High CO2 Sorption Capacity at Intermediate Temperatures under Dry and Wet Conditions. *Chem. Eng. J.* **2016**, *291*, 161–173.

(25) Zhao, X.; Ji, G.; Liu, W.; He, X.; Anthony, E. J.; Zhao, M. Mesoporous MgO Promoted with NaNO3/NaNO2 for Rapid and High-Capacity CO2 Capture at Moderate Temperatures. *Chem. Eng. J.* **2018**, *332* (September 2017), 216–226.

(26) Pozzo, A. D.; Armutlulu, A.; Rekhtina, M.; Abdala, P. M.; Mu, C. R. CO 2 Uptake and Cyclic Stability of MgO-Based CO 2 Sorbents Promoted with Alkali Metal Nitrates and Their Eutectic Mixtures. *ACS Appl. Energy Mater.* **2019**, *2*, 1295–1307.

(27) Trivino, M. L. T.; Hiremath, V.; Seo, J. G. Stabilization of NaNO3-Promoted Magnesium Oxide for High- Temperature CO2 Capture. *Environ. Sci. Technol.* **2018**, *52*, 11952–11959.

(28) Jin, S.; Ho, K.; Lee, C. H. Facile Synthesis of Hierarchically Porous MgO Sorbent

Doped with CaCO3 for Fast CO2 Capture in Rapid Intermediate Temperature Swing Sorption. *Chem. Eng. J.* **2018**, *334*, 1605–1613.

(29) Jin, S.; Ko, K.; Lee, C. Direct Formation of Hierarchically Porous MgO-Based Sorbent Bead for Enhanced CO 2 Capture at Intermediate Temperatures. *Chem. Eng. J.* **2019**, *371* (February), 64–77.

(30) Wang, L.; Zhou, Z.; Hu, Y.; Cheng, Z.; Fang, X. Nanosheet MgO-Based CO 2 Sorbent Promoted by Mixed-Alkali-Metal Nitrate and Carbonate : Performance and Mechanism. *Ind. Eng. Chem. Res.* **2017**, *56*, 5802–5812.

(31) Liu, M.; Vogt, C.; Chaffee, A. L.; Chang, S. L. Y. Nanoscale Structural Investigation of Cs2CO3-Doped MgO Sorbent for CO2 Capture at Moderate Temperature. *J. Phys. Chem. C* **2013**, *117*, 17514–17520.

(32) IPCC. *CARBON DIOXIDE CAPTURE AND STORAGE*; Cambridge University Press: New York, 2005.

(33) Thommes, M.; Kaneko, K.; Neimark, A. V; Olivier, J. P.; Rodriguez-Reinoso, F.; Rouquerol, J.; Sing, K. S. W. Physisorption of Gases , with Special Reference to the Evaluation of Surface Area and Pore Size Distribution (IUPAC Technical Report). *Pure Appl. Chem.* **2015**, *87*, 1051–1069.

(34) Thommes, M.; Cychosz, K. A. Physical Adsorption Characterization of Nanoporous Materials : Progress and Challenges. *Adsorption* **2014**, *20*, 233–250.

(35) Prashar, A. K.; Seo, H.; Choi, W. C.; Kang, N. Y.; Park, S.; Kim, K.; Min, D. Y.;

Kim, H. M.; Park, Y. K. Factors Affecting the Rate of CO2 Absorption after Partial Desorption in NaNO3 - Promoted MgO. *Energy and Fuels* **2016**, *30*, 3298–3305.

(36) Gao, W.; Zhou, T.; Gao, Y.; Louis, B.; O'Hare, D.; Wang, Q. Molten Salts-Modified MgO-Based Adsorbents for Intermediate-Temperature CO2 Capture : A Review. *J. Energy Chem.* **2017**, *26* (5), 830–838.

(37) Evans, J. V.; Whateley, T. L. Infra-Red Study of Adsorption of Carbon Dioxide and Water on Magnesium Oxide. *Trans. Faraday Soc.* **1967**, *63*, 2769–2777.

(38) Du, H.; Williams, C. T.; Ebner, A. D.; Ritter, J. A. In Situ FTIR Spectroscopic Analysis of Carbonate Transformations during Adsorption and Desorption of CO2 in K-Promoted HTlc. *Chem. Mater.* **2010**, *22*, 3519–3526.

(39) Li, H.; Kawajiri, Y.; Grover, M. A.; Rousseau, R. W. Modeling of Nucleation and Growth Kinetics for Unseeded Batch Cooling Crystallization. *Ind. Eng. Chem. Res.* **2017**, *56*, 4060–4073.

(40) Botsaris, G. D. Secondary Nucleation - A Review. In *Secondary Nucleation - A Review*; Springer: Boston, 1976; pp 3–22.

(41) Mullin, J. W. Crystallization. In *Crystallization*; Butterworth-Heinemann, 2001; pp 181–215.

CHAPTER 3. INTEGRATED CAPTURE AND CONVERSION OF CO_2 INTO METHANE USING $NANO_3/MGO + RU/AL_2O_3$ AS A CATALYTIC SORBENT

Parts of this chapter are adapted from 'Park, S. J.; Bukhovko, M. P.; Jones, C. W., Integrated Capture and conversion of CO_2 into methane using $NaNO_3/MgO + Ru/Al_2o_3$ as a catalytic sorbent. *Chem. Eng. J.* **2021**, 3, 130369' with permission from Elsevier.

3.1 Introduction

Global CO_2 emissions have been rising since the early 1900s and are expected to increase further as future energy consumption rates increase.[1] This has resulted in the atmospheric CO_2 concentration growing to reach 400 ppm in 2015, compared to 280 ppm before the industrial revolution. As CO_2 is a major contributor to climate change, reduction in CO_2 emissions has become an urgent issue requiring multiple technology and policy solutions.[2,3] To this end, numerous studies targeting capture and sequestration of CO_2 from flue gas have been published, for example using amine solutions,[4–8] solid sorbents,[9,10] or membranes[6,11] to achieve the separation. In parallel, there is keen interest in utilization of CO_2,[12–15] typically via catalytic conversion to value added products. Recently, a method that combines the two processes in a process intensification approach has been proposed by Farrauto.[16–18] In this approach, compositions previously referred to as dual function materials (DFM), which has more than one functionality such as CO_2 sorption or catalytic activity in a single grain, are proposed to promote the combined capture and methanation in a single reactor. In this approach, capture and catalytic conversion of CO_2 to methane occur at isothermal conditions, with the DFM used to capture CO_2 from a flue gas stream

in the first stage of the process, followed by subsequent catalytic conversion of the adsorbed CO_2 to methane with the addition of hydrogen. Thus, instead of desorbing the captured CO_2 by temperature swing or pressure swing, the H_2 feed directly converts the captured CO_2 to methane in the second stage of the process. Farrauto et al. proposed that such a combined process could potentially be more advantageous than a traditional CCS process, as the energy intensive temperature swing process for sorbent regeneration and any cost regarding transportation or storage of sequestered CO_2 could be mitigated. As a result, numerous studies have been conducted regarding combined capture and methanation processes using various types of DFMs and catalytic sorbents, which is usually synthesized through physical mixing of a sorbent and a catalyst , and unlike DFMs, have adsorptive site and catalytic site at separate grain, including those composed of CaO,[16] Na_2CO_3,[19,20] K_2CO_3,[21] and MgO[22,23] as adsorptive sites and Ni[24–26], Ru,[18,27–29] and Rh[17] as catalytic, hydrogenation sites.

However, the CO_2 capture sorption capacity (mmol CO_2/g) and methane production capacity (mmol CH_4/g) obtained to date in a cycle of capture and methanation under simulated flue gas conditions remains modest. Materials that use CaO or $NaCO_3$ as sorptive sites and Ru or Ni as catalytic sites typically show CO_2 sorption capacities between 0.3 and 0.7 mmol CO_2/g within 15 ~ 60 min of CO_2 exposure (7.5% ~ 50% CO_2/N_2) and methane production capacities between 0.2 and 0.6 mmol CH_4/g within 15 ~ 60 min under H_2 feed (15% ~ 60% H_2/N_2). [24,25,30,31] One of the highest CO_2 sorption and methane production capacities reported to date was obtained using (Li/Na/K)NO_3/MgO+Ru/CeO_2 by Sun et al.[23] However, this was elevated under CO_2 concentration conditions relevant to precombustion CO_2 capture (~65%). To apply such a combined capture and methanation

process to existing natural gas combustion plants, it is important to obtain higher CO_2 capture capacities and methane production capacities using conditions corresponding to flue gas streams (~5-10% CO_2). Recently it was reported that alkali metal promoted MgO sorbents show high sorption capacities in a temperature range between 250°C ~ 325°C in CO_2 concentrations that correspond to both precombustion (>65% CO_2)[22,32–50] and post combustion (10~15% CO_2) CO_2 capture regimes.[51–54] It was also found that such sorbent materials are capable of sorbing and desorbing CO_2 under isothermal conditions by simply switching the feed gas from CO_2 containing gas to a purge gas.[52] As the temperature range under which the sorbent performs well corresponds with temperature range for CO_2 methanation, we hypothesized that utilizing such sorbent materials in catalytic sorbent compositions may result in a good performance in combined capture and methanation processes.[12,55–57]

In this chapter, catalytic sorbents comprised of a physical mixture of $NaNO_3$/MgO (sorbent) and Ru/Al_2O_3 (catalyst) prepared using different methods are evaluated in combined capture and conversion cycles. The CO_2 sorption behavior of the prepared materials is studied through thermogravimetric analysis, and catalytic performance is evaluated using spectroscopic observations and fixed bed reaction experiments. Lastly, the performance of the catalytic sorbents over multiple cycles of combined capture and methanation is presented.

3.2 Experimental Section

3.2.1 Chemicals and Materials

Urea (ACS reagent, 99%), magnesium acetate tetrahydrate (Reagent Plus, 99%), ammonium solution (2 M in methanol), and sodium nitrate, γ-aluminum oxide were obtained from Sigma Aldrich. Ruthenium nitrosyl nitrate was obtained from Alfa Aesar. Cylinders of 10% CO_2/He, CO_2, H_2, N_2, and He were obtained from Airgas.

3.2.2 Synthesis of mesoporous MgO and impregnation of $NaNO_3$

Mesoporous MgO was synthesized through a modified method described in the literature. [47,52] First, 28.83 g of urea and 34.31 g of magnesium acetate tetrahydrate were added to 100 mL of distilled water and stirred for 1 h to ensure all salts were completely dissolved. Then 0.2 mL of ammonia solution was added to the mixture and stirred for an additional 30 min. The solution was then equally distributed to 4 different 45 mL Teflon autoclaves, and heated at 180 °C for 8 h. After cooling to room temperature, white precipitates were recovered by filtration from Teflon autoclaves and washed together with 2 L of distilled water followed by 2 L of ethanol. The white powder was then calcined in static air at 600 °C for 5 h. 17% $NaNO_3$/MgO was synthesized through incipient wetness impregnation of sodium nitrate salt on synthesized mesoporous MgO. $NaNO_3$ impregnated sorbents were then calcined at 350 °C in static air for 30 min. It should be noted that 17% weight loading was chosen based on our previous observation that this loading showed highest sorption capacity among different weight loading.[52]

3.2.3 Synthesis of Ru/Al_2O_3 catalysts

To synthesize different loadings of Ru/Al_2O_3 catalyst, a predetermined amount of $Ru(NO)_3(NO_3)_3$, corresponding to 0.25%, 0.5%, 1% 2% Ru/Al_2O_3, were dissolved in distilled water to obtain stock solutions of different $Ru(NO)_3(NO_3)_3$ concentrations. The

solution of different concentrations was added to γ-Al_2O_3, and the solid was then calcined at 450 °C for 2 h under static air. The temperature ramp was 5 °C/min rate.

3.2.4 Synthesis of catalytic sorbents

Catalytic sorbents for use in combined capture and conversion cycles were prepared using two different methods. In one case, 17% $NaNO_3$/MgO and x% Ru/Al_2O_3 were each separately pressed into a pellet at 1000 psi, sieved between 125 and 425 microns, and packed as two separate beds, with a 17% $NaNO_3$/MgO bed being on top of the x% Ru/Al_2O_3 bed. Such samples are noted as x%Ru/Al_2O_3_2B, with 2B signifying use of two separate beds. In another method, 17% $NaNO_3$/MgO and x% Ru/Al_2O_3 were mixed together and vortexed for 30 min, then pelletized and sieved to sizes between 125 and 425 microns. Such samples are noted as x%Ru/Al_2O_3_MP, with MP signifying mixed-then-pelletized. In both cases, the mass ratio between 17% $NaNO_3$/MgO and Ru/Al_2O_3 catalyst was 2:1. While samples prepared using the two methods above were the only ones tested for combined capture and conversion cycles, additional samples were prepared using additional methods for study of the sorption behavior of the synthesized catalytic sorbents. These samples were prepared similarly to the MP samples but were not pelletized after the thorough mixing of 17% $NaNO_3$/MgO and x% Ru/Al_2O_3. Such samples are noted as x%Ru/Al_2O_3_M, with M signifying powder mixing only, without pellitization. Similarly, the mass ratio between 17% $NaNO_3$/MgO and Ru/Al_2O_3 catalyst was always 2:1. In addition to the synthesized catalytic sorbents, 5% $NaNO_3$/1% Ru/Al_2O_3 was also synthesized for reaction pathway investigation purposes for $NaNO_3$ containing 1% Ru/Al_2O_3 catalysts. This sample was prepared by incipient wetness impregnation of the

$NaNO_3$ salt to calcined 1% Ru/Al_2O_3 catalyst followed by calcination at 350 °C in static air for 30 min.

3.2.5 Material characterization

N_2 physisorption measurements were performed using a Micromeritics Tristar II 3020 at 77 K. Approximately 150 mg of sorbents were used for each run. All sorbents were degassed at 110 °C for 6 h prior to N_2 physisorption measurements. X-ray diffraction (XRD) was performed on an Empyrean PANalytical diffractometer using Cu Kα radiation operated at 40kV and 40mA. XRD patterns were obtained in the range from 25° to 80° 2θ angle using a 0.033° step size. Chemisorption experiments, including temperature programmed reduction (TPR) and pulse CO chemisorption, were performed using a Micromeritics AutoChem II 2920. For TPR experiments, approximately 50 mg of catalyst was placed into a U-shape quartz tube on top of a quartz wool bed. Samples were then pretreated at temperature of 200 °C for 2 h under 20 mL/min of He to remove any preadsorbed species. Samples were then cooled to 50 °C, and the gas was switched to 20 mL/min of 10% H_2/He. Temperature was then increased to 800 °C at 5 °C/min. The outlet gas passed through a liquid acetone/nitrogen trap first, then through a thermal conductivity detector (TCD). For pulse CO chemisorption, approximately 50 mg of catalyst was placed into the quartz tube on a bed of quartz wool, similar to a TPR experiment. Then the sample was heated to 350 °C at 5 °C /min and held for 1 h under a 10% H_2/He flow. After the reduction step, the gas was switched to He for 30 min to remove any adsorbed species. The temperature was cooled to 30 °C, which was then followed by CO pulse testing. Doses of 10% CO/He were pulsed through the sample bed and analyzed using the TCD. Once saturation was reached, He was passed through sample bed for 60 min.

3.2.6 In situ FTIR spectroscopy

A Thermo Nicolet iS10 IR spectrometer with a mercury cadmium telluride (MCT) detector was used for in situ FTIR spectroscopy experiments. Samples were pressed to a thin pellet and placed in a Harrick transmission flow cell with BaF_2 window. The sample was then pretreated under 10% H_2/N_2 at 50 mL/min flow at temperature of 350 °C for 1 h. The temperature was next cooled down to 300 °C, and 10% CO_2/40% H_2/N_2 was flowed into the cell at 50 mL/min for 90 min. Afterwards, the CO_2 feed was stopped and was switched to 40% H_2/N_2 at 50 mL/min for another 90 min.

3.2.7 CO_2 sorption experiments

A Netzsch TGA (STA449F3 Jupiter) was used to measure sorption capacities of the sorbents. Approximately 10 mg of sorbent was loaded on an alumina sample pan. For the single cycle sorption measurements, the sample was heated to 350 °C at a rate of 10 °C/min under N_2 flow of 150 mL/min. The sample was pretreated at 350 °C for 1 h under N_2 flow to desorb any H_2O or CO_2 from the sample. Then the temperature was cooled to the temperature of interest (280, 300, or 320 °C) and equilibrated for 15 min. Afterwards, the gas feed was switched from N_2 to 15% H_2O/N_2 at 150 mL/min for 2 h. A steam generator (Netzsch) was used to produce a stable output of water vapor that was diluted with N_2 to achieve the 15% H_2O/N_2 mixture. Next, the gas feed was switched to 10% CO_2/15% H_2O/N_2 flow (150 mL/min) for 12 h. The mass change was dynamically measured, and the sorption capacity was calculated based on the mass increase. The adsorbed species were then desorbed using N_2 (150 mL/min) at the prior sorption temperature.

3.2.8 Combined capture and conversion cycles

A fixed bed reactor constructed from a stainless steel tube with inner diameter of ¼" was used at a total pressure of 1 atm. The stainless steel tube was placed inside an electric furnace, and a K-type thermocouple was used for temperature control. During a typical experiment, 450 mg of catalytic sorbent was used, with the two ends of the bed fixed by quartz wool. For the x%Ru/Al_2O_3_2B samples, 150 mg x%Ru/Al_2O_3 was loaded first into the stainless steel tube to place it on the bottom bed, and then 300 mg of 17% $NaNO_3$/MgO sample was loaded subsequently to place it above the x%Ru/Al_2O_3 bed. For the x%Ru/Al_2O_3_MP samples, 450 mg of the sample was loaded all at once. The catalytic sorbents were reduced at 350 °C for 1 h in 10% H_2/N_2 at 20 mL/min. After reduction was completed, the gas feed was switched to 20 mL/min of N_2, and the temperature was cooled to 300 °C. Once the temperature stabilized at 300 °C, the feed was switched to 10% CO_2/N_2 with 11% absolute humidity, and the sample was exposed to CO_2 containing feed for 3 h. To obtain 11% absolute humidity, the CO_2 stream went through a bubbler containing distilled water, which was maintained at a temperature of 54 °C throughout the experiment, by placing the bubbler in a heated oil bath. Calculation for absolute humidity is shown in the **Section B.2 of Appendix B.**. After the capture step, the reactor was purged with 20 mL/min of N_2 for 15 min, and the feed was then switched to 10% H_2/N_2 for 6 h. The product composition was analyzed by an Agilent 7890 gas chromatograph (GC) equipped with two TCDs (Molecular Sieve 5A and Hayesep column) and a flame ionization detector (PoraBond U column) during the combined cycle. In between the reactor and GC, an ice trap was present to condense steam from the outlet stream before entering the GC. To calculate the CO_2 sorption capacity and methane production capacity, equation 3.1 and 3.2

were used. It should be noted that EB represents run performed with an empty bed (dotted blackline in Figure B.3) and SB represents a run with a sample-containing bed (solid blackline in Figure B.3). $\dot{n}$ represents total molar flow rate. $C_{f,CO2}$ and $C_{i,CO2}$ represent concentrations of CO_2 in the outlet stream at two different time points. t_f and t_i represent two different time points of the GC measurements. For any given two data points, the trapezoidal rule was used to calculate the moles of CO_2 released in the outlet in a given time interval. These numbers were summed over 180 minutes to obtain the number of moles of CO_2 released over 180 minutes. The number of moles of CO_2 under the solid black line was subtracted from the number of moles of CO_2 under the dotted black line to calculate the total number of moles of captured CO_2. The captured moles of CO_2 were divided by the mass of catalytic sorbent (m) to obtain the CO_2 sorption capacity. A similar method was used to calculated the methane production capacity using the concentration of CH_4 in the outlet.

$$CO_2\ sorption\ capacity = \frac{\left\{\left[\sum\frac{\dot{n}\left(C_{f,CO2}+C_{i,CO2}\right)*\left(t_f-t_i\right)}{2}\right]_{EB}-\left[\sum\frac{\dot{n}\left(C_{f,CO2}+C_{i,CO2}\right)*\left(t_f-t_i\right)}{2}\right]_{SB}\right\}}{m} \quad \text{Eq 3.1}$$

$$Methane\ production\ capacity = \frac{\left[\sum\frac{\dot{n}\left(C_{f,CH4}+C_{i,CH4}\right)*\left(t_f-t_i\right)}{2}\right]_{SB}}{m} \quad \text{Eq 3.2}$$

Furthermore, to calculate the fraction of captured CO_2 utilized for methane production and the conversion of desorbed CO_2 (shown in Table B.2), equation 3.3 and 3.4 were used. Values for CO_2 adsorbed, CH_4 produced, and unreacted CO_2 were obtained from Figure 3.4.

$$Faction\ of\ captured\ CO_2\ utilized\ (\%) = \frac{(CH_4\ produced + unreacted\ CO_2)}{CO_2\ adsorbed} * 100 \quad \text{Eq 3.3}$$

$$Conversion\ of\ CO_2\ in\ methanation\ stage(\%) = \frac{CH_4\ produced}{CH_4\ produced + unreacted\ CO_2} * 100 \quad \text{Eq 3.4}$$

3.2.9 Rate order measurements/catalytic activity measurement

The same reactor set up deployed in the combined capture and conversion cycle was used for catalytic activity measurements. Typically, 40 mg of sample was loaded into the stainless steel fixed bed reactor, and again both ends were fixed by quartz wool. Reaction orders with respect to H_2 and CO_2 were determined in a series of experiments by varying the concentration of one reactant while fixing the concentration of the other reactant. The N_2 flow was varied accordingly to keep the reactor feed constant at 20 mL/min. Calculations were performed to rule out heat and mass-transfer effects, as shown in **Section B.1 of Appendix B**. In a typical experiment, the sample was reduced at 350 °C for 1 h in 10% H_2/N_2 at 20 mL/min. After reduction was completed, the gas feed was switched to 20 mL/min of N_2, and the temperature was cooled to 300 °C. Then the feed containing varying partial pressures of CO_2, H_2, and balance N_2 was flowed through the bed. The activation energy for CO_2 methanation over different catalysts or catalytic sorbents was also determined by measuring the methane production rate at different reaction temperatures between 280 °C and 320 °C, while keeping the reaction feed constant at 10% CO_2/40% H_2/N_2.

3.3 Experimental Section

3.3.1 Material Characterization

The porosity of the synthesized catalysts and sorbents was assessed through N_2 physisorption, as shown in Table 3.1. For the Ru/Al_2O_3 catalysts, a small decrease in both surface area and pore volume was observed compared to bare Al_2O_3 support, indicating the presence of RuO_2 particles loaded inside the pores of the Al_2O_3 support. For the 17% $NaNO_3$/MgO sorbent, a relatively significant decrease in BET surface area and pore volume was observed. This is likely because of the high mass loading of $NaNO_3$ on the MgO support, and due to the fact that during calcination at 350 °C after incipient wetness impregnation, $NaNO_3$ becomes molten and becomes mobile within the pores of MgO, thereby causing pore blocking.

Table 3.1. Textural properties of synthesized sorbents and catalysts

Sample	BET surface area (m^2/g)	Pore volume (cm^3/g)	Ru dispersion (%)
MgO	110	0.46	-
17% $NaNO_3$/MgO	67	0.29	-
Al_2O_3	133	0.91	-
0.25% Ru/Al_2O_3	132	0.73	28.4
0.5% Ru/Al_2O_3	130	0.73	18.9
1% Ru/Al_2O_3	127	0.71	11.5
2% Ru/Al_2O_3	124	0.70	10.4

Figure 3.1 (a) shows XRD patterns for the Ru/Al_2O_3 catalysts. The peaks observed in the patterns measured for Ru/Al_2O_3 catalysts were assigned to three different phases - RuO_2, γ–Al_2O_3, and α–Al_2O_3, the latter being present as a trace impurity. By applying the Scherrer equation to the peak at 28.0°, the RuO_2 crystalline sizes were calculated to be 22.1 nm, 24.1 nm, 25.7 nm, and 27.9 nm for the 0.25%Ru, 0.5%, 1%, and 2% Ru/Al_2O_3, respectively. Figure 3.1 (b) shows XRD patterns of MgO and 17% $NaNO_3$/MgO. The peaks observed in 17% $NaNO_3$/MgO were assigned to two different phases - MgO and $NaNO_3$.

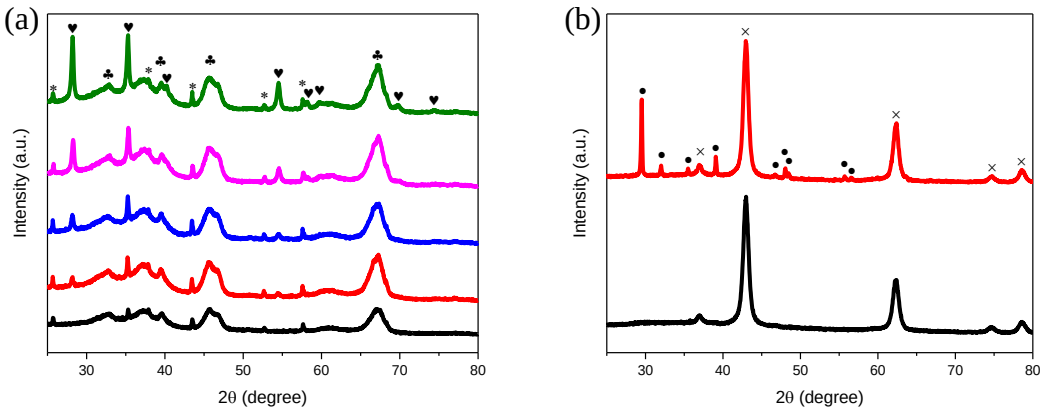

Figure 3.1. XRD pattern of (a) Al_2O_3 and Ru/Al_2O_3 catalysts. Bare Al_2O_3, 0.25%, 0.5%, 1%, and 2% Ru weight loading from bottom to top, and (b) MgO and 17% $NaNO_3$/MgO. Asterisk (*) represents α–Al_2O_3, clubs (♣) represent γ–Al_2O_3, and heart (♥) represent RuO_2, solid

The reducibility of the Ru/Al_2O_3 catalysts was studied through temperature programmed reduction (TPR), as shown in Figure 3.2. For 0.25% Ru/Al_2O_3, the H_2 consumption peak was observed at a temperature of 130 °C. As the loading of Ru increased to 0.5%, another peak was observed at 160 °C, and the peak intensity further increased as the Ru loading increased to 2 %. The peak at 130 °C is assigned to the reduction of well dispersed RuO_2 species to Ru, while the peak at 160 °C is associated with the reduction of more crystalline RuO_2 species.[58–60] This interpretation corresponds to the fact that the peak intensity at 160 °C increased as the Ru loading increased, since more RuO_2 species exist in a crystalline form at higher metal loadings.

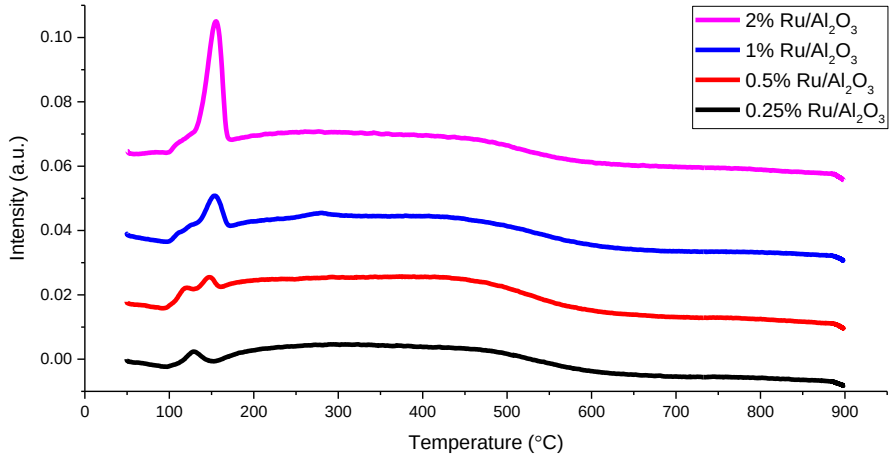

Figure 3.2. H_2-TPR profiles of Ru/Al_2O_3 catalysts.

3.3.2 CO_2 sorption experiments

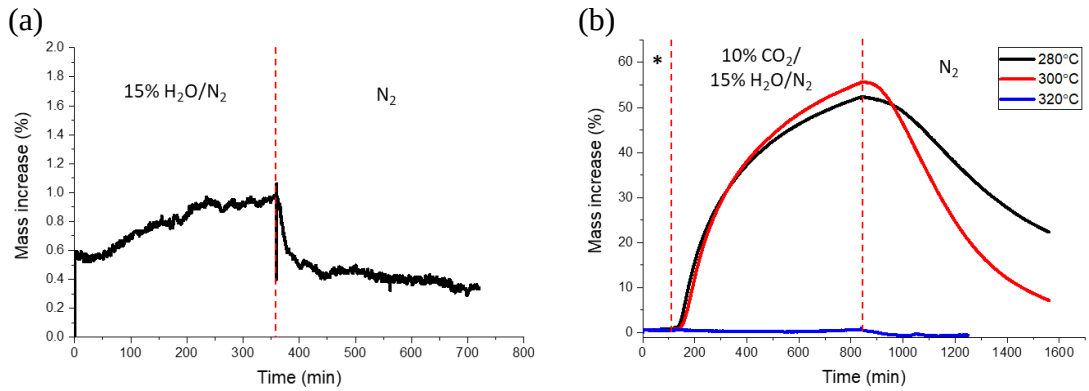

Figure 3.3. (a) Change in mass of the 17% $NaNO_3$/MgO sorbent (a) under 15% H_2O/N_2 flow for 6 h, followed by a nitrogen purge for 6 h at 300 °C, and (b) under 10% CO_2/15% H_2O/N_2 flow for 12 h, followed by a nitrogen purge for 12 h at 280 °C, 300 °C, and 320 °C. The region denoted by the asterisk (*) in figure (b) is 15% H_2O/N_2 flow for 2 h.

Using a thermogravimetric analyzer, the change in mass of the 17% $NaNO_3$/MgO sorbent under a 15% H_2O/N_2 flow or a 10% CO_2/15% H_2O/N_2 flow was measured, as shown in Figure 3.3. This gas composition was used, since typical flue gas is composed of 5~15% CO_2 and 10~25% H_2O in volume.[61,62] Also, it has recently been reported that the

presence of H_2O enhances CO_2 sorption performance, as $Mg(OH)_2$, which captures CO_2 much more rapidly than MgO, is first formed in the presence of steam.[53,63,64] The assessment of the mass change under 15% H_2O/N_2 at 300 °C was performed to observe how much water is adsorbed by the sorbent at a temperature relevant to CO_2 methanation, as shown in Figure 3.3 (a). The mass increase after 6 h of exposure to 15% H_2O/N_2 was approximately 1%, indicating very little water sorption under such conditions. When the feed gas was switched to N_2 flow, the mass decreased from 1% to 0.3%, indicating that most of adsorbed water was easily desorbed, even at isothermal conditions. Based on these observations in Figure 3.3 (a), it was assumed that the mass increase due to water uptake is negligible during the subsequent 10% CO_2/15% H_2O/N_2 flow conditions.

Figure 3.3 (b) shows the change in mass of the 17% $NaNO_3$/MgO sorbent under 10% CO_2/15% H_2O/N_2 flow at different temperatures. It should be noted that for the first two hours, the sorbent was exposed to a flow of 15% H_2O/N_2 to first 'saturate' the sorbent with humidity, thereby minimizing the effect of adsorption of water in the subsequent mass change during 10% CO_2/15% H_2O/N_2 flow. At 280 °C, 0.8% mass increase was observed after 2 h of 15% H_2O/N_2 flow, which then showed 52% mass increase after 12 h of 10% CO_2/15% H_2O/N_2 flow. This indicates approximately 51% mass increase is due to CO_2 sorption, which is equivalent to a sorption capacity of 11.6 mmol CO_2/g sorbent. When the feed was switched to N_2, the mass decreased to 22% after 12 h, indicating 59% of the captured CO_2, equivalent to 6.8 mmol CO_2/g sorbent, was desorbed. At 300 °C, 0.6% mass increase was observed after 2 h of 15% H_2O/N_2 flow, and 56% mass increase was observed after 12 h of 10% CO_2/15% H_2O/N_2 flow. This implies that approximately 55% mass increase was due to sorption of CO_2, which is equivalent to a sorption capacity of 12.5

mmol CO_2/g sorbent. After exposure to 12 h of N_2 flow at isothermal conditions, the mass is decreased to 7%, indicating 89% of the captured CO_2, equivalent to 11.1 mmol CO_2/g sorbent, was desorbed. Comparing data obtained at 280 °C and at 300 °C, it was observed that both the CO_2 sorption and desorption capacity were higher at 300 °C. While it is easy to understand the CO_2 desorption capacity being higher at 300 °C, it was not immediately clear why the sorption capacity was higher as well. However, this observation can be explained by considering the mechanism of CO_2 sorption by such sorbents. It was previously reported that the CO_2 sorption mechanism for such alkali metal promoted MgO sorbents was composed of two stages: (i) dissolution of CO_2 within the molten alkali metal to form stable nuclei of $MgCO_3$ and (ii) growth of the stable $MgCO_3$ nuclei.[43,52] At lower temperatures, the solubility of CO_2 within the molten medium would be higher, so formation of stable nuclei of $MgCO_3$ will be relatively fast, but growth of $MgCO_3$ nuclei may be slower, owing to decreased reaction kinetics. So, at 280 °C, it is likely that formation of stable $MgCO_3$ nuclei is faster than sorption at 300 °C, while the growth of $MgCO_3$ is slower, leading to a slightly lower 12 h sorption capacity. As a matter of fact, the CO_2 uptake is higher at 280 °C than 300 °C until the 330 min mark, indicating a faster initial CO_2 uptake at that temperature. At 320 °C, the CO_2 sorption capacity was very low, with the mass increase being lower than 1% throughout the 12 h of 10% CO_2/15% H_2O/N_2 flow. This indicates that at temperature of 320 °C, the solubility of CO_2 within the molten alkali medium was likely too low for formation of stable $MgCO_3$ nuclei, and therefore the growth phase of $MgCO_3$, which corresponds to the rapid sorption stage, was not effectively initiated. A temperature programmed desorption (TPD) experiment using 17% $NaNO_3$/MgO sorbent after 12 h of exposure to 10% CO_2/15% H_2O/N_2 flow was also

performed, as shown in Figure B.1. A sharp decrease in mass from 99% to 72% is observed as the temperature increases from 350 °C to 430 °C, indicating decomposition of $MgCO_3$. Further decrease in mass from 71% to 65% is observed as the temperature increases from 560 °C to 700 °C, most likely indicating decomposition of $NaNO_3$, as decomposition of $NaNO_3$ to $NaNO_2$ and N_2O was previously reported at temperatures above 550 °C. [65]

For combined capture and conversion scenarios, the 17% $NaNO_3$/MgO behaves as a CO_2 storage medium that captures and stores CO_2 during the capture step and releases CO_2 for methane production in the methanation step, so it is convenient to have high CO_2 sorption and desorption capacities at isothermal conditions. High CO_2 sorption capacity leads to a large amount of CO_2 that can be captured, and a high desorption capacity indicates that higher portion of the captured CO_2 in the capture stage becomes mobile during the conversion step and can reach the active sites for methanation reaction, thereby leading to higher methane production. So based on the results obtained from the sorption and desorption capacity measurements at different temperatures, 300 °C was selected as the temperature to be tested for the combined capture and conversion cycles for this material. To observe how the sorption and desorption capacities change over multiple cycles, 8 cycles of isothermal sorption and desorption were performed, as shown in Figure B.2. It should be noted that for this 8 cycle experiment, both the sorption and desorption steps were performed for 3 h each, to allow them to approach completion. From Figure B.2 and Table B.1, it was observed that the sorbent is capable of sorbing and desorbing large amounts of CO_2 over multiple cycles by simply switching the feed gas from CO_2 containing gas to purge gas. During the first 4 cycles, the sorbent showed high sorption capacities of over 6 mmol CO_2/g and desorption capacities of >4 mmol CO_2/g. However, as the number

of sorption cycles increased, a significant decrease in both the sorption and desorption capacities was observed, with 2.5 mmol CO_2/g sorption capacity and 1.5 mmol CO_2/g desorption capacity in the 8th cycle. This corresponds to previously reported findings, as it was reported that this type of sorbent undergoes excessive sintering at these high temperatures, mainly due to sintering of the MgO support, leading to significant losses in surface area, as well as potential evaporation or redistribution of the $NaNO_3$ promoter, which may also contribute to the decreased sorption capacity over multiple cycles. [52] This property remains the main drawback of this sorbent, and improvement of the stability of the sorbent remains a target for future study. Regardless, due to the high sorption/desorption capacities in the initial cycles, this sorbent was further tested for combined capture and conversion experiments described below.

3.3.3 Combined CO_2 Capture and Conversion Experiments

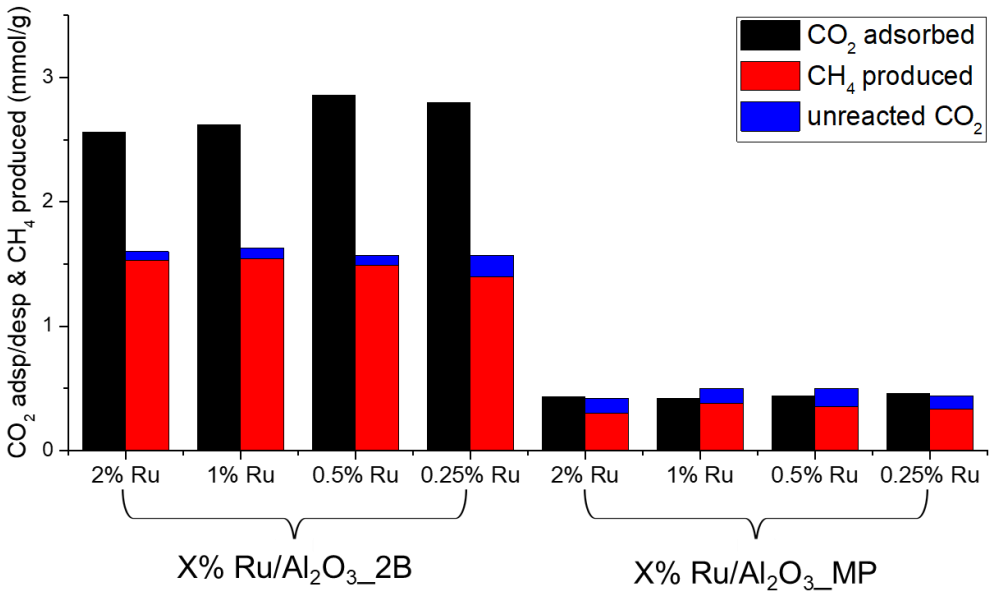

Figure 3.4. CO_2 adsorbed/desorbed and CH_4 produced in one cycle of combined CO_2 capture and conversion. CO_2 adsorption step was 3 h and conversion step was 6 h.

The amount of CO_2 adsorbed and methane produced in a single combined capture and conversion cycle for different catalytic sorbents is shown in Figure 3.4, and plots showing the concentration of CO_2, CH_4, and H_2 in the outlet streams for each catalytic sorbent are shown in Figure B.3. A noteworthy difference in both CO_2 adsorption and methane production performance can be observed between the two bed (2B) samples and mixed pellet (MP) samples. For all 2B samples, the 3 h CO_2 sorption capacities were similar, showing similar sorption capacities between 2.6 and 2.9 mmol CO_2/g. Of the components of the catalytic sorbent (17% $NaNO_3$/MgO and x%Ru/Al_2O_3), the 17% $NaNO_3$/MgO was shown to be the component that most effectively adsorbed CO_2. Since the 17% $NaNO_3$/MgO and x%Ru/Al_2O_3 particles exist as two separate beds in the 2B experiments, the loading of Ru in the Ru/Al_2O_3 should not affect the CO_2 sorption by the 17% $NaNO_3$/MgO, and therefore it is not surprising that all four 2B samples showed similar CO_2 sorption capacities. During the conversion step, all the 0.5%, 1%, 2% Ru/Al_2O_3_2B samples showed similar methane production performance of 1.5 mmol CH_4/g. The amount of unreacted CO_2 was also similar, with values between 0.07 and 0.09 mmol CO_2/g among these three samples. For the 0.25%_2B sample, a slightly decreased methane production of 1.4 mmol CH_4/g was observed, while the amount of unreacted CO_2 was increased to 0.17 mmol CO_2/g. This indicates that for the 0.25% Ru/Al_2O_3_2B sample, the number active sites for CO_2 methanation was too low, which caused an increase in the amount of unreacted CO_2 and a decrease in the methane production. For the 0.5%, 1%, 2% Ru/Al_2O_3_2B samples, there appear to be a sufficient number of active sites such that a further increase in the Ru loading above 0.5% did not make a significant change in the total methane production. While 2B samples generally showed high CO_2 sorption capacities and

methane production capacities, only 55% ~ 62% of the captured CO_2 was converted to methane or released as unreacted CO_2 in the 6 h methanation step, as shown in Table B.2. This indicates a significant fraction of CO_2 is still bound to adsorptive site, and is not able to participate in the catalytic reaction in the methanation step in the combined cycle. For the 0.5%, 1%, 2%Ru/Al_2O_3_2B samples, a high conversion of the desorbed CO_2 was observed, showing conversion equal to or greater than 95%, as shown in Table B.2. For 0.25% Ru/Al_2O_3_2B, slightly decreased conversion of 89% was observed, most likely due to a decrease in the number of hydrogenation active sites, as previously mentioned. While increasing the time of the methanation step is one method to increase the fraction of captured CO_2 utilized in the methanation step, such long methanation times are not ideal for an industrial application, and therefore further studies to increase kinetics of both the CO_2 sorption and desorption steps are needed for such materials. Likely, process configurations differing from fixed beds will be advantageous.

In general, the MP samples showed much lower CO_2 sorption capacities and methane production capacities than 2B samples, regardless of the loading of Ru. This observation was initially surprising given that both the 2B samples and MP samples are physical mixtures between 17% $NaNO_3/MgO$ and x% Ru/Al_2O_3 with the same mass ratio, just with different configurations. Regardless of the Ru loading, all MP samples showed sorption capacities lower than 0.5 mmol CO_2/g in the CO_2 sorption stage. While clear correlations between the ruthenium loading and methane produced or unreacted CO_2 were not observed, all four MP samples showed very low methane production capacities between 0.3 mmol CH_4/g and 0.4 mmol CH_4/g, and unreacted CO_2 fractions of 0.12 mmol CO_2/g and 0.15 mmol CO_2/g. For MP samples, nearly all the captured CO_2 was converted to methane or

released as unreacted CO_2 in the methanation step, as shown in Table B.2. On the other hand, lower conversion of desorbed CO_2 than 2B samples were observed, showing conversions of 70% ~ 76%. For 0.5% Ru/Al_2O_3_MP and 1% Ru/Al_2O_3_MP, the sum of the CH_4 produced and unreacted CO_2 in the methanation step exceeded measured CO_2 adsorbed in the CO_2 capture step, and this may be due to small errors in the measurement of the CO_2 sorption capacity. This decreased sorption capacity and methane production capacity, along with lower conversion of the desorbed CO_2, indicate the mixed-then-pelletized (MP) method of preparing these catalytic sorbents is not as effective for the combined capture and methanation cycle.

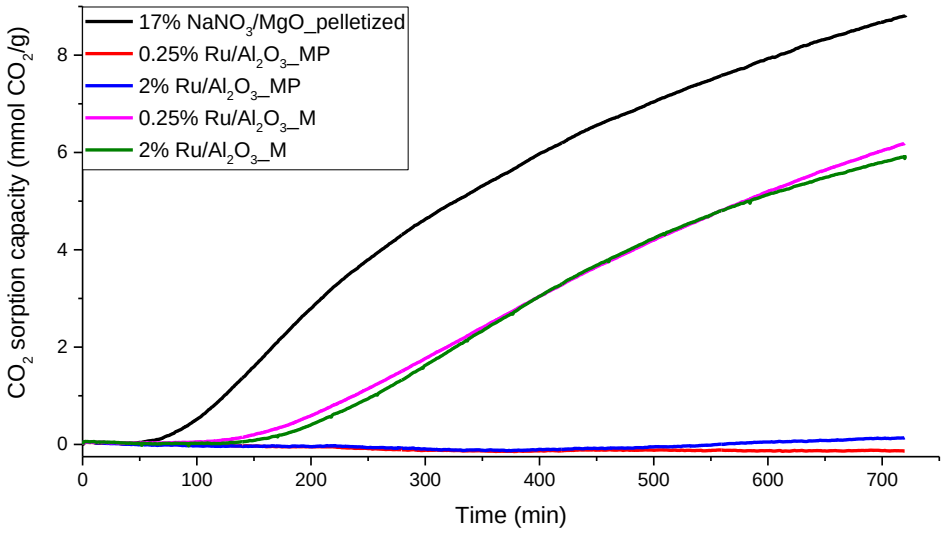

Figure 3.5. Change in mass of different samples at 300 °C under 10% CO_2/15% H_2O/N_2 flow for 12 h. Samples were first exposed to flow of 15% H_2O/N_2 before exposure to 10% CO_2/15% H_2O/N_2 flow.

To further probe the cause of the significant decrease in CO_2 sorption capacity in the MP samples, additional sorption capacity measurements were performed on the

catalytic sorbents prepared by the different methods. To test if pelletizing and sieving the mixed composition caused the observed decrease in sorption capacities, a pelletized then sieved 17% $NaNO_3$/MgO sample (noted as 17% $NaNO_3$/MgO_pelletized) was evaluated in sorption capacity measurements, as shown in Figure 3.5. A 12 h sorption capacity of 9 mmol CO_2/g was obtained for the sample, which is approximately 72% of the sorption capacity of the non-pelletized powder sorbent at the same conditions, as observed in Figure 3.3 (12.5 mmol CO_2/g). This observation showed that pelletizing the material at a pressure of 1000 psig yielded only a moderate decrease in sorption capacity, and was not likely the main cause of the significant decrease in sorption capacity observed in the MP samples. A similar experiment was performed on the 0.25% Ru/Al_2O_3_M and 2% Ru/Al_2O_3_M samples, samples prepared by physically mixing 0.25% Ru/Al_2O_3 or 2% Ru/Al_2O_3 and 17% $NaNO_3$/Al_2O_3, but without pelletization. The 0.25% Ru/Al_2O_3_M sample showed a sorption capacity of 6.2 mmol CO_2/g and 2% Ru/Al_2O_3_M sample showed similar sorption capacity of 5.9 mmol CO_2/g. If the obtained sorption capacity were normalized to the mass of 17% $NaNO_3$/MgO sorbent only, the sorption capacity becomes 9.3 mmol CO_2/g and 8.9 mmol CO_2/g (Mass ratio of 17% $NaNO_3$/MgO : Ru/Al_2O_3 = 2:1). This observation indicates that physically mixing the 17% $NaNO_3$/MgO and Ru/Al_2O_3 is likely not the main factor that caused the significant decrease in sorption capacity in the MP samples either. Therefore, it was hypothesized that physically mixing and pelletizing the 17% $NaNO_3$/MgO and Ru/Al_2O_3 together is what significantly decreases the sorption performance of the catalytic sorbent. We suggest that when the two components become tightly bound together, the basic molten $NaNO_3$ may transfer to the acidic Al_2O_3 support,

leading to a quenching of the basic properties of the promoter, leading to loss in functionality of the $NaNO_3$ as a promoter in the CO_2 sorbent.

3.3.4 Reaction Order, Activation Energy and FTIR Measurements

Based on the results from the previous section, clear differences in the CO_2 sorption behavior were observed between the 2B samples and the MP samples. However, these data do not allow insight into reaction pathways in the catalytic sorbents made via the two methods. To probe the reaction pathways during CO_2 methanation, reaction order measurements for CO_2 and H_2 were conducted, and apparent activation energies were calculated from the reactivity data. Three different samples, 1% Ru/Al_2O_3, 1%Ru/Al_2O_3_MP, and 5% $NaNO_3$/1%Ru/Al_2O_3, were evaluated in these reactivity experiments.

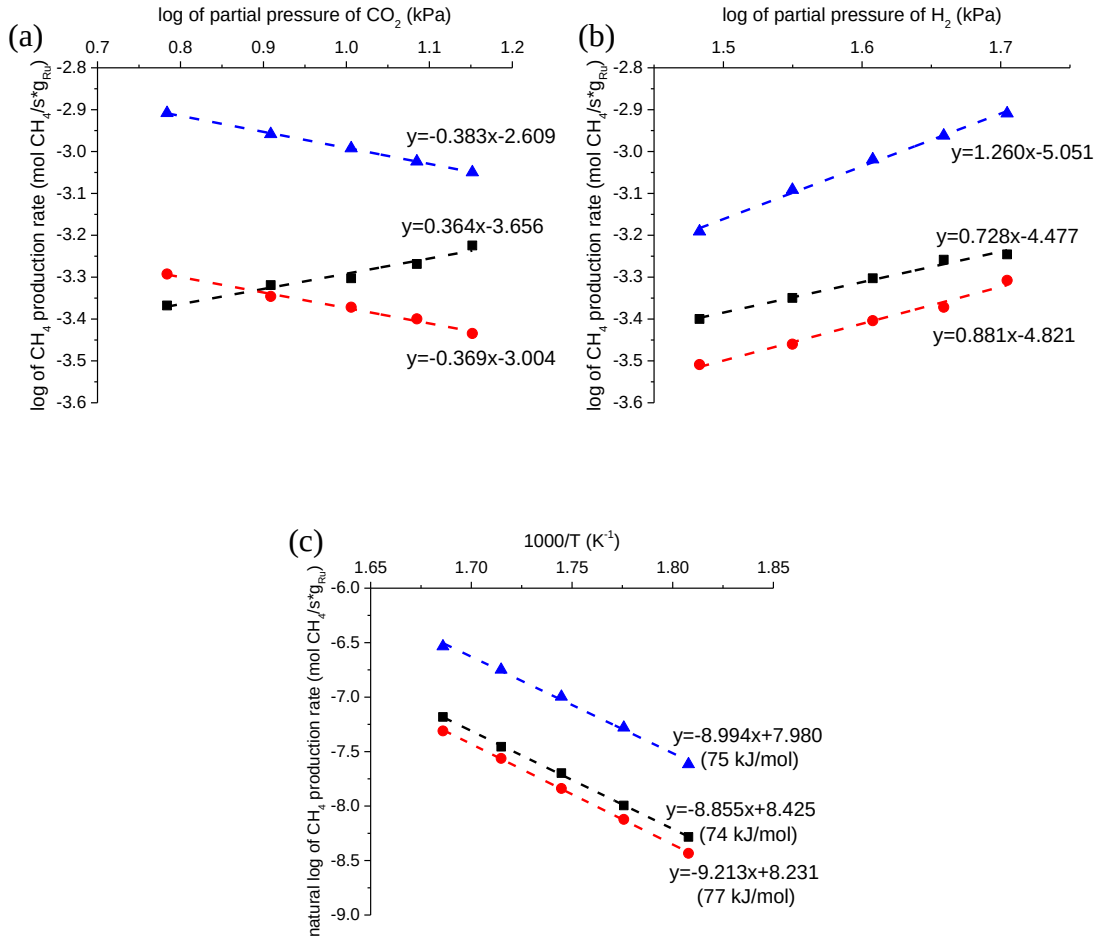

Figure 3.6. (a) CO_2 reaction order, (b) H_2 reaction order, and (c) activation energy measured for CO_2 methanation reaction over different catalysts (Black square = 1%Ru/Al_2O_3, red circle = 1%Ru/Al_2O_3_MP, blue triangle = 5% $NaNO_3$/1%Ru/Al_2O_3).

As observed in Figure 3.6, 1% Ru/Al_2O_3 showed a CO_2 order of 0.36 and H_2 order of 0.73. The higher H_2 order than CO_2 order likely indicates that CO_2 is more tightly bound on the catalyst surface than H_2, leading higher CO_2 than H_2 surface coverage. The CO_2 reaction orders decreased to negative orders for the $NaNO_3$ containing samples, with the 1% Ru/Al_2O_3_MP catalytic sorbent showing an order of -0.37 and the 5% $NaNO_3$/1%Ru/Al_2O_3 material having an order of -0.38. On the other hand, the H_2 reaction order increased for the $NaNO_3$ containing samples, with the 1% Ru/Al_2O_3_MP material

having a reaction order of 0.88 and the 5% $NaNO_3$/1%Ru/Al_2O_3 an order of 1.26. These changes in reaction orders imply that the CO_2 coverage increased and the H_2 coverage decreased for $NaNO_3$ containing samples. As previously reported, the molten alkali metal ion medium is capable of dissolving CO_2. This property of $NaNO_3$ facilitates CO_2 surface sorption, leading to increased CO_2 coverage. The fact that similar negative orders in CO_2 and increases in H_2 order were observed in both the 1%Ru/Al_2O_3_MP and 5%$NaNO_3$/1%Ru/Al_2O_3 may be indicating that the molten $NaNO_3$ may be near the ruthenium sites for the 1%Ru/Al_2O_3_MP, even though the $NaNO_3$ was not directly impregnated on the same Al_2O_3 support. The transfer of molten $NaNO_3$ from MgO sites to near the Ru sites is consistent with the hypothesized causes for reduced CO_2 sorption in the sorption experiments over the MP samples, as discussed above. Activation energies for all three samples were calculated using the data shown in Figure 3.6 (c). Unlike the reaction orders, the activation energies were similar among all three samples, with 1% Ru/Al_2O_3 showing an E_a of 74 kJ/mol, 1%Ru/Al_2O_3_MP having an E_a of 75 kJ/mol and 5%$NaNO_3$/1%Ru/Al_2O_3 yielding an E_a of 77 kJ/mol. The similarity in activation energy may imply that the three catalysts have similar rate determining steps (RDS).

CO was observed as a side product for the 1% Ru/Al_2O_3_MP (mixed-then-pelletized) and 5% $NaNO_3$/1%Ru/Al_2O_3 catalysts, while the 1%Ru/Al_2O_3 material did not produce significant CO. Plots to generate reaction orders and activation energies for CO formation are shown in Figure B.4. The CO_2 reaction order was 0.96 for the 1% Ru/Al_2O_3_MP catalyst and 1.13 for the 5% $NaNO_3$/1%Ru/Al_2O_3 sample. The H_2 reaction order was -0.54 for 1% Ru/Al_2O_3_MP and -0.79 for 5% $NaNO_3$/1%Ru/Al_2O_3. The activation energy for CO formation was higher than for CH_4 formation, being 95 kJ/mol

for 1% Ru/Al_2O_3_MP and 101 kJ/mol for 5% $NaNO_3$/1%Ru/Al_2O_3. For both samples, CO formation was elevated at higher CO_2 concentrations and lower H_2 concentrations, a trend opposite that of methane formation. The differences in activation energy suggest different rate determining steps for reverse water gas shift and methanation reactions.

For additional insight into the CO_2 methanation pathways over the three different catalysts, in-situ FTIR experiments were performed. In these experiments, after 90 minutes of methanation reaction, the CO_2 feed was stopped and spectra were taken for another 90 minutes under only a H_2/N_2 feed to observe how the surface species evolved in the absence of CO_2. The FTIR spectra of for the 1% Ru/Al_2O_3 catalyst are shown in Figure 3.7.

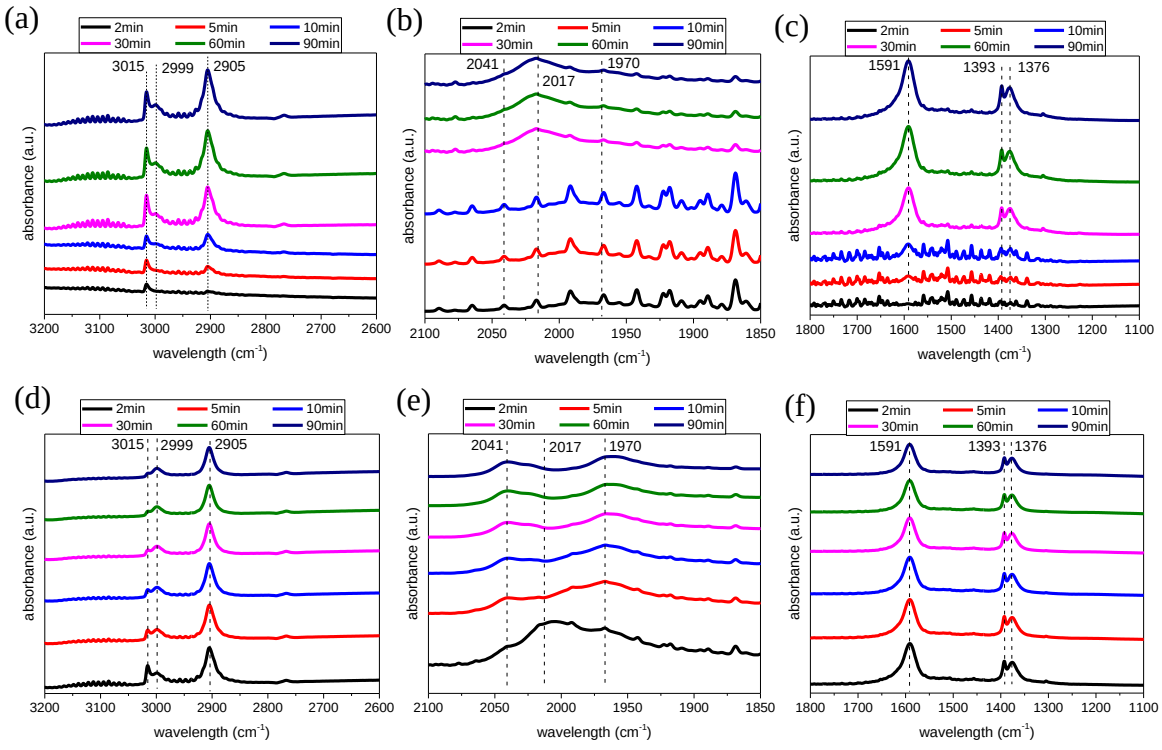

Figure 3.7. FTIR spectra of 1% Ru/Al_2O_3 during the CO_2 methanation under 10% CO_2/40% H_2/N_2 at 300 °C (a) from 2600 cm^{-1} to 3200 cm^{-1}, (b) from 1850 cm^{-1} to 2100 cm^{-1}, and (c) from 1100 cm^{-1} to 1800 cm^{-1}, and after feed switch to 40% H_2/N_2 (d) from 2600 cm^{-1} to 3200 cm^{-1}, (e) from 1850 cm^{-1} to 2100 cm^{-1}, and (f) from 1100 cm^{-1} to 1800 cm^{-1}.

The spectra were divided into three regimes, as the peaks in carbonyl region were much smaller than the peaks in the carbonate region and C-H region. During the first 90 minutes of 10% CO_2/40% H_2/N_2 flow, three peaks at 1591 cm^{-1}, 1393 cm^{-1}, and 1376 cm^{-1} were observed in the carbonate region, indicating formation of surface formate species.[66,67] An intense band observed at 2905 cm^{-1} and a shoulder observed at 2999 cm^{-1} appeared in the C-H region, which also indicated formation of formate species. In the carbonyl region, a peak at 2017 cm^{-1}, and two shoulders at 2041 cm^{-1} and 1970 cm^{-1}, were observed. The peak at 2017 cm^{-1} was assigned to linear carbonyl species, and the two shoulders at 2041 cm^{-1} and 1970 cm^{-1} correspond to dicarbonyl species on Ru metal.[67–71] The peak at 3015 cm^{-1} was assigned to methane. When the feed was switched to 40% H_2/N_2 flow alone, the peak at 2017 cm^{-1} decreased quickly and became unobservable after 10 minutes. On the other hand, the peaks indicating formate species or dicarbonyl species showed very little change in intensity throughout the 90 minutes after the feed switch. These observations show that the linear carbonyl species were unstable after the CO_2 feed stopped, whereas the dicarbonyl species and formate species were very stable under the same conditions. Based on this observation, it was hypothesized that linear carbonyl species are potential reaction intermediates for the CO_2 methanation reaction over 1% Ru/Al_2O_3 catalysts, while dicarbonyl species and formate species are likely spectator species.

While similar experiments were performed on the 1%Ru/Al_2O_3_MP sample (shown in Figure B.5), it was difficult to observe the characteristic peaks that correspond to possible intermediates for the CO_2 methanation. An intense peak at 1584 cm^{-1} was formed upon exposure to 10% CO_2/40%H_2/N_2. This peak is assigned to bidentate carbonate

species formed on the MgO support.[72,73] The wide band at 1234 cm^{-1} likely corresponds to a deformation mode of hydroxyl groups.[73] Other notable peaks observed at 1815 cm^{-1}, 2543 cm^{-1}, 2625 cm^{-1}, 2916 cm^{-1}, and 3040 cm^{-1} indicate formation of $Na_2Mg(CO_3)_2$, through interaction of inorganic ions of $NaNO_3$ and MgO with dissolved CO_2 in the molten medium.[74] As shown in Figure B.6, these peaks also correspond well to peaks observed on 17% $NaNO_3$/MgO after 90 min exposure of 10% CO_2/N_2, indicating that such peaks do not represent intermediate or surface species related to CO_2 methanation at metal sites. While formation of methane was evidenced by the peak at 3015 cm^{-1}, other species on the Ru surface or Al_2O_3 surface were hard to discern, most likely because the 1%Ru/Al_2O_3 was too dilute in the 1%Ru/Al_2O_3_MP sample (17% $NaNO_3$/MgO:1% Ru/Al_2O_3 = 2:1 mass ratio).

Because of the difficulty observing surface species on Ru or Al_2O_3 with the 1%Ru/Al_2O_3_MP catalyst, as an alternative sample was prepared whereby $NaNO_3$ was directly impregnated onto 1% Ru/Al_2O_3 to synthesize a 5% $NaNO_3$/1%Ru/Al_2O_3 material. Under the assumption that transfer of $NaNO_3$ from 17% $NaNO_3$/MgO to 1% Ru/Al_2O_3 does occur in the MP samples, we hypothesized that the 5% $NaNO_3$/1% Ru/Al_2O_3 material may give insights regarding the effect of $NaNO_3$ on the methanation reaction. The FTIR spectra during CO_2 methanation and after the CO_2 feed was stopped are shown in Figure 3.8.

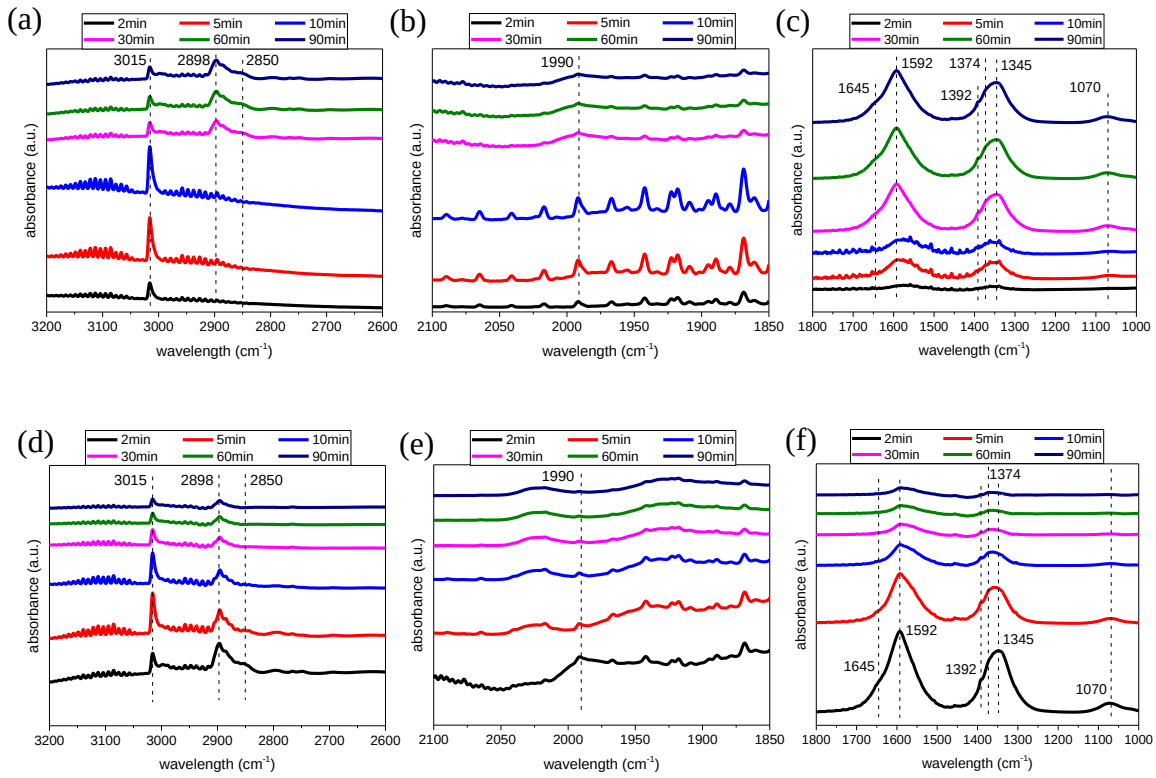

Figure 3.8. FTIR spectra of 5% $NaNO_3$/1% Ru/Al_2O_3 during CO_2 methanation under 10% CO_2/40% H_2/N_2 at 300 °C (a) from 2600 cm^{-1} to 3200 cm^{-1}, (b) from 1850 cm^{-1} to 2100 cm^{-1}, and (c) from 1000 cm^{-1} to 1800 cm^{-1}, and after feed switch to 40% H_2/N_2 (d) from 2600 cm^{-1} to 3200 cm^{-1}, (e) from 1850 cm^{-1} to 2100 cm^{-1}, and (f) from 1000 cm^{-1} to 1800 cm^{-1}.

The peaks observed at 2998 cm^{-1}, 2898 cm^{-1}, 2850 cm^{-1}, 1592 cm^{-1}, 1392 cm^{-1}, 1374 cm^{-1}, and 1070 cm^{-1} were assigned to surface formate species interacting with neighboring Na ions. A shoulder at 2850 cm^{-1} and the wide band at 1070 cm^{-1}, which were not observed on the 1% Ru/Al_2O_3, are characteristic peaks of sodium formate, which imply that surface formate species are likely interacting with Na^+ ions of $NaNO_3$. This type of formate is different in nature to formate on the unpromoted alumina support, as it was recently reported that formate species interacting with alkali metal ions do not adsorb as strongly on the support, and are only stable under the hydrogenation feed.[66] Carbonyl peaks of similar shape as in 1% Ru/Al_2O_3, but in a slightly lower wavelength, were observed as

well. The peak observed at 1990 cm^{-1} was assigned to dihydrogen carbonyl species, as it has been reported that when H_{ad} and CO_{ad} are adsorbed on same site, it results in carbonyl bands appearing at lower frequencies.[66,75,76] In addition to dihydrogen carbonyl and surface formate species, peaks at 1345 cm^{-1}, indicating bidentate carbonate species, and a shoulder at 1645 cm^{-1}, indicating bicarbonate species, were observed during the methanation reaction. Unlike in the case of 1% Ru/Al_2O_3, as the feed switches to 40% H_2/N_2, peaks indicating not only carbonyl species, but formate, carbonate, and bicarbonate species also decrease. This result may indicate that while formate was a spectator species over the 1% Ru/Al_2O_3 catalyst, it may be a true reaction intermediate along with carbonate and bicarbonate species over the 5% $NaNO_3$/1%Ru/Al_2O_3 catalyst. Further transient kinetics and operando studies to test this hypothesis are shown in Chapter 4.

3.3.5 Kinetic Analysis and Rate Law Derivation

Based on the data obtained from reaction order measurements and spectra obtained from FTIR experiments, two different reaction pathways were proposed for 1% Ru/Al_2O_3 and 5% $NaNO_3$/1%Ru/Al_2O_3, and rate laws consistent with experimental observations were derived for each proposed series of elementary steps, as shown in Table 3.2 and Table 3.3. For 1% Ru/Al_2O_3, linear carbonyl species were hypothesized as reaction intermediates, while formate species were hypothesized to be a spectator species. Carbonyl species are commonly observed in dissociative mechanisms, so it is likely that the CO_{ad} species observed are formed through the dissociation of CO_2 on Ru^0 surface.[77] To this end, a plausible pathway whereby dissociation of H_2 into two H_{ad} atoms (step 1), adsorption of CO_2 into $CO_{2,ad}$ (step 2), and quick dissociation of $CO_{2,ad}$ into CO_{ad} and O_{ad} (step 3) both occur on the surface of Ru^0 was considered, which is likely followed by H-assisted CO_{ad}

dissociation (step 4). Multiple hydrogenation steps of $CH_{x,ad}$ species (step 5~7) that result from dissociation of CO_{ad} then lead to eventual formation of methane. O_{ad} formed from direct dissociation of CO_2 or CO_{ad} is hydrogenated to form H_2O (step 9~11). Based on assumptions that the CO dissociation step is the rate determining step (RDS) and that H_2O_{ad} formation step is irreversible, a rate law was derived for the proposed series of steps, shown in equation 3.5. According to the derived rate law, the H_2 reaction order can vary from 0.75 to -0.25, and CO_2 reaction order can vary from 0.5 to -0.5. The observed reaction order of 0.72 for H_2 and 0.39 for CO_2 fits within the derived rate law parameters, supporting the plausibility of the rate law. While both direct dissociation of CO (CO* -> C* + O*) and H-assisted dissociation of CO (CO* + H* -> CH* + O*) have been previously proposed as possible RDSs for the CO_2 methanation reaction, the relatively high H_2 reaction order of 0.73 was not obtained by setting direct CO dissociation as the RDS, and therefore it was assumed that H-assisted CO dissociation is more likely the RDS over the 1% Ru/Al_2O_3 catalyst. Detailed derivation of the rate law is shown in **Section B.4** and **B.5** of **Appendix B**.[68,70,71,75,78–84]

While carbonyl species are generally accepted as true reaction intermediates in CO_2 methanation reactions over Ru/Al_2O_3, the reaction pathway for the formation of the carbonyl intermediate is yet unclear. Our proposed pathway, shown in Table 3.2, aligns with multiple works that proposed direct dissociation of CO_2 to CO* and O*, followed by hydrogenation of carbonyl species as the dominant pathway for CH_4 formation, including works by Solymosi et al.[68,75,78,79,81,84] However, Marwood et al. reported that while carbonyl species (CO*) are true reaction intermediates, H-assisted dissociation of CO_2, in which bicarbonate species are formed first, then followed by formation of formate and

carbonyl species on the metal-support interface, is the more dominant pathway than direct dissociation of CO_2 over Ru/Al_2O_3 catalysts.[70,71,80,82,83] In this work, direct dissociation of CO_2 was assumed, because bicarbonate species were not observed in our IR spectra, similar to other experimental works that proposed direct dissociation of CO_2 as the main reaction mechanism. However, we are hesitant to conclusively state that direct dissociation of CO_2 is generally the dominant pathway for methane formation over Ru/Al_2O_3 catalysts for several reasons. First, it is possible that bicarbonate species (HCO_3*) exist at a very low surface coverage, such that they are not observed in the IR spectra. If bicarbonates species do exist, but rapidly convert to formate species, it is possible that such intermediates would not be observed. Second, there have been reports that the structure of the Ru domains, which is affected by the weight loading of the metal, affects the CO_2 dissociation pathway, and thereby CO_2 hydrogenation behavior.[85,86] While our work aligns with other works that proposed a direct CO_2 dissociation pathway, it is possible that Ru/Al_2O_3 catalysts reported in other works, synthesized by different methods and at different metal loadings, favored other reaction pathways, such as H-assisted CO_2 dissocation, in the formation of methane. At this stage, based on our in-situ FTIR data and kinetic analysis, we conservatively propose the direct dissociation of CO_2 to CO* and O* species is more plausible than other pathways over $1\%Ru/Al_2O_3$ catalyst.

Table 3.2. Proposed series of steps for CO_2 methanation over 1% Ru/Al_2O_3 catalyst. Asterisk (*) denotes Ru site.

Step	Reaction
1	$H_2(g) + 2* \leftrightarrow 2H*$
2	$CO_2(g) + * \leftrightarrow CO_2*$
3	$CO_2* + * \leftrightarrow CO* + O*$
4 (RDS)	$CO* + H* \leftrightarrow CH* + O*$
5	$CH* + H* \rightarrow CH_2* + *$

6	CH_2+* + H* ↔ CH_3* + *
7	CH_3* + H* ↔ CH_4* + *
8	CH_4* ↔ CH_4(g) + *
9	O* +H* ↔ OH* + *
10	OH* +H* → H_2O* + *
11	H_2O* ↔ H_2O(g) + *

$$r_4 = \frac{\sqrt{\frac{k_4 k_{10} {K_1}^{1.5} K_2 K_3 K_9}{2}}[H_2]^{0.75}[CO_2]^{0.5}{[*]_{total}}^2}{(1+K_1^{0.5}[H_2]^{0.5}+\sqrt{\frac{k_{10}{K_1}^{0.5}K_2K_3K_9}{2k_4}}[H_2]^{0.25}[CO_2]^{0.5})^2} \quad \text{Eq 3.5}$$

For the 5% $NaNO_3$/1% Ru/Al_2O_3 catalyst, based on observation from in-situ FTIR spectra, bicarbonate, carbonate, formate, and carbonyl species are hypothesized to be reaction intermediates. As previously mentioned, formate or bicarbonate species are commonly observed intermediates for H-assisted dissocation of CO_2, and can be formed by adsorption of CO_2 on the support.[70,71,80,82,83] Carbonyl species are also observed as intermediate species from the FTIR experiments, so it is likely that CO_2 first adsorbs on the support, and transfer of carbon containing species to Ru^0 sites occurs, implying that the reaction occurs on the support-metal interface for the $NaNO_3$ containing catalyst. The fact that 5% $NaNO_3$/1%Ru/Al_2O_3 has a similar activation energy as the 1%Ru/Al_2O_3 catalyst implies that the carbonyl dissociation step is the likely RDS, similar to 1%Ru/Al_2O_3, giving additional support that the reaction occurs at the interface of the support and metal. So it is likely that while the H_2 dissociation (step 1) occurs on the Ru^0 site, CO_2 first adsorbs on –O site of the Al_2O_3 support (step 2) to form carbonate species. H_{ad} species and carbonate species can interact to form bicarbonate species (step 3), which then can dissociate to formate species and hydroxyl species on Ru^0 (step 4). After formate formation on the

support, transfer of carbon containing species to Ru^0 site might occur, leading to formation of H_{ad} and CO_{ad} species on the metal sites. As noted above, a lower wavelength of adsorbed carbonyl species likely indicates formation of dihydrogen carbonyl species, so it was assumed dihydrogen carbonyl species are formed from H_{ad} species and CO_{ad} species (step 6~7). This dihydrogen carbonyl species is dissociated to $CH_{x,ad}$ and OH_{ad} species (step 8), and the two species are further hydrogenated to form CH_4 (step 9~11) and H_2O (step 12~13). Using dissociation of dihydrogen carbonyl species as the rate determining step, a rate law was derived for the proposed pathway, as shown in equation 3.6. For derived rate law, the H_2 reaction order can vary from 1.75 to -0.5, and CO_2 reaction order can vary from 0.5 to -0.5. The observed reaction order of 1.26 for H_2 and -0.38 for CO_2 for 5% $NaNO_3$/1% Ru/Al_2O_3 corresponds with the reaction order range for the derived rate law. Clear indication of bicarbonate species and formate species, along with correspondence of the obtained reaction order to derived reaction rate law supports the hypothesis of an H-assisted CO_2 dissociation mechanism becoming more dominant in the presence of $NaNO_3$. Wang et al. previously reported that in the proposed H-assisted CO_2 dissociation mechanism, formate species near the metal-support interface are the species that participate in the reaction as intermediates, while formate species far from the metal particles are spectator species.[71] A recent study also reported that formate species are less tightly bound on the Al_2O_3 support in the presence of alkali promoters (potassium).[66] Based on these recent findings and our experimental data, we hypothesized that formate species that are far from Ru particles that behaved as spectator species in absence of $NaNO_3$, become more 'mobile' in the presence of $NaNO_3$, and participate as reaction intermediates, promoting H-assisted dissociation of CO_2. However, it is difficult to firmly conclude that such proposed reaction

mechanism is the dominant mechanism without any transient kinetics and/or operando studies. As previously mentioned, future transient kinetics and operando studies are to test the mentioned hypothesis is shown in Chapter 4.

Table 3.3. Proposed mechanism for CO_2 methanation over 5%$NaNO_3$/1% Ru/Al_2O_3 catalyst and derived rate law. Asterisk (*) denotes Ru site, and S denotes –O site on Al_2O_3 support.

Step	Reaction
1	$H_2(g) + 2* \leftrightarrow 2H*$
2	$CO_2(g) + S \leftrightarrow CO_2\text{-}S$
3	$CO_2\text{-}S + H* \leftrightarrow HCO_2\text{-}S + *$
4	$HCO_2\text{-}S + H* \leftrightarrow HCO\text{-}S + OH*$
5	$HCO\text{-}S + 2* \rightarrow H* + CO* + S$
6	$CO{+}* + H* \leftrightarrow H*CO + *$
7	$H*CO + H* \leftrightarrow H_2*CO + *$
8 (RDS)	$H_2*CO + H* \leftrightarrow CH_2* + OH*$
9	$CH_2* + H* \leftrightarrow CH_3* + *$
10	$CH_3* + H* \leftrightarrow CH_4* + *$
11	$CH_4* \leftrightarrow CH_4 + *$
12	$OH* + H* \rightarrow H_2O* + *$
13	$H_2O* \leftrightarrow H_2O(g) + *$

$$r_8 = \frac{\sqrt{\frac{k_8 k_{12} {K_1}^{1.5} K_2 K_3 K_4 K_5 K_6 K_7}{2}}[H_2]^{1.25}[CO_2]^{0.5}[*]_{\text{total}}{}^2}{(1+\mathrm{K}_1^{0.5}[\mathrm{H}_2]^{0.5}+\sqrt{\frac{k_{12} K_2 K_3 K_4 K_5}{2k_8 {K_1}^{0.5} K_6 K_7}}[H_2]^{-0.25}[CO_2]^{0.5}+ \sqrt{\frac{k_{12} {K_1}^{0.5} K_2 K_3 K_4 K_5 K_6}{2k_8 K_7}}[H_2]^{0.25}[CO_2]^{0.5}+\sqrt{\frac{k_{12} {K_1}^{1.5} K_2 K_3 K_4 K_5 K_6 K_7}{2k_8}}[H_2]^{0.75}[CO_2]^{0.5})^2} \quad \text{Eq 3.6}$$

3.3.6 Combined CO_2 Capture and Conversion over Multiple Cycles

Finally, to observe the stability of the catalytic sorbents over multiple cycles, the 1% Ru/Al_2O_3_2B sample was selected for testing over 5 cycles of combined CO_2 capture and conversion. Cyclic experiments were performed with two different methods. For first

experiment, all 5 cycles of capture and methanation were performed at isothermal conditions of 300 °C. CO_2 sorption was performed for 3 h under 10% CO_2/N_2 with 11% absolute humidity flow and methanation was performed for 6 h under 10% H_2/N_2, the same as previous experiments. In the second experiment, during the first cycle, CO_2 sorption was performed for 10 h at 300 °C and methanation was performed at 320 °C for 3 h. After methanation at 320 °C, the temperature was cooled to 300 °C at 10 °C/min in a N_2 flow, and the following 4 cycles were performed the same as the first experiment. The second method was performed due to a recent report that the CO_2 sorption rate was higher for partially a desorbed $NaNO_3$ promoted MgO sorbent than a fresh sorbent.[45] It was also reported that the degree of increase in the sorption rate was higher as more CO_2 was sorbed in the first cycle and when a larger fraction of the captured CO_2 was desorbed during the partial desorption. Second set of cyclic experiments was performed to test if this type of property can be used to obtain higher sorption and methane production capacities in a combined capture and conversion cycle.

Calculated CO_2 sorption capacities and CH_4 production capacities over 5 cycles at the isothermal condition of 300 °C are shown in Figure 3.9 (a), and a plot showing the concentration of CO_2, CH_4, and H_2 in the outlet stream is shown in Figure B.7. The CO_2 sorption capacity is similar in the first two cycles, with a sorption capacity of 2.57 mmol CO_2/g and 2.59 mmol CO_2/g. Starting from the third cycle, the CO_2 sorption capacity decreased over subsequent cycles, showing 2.34, 2.01, 1.78 mmol CO_2/g sorption capacity. This trend is similar to what was observed in TGA experiments, as observed in Figure B.2, indicating deactivation of the 17% $NaNO_3$/MgO sorbent over multiple cycles, thereby leading to decreased sorption capacity. On the other hand, the decrease in methanation

capacity was much less significant than the decrease in CO_2 sorption capacity. Methane production of 1.59 mmol CH_4/g was observed in the first cycle and showed a similar methane production capacity in the first three cycles, then decreasing to 1.45 mmol CH_4/g in the 4th cycle, and to 1.34 mmol CH_4/g in the 5th cycle. This trend in methanation capacity aligns with what was observed from isothermal sorption and desorption cycles as shown in Figure B.2, as the desorption capacity tended to be similar in first 4 cycles, then started to decrease rapidly from cycles afterwards.

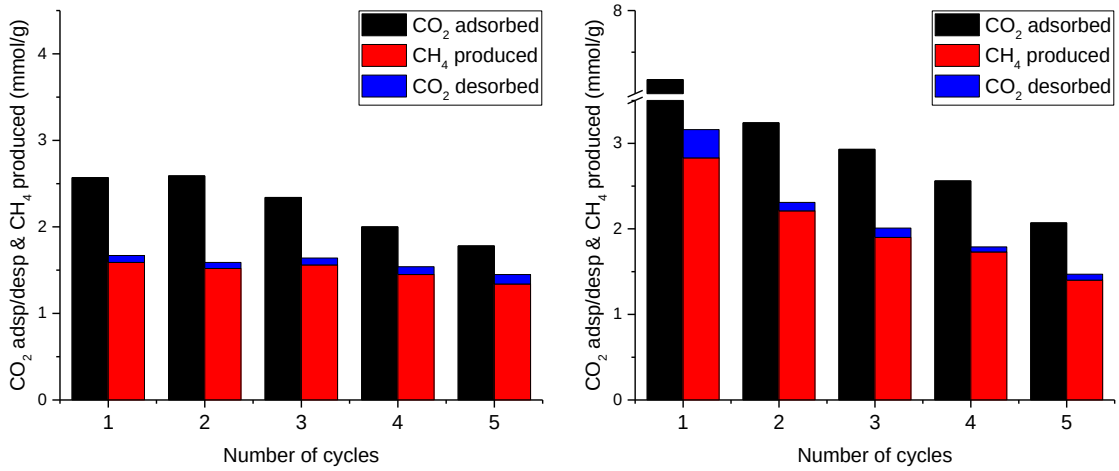

Figure 3.9. Amount of CO_2 adsorbed/desorbed and CH_4 produced over five cycles of combined CO_2 capture and conversion for the 1% Ru/Al_2O_3_2B sample. (a) CO_2 sorption step was 3 h and methanation step was 6 h. Temperature was isothermal at 300 °C throughout 5 cycles. (b) CO_2 sorption step was 10 h at 300 °C and methanation step was 3 h at 320 °C in the first cycle. The temperature was reduced to 300 °C after the first cycle and had equivalent conditions as (a) in the remaining 4 cycles. For both cases, there was a 15 min N_2 purge step between the capture step and methanation step.

Calculated CO_2 sorption capacities and CH_4 production capacities for cyclic experiments using 320 °C methanation for the first cycle are shown in Figure 3.9 (b), and the plot showing the concentrations of CO_2, CH_4, and H_2 detected is shown in Figure B.8. In the first 10 h sorption step, a sorption capacity of 7.17 mmol CO_2/g was observed. In the

3 h 10% H_2/N_2 flow at 320 °C, a methane production capacity of 2.83 mmol CH_4/g and unreacted CO_2 of 0.33 mmol CO_2/g were observed. In the second cycle, a sorption capacity of 3.24 mmol CO_2/g and methane production capacity of 2.21 mmol CH_4/g were observed, showing a 25% increase in sorption capacity and 39% increase in methane production capacity compared to the highest values obtained from Figure 3.9 (a). Such an increase in sorption and methane production shows the unique properties of the partially desorbed $NaNO_3$ loaded MgO sorbent do lead to significant improvements in performance of the catalytic sorbent in capture and conversion cycles.

The sorption and desorption capacities reported here are among the highest values reported in a single cycle of combined capture and conversion in simulated flue gas (~10% CO_2) reported to date.[87] The sorption and methanation capacities run isothermally in the following cycles decreased much faster than the case without a 320 °C methanation step, with sorption capacities of 2.93, 2.56, 2.07 mmol CO_2/g and methane production capacity of 1.90, 1.73, 1.40 mmol CH_4/g in the following cycles. This may indicate that performing methanation at the higher temperature of 320 °C may be accelerating the MgO sorbent deactivation over cycling. So while high sorption and methane production were observed using these materials, improvement in sorbent stability remains as challenge. This stability is likely associated with MgO's tendency to sinter upon thermal cycling. Also, 3 h duration for CO_2 sorption step and 6 h duration for methanation step is far from ideal for industrial application, and therefore, further study to improve sorption and methanation kinetics will be needed for such materials.

3.4 Conclusion

Catalytic sorbents were synthesized by physically mixing $NaNO_3$ promoted MgO with Al_2O_3 supported ruthenium. Utilization of two separate beds of the two components, sorbent then catalyst, was more effective in combined capture and conversion than using a single bed of mixed-then-pelletized $NaNO_3$/MgO + Ru/Al_2O_3. Similar CO_2 sorption capacities between 2.57 mmol CO_2/g and 2.87 mmol CO_2/g and methanation capacities between 1.51 mmol CH_4/g and 1.54 mmol CH_4/g were observed from the 0.5%, 1%, 2% Ru/Al_2O_3_2B samples, while a decreased methane production capacity of 1.37 mmol CH_4/g was observed from 0.25% Ru/Al_2O_3_2B. The CO_2 capture performance of $NaNO_3$/MgO was significantly reduced upon mixing-then-pelletizing with Ru/Al_2O_3, possibly due to transfer of basic promoter - molten $NaNO_3$ - to the acidic Al_2O_3 support, quenching the basicity of the promoter.

To understand potential CO_2 methanation reaction pathways over the different catalysts, in-situ FTIR measurements were performed during the CO_2 methanation reaction over 1% Ru/Al_2O_3 and 5% $NaNO_3$/1%Ru/Al_2O_3. Based on the spectra obtained, it was hypothesized that carbonyl species were likely reaction intermediates over 1% Ru/Al_2O_3, while formate species were spectators. On the other hand, for 5% $NaNO_3$/1%Ru/Al_2O_3, both carbonyl and formate species, along with carbonate and bicarbonate species, were likely reaction intermediates. Reaction order measurements for CO_2 and H_2 combined with hypothetical reaction mechanisms and rate laws for CO_2 methanation were developed for the two catalysts.

Combined CO_2 capture and conversion cycles were performed at 300 °C for the 1%Ru/Al_2O_3_2B sample. While the material yielded similar CO_2 sorption capacities of 2.6 mmol CO_2/g and methane production capacities of 1.5 mmol CH_4/g in the first two cycles, a decrease in performance was observed over subsequent cycles, showing 1.78 mmol CO_2/g and 1.34 mmol CH_4/g in the fifth cycle. When the methanation temperature was increased to 320 °C in the first cycle, then cooled to 300 °C from the second cycle, both the sorption and methane production capacities were significantly increased to 3.2 mmol CO_2/g and 2.2 mmol CH_4/g. However, both CO_2 sorption and methane production still decreased over subsequent cycles, likely due to deactivation of the $NaNO_3$/MgO sorbent. While further study to improve sorbent stability and kinetics of sorption and methanation is needed, these sorption and methane production capacities are among the highest among reported combined capture and methanation of CO_2 in flue gas conditions.[87]

Lastly, as a closing remark, while capture and conversion cycles were performed in a fixed bed by switching the feed gas between CO_2 and H_2, with an N_2 purge in between, such an approach is unlikely to be efficient in an actual industrial process. Rather, a more viable method to perform combined capture and conversion process is through chemical-looping,[88,89] whereby the catalytic sorbents are cycled between two reactors, one with H_2 feed and the other with CO_2 feed. However, published studies regarding chemical looping for combined capture and conversion applications are limited. Therefore, it is believed that further future studies regarding chemical looping are needed to move the general integrated capture and conversion approach towards viable practice.

3.5 Reference

(1) Boden, T. A.; Marland, G.; Andres, R. J. Global, Regional, and National Fossil-Fuel CO_2 Emissions. Carbon Dioxide Information Analysis Center, Oak Ridge National Laboratory, U.S. Department of Energy. **2017**.

(2) Intergovernmental Panel on Climate Change. *Climate Change 2014 : Mitigation of Climate Change*; Cambridge University Press, 2014.

(3) Earth System Research Laboratory. Trends in Atmospheric Carbon Dioxide.

(4) Yu, C.-H.; Huang, C.-H.; Tan, C.-S. A Review of CO_2 Capture by Absorption and Adsorption. *Aerosol Air Qual. Res.* **2012**, *12* (5), 745–769.

(5) Yang, H.; Xu, Z.; Fan, M.; Gupta, R.; Slimane, R. B.; Bland, A. E.; Wright, I. Progress in Carbon Dioxide Separation and Capture: A Review. *J. Environ. Sci.* **2008**, *20* (1), 14–27.

(6) Figueroa, J. D.; Fout, T.; Plasynski, S.; McIlvried, H.; Srivastava, R. D. Advances in CO_2 Capture Technology — The U.S. Department of Energy's Carbon Sequestration Program. *Int. J. Greenh. Gas Control* **2008**, *2*, 9–20.

(7) Leung, D. Y. C.; Caramanna, G.; Maroto-Valer, M. M. An Overview of Current Status of Carbon Dioxide Capture and Storage Technologies. *Renew. Sustain. Energy Rev.* **2014**, *39*, 426–443.

(8) Rao, A. B.; Rubin, E. S. A Technical , Economic , and Environmental Assessment of Amine-Based CO_2 Capture Technology for Power Plant Greenhouse Gas Control.

Environ. Sci. Technol. **2002**, *36*, 4467–4475.

(9) Choi, S.; Drese, J. H.; Jones, C. W. Adsorbent Materials for Carbon Dioxide Capture from Large Anthropogenic Point Sources. *ChemSusChem* **2009**, *2* (9), 796–854.

(10) Wang, Q.; Luo, J.; Zhong, Z.; Borgna, A. CO_2 Capture by Solid Adsorbents and Their Applications : Current Status and New Trends. *Energy Environ. Sci.* **2011**, *4* (42), 42–55.

(11) Alessandro, D. M. D.; Smit, B.; Long, J. R. Carbon Dioxide Capture : Prospects for New Materials. *Angew. Chemie - Int. Ed.* **2010**, *49*, 6058–6082.

(12) Wang, W.; Wang, S.; Ma, X.; Gong, J. Recent Advances in Catalytic Hydrogenation of Carbon Dioxide. *Chem. Soc. Rev.* **2011**, *40* (7), 3703–3727.

(13) Song, C. Global Challenges and Strategies for Control, Conversion and Utilization of CO2 for Sustainable Development Involving Energy , Catalysis , Adsorption and Chemical Processing. *Catal. Today* **2006**, *115*, 2–32.

(14) Appel, A. M.; Bercaw, J. E.; Bocarsly, A. B.; Dobbek, H.; Dubois, D. L.; Dupuis, M.; Ferry, J. G.; Fujita, E.; Hille, R.; Kenis, P. J. A.; et al. Frontiers, Opportunities, and Challenges in Biochemical and Chemical Catalysis of CO_2 Fixation. *Chem. Rev.* **2013**, *113*, 6621–6658.

(15) Kondratenko, E. V.; Mul, G.; Baltrusaitis, J.; Larrazabal, G. O.; Perez-Reamirez, J. Status and Perspectives of CO_2 Conversion into Fuels and Chemicals by Catalytic, Photocatalytic and Electrocatalytic Processes. *Energy Environ. Sci.* **2013**, *6*, 3112–

3135.

(16) Zheng, Q.; Farrauto, R.; Chau Nguyen, A. Adsorption and Methanation of Flue Gas CO_2 with Dual Functional Catalytic Materials: A Parametric Study. *Ind. Eng. Chem. Res.* **2016**, *55* (24), 6768–6776.

(17) Duyar, M. S.; Wang, S.; Arellano-Treviño, M. A.; Farrauto, R. J. CO_2 Utilization with a Novel Dual Function Material (DFM) for Capture and Catalytic Conversion to Synthetic Natural Gas: An Update. *J. CO_2 Util.* **2016**, *15*, 65–71.

(18) Duyar, M. S.; Treviño, M. A. A.; Farrauto, R. J. Dual Function Materials for CO_2 Capture and Conversion Using Renewable H2. *Appl. Catal. B Environ.* **2015**, *168–169*, 370–376.

(19) Proaño, L.; Tello, E.; Arellano-Trevino, M. A.; Wang, S.; Farrauto, R. J.; Cobo, M. In-Situ DRIFTS Study of Two-Step CO_2 Capture and Catalytic Methanation over Ru, "Na_2O"/Al_2O_3 Dual Functional Material. *Appl. Surf. Sci.* **2019**, *479*, 25–30.

(20) Bermejo-López, A.; Pereda-Ayo, B.; González-Marcos, J. A.; González-Velasco, J. R. Mechanism of the CO_2 Storage and in Situ Hydrogenation to CH_4. Temperature and Adsorbent Loading Effects over Ru-CaO/Al_2O_3 and Ru-Na_2CO_3/Al_2O_3 Catalysts. *Appl. Catal. B Environ.* **2019**, *256*, 117845.

(21) Omodolor, I. S.; Otor, H. O.; Andonegui, J. A.; Allen, B. J.; Alba-Rubio, A. C. Dual-Function Materials for CO_2 Capture and Conversion : A Review. *Ind. Eng. Chem. Res.* **2020**, *59*, 17612–17631.

(22) Hu, Y.; Guo, Y.; Sun, J.; Li, H.; Liu, W. Progress in MgO Sorbents for Cyclic CO_2 Capture : Review. *J. Mater. Chem. A* **2019**, *7*, 20103–20120.

(23) Sun, H.; Zhang, Y.; Guan, S.; Huang, J.; Wu, C. Direct and Highly Selective Conversion of Captured CO_2 into Methane through Integrated Carbon Capture and Utilization over Dual Functional Materials. *J. CO_2 Util.* **2020**, *38*, 262–272.

(24) Arellano-Treviño, M. A.; He, Z.; Libby, M. C.; Farrauto, R. J. Catalysts and Adsorbents for CO_2 Capture and Conversion with Dual Function Materials : Limitations of Ni-Containing DFMs for Flue Gas Applications. *J. CO_2 Util.* **2019**, *31*, 143–151.

(25) Proaño, L.; Arellano-treviño, M. A.; Farrauto, R. J.; Figueredo, M.; Jeong-Potter, C. W.; Cobo, M. Mechanistic Assessment of Dual Function Materials, Composed of Ru-Ni , Na_2O/Al_2O_3 and Pt-Ni , Na_2O/Al_2O_3 , for CO_2 Capture and Methanation by in-Situ DRIFTS. *Appl. Surf. Sci.* **2020**, *533*, 147469.

(26) Bermejo-López, A.; Pereda-Ayo, B.; González-Marcos, J. A.; González-Velasco, J. R. Ni Loading Effects on Dual Function Materials for Capture and In-Situ Conversion of CO2 to CH4 Using CaO or Na2CO3. *J. CO2 Util.* **2019**, *34*, 576–587.

(27) Duyar, M. S.; Ramachandran, A.; Wang, C.; Farrauto, R. J. Kinetics of CO_2 Methanation over Ru/γ-Al_2O_3 and Implications for Renewable Energy Storage Applications. *J. CO_2 Util.* **2015**, *12*, 27–33.

(28) Wang, S.; Schrunk, E. T.; Mahajan, H.; Farrauto, R. J. The Role of Ruthenium in

CO_2 Capture and Catalytic Conversion to Fuel by Dual Function Materials (DFM). *Catalysts* **2017**, *7*, 88.

(29) Cimino, S.; Boccia, F.; Lisi, L. Effect of Alkali Promoters (Li, Na, K) on the Performance of Ru/Al_2O_3 Catalysts for CO_2 Capture and Hydrogenation to Methane. *J. CO_2 Util.* **2020**, *37*, 195–203.

(30) Arellano-Treviño, M. A.; Kanani, N.; Jeong-Potter, C. W.; Farrauto, R. J. Bimetallic Catalysts for CO_2 Capture and Hydrogenation at Simulated Flue Gas Conditions. *Chem. Eng. J.* **2019**, *375*, 121953.

(31) Wang, S.; Farrauto, R. J.; Karp, S.; Jeon, J. H.; Schrunk, E. T. Parametric , Cyclic Aging and Characterization Studies for CO2 Capture from Flue Gas and Catalytic Conversion to Synthetic Natural Gas Using a Dual Functional Material (DFM). *J. CO_2 Util.* **2018**, *27*, 390–397.

(32) Zhang, K.; Li, X. S.; Li, W.; Rohatgi, A.; Duan, Y.; Singh, P.; Li, L.; King, D. L. Phase Transfer-Catalyzed Fast CO2 Absorption by MgO-Based Absorbents with High Cycling Capacity. *Adv. Mater. Interfaces* **2014**, *1*, 1400030.

(33) Gao, W.; Zhou, T.; Gao, Y.; Wang, Q.; Lin, W. Study on MNO_3/NO_2 (M = Li, Na, and K)/MgO Composites for Intermediate-Temperature CO_2 Capture. *Energy & Fuels* **2018**, *33* (2), 1704–1712.

(34) Wang, K.; Zhao, Y.; Clough, P. T.; Zhao, P.; Anthony, E. J. Structural and Kinetic Analysis of CO_2 Sorption on $NaNO_2$-Promoted MgO at Moderate Temperatures. *Chem. Eng. J.* **2019**, *372*, 886–895.

(35) Kwak, J.; Kim, K.; Oh, K.; Kwon, Y. Performance Enhancement of All-Solid CO_2 Absorbent Based on Na_2CO_3 - Promoted MgO by Using ZrO_2 Dispersant. *Int. J. Greenh. Gas Control* **2019**, *81* (September 2018), 38–43.

(36) Vu, A. T.; Park, Y.; Jeon, P. R.; Lee, C. H. Mesoporous MgO Sorbent Promoted with KNO_3 for CO_2 Capture at Intermediate Temperatures. *Chem. Eng. J.* **2014**, *258*, 254–264.

(37) Harada, T.; Brown, P.; Hatton, T. A. Nonvolatile Colloidal Dispersion of MgO Nanoparticles in Molten Salts for Continuous CO_2 Capture at Intermediate Temperatures. *ACS Sustain. Chem. Eng.* **2019**, *7*, 7979–7986.

(38) Cui, H.; Zhang, Q.; Hu, Y.; Peng, C.; Fang, X.; Cheng, Z.; Galvita, V. V; Zhou, Z. Ultrafast and Stable CO_2 Capture Using Alkali Metal Salt-Promoted MgO-$CaCO_3$ Sorbents. *ACS Appl. Mater. Interfaces* **2018**, *10*, 20611–20620.

(39) Kwak, J.; Oh, K.; Kim, K.; Lee, J.; Kwon, Y. CO_2 Absorption and Desorption Characteristics of MgO-Based Absorbent Promoted by Triple Eutectic Alkali Carbonate. *Phys. Chem. Chem. Phys.* **2019**, No. 21, 20805–20813.

(40) Kim, K.; Han, J. W.; Lee, K. S.; Lee, W. B. Promoting Alkali and Alkaline-Earth Metals on MgO for Enhancing CO_2 Capture by First-Principles Calculations. *Phys. Chem. Chem. Phys.* **2014**, *16*, 24818–24823.

(41) Lee, S. C.; Cha, S. H.; Kwon, Y. M.; Park, M. G.; Hwang, B. W.; Park, Y. K.; Seo, H. M.; Kim, J. C. Effects of Alkali-Metal Carbonates and Nitrates on the CO_2 Sorption and Regeneration of MgO-Based Sorbents at Intermediate Temperatures.

Korean J. Chem. Eng. **2016**, *33* (12), 3448–3455.

(42) Kwak, J.; Kim, K.; Yoon, J. W.; Oh, K.; Kwon, Y. Interfacial Interactions Govern the Mechanisms of CO_2 Absorption and Desorption on A_2CO_3-Promoted MgO (A=Na, K,Rb, and Cs) Absorbents. *J. Phys. Chem. C* **2018**, *122*, 20289–20300.

(43) Harada, T.; Simeon, F.; Hamad, E. Z.; Hatton, T. A. Alkali Metal Nitrate-Promoted High-Capacity MgO Adsorbents for Regenerable CO_2 Capture at Moderate Temperatures. *Chem. Mater.* **2015**, *27*, 1943–1949.

(44) Qiao, Y.; Wang, J.; Zhang, Y.; Gao, W.; Harada, T.; Huang, L.; Hatton, T. A.; Wang, Q. Alkali Nitrates Molten Salt Modified Commercial MgO for Intermediate-Temperature CO_2 Capture : Optimization of the Li/Na/K Ratio. *Ind. Eng. Chem. Res.* **2017**, *56*, 1509–1517.

(45) Prashar, A. K.; Seo, H.; Choi, W. C.; Kang, N. Y.; Park, S.; Kim, K.; Min, D. Y.; Kim, H. M.; Park, Y. K. Factors Affecting the Rate of CO_2 Absorption after Partial Desorption in $NaNO_3$ - Promoted MgO. *Energy and Fuels* **2016**, *30*, 3298–3305.

(46) Zhang, K.; Li, X. S.; Chen, H.; Singh, P.; King, D. L. Molten Salt Promoting Effect in Double Salt CO_2 Absorbents. *J. Phys. Chem. C* **2016**, *120* (2), 1089–1096.

(47) Zhao, X.; Ji, G.; Liu, W.; He, X.; Anthony, E. J.; Zhao, M. Mesoporous MgO Promoted with $NaNO_3/NaNO_2$ for Rapid and High-Capacity CO_2 Capture at Moderate Temperatures. *Chem. Eng. J.* **2018**, *332* (September 2017), 216–226.

(48) Jo, S.; An, Y.; Kim, K.; Choi, S.; Kwak, J.; Oh, K.; Kwon, Y. Mechanisms of

Absorption and Desorption of CO_2 by Molten NaNO3-Promoted MgO. *Phys. Chem. Chem. Phys.* **2017**, *19*, 6224–6232.

(49) Pozzo, A. D.; Armutlulu, A.; Rekhtina, M.; Abdala, P. M.; Müller, C. R. CO_2 Uptake and Cyclic Stability of MgO-Based CO_2 Sorbents Promoted with Alkali Metal Nitrates and Their Eutectic Mixtures. *ACS Appl. Energy Mater.* **2019**, *2*, 1295–1307.

(50) Jin, S.; Ho, K.; Vu, A.; Lee, C. Salt-Composition-Controlled Precipitation of Triple-Salt-Promoted MgO with Enhanced CO_2 Sorption Rate and Working Capacity. *Energy & Fuels* **2017**, *31* (9), 9725–9735.

(51) Lee, H.; Triviño, T. L. M.; Hwang, S.; Kwon, S. H.; Lee, S. G.; Moon, J. H.; Yoo, J.; Seo, J. G. In Situ Observation of Carbon Dioxide Capture on Pseudo-Liquid Eutectic Mixture-Promoted Magnesium Oxide. *ACS Appl. Mater. Interfaces* **2018**, *10*, 2414–2433.

(52) Park, S. J.; Kim, Y.; Jones, C. W. NaNO3-Promoted Mesoporous MgO for High-Capacity CO_2 Capture from Simulated Flue Gas with Isothermal Regeneration. *ChemSusChem* **2020**, *13* (11), 2988–2995.

(53) Vu, A. T.; Ho, K.; Jin, S.; Lee, C. H. Double Sodium Salt-Promoted Mesoporous MgO Sorbent with High CO_2 Sorption Capacity at Intermediate Temperatures under Dry and Wet Conditions. *Chem. Eng. J.* **2016**, *291*, 161–173.

(54) Trivino, M. L. T.; Hiremath, V.; Seo, J. G. Stabilization of NaNO3-Promoted Magnesium Oxide for High- Temperature CO_2 Capture. *Environ. Sci. Technol.* **2018**, *52*, 11952–11959.

(55) Wang, W.; Gong, J. Methanation of Carbon Dioxide: An Overview. *Front. Chem. Eng.* **2011**, *5* (1), 2–10.

(56) Aziz, M. A. A.; Jalil, A. A.; Triwahyono, S.; Ahmad, A. CO_2 Methanation over Heterogeneous Catalysts: Recent Progress and Future Prospects. *Green Chem.* **2015**, *17* (5), 2647–2663.

(57) Younas, M.; Kong, L. L.; Bashir, M. J. K.; Nadeem, H.; Shehzad, A.; Sethupathi, S. Recent Advancements, Fundamental Challenges, and Opportunities in Catalytic Methanation of CO_2. *Energy & Fuels* **2016**, *30*, 8815–8831.

(58) Lanza, R.; Jaras, S. G.; Canu, P. Partial Oxidation of Methane over Supported Ruthenium Catalysts. *Appl. Catal. A Gen.* **2007**, *325*, 57–67.

(59) Betancourt, P.; Rives, A.; Hubaut, R.; Scott, C. E.; Goldwasser, J. A Study of the Ruthenium-Alumina System. *Appl. Catal. A Gen.* **1998**, *170*, 307–314.

(60) Chen, L.; Zhu, Y.; Zheng, H.; Zhang, C.; Zhang, B.; Li, Y. Aqueous-Phase Hydrodeoxygenation of Carboxylic Acids to Alcohols or Alkanes over Supported Ru Catalysts. *J. Mol. Catal. A Chem.* **2011**, *351*, 217–227.

(61) Artanto, Y.; Jansen, J.; Pearson, P.; Do, T.; Cottrell, A.; Meuleman, E.; Feron, P. Performance of MEA and Amine-Blends in the CSIRO PCC Pilot Plant at Loy Yang Power in Australia. *Fuel* **2012**, *101*, 264–275.

(62) Song, C.; Pan, W.; Srimat, S. T.; Zheng, J.; Li, Y.; Wang, Y.; Xu, B.-Q.; Zhu, Q.-M. *Tri-Reforming of Methane over Ni Catalysts for CO_2 Conversion to Syngas With*

Desired H_2/CO Ratios Using Flue Gas of Power Plants Without CO_2 Separation; Elsevier Masson SAS, 2004; Vol. 153.

(63) Han, K. K.; Zhou, Y.; Chun, Y.; Zhu, J. H. Efficient MgO-Based Mesoporous CO_2 Trapper and Its Performance at High Temperature. *J. Hazard. Mater.* **2012**, *203–204*, 341–347.

(64) Jin, S.; Ho, K.; Lee, C. H. Facile Synthesis of Hierarchically Porous MgO Sorbent Doped with $CaCO_3$ for Fast CO_2 Capture in Rapid Intermediate Temperature Swing Sorption. *Chem. Eng. J.* **2018**, *334*, 1605–1613.

(65) Kawai, K.; Fukuda, T.; Nakano, Y.; Takeshita, K. Thermal Decomposition Analysis of Simulated High-Level Liquid Waste in Cold-Cap. *J. Nucl. Sci. Technol.* **2016**, *44* (2).

(66) Heyl, D.; Rodemerck, U.; Bentrup, U. Mechanistic Study of Low-Temperature CO_2 Hydrogenation over Modified Rh/Al2O3 Catalysts. *ACS Catal.* **2016**, *6*, 6275–6284.

(67) Zheng, J.; Wang, C.; Chu, W.; Zhou, Y.; Kohler, K. CO_2 Methanation over Supported Ru/Al_2O_3 Catalysts : Mechanistic Studies by In Situ Infrared Spectroscopy. *ChemistrySelect* **2016**, *1*, 3197–3203.

(68) Eckle, S.; Anfang, H.; Behm, R. J. Reaction Intermediates and Side Products in the Methanation of CO and CO_2 over Supported Ru Catalysts in H_2 -Rich Reformate Gases. *J. Phys. Chem. C* **2011**, *115* (4), 1361–1367.

(69) Chin, S. Y.; Williams, C. T.; Amiridis, M. D. FTIR Studies of CO Adsorption on

Al_2O_3- and SiO_2-Supported Ru Catalysts. *J. Phys. Chem. B* **2006**, *110*, 871–882.

(70) Guo, Y.; Mei, S.; Yuan, K.; Wang, D.; Liu, H.; Yan, C.; Zhang, Y. Low-Temperature CO2 Methanation over CeO_2-Supported Ru Single Atoms, Nanoclusters, and Nanoparticles Competitively Tuned by Strong Metal−Support Interactions and H - Spillover Effect. *ACS Catal.* **2018**, *8*, 6203–6215.

(71) Wang, X.; Hong, Y.; Shi, H.; Szanyi, J. Kinetic Modeling and Transient DRIFTS–MS Studies of CO_2 Methanation over Ru/Al_2O_3 Catalysts. *J. Catal.* **2016**, *343*, 185–195.

(72) Fisher, J. C.; Siriwardane, R. V. $Mg(OH)_2$ for CO_2 Capture from High-Pressure, Moderate-Temperature Gas Streams. *Energy & Fuels* **2014**, *28*, 5936–5941.

(73) Evans, J. V.; Whateley, T. L. Infra-Red Study of Adsorption of Carbon Dioxide and Water on Magnesium Oxide. *Trans. Faraday Soc.* **1967**, *63*, 2769–2777.

(74) Chukanov, N. V.; Chervonnyi, A. D. *IR Spectra of Minerals and Related Compounds, and Reference Samples ' Data*; Springer, 2016.

(75) Solymosi, F.; Erdohelyi, A.; Kocsis, M. Methanation of CO_2, on Supported Ru Catalysts. *Faraday. Trans. 1* **1981**, *77*, 1003–1012.

(76) Karelovic, A.; Ruiz, P. Mechanistic Study of Low Temperature CO_2 Methanation over Rh/TiO_2 Catalysts. *J. Catal.* **2013**, *301*, 141–153.

(77) Miao, B.; Ma, S. S. K.; Wang, X.; Su, H.; Chan, S. H. Catalysis Mechanisms of CO_2 and CO Methanation. *Catal. Sci. Technol.* **2016**, *6* (12), 4048–4058.

(78) Raghu, A. K.; Kaisare, N. S. Microkinetic Modeling and Analysis of CO_2 Methanation on Ruthenium. *Ind. Eng. Chem. Res.* **2020**, *59*, 16161–16169.

(79) Weatherbee, G. D.; Bartholomew, C. H. Hydrogenation of CO_2 on Group VIII Metals. *J. Catal.* **1982**, *77*, 460–472.

(80) Marwood, M.; Doepper, R.; Renken, A. In-Situ Surface and Gas Phase Analysis for Kinetic Studies under Transient Conditions. The Catalytic Hydrogenation of CO_2. *Appl. Catal. A Gen.* **1997**, No. 151, 223–246.

(81) Avanesian, T.; Gusmão, G. S.; Christopher, P. Mechanism of CO_2 Reduction by H_2 on Ru(0001) and General Selectivity Descriptors for Late-Transition Metal Catalysts. *J. Catal.* **2016**, *343*, 86–96.

(82) Falbo, L.; Visconti, C. G.; Lietti, L.; Szanyi, J. The Effect of CO on CO_2 Methanation over Ru/Al_2O_3 Catalysts : A Combined Steady-State Reactivity and Transient DRIFT Spectroscopy Study. *Appl. Catal. B Environ.* **2019**, *256*, 117791.

(83) Navarro-jaén, S.; Szego, A.; Bobadilla, L. F.; Laguna, Ó. H.; Romero-Sarria, F.; Centeno, M. A.; Odriozolo, J. A. Operando Spectroscopic Evidence of the Induced Effect of Residual Species in the Reaction Intermediates during CO_2 Hydrogenation over Ruthenium Nanoparticles. *ChemCatChem* **2019**, *11*, 2063–2068.

(84) Chiorescu, I.; Arce-ramos, J.; Li, W.; Genest, A.; Rösch, N. Surface Science CO_2 Reduction by H_2 to CHO on Ru (0001): DFT Evaluation of Three Pathways. *Surf. Sci.* **2019**, *681*, 54–58.

(85) Yan, Y.; Wang, Q.; Jiang, C.; Yao, Y.; Lu, D.; Zheng, J.; Dai, Y.; Wang, H.; Yang, Y. Ru/Al_2O_3 Catalyzed CO_2 Hydrogenation : Oxygen-Exchange on Metal-Support Interfaces. *J. Catal.* **2018**, *367*, 194–205.

(86) Kwak, J. H.; Kovarik, L.; Szanyi, J. CO_2 Reduction on Supported Ru/Al_2O_3 Catalysts: Cluster Size Dependence of Product Selectivity. *ACS Catal.* **2013**, *3* (11), 2449–2455.

(87) Jo, S.; Woo, J.; Lee, J.; Kim, T.; Kang, H.; Lee, S.; Kim, J. A Novel Integrated CO_2 Capture and Direct Methanation Process Using Ni/CaO Catal-Sorbents. *Sustain. Energy Fuels* **2020**, *4*, 4679–4687.

(88) Lyngfelt, A.; Leckner, B.; Mattisson, T. A Fluidized-Bed Combustion Process with Inherent CO_2 Separation; Application of Chemical-Looping Combustion. *Chem. Eng. Sci.* **2001**, *56*, 3101–3113.

(89) Hossain, M. M.; de Lasa, H. I. Chemical-Looping Combustion (CLC) for Inherent CO_2 Separations—a Review. *Chem. Eng. Sci.* **2008**, *63*, 4433–4451.

CHAPTER 4. CO_2 METHANATION REACTION PATHWAYS OVER UNPROMOTED AND $NANO_3$-PROMOTED RU/AL_2O_3 CATALYSTS

4.1 Introduction

Global atmospheric carbon dioxide levels have increased throughout the last century, and as CO_2 has been reported to be one of main contributors to climate change, necessitating emissions reductions and CO_2 sequestration and utilization.[1–3] Among different products that can be easily produced from CO_2, methane production via hydrogenation of CO_2 is attractive, as there is already existing infrastructure for transport and storage of natural gas. The reaction between CO_2 and H_2 to produce CH_4, also known as the Sabatier reaction, is thermodynamically favorable reaction, with ΔG_{298K} = -113 kJ/mol. Catalytic methanation of CO_2 is typically performed between 200 °C ~ 450 °C at atmospheric pressure, which are milder conditions than production of other higher hydrocarbons or oxygenates.[4,5] Over the years, numerous studies has been conducted on CO_2 methanation using different supported metal catalysts, including Fe, Ni, Pd, Ru, and Rh.[6–9] In particular, supported ruthenium has been reported as the catalyst with the highest selectivity towards methane.

There have been numerous studies regarding CO_2 methanation mechanisms over ruthenium supported on different oxide supports (i.e. Al_2O_3, TiO_2, CeO_2), and it is widely accepted that CO_2 methanation occurs through a carbonyl intermediate (CO*). However, there is still not a consensus regarding how the carbonyl species are formed. Two general

schemes have been proposed in the literature. In one scheme, CO_2 dissociates to adsorbed CO* and O* species, and CO* reacts with surface hydrogen to form methane. In the other proposed scheme, CO* is formed through reverse water gas shift reaction (RWGS) via formate species (HCOO*) as an intermediate.

Much effort has been put into synthesizing supported ruthenium catalysts with improved activity and selectivity by including different additives or promoters, and many studies reported that alkali (Na, K, Li)[10–14] or alkaline earth metals (Mg, Ca, Ba)[15–19] provide improved performance. For example, Li et al. reported that alkali nitrate promoted Ru/Al_2O_3 showed up to three times higher methane production rates compared to unpromoted Ru/Al_2O_3. The improvement in methanation activity was attributed to modification of the Ru metal local density by electron donation of alkali promoters. Panagogiotopoulou et al. also reported that alkali metal (e.g. K, Li, or Na) loaded Ru/TiO_2 showed higher conversion of CO_2 than catalysts without additives, while still showing higher selectivity toward methane, between temperatures of 200 °C and 450 °C. However, the reaction pathway toward CH_4 formation over such alkali promoted ruthenium catalysts, whether similar or different to unpromoted ruthenium catalysts, remains unclear.

Furthermore, there is a growing interest in utilizing ruthenium catalysts and alkali metal promoted sorbents to synthesize dual function materials (DFM) or catalytic sorbents for integrated capture and methanation of CO_2.[20–27] Alkali metal or alkali salts can enhance the sorption of CO_2 under reaction conditions, changing the surface coverages of the catalysts. To this end, we seek to develop a thorough understanding of CO_2 methanation mechanism(s) over alkali promoted ruthenium catalysts, with this understanding being crucial for designing effective DFMs/catalytic sorbents.

The present work aims to probe CO_2 methanation reaction pathway over Ru/Al_2O_3 and $NaNO_3/Ru/Al_2O_3$ catalysts, with the former catalyst a well-studied model system and the latter a candidate DFM. Kinetic measurements, identifying apparent H_2 and CO_2 reaction orders, along with apparent activation energies, have been performed over the different catalysts. The catalysts are further characterized through chemisorption experiments and transmission electron microscopy (TEM), while reaction pathways studied through in situ DRIFT measurements during the CO_2 methanation reaction, as well as steady state isotopic transient kinetic experiments utilizing $^{12}CO_2$ to $^{13}CO_2$ feeds.

4.2 Experimental Section

4.2.1 Synthesis of Ru/Al_2O_3 and $NaNO_3/Ru/Al_2O_3$ catalysts

To synthesize 1% and 5% Ru/Al_2O_3 catalysts, a predetermined amount of ruthenium (III) nitrosyl nitrate ($Ru(NO)_3(NO_3)_3$, Alfa Aesar) was dissolved in distilled water to obtain stock solutions of different concentrations. Using incipient wetness impregnation, the prepared solution was added to γ-Al_2O_3 (Sasol). After impregnation, the samples were first dried at 100 °C for 4 h then calcined at 450 °C for 2 h in 21% O_2/He (flow rate =100 mL/min). The temperature ramp was 5 °C/min. Sodium nitrate addition to synthesize 5% $NaNO_3$/1% Ru/Al_2O_3 and 5% $NaNO_3$/5% Ru/Al_2O_3 catalysts was performed by incipient wetness impregnation of $NaNO_3$ (sigma Aldrich), using distilled water as solvent, to the calcined 1% Ru/Al_2O_3 and 5% Ru/Al_2O_3 catalysts. Then the samples were calcined at 350 °C in static air for 30 min. A control catalysts was also synthesized, in which, incipient wetness impregnation of distilled water, in absence of $NaNO_3$, was performed to the calcined 1% Ru/Al_2O_3 and 5% Ru/Al_2O_3. Then the samples were calcined at 350 °C in

static air for 30 min. These samples were used to compare metal dispersion to $NaNO_3$ loaded catalysts and observe whether the change in metal dispersion was due to presence of $NaNO_3$ or the synthesis method. These samples will be labeled as x% $Ru/Al_2O_3\_H_2O$.

4.2.2 Characterization

4.2.2.1 Transmission electron microscopy

Scanning transmission electron microscopy (STEM) images were collected on an HD 2700 Hitatchi aberration corrected STEM. Catalyst samples dispersed in acetone were dropped on holey carbon coated Cu grids.

4.2.2.2 CO Chemisorption

Pulse CO chemisorption were performed using a Micromeritics AutoChem II 2920. Approximately 50 mg of samples were loaded into a U-shape quartz tube on a bed of quartz wool. The samples were then heated 350 °C and held for 1 h under 10% H_2/He flow. Heating ramp of 5 °C/min was used. The gas is then switched to He flow for 30 min to remove any adsorbed species. The temperature was then lowered to 30 °C, which was followed by CO pulse testing. Doses of 10% CO/He were flowed through the sample bed and analyzed by thermal conductivity detector. After saturation with CO was reached, He passed through the sample bed for 60 min. Stoichiometry of Ru/CO = 1.667 was used to calculate metal dispersion.[28,29]

4.2.3 Reaction Measurements

The catalytic reactions were performed in a stainless steel tube reactor with inner diameter of ¼" at a total pressure of 1 atm. The stainless steel tube was placed inside an electric furnace, and a K-type thermocouple was used for temperature control. All catalysts were first pressed at 1000 psi to form pellets, and then crushed and sieved between 125 and 425 microns in size, and for each experiment ~25 mg of sieved catalysts were used. A gas hourly space velocity of 48000 mL g^{-1} h^{-1} was used. In a typical experiment, the samples were reduced at 350 °C for 1 h in 10% H_2/N_2 at 20 mL/min. After the reduction step, temperature was cooled to 260 °C. Then the feed containing 10~40% of CO_2 and 20~50% H_2, and balance N_2 was used to for reactions, including reaction order measurements. Total flow was always kept constant at 20 mL/min. The apparent activation energy was also determined by measuring the methane production rate at varying reaction conditions between 220 °C and 300 °C. In all cases, CO_2 conversion was kept under 15%, and calculations were performed to ensure heat and mass transfer effects were negligible, as shown in the supporting information.

4.2.4 In situ DRIFTS experiments

In situ diffuse reflectance infrared Fourier transform spectroscopic (DRIFTS) experiments were performed using a Harrick Praying Mantis high-temperature reaction chamber with ZnSe window to observe surface species on the catalysts during the CO_2 methanation reaction. The spectrometer used for the experiments was a Thermo Nicolet iS10 IR spectrometer with a mercury cadmium telluride (MCT) detector. Two different types of experiments were performed. In one set of experiments, samples were pretreated under 10% H_2/N_2 at 40 mL/min at a temperature of 350 °C for 1 h. The temperature was then lowered to 50 °C, and a background scan was taken under He flow. Then a flow of

5% CO_2/20% H_2/N_2 at 40 mL/min flowrate was passed through the cell, and a scan was taken at every 50 °C interval between 50 °C and 300 °C. In another set of experiments, samples were pretreated at similar conditions above, but the temperature was cooled to 260 °C, and a background scan was taken under He flow. Then a flow of 5% CO_2/20% H_2/N_2 at 40 mL/min was passed through the cell for 60 min. At the end of 60 min, the CO_2 feed was stopped and the gas was switched to 20% H_2/N_2 flow, while keeping the flowrate constant at 40 mL/min for another 60 min.

4.2.5 Steady State Isotopic Transient Kinetic Analysis

For the surface species observed during the CO_2 methanation reaction, to distinguish reaction intermediates from spectator species on the different catalysts, steady state isotopic transient kinetic analysis (SSITKA) experiments were performed. In a typical experiment, samples were pretreated under 10% H_2/N_2 at 40 mL/min at temperature of 300 °C for 1 h. The temperature was then lowered to 260 °C, and a background scan was taken at He flow. Then a flow of 5% $^{12}CO_2$/20% H_2/N_2 at 40 mL/min flowrate was flowed into the cell. Once an equilibrium was reached, the flow was switched to 5% $^{13}CO_2$/20% H_2/N_2 at 40 mL/min. The change in intensity of $^{12}CO_2/^{13}CO_2$ related surface species observed through DRIFT spectra and the concentration of $^{16}CH_4/^{17}CH_4$ in the cell outlet measured by a mass spectrometer were analyzed to identify kinetically relevant reaction intermediates. To check whether the experimentally observed shift that occurred upon switching from $^{12}CO_2$ to $^{13}CO_2$ flow fit the theoretical shift for each surface species, equation 4.1 and equation 4.2 were used, where wavelength is represented by ν, and reduced mass is represented by μ, while the mass of each atom is represented by m_A or m_B.

$$\frac{\nu_{C^{13}}}{\nu_{C^{12}}} = \sqrt{\frac{\mu_{C^{12}}}{\mu_{C^{13}}}} \qquad \text{Eq. 4.1}$$

$$\mu = \frac{m_A m_B}{m_A + m_B} \qquad \text{Eq. 4.2}$$

4.3 Experimental Section

4.3.1 Characterization

Particle size distribution analysis and on obtained TEM images and CO chemisorption experiments were performed to obtain metal dispersion of synthesized catalysts, as shown in Table 4.1. It should be noted that the metal dispersion obtained from CO chemisorption were higher than those obtained from those obtained from analysis of TEM images. This is likely because there was an overestimation of surface ruthenium site as stoichiometry of Ru/CO = 1.667 was used. Stoichiometry of Ru/CO between 1.5 and 2 have been commonly used to measure ruthenium dispersion, as it previously been reported that bridging carbonyl are more dominant than linear or dicarbonyl.[28–30] However, CO chemisorption has been reported to be dependent on particle size of Ru, with dicarbonyl or tricarbonyl becoming more dominant for smaller particle size. The synthesized catalysts in our work had quite high distribution in particle size, as shown in Figure C.1, potentiontially making it difficult to obtain accurate dispersion from CO chemisorption. Therefore in calculation of turnover frequency, dispersion obtained from analysis of TEM images were used. It should be noted that if stoichiometry of Ru/CO=1 is used, the metal dispersion from CO chemisorption corresponds well to the dispersion data obtained from TEM analysis, as shown in Table C.1.

Observations of metal dispersion obtained from two different analysis showed that there were not much difference in metal dispersion between catalysts of 1% metal loading and 5% metal loading. $NaNO_3$ loaded catalysts showed much decrease in metal dispersion, indicating that addition of $NaNO_3$ and calcining at 350 °C caused decrease in dispersion of catalysts. To check if the observed decrease in metal was due to presence of $NaNO_3$ or the synthesis method, similar analyses were performed to x% $Ru/Al_2O_3\_H_2O$ catalysts, which were synthesized using similar method as $NaNO_3$/x% Ru/Al_2O_3 catalysts, in absence of $NaNO_3$. Both dispersion data from TEM analysis and CO chemisorption showed comparable metal dispersion between $NaNO_3$/x% Ru/Al_2O_3 and x% $Ru/Al_2O_3\_H_2O$ catalysts. This indicated that the decrease in metal dispersion was not necessarily due to presence of $NaNO_3$, but likely due to additional calcination at 350 °C.

Table 4.1. Metal dispersion of different catalysts measured by CO chemisorption and TEM particle size distribution analysis. For average particle size measured by TEM, at least 240 particles were used for all catalysts. For metal dispersion by CO chemisorption, Ru/CO = 1.667 was assumed.

	Average particle size – TEM analysis (nm)	Metal dispersion - TEM analysis (%)	Metal dispersion – CO chemisorption (%)
1% Ru/Al_2O_3	12.1 ± 6.9	9.1	15.5
5% Ru/Al_2O_3	11.6 ± 5.7	9.3	14.4
$NaNO_3$/1% Ru/Al_2O_3	17.3 ± 10.9	6.4	8.9
$NaNO_3$/5% Ru/Al_2O_3	16.6 ± 9.4	6.6	7.7
1% $Ru/Al_2O_3\_H_2O$	24.1 ± 13.1	4.6	7.9
5% $Ru/Al_2O_3\_H_2O$	17.4 ± 14.1	6.3	8.3

4.3.2 Kinetic Measurments

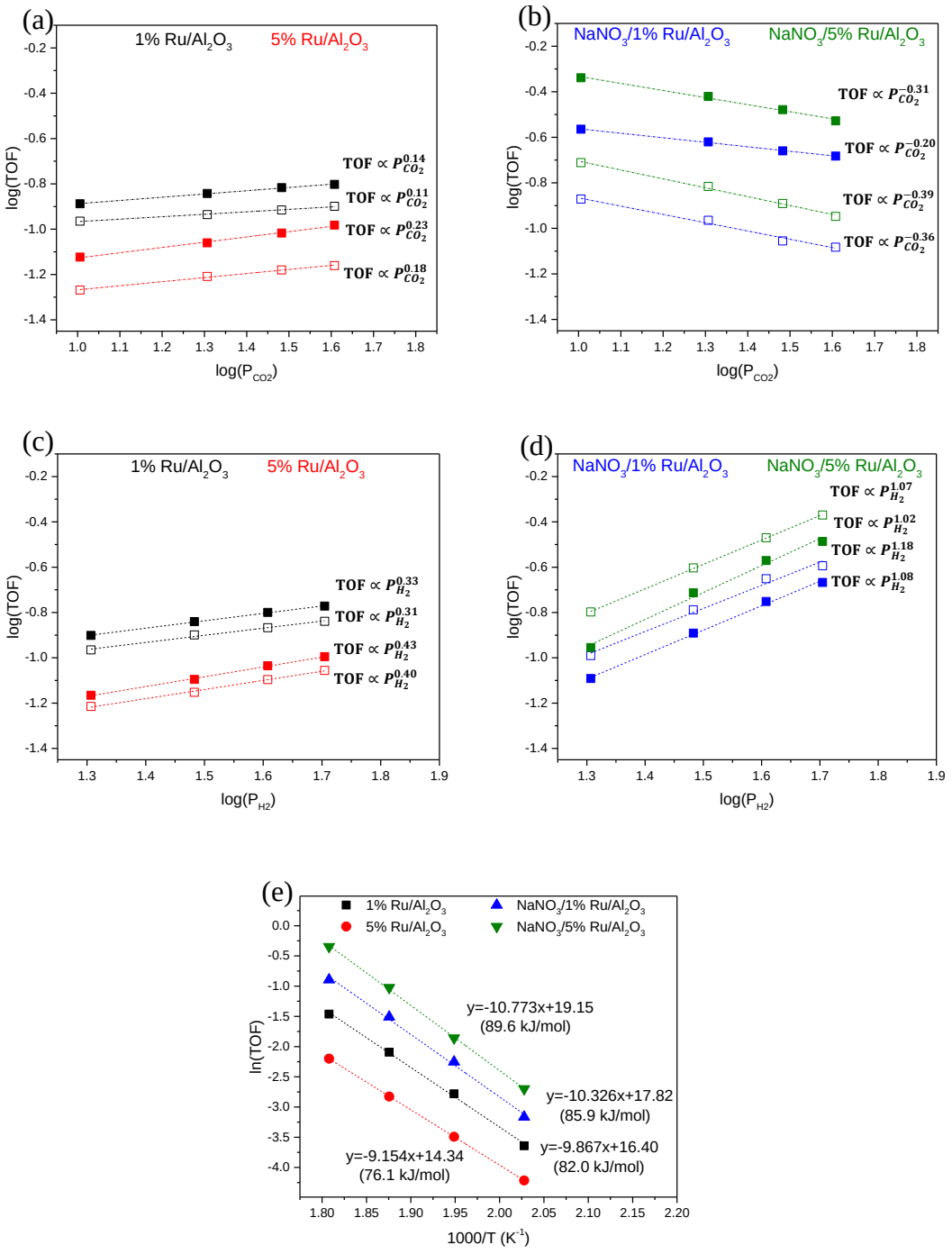

Figure 4.1. CO_2 reaction order for (a) Ru/Al_2O_3 catalysts and (b) $NaNO_3/Ru/Al_2O_3$ catalysts (filled points = 40% H_2 and hollow points = 20% H_2). H_2 reaction order for (c) Ru/Al_2O_3 catalysts and (d) $NaNO_3/Ru/Al_2O_3$ catalysts (filled points = 40% CO_2 and hollow points = 20% CO_2). (e) Arrhenius plot for CO_2 methanation in the temperature range between 220 °C and 280 °C for both Ru/Al_2O_3 and $NaNO_3/Ru/Al_2O_3$ catalysts.

Figure 4.1 (a) shows the dependence of the CH_4 formation rate on the CO_2 partial pressure over different catalysts. For 1% Ru/Al_2O_3, the CO_2 reaction order of 0.14 (40% H_2) and 0.11 (20% H_2) was observed, while 5% Ru/Al_2O_3 showed a CO_2 reaction order of 0.23 (40% H_2) and 0.18 (20% H_2). For $NaNO_3$/1% Ru/Al_2O_3, the CO_2 reaction order of -0.20 (40% H_2) and -0.36 (20% H_2), while $NaNO_3$/5% Ru/Al_2O_3 showed a CO_2 reaction order of -0.31 (40% H_2) and -0.39 (20% H_2). Negative CO_2 reaction orders for the $NaNO_3$ loaded samples imply that addition of $NaNO_3$ to Ru/Al_2O_3 caused an increase in surface coverage of either CO_2 or CO_2-derived species on the catalyst surface. It was previously reported that molten alkali metal ions can dissolve CO_2.[31–34] This property of $NaNO_3$ may have led to increased CO_2 coverage on the surface, thereby decreasing CO_2 reaction orders to negative values. For all four samples, CO_2 reaction orders were higher at higher H_2 partial pressure. This can be attributed to competitive adsorption between H_2 and CO_2. An increase in H_2 partial pressure leads to a higher surface coverage of H* species, which causes a decrease in the surface coverage of CO_2-related reaction intermediates, leading to increased CO_2 reaction orders.

Figure 4.1 (b) shows the dependence of CH_4 formation rate on H_2 partial pressure over different catalysts. For, 1% Ru/Al_2O_3, H_2 reaction orders of 0.33 (40% CO_2) and 0.31 (20% CO_2) were observed, while 5% Ru/Al_2O_3 showed H_2 reaction orders of 0.43 (40% CO_2) and 0.40 (20% CO_2). For sodium nitrate promoted samples, $NaNO_3$/1% Ru/Al_2O_3 showed H_2 reaction orders of 1.07 (40% CO_2) and 1.02 (20% CO_2), while $NaNO_3$/5% Ru/Al_2O_3 showed H_2 reaction orders of 1.18 (40% CO_2) and 1.08 (20% CO_2). Regardless of the loading of ruthenium, addition of $NaNO_3$ caused a significant increase in the H_2 reaction order, leading to decreased H surface coverage. It should be noted that the

observed H_2 reaction orders for $NaNO_3$ loaded catalysts are much higher than those values previously reported for supported ruthenium catalysts. Prairie et al. reported a H_2 reaction order of 0.57 over Ru/TiO_2 at 110 °C, while Szanyi et al reported H_2 reaction orders between 0.3 and 0.5 over different Ru/Al_2O_3 catalysts at reaction temperatures between 240 °C and 300 °C.[30,35] Farrauto et al. reported a slightly higher order of 0.88 over a Ru/Al_2O_3 catalyst at a temperature of 230 °C.[22] Previous studies that performed similar H_2 reaction order measurements over other noble metals, such as Pd or Rh, also reported orders between 0.5 and 0.8.[36,37] While dissociation or C-O bond of carbonyl species with assistance of surface H* species is considered as a consensus rate determining step in the CO_2 methanation reaction in supported ruthenium catalysts, the high H_2 reaction order observed for $NaNO_3$ loaded Ru/Al_2O_3 catalysts indicates that $NaNO_3$ loaded Ru/Al_2O_3 catalysts may have different or additional kinetically relevant step(s) to Ru/Al_2O_3 catalysts. Similar to what was observed in CO_2 reaction orders, H_2 reaction orders were also higher with higher partial pressures of CO_2.

Figure 4.1 (c) shows the apparent activation energy of CO_2 methanation reaction over different catalysts under $10\%CO_2/40\%H_2/N_2$ flow. Apparent activation energies of 82 kJ/mol and 76 kJ/mol were observed for 1% Ru/Al_2O_3 and 5% Ru/Al_2O_3. The obtained activation energy aligns with previously reported values for supported ruthenium catalysts, as Prairie et al. reported an apparent activation energy of 79 kJ/mol over Ru/Al_2O_3 catalysts, and Szanyi et al. reported activation energies between 65 kJ/mol ~ 80 kJ/mol over different metal loadings of Ru/Al_2O_3 catalysts.[30,35,38] Upon addition of $NaNO_3$, both promoted catalysts here showed an increase in the apparent activation energy, with values of 86 kJ/mol and 90 kJ/mol for $NaNO_3$/1% Ru/Al_2O_3 and $NaNO_3$/5% Ru/Al_2O_3. Based on

this increase, which is more notably observed in the 5% loading catalysts, we considered whether there may be a change in the rate determining step, or inclusion of additional kinetically relevant steps for $NaNO_3/Ru/Al_2O_3$ catalysts. The observed increase in the activation energy upon addition of $NaNO_3$ agrees well with previous reported alkali salt promoted ruthenium catalysts.[13]

4.3.3 In-situ DRIFT measurements

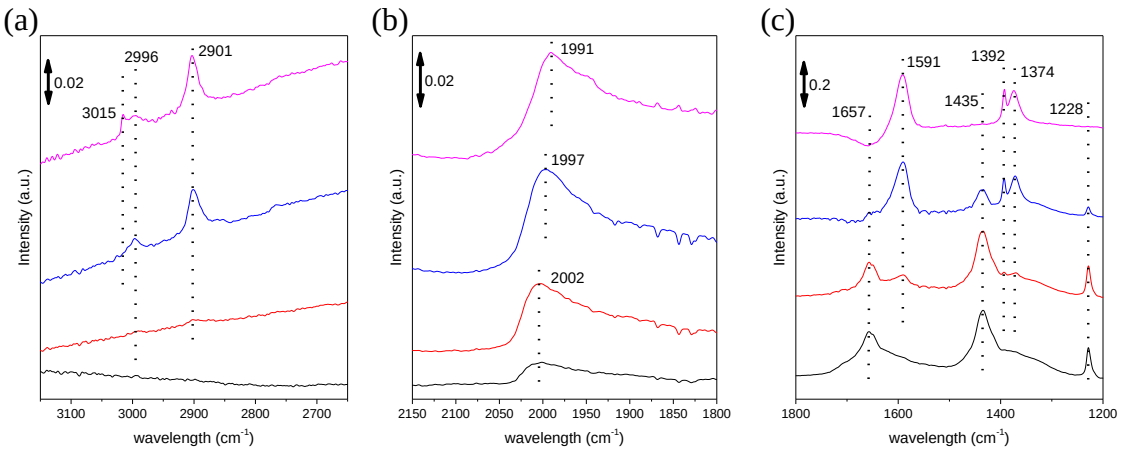

Figure 4.2. DRIFT spectra taken over 5% Ru/Al_2O_3 under $5\%CO_2/20\%H_2/N_2$ flow at 40mL/min in different temperatures of 50 °C (black), 100 °C (red), 200 °C (blue), 300 °C (pink) at wavelength range of (a) 850cm^{-1} to 2150cm^{-1}, (b) 1800 cm^{-1} to 2150 cm^{-1}, and (c) 2650 cm^{-1} to 3150cm^{-1}.

To observe the species formed during the CO_2 methanation reaction, in situ DRIFT experiments were performed. Figure 4.2 shows spectra taken at 30 °C, 100 °C, 200 °C, 300 °C in a flow of 10% CO_2/40% H_2/N_2 at 40 mL/min over the $5\%Ru/Al_2O_3$ catalyst. At 30 °C, prominent peaks at 1657 cm^{-1}, 1435 cm^{-1}, and 1228 cm^{-1} were observed, and these species are assigned to bicarbonate species.[30,36,39,40] This indicates that CO_2, in the presence of H_2, initially adsorbs on surface of $5\%Ru/Al_2O_3$ catalysts in form of surface bicarbonate species at low temperatures. A band at 2002 cm^{-1} was also observed, indicating formation of linear carbonyl species.[41–43] At 100 °C, formation of new peaks at 1591cm^{-1}, 1392 cm^{-}

^{1}, and 1374 cm^{-1}, along with small bands at 2996 cm^{-1} and 2901 cm^{-1} were observed, indicating formate species were formed as the temperature increased to 100 °C.[44–46] The intensities of these peaks continued to increase as the temperature increased to 300 °C, implying that surface formate species become more prevalent on the catalyst surface as the temperature increases. On the other hand, the intensity of peaks indicating bicarbonate species decreased as the temperature increased, becoming completely unobservable by a temperature of 300 °C. This suggests that the bicarbonate species were either consumed as a reaction intermediate or were desorbed from the catalyst surface as the temperature increased. Similar to formate species, the intensity of the linear carbonyl peak increased with an increase in temperature. The peak at 2002 cm^{-1} also slightly shifted to 1997 cm^{-1} at 200 °C and 1991 cm^{-1} at 300 °C. This shift has been previously attributed to a decrease of dipole-dipole coupling owing to a decrease in surface coverage.[47] At 200 °C, a new peak at 3015 cm^{-1} was observed, indicating formation of methane. Overall, DRIFT spectra taken at different temperatures over 5% Ru/Al_2O_3 showed that bicarbonate, formate, and carbonyl species were observed during the CO_2 methanation reaction, and methane is likely formed by a reaction path that includes one or more of these observed species as reaction intermediates.

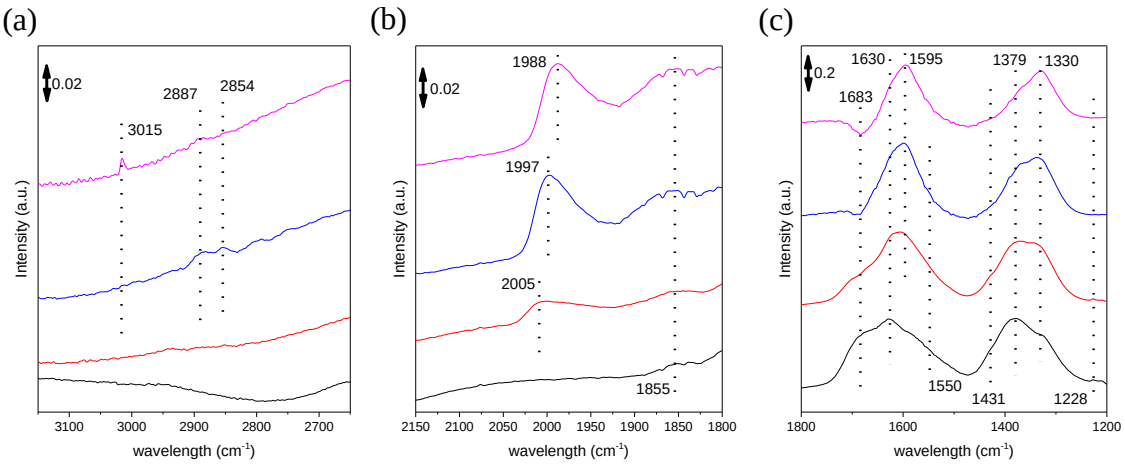

Figure 4.3. DRIFT spectra taken over $NaNO_3$/5% Ru/Al_2O_3 under 5%CO_2/20%H_2/N_2 flow at 40mL/min in different temperatures of 50 °C (black), 100 °C (red), 200 °C (blue), 300 °C (pink) at wavelength range of (a) 850 cm^{-1} to 215 0cm^{-1}, (b) 1800 cm^{-1} to 2150 cm^{-1} and (c) 2650 cm^{-1} to 3150cm^{-1}.

Figure 4.3. shows spectra taken over $NaNO_3$/5% Ru/Al_2O_3 at various temperatures in a flow of 5% CO_2/20% H_2/N_2 at 40 mL/min. At 50 °C, a wide band centered at 1629 cm^{-1} and 1379 cm^{-1}, along with shoulders at 1683 cm^{-1}, 1550 cm^{-1}, 1431 cm^{-1}, and 1330 cm^{-1}, was observed. Species observed at 1550 cm^{-1} and 1379 cm^{-1} were assigned to monodentate carbonate, and those observed at 1630 cm^{-1} and 1328 cm^{-1} were assigned to bidentate carbonate.[48–50] A small peak observed at 1228 cm^{-1} along with the shoulder observed at 1431 cm^{-1} were assigned to bicarbonate species. A shoulder at 1683 cm^{-1} was assigned to CO_2^- species, as it was previously reported that the presence of alkali metal atoms decreases the work function of the surface, leading to charge transfer to an empty CO_2 π-orbital.[14,51,52] As the temperature increased to 100 °C, a new peak was formed at 1595 cm^{-1}, indicating formation of formate species, while the intensities of peaks at 1379 cm^{-1}, 1550 cm^{-1} and 1683 cm^{-1} decreased, implying the surface became more deficient of monodentate carbonate and CO_2^- species. On the other hand, intensities of peaks at 1328

cm^{-1} and 1630 cm^{-1} became more intense as the temperature increased, which suggests that bidentate carbonate species became more prevalent with the temperature increase. A new peak at 2005 cm^{-1} was also formed, assigned to linear carbonyl species. Similar to what was observed over 5% Ru/Al_2O_3, a shift towards lower wavelengths was observed as the temperature increased. At 200 °C, additional two peaks were observed at 2887 cm^{-1} and 2854 cm^{-1}, which are assigned to formate species. A small peak at 3015 cm^{-1} was observed as well, meaning methane formation started to occur at a temperature of 200 °C. Overall, the main difference in the spectra between $NaNO_3$/5% Ru/Al_2O_3 and 5% Ru/Al_2O_3 catalysts was that presence of monodentate and bidentate carbonate species for $NaNO_3$ loaded samples at lower temperatures. While bicarbonate species were present in both catalysts, carbonate species showed much higher peak intensities over the $NaNO_3$/5% Ru/Al_2O_3 catalyst, indicating carbonate species were more dominant over that catalyst surface than the bicarbonate species. Carbonyl species and formate species were observed on both catalysts as the temperature increased.

Similar DRIFT spectra were taken over 1%Ru/Al_2O_3 (Figure C.2) and $NaNO_3$/1%Ru/Al_2O_3 (Figure C.3) under 5% CO_2/20%H_2/N_2 at 40 mL/min at various reaction temperature. Species observed on 1% Ru/Al_2O_3 were generally similar to those observed in 5% Ru/Al_2O_3, showing bicarbonate, formate, and carbonyl species. On the other hand, there were few differences observed in the spectra of $NaNO_3$/1% Ru/Al_2O_3 and $NaNO_3$/5% Ru/Al_2O_3. For $NaNO_3$/1% Ru/Al_2O_3, there was a sharp peak observed at 1305 cm^{-1}. This peak was assigned to inorganic oxylate species on the Al_2O_3 support.[42,53] While $NaNO_3$/5% Ru/Al_2O_3, did not show a prominent peak at 1305 cm^{-1}, it did show a wide shoulder ranging from 1320 cm^{-1} to 1260 cm^{-1}, indicating that similar oxylate species are

present for $NaNO_3$/5%Ru/Al_2O_3 as well. It is likely that the oxylate peak was less observable for $NaNO_3$/5% Ru/Al_2O_3 due to the more prominent bidentate carbonate peak. Another difference was that a wide band at 1855 cm^{-1} was observed over $NaNO_3$/5%Ru/Al_2O_3, while this band was not observed over $NaNO_3$/1%Ru/Al_2O_3. This band was assigned to bridged carbonyl species. In general, the intensity of carbonyl peaks was higher for the 5% Ru loading catalysts. Multiple previous works showed that bridged carbonyls typically are very low intensity bands.[36,37,42,43,45] Therefore, it was hypothesized that the bridged carbonyl species are most likely present in both $NaNO_3$/1%Ru/Al_2O_3 and $NaNO_3$/5%Ru/Al_2O_3 catalysts, but became more observable over the $NaNO_3$/5%Ru/Al_2O_3 catalyst, as the total exposed ruthenium surface area increased with higher metal loading, making various Ru-$(CO)_x$ species more detectable.

4.3.4 SSITKA Analysis

While multiple surface species were observed through in situ DRIFT experiments during the methanation reaction, reaction intermediates and spectator species cannot be distinguished by DRIFT spectra alone. To this end, an isotopic transient experiment was performed over the previously tested four catalysts. Initially, a mixture of 5% $^{12}CO_2$/20% H_2/N_2 was flowed at 40 mL/min. Once an equilibrium was observed in the IR spectra, the reactant was switched to $^{13}CO_2$/20%H_2/N_2 at same flow rate. The outlet of the IR cell was analyzed using a mass spectrometer.

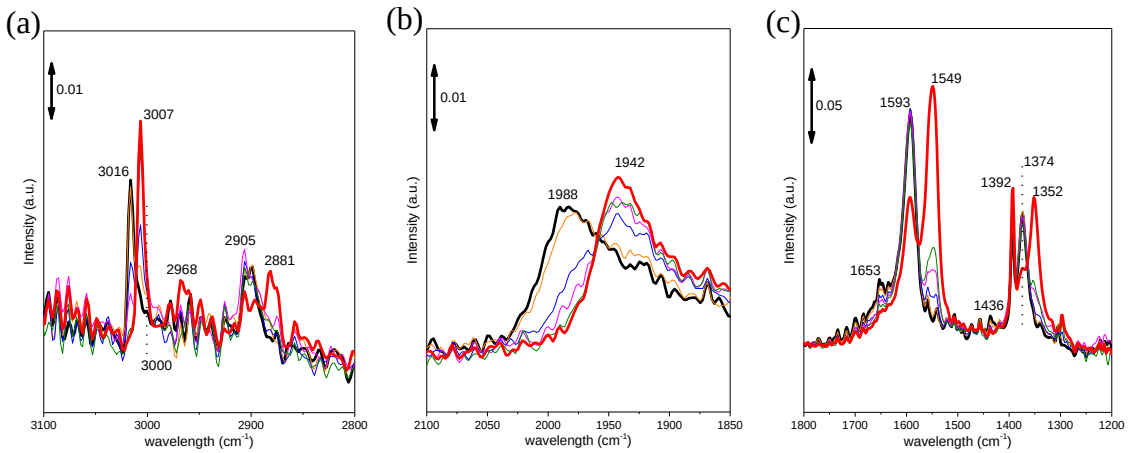

Figure 4.4. In situ DRIFT spectra taken over 5% Ru/Al_2O_3 catalysts at wavelength range of (a) 850 cm^{-1} to 2150 cm^{-1}, (b) 1800 cm^{-1} to 2150 cm^{-1}, and (c) 2650 cm^{-1} to 3150 cm^{-1} at temperature of 260 °C under flow of 5% $^{12}CO_2$/20% H_2/N_2 (black, thickened) and after switch to 5% $^{13}CO_2$/20% H_2/N_2 flow. (28 s (orange), 56 s (blue), 85 s (pink), 113 s (green), and 8 min (red, thickened)).

Figure 4.4 shows the IR spectra after changing the flow from $^{12}CO_2/H_2$/He to $^{13}CO_2/H_2$/He at a temperature of 260 °C over 5% Ru/Al_2O_3. Initial peaks observed under $^{12}CO_2/H_2$/He flow were similar to those observed in Figure 4.2. Linear carbonyl species at 1988 cm^{-1}, formate species at 2905 cm^{-1}, 1593cm^{-1}, 1392cm^{-1}, and 1374 cm^{-1} were observed. Very small peaks at 1653 cm^{-1} and 1436 cm^{-1} indicated that bicarbonate species are present as well. After switching the $^{12}CO_2$ feed to $^{13}CO_2$, the linear ^{12}CO peak at 1988 cm^{-1} started to decrease immediately, while a new ^{13}CO peak was formed at 1942 cm^{-1}. The ^{12}CO peak became completely unobservable within 2 min. The formate species behaved very differently from the carbonyl species in that the $H^{12}COO$ peak at 1593 cm^{-1} showed a very slow decrease upon switching to $^{13}CO_2$. The intensity of the $H^{12}COO$ only decreased by 40% within 8 minutes after the switch. Furthermore, the formation of the ^{13}-formate peak at 1549 cm^{-1} was much slower than that of the ^{13}CO, continuing to increase until the 8 minute mark after the switch. Changes in the normalized peak intensity observed

in DRIFT spectra of the carbonyl and formate species are plotted as shown in Figure 5 (a). As observed in the figure, the ^{12}CO and $H^{12}COO$ species decomposed at a very different rate, with ^{12}CO showing a decrease faster than the ^{12}-formate by an order of magnitude. Furthermore, the rate of decay observed for ^{12}CO peak was similar to the rate of decay observed for $^{12}CH_4$, as observed in Figure 5 (b). The formation rate of ^{13}CO was also much faster than $H^{13}COO$, with the ^{13}CO species reaching a stable intensity within 150 s after the switch. Similarly, the $^{13}CH_4$ mass spectroscopy intensity also reached an equilibrium by 150 s. Based on the observation that the decay of the ^{12}CO species occurred at very similar rate to that of $^{12}CH_4$, as well as formation of ^{13}CO species occurred at similar time scale to $^{13}CH_4$, it is suggested that the linear carbonyl species is a true reaction intermediate for the methanation reaction. Both the decay of $H^{12}COO$[1] and formation of $H^{13}COO$ occurred at very different rates to that of methane formation, indicating that formate species are most likely not a major reaction intermediate for the CO_2 methanation reaction. It was a challenge to conclude whether the bicarbonate species were reaction intermediates using the spectra obtained over 5% Ru/Al_2O_3, because the intensity of the peaks at 1653 cm^{-1} and 1436 cm^{-1} was very low, thereby making it difficult to perform the analysis done for CO and formate species.

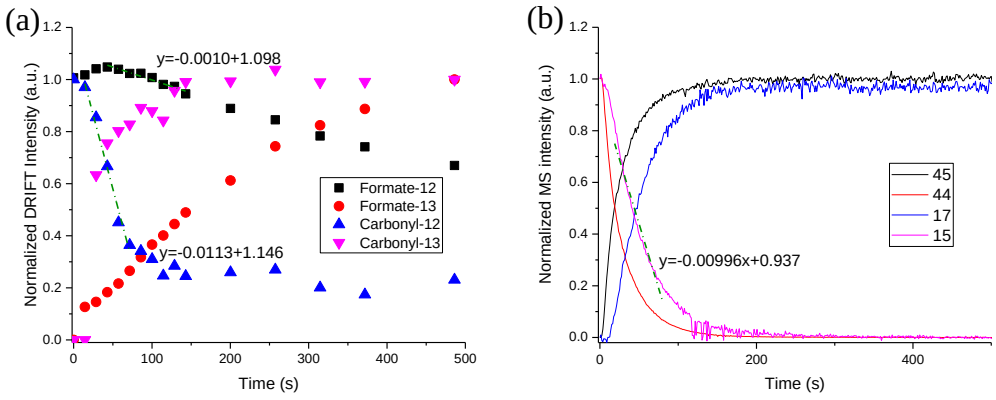

Figure 4.5. (a) Change in normalized DRIFT spectra intensity of observed surface species and (b) change in normalized mass spectroscopy intensity of $^{12}CO_2$, $^{13}CO_2$, $^{12}CH_4$, and $^{13}CH_4$, after switching from 5% $^{12}CO_2$/20% H_2/He flow to 5% $^{13}CO_2$/20% H_2/He flow over 5%Ru/Al_2O_3 catalysts at a temperature of 260 °C. Total flow rate was constant at 40 mL/min.

Similar transient isotopic experiments were performed over 1% Ru/Al_2O_3 as well, with Figure C.4 showing the IR spectra and Figure C.5 showing the normalized intensity of selected species observed in the IR spectra along with mass spectroscopy results. As observed in Figure C.5, linear carbonyl and formate species showed similar trends as for the 5% Ru/Al_2O_3 catalyst. Linear carbonyl species showed a rapid exchange between the ^{12}CO (1992 cm^{-1}) and ^{13}CO (1954 cm^{-1}) species after the switch. For the formate species, the decomposition of $H^{12}COO$ peaks was much slower than for 5%Ru/Al_2O_3. As observed in Figure C.4 (a), the peak in 2904 cm^{-1} showed an intensity change of less than 1 %, even after 8 min of flow with $^{13}CO_2$. For bicarbonate species (HCO_3), as observed with the peak at 1653 cm^{-1}, a rapid decomposition of $H^{12}CO_3$ species after the switch could be observed. An increase in the peak at 1595 cm^{-1} along with formation of a shoulder at 1605 cm^{-1} were also observed after the switch. The peak at 1653 cm^{-1} represents O-^{12}C-O asymmetric stretching, and using equation 4.1, a peak shift to 1606 cm^{-1} is calculated for the same species with ^{13}C, which matches very well with the shoulder formed.[45] Also, as previously mentioned, peaks indicating $H^{12}COO$ species showed very small changes in intensity, so it is unlikely the peak increase in 1595 cm^{-1} is representing an increase in $H^{12}COO$ coverage. Therefore, the increase in intensity of the 1595 cm^{-1} peak as well as formation of a shoulder at 1605 cm^{-1} are attributed to formation of $H^{13}CO_3$ after the switch. Under the assumption that the change in intensity of the 1595 cm^{-1} peak is essentially negligible, the change in the normalized intensity for $H^{12}CO_3$ and $H^{13}CO_3$ species are plotted as shown in Figure

C.5 (a). It should be noted that the IR intensity for $H^{12}COO$ was not plotted, as there was negligible change in intensity. It was observed that the decomposition rates of the ^{12}CO and $H^{12}CO_3$ bands were very similar. Also, these rates were very similar to the rate of decay for the $^{12}CH_4$ mass spectroscopy signal, as observed in Figure C.5(b). Based on these observations, it is hypothesized that the linear carbonyl species and bicarbonate species are likely reaction intermediates for the CO_2 methanation reaction, while formate species are likely a spectator species over the 1% Ru/Al_2O_3 catalysts. While a definitive statement cannot be made about intermediacy of the bicarbonate species over 5%Ru/Al_2O_3 catalysts, based on the fact that similar behavior for carbonyl and formate species was observed, along with similar reaction orders for CO_2 and H_2 along with a similar activation energy for the two catalysts, it is plausible that the bicarbonate species are reaction intermediates over the 5% Ru/Al_2O_3 catalyst as well.

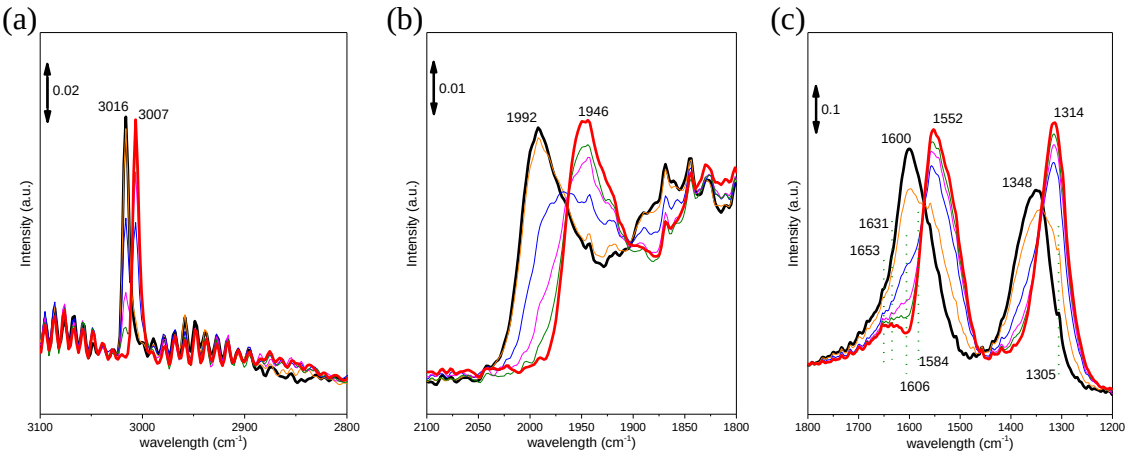

Figure 4.6. In situ DRIFT spectra taken over $NaNO_3$/5% Ru/Al_2O_3 catalysts at wavelength range of (a) 850cm^{-1} to 2150cm^{-1}, (b) 1800 cm^{-1} to 2150 cm^{-1}, and (c) 2650 cm^{-1} to 3150 cm^{-1} at temperature of 260 °C under flow of 5% $^{12}CO_2$/20% H_2/N_2 (black, thickened) and after switch to 5% $^{13}CO_2$/20% H_2/N_2 flow. (28 s (orange), 56 s (blue), 85 s (pink), 113 s (green), and 8 min (red, thickened)).

Figure 4.6 shows IR spectra after changing the flow from $^{12}CO_2/H_2/He$ to $^{13}CO_2/H_2/He$ at a temperature of 260 °C over the $NaNO_3$/5% Ru/Al_2O_3 catalyst. Under $^{12}CO_2/H_2/He$ flow, linear carbonyl species at 1992 cm^{-1}, formate species at 1600 cm^{-1}, bicarbonate species at 1653 cm^{-1}, bidentate carbonate species at 1630 cm^{-1} and 1348 cm^{-1}, and oxylate species at 1305 cm^{-1} were observed. Similar to the Ru/Al_2O_3 catalysts, linear carbonyl species showed a rapid exchange between ^{12}CO and ^{13}CO species, as observed in Figure 4.6 (b). The peak at 1992 cm^{-1} decomposed quickly and became unobservable approximately 2 min after switching to $^{13}CO_2$ flow, and a new peak for ^{13}CO was formed at 1946 cm^{-1}, which also reached a stable intensity over a similar interval. The formate species, however, showed a different trend from the Ru/Al_2O_3 catalysts. As observed in Figure 4.6 (c), the intensity of the peak at 1600 cm^{-1} rapidly decreased upon switching to $^{13}CO_2$. Also, a quick increase in the intensity of a new peak at 1552 cm^{-1} was observed. This observation implies that addition of $NaNO_3$ altered to some degree the reaction pathway(s) for CO_2 methanation, and formate species are likely also reaction intermediates for CO_2 methanation over $NaNO_3$/5% Ru/Al_2O_3. For bicarbonate species, while the intensity of the shoulder at 1653 cm^{-1} did decrease after the switch, the decrease in intensity was only by 37%, suggesting it is a relatively stable species that did not fully decompose, even 8 minutes after switching the feed to $^{13}CO_2$. Furthermore, if the bicarbonate species are reaction intermediates, a peak at 1606 cm^{-1}, with similar intensity as 1653 cm^{-1} in $^{12}CO_2$ flow should be observed after the switch. However, there was no distinct peak or band observed at 1606 under $^{13}CO_2$ flow, which indicates that bicarbonate species are most likely not a methanation reaction intermediate. The change in normalized intensity of the carbonyl, formate, and bicarbonate peaks are plotted in Figure 4.7 (a), and it could be

observed that the decomposition of ^{12}CO and $H^{12}COO$ species showed similar rates to the decay rate of the $^{12}CH_4$ signal obtained from mass spectroscopy, as shown in Figure 4.7 (b). The decomposition rate of ^{12}-bicarbonate species was clearly much slower than the decomposition of the other two species. While the differences in decomposition rates between the hypothesized reaction intermediate (carbonyl and formate) and spectator species (bicarbonate) were not as stark as in case of 5% Ru/Al_2O_3, where an order of magnitude difference was observed between the decomposition rate of carbonyl and formate species, this in part could be due to the fact that the peak in 1653 cm^{-1} had some overlap with both carbonate peak at 1630 cm^{-1} and the formate peak at 1600 cm^{-1}, making accurate quantification more challenging. The difference in decomposition rates combined with stable band observed at 1653 cm^{-1}, even long after switching to $^{13}CO_2$, shows that the bicarbonate species are most likely not reaction intermediates. The bidentate carbonate species observed at the 1631 cm^{-1} shoulder and 1348 cm^{-1} peak was more difficult to analyze than the other species, because carbonate bands are typically broad and this led to overlap between the $^{12}CO_3$ bands and $^{13}CO_3$ bands, thereby making it difficult to establish a stable baseline before and after the isotopic switch. While a quantitative analysis of the peak intensity was hard to perform, a more qualitative analysis of the peak shift was used to assess whether bidentate carbonate species might be reaction intermediates. The peak at 1630 cm^{-1} represents the asymmetric O-C-O stretching of bidentate carbonate, so using equation 4.1, a newly formed ^{13}-bidentate carbonate should have a similar intensity at 1584 cm^{-1}.[50,54] As observed in Figure 4.6 (c), a very similar IR intensity was observed between the shoulder at 1630 cm^{-1} under $^{12}CO_2$ flow and the new shoulder formed at 1584 cm^{-1} under $^{13}CO_2$. The peak at 1349 cm^{-1} represents the symmetric O-C-O stretching. Thus,

under $^{13}CO_2$ flow, a shift to 1311 cm^{-1} should be observed, according to equation 4.1. As observed in Figure 4.6. (c), a clear peak was observed 1314 cm^{-1}, which aligns well with the expected shift. One thing to note is that the intensity of the newly formed peak at 1314 cm^{-1} was much larger than the initial 1349 cm^{-1} peak. This is attributed to presence of the oxylate species observed at 1305 cm^{-1} as well. While a quick isotopic exchange for bidentate carbonate occurred, it is likely that the ^{12}-oxylate species were still present after the switch, making the newly formed bidentate $^{13}CO_3$ peak stack on the existing oxylate peak, leading to the higher intensity observed at 1314 cm^{-1}. As the newly formed bidentate $^{13}CO_3$ peaks corresponded well with the calculated shift, it is suggested that the bidentate carbonate species are also reaction intermediates for the CO_2 methanation reaction, along with the linear carbonyl and formate species. Similar transient isotopic experiments were also performed over $NaNO_3$/1% Ru/Al_2O_3, as shown in Figure C.6 and Figure C.7, and peak shapes along with peak shifts that occurred after switching to $^{13}CO_2$ were very similar to those observed for $NaNO_3$/5% Ru/Al_2O_3. Based on these observations, it was concluded that both catalysts most likely follow a similar reaction pathway, which includes bidentate carbonate, formate, and linear carbonyl species as reaction intermediates in the path to methane.

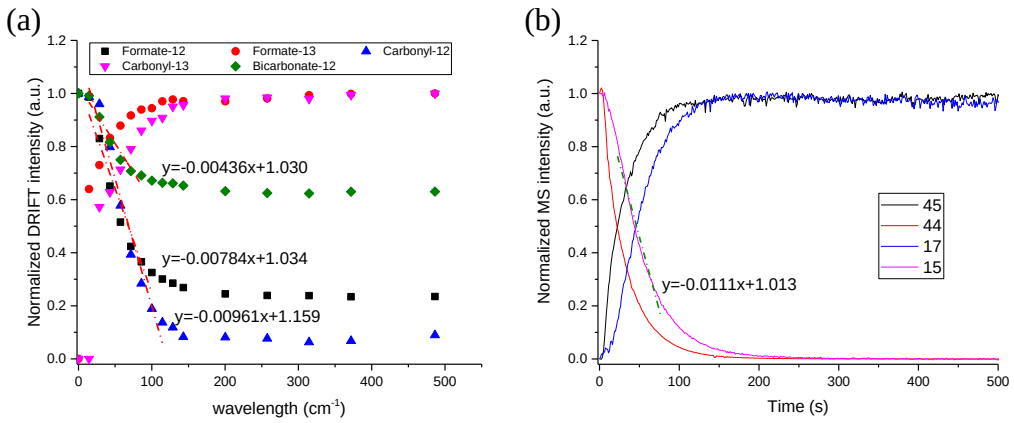

Figure 4.7. (a) Change in normalized DRIFT spectra intensity of observed surface species and (b) change in normalized mass spectroscopy intensity of $^{12}CO_2$, $^{13}CO_2$, $^{12}CH_4$, and $^{13}CH_4$, after switching from 10% $^{12}CO_2$/40% H_2/He flow to 10% $^{13}CO_2$/40% H_2/He flow over $NaNO_3$/5%Ru/Al_2O_3 catalysts at temperature of 260 °C. Total flow rate was constant at 40 mL/min.

4.3.5 Kinetic Modeling

Combining reaction orders calculated from kinetic measurements and spectral observations made from DRIFTS and SSITKA IR experiments, a sequence of reaction steps is proposed for methanation over Ru/Al_2O_3, as shown in Table 4.1. Since bicarbonate species, which was found to be a reaction intermediate from isotopic exchange experiments, are known to readily form on the surface of alumina support, the interface between the metal and support is suggested to provide the reactive sites for both catalysts. For the Ru/Al_2O_3 catalyst, bicarbonate and linear carbonyl species were hypothesized to be a reaction intermediates, while formate species were hypothesized to be a spectator species. So it is likely that CO_2 initially forms a bicarbonate species, which eventually decomposes to form a linear carbonyl species, which then reacts with surface H* species to form methane. To this end, the initials steps of the proposed sequence over this catalyst was the dissociation of H_2 into two H* atoms (step 1), and adsorption of CO_2 on hydroxyl groups on the metal-support interface to form bicarbonate species, CO_3H* (step 2). While

bicarbonate and linear carbonyl species were the only surface intermediates observed by IR, it is difficult to imagine formation of linear carbonyl from bicarbonate in a single elementary step. The two hypothesized pathways to form linear carbonyl species were: i) CO_2 adsorbed on an OH-S site on alumina surface transfers to the Ru metal site near the metal-support interface to form CO_2* (Table 4.2, step 3), which then reacts with H* to form CO* and OH* (Table 4.2, step 4). ii) Hydrogenation of CO_3H to form a carboxylic intermediate, COOH-S (Table C.2, step 3), which then dissociates to CO* and OH* (Table C.2, step 4). Because no other reaction intermediates were observed from our transient isotopic experiments, we hypothesize that the CO_2* pathway is more significant. However, the COOH* pathway could be plausible as well, assuming the COOH* species has low surface coverage. As both steps form CO* and share the same rate determining step, as well as other elementary steps afterwards, thereby forming the same rate law, it was not possible to definitively state whether one path is more likely than the other from the available data. While formyl species (HCO*) could be another intermediate that may be in the reaction path from bicarbonate species to form CO*, it was conceptually hard to justify dissociating the C-H bond of HCO* to form CO* to then react with H* again to form CH*, so the formyl species was excluded from potential reaction intermediate. The proposed elementary rate law assuming the COOH* path is shown in Table C.2. Numerous studies reported that the breaking of the C-O bond has the highest energy barrier over similar catalysts, and therefore the reaction of CO* with H* to break the carbonyl bond was taken as the rate determining step here. The formed C* species are then hydrogenated to form the final product, methane.[55–59]

Table 4.2. Proposed elementary step for CO_2 methanation over Ru/Al_2O_3 catalysts

Step	Reaction
1	$H_2(g) + 2* \leftrightarrow 2H*$
2	$CO_2(g) + OH\text{-}S \leftrightarrow CO_3H\text{-}S$
3	$CO_3H\text{-}S + * \leftrightarrow CO_2* + OH\text{-}S$
4	$CO_2* + H* \leftrightarrow CO* + OH*$
5 (RDS)	$CO* + H* \rightarrow C* + OH*$
6	$C* + H* \leftrightarrow CH* + *$
7	$CH* + H* \leftrightarrow CH_2* + *$
8	$CH_2+* + H* \leftrightarrow CH_3* + *$
9	$CH_3* + H* \leftrightarrow CH_4* + *$
10 (irreversible)	$OH* + H* \rightarrow H_2O* + *$
11	$CH_4* \leftrightarrow CH_4(g) + *$
12	$H_2O* \leftrightarrow H_2O(g) + *$

Assuming step 5 is the rate determining step, and all steps prior to step 5 are quasi-equilibrated, a rate law was derived as shown in equation 4.3. Step 10 is also assumed to be irreversible, as previous DFT studies reported that it is the a step with one of highest activation barriers in formation of water.[55,56] The derivation of equation 4.3 is shown in Table C.3.

$$r = \frac{\frac{\sqrt{\left(k_5 k_{10} K_4 K_3 K_2 K_1^{\frac{3}{2}}\right)}}{2} P_{CO_2}^{\frac{1}{2}} P_{H_2}^{\frac{3}{4}}}{\left(1+\sqrt{K_1 P_{H_2}}+K_3 K_2 P_{CO_2}+\sqrt{K_4 K_3 K_2 K_1^{\frac{1}{2}}} P_{CO_2}^{\frac{1}{2}} P_{H_2}^{\frac{1}{4}}\left(\sqrt{\frac{k_{10}}{2k_5}}+\sqrt{\frac{2k_5}{k_{10}}}\right)\right)^2} \qquad \text{Eq. 4.3}$$

Furthermore, experimental data obtained from Figure 4.1 (a) and Figure 4.1 (b) were fitted to the derived rate law (equation 4.3) for the Ru/Al_2O_3 catalyst, as shown in Figure 4.8. Experimental data for both 1% Ru/Al_2O_3 and 5% Ru/Al_2O_3 fit the derived rate law well, showing a slope of nearly 1 for both samples with an R^2 value of 0.940 for 1%

Ru/Al_2O_3 and 0.933 for 5% Ru/Al_2O_3. The average error between the calculated and experimental TOFs was 2.7 % for 1% Ru/Al_2O_3 and 3.6% for 5% Ru/Al_2O_3. The kinetic constants obtained from the kinetic modeling are presented in Table 4.3. Comparing the values obtained for k_5 and k_{10} in both catalysts, k_5 had values lower than k_{10} by at least an order of magnitude, implying that k_5 has higher energy barrier, further corroborating the assignment that step 5 is a RDS in the reaction. Calculated surface coverage of the reaction intermediates are shown in Table C.4 and Table C.5. It can be observed that for both Ru/Al_2O_3 catalysts, surface coverages of the CO_2* intermediate were very low, which may be why an intermediate species between the bicarbonate and linear carbonyl species could not be observed in the IR spectra. The fact that CO* shows such a high surface coverage aligns with the assumption that step 5 is the RDS, and species participating in the RDS usually show the highest coverage.

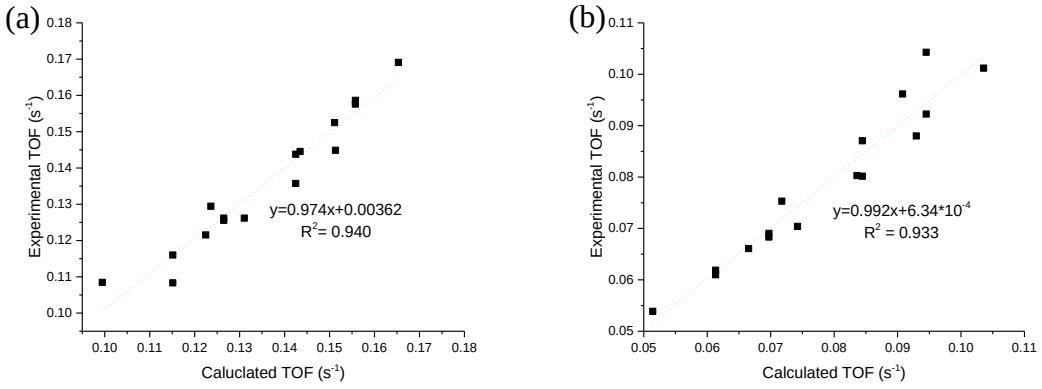

Figure 4.8. Calculated TOFs vs experimental TOFs for (a) 1% Ru/Al_2O_3 and (b) 5% Ru/Al_2O_3.

Table 4.3. Calculated kinetic constants for 1% Ru/Al_2O_3 and 5% Ru/Al_2O_3 catalysts at temperature of 260 °C.

Kinetic constants	1% Ru/Al_2O_3	5% Ru/Al_2O_3
K1 (kPa^{-1})	0.0175	0.00224
K_2 K_3 (kPa^{-1})	$5.24*10^{-6}$	$4.60*10^{-6}$
K_4	342	273
k_5 (s^{-1})	1.46	1.78
k_{10} (s^{-1})	74.0	137

For the $NaNO_3/Ru/Al_2O_3$ catalysts, a different reaction pathway was hypothesized, since the reaction intermediates determined from transient isotopic experiments were different from the unpromoted Ru/Al_2O_3 catalysts, and the CO_2 and H_2 reaction orders do not correspond to the rate law shown in equation 4.3. From previous activation energy measurements (Figure 4.1 (c)), an increase in activation was observed upon addition of $NaNO_3$ to the Ru/Al_2O_3 catalysts, so it was hypothesized that a change in the RDS, or an addition of another irreversible step could play a role when $NaNO_3$ was added to the catalysts. Furthermore, the increased H_2 reaction order likely implied that the hydrogenation of an already hydrogenated product could be important in the rate determining step over $NaNO_3/Ru/Al_2O_3$ catalysts. Previous DFT studies reported that while C-O bond breaking from carbonyl or formyl species has the highest energy barrier on supported Ru catalysts, thereby becoming the rate determining step, it was also reported that hydrogenation of CH_3* to form adsorbed methane is also a step that has a comparable energy barrier.[55,57,58] Duan et al. reported an energy barrier of 143 kJ/mol (1.48 ev) for reaction between formyl species and H* that leads to C-O bond breaking and 125 kJ/mol (1.30 ev) for reaction between CH_3* and H* to form CH_4*. Mushrif et al. also reported an activation barrier of 198 kJ/mol for reaction of CO* and H* to break C-O bonds, while 105 kJ/mol for CH_4* formation through reaction of CH_3* and H*. Combining our experimental

observations with previously reported DFT studies, it was hypothesized that an additional kinetically relevant irreversible step of CH_3* and H* to form CH_4* could be important. A sequence of elementary and lumped steps for a reaction pathway that assumes two irreversible steps was developed for $NaNO_3/Ru/Al_2O_3$ catalysts, as shown in Table 4.4.

Table 4.4. Proposed elementary step for CO_2 methanation over $NaNO_3/Ru/Al_2O_3$ catalysts

Step	Reaction
1	$H_2(g) + 2* \leftrightarrow 2H*$
2	$CO_2(g) + O\text{-}S \leftrightarrow CO_3\text{-}S$
3	$CO_3\text{-}S + H* \leftrightarrow HCOO* + O\text{-}S$
4	$HCOO* + * \leftrightarrow CO* + OH*$
5 (irreversible)	$CO* + H* \rightarrow C* + OH*$
6	$C* + H* \leftrightarrow CH* + *$
7	$CH* + H* \leftrightarrow CH_2* + *$
8	$CH_2+* + H* \leftrightarrow CH_3* + *$
9 (irreversible)	$CH_3* + H* \rightarrow CH_4* + *$
10 (irreversible)	$OH* + H* \rightarrow H_2O* + *$
11	$CH_4* \leftrightarrow CH_4(g) + *$
12	$H_2O* \leftrightarrow H_2O(g) + *$

For $NaNO_3/Ru/Al_2O_3$ catalysts, carbonates and formate species, as well as carbonyl species were determined to be observable reaction intermediates. So the initial steps in the proposed sequence were dissociation of H_2 into two H* atoms (Table 4.4, step 1) and adsorption of CO_2 on an oxide group (or $NaNO_3$ melt) on the support near the support-metal interface, to form bidentate carbonate species (Table 4.4, step 2). Then, the bidentate carbonate species would react with surface hydrogen to form formate species (Table 4.4, step 2), followed by dissociation of the formate to form linear carbonyl species (Table 4.4, step 4). Then the carbonyl species react with a surface hydrogen to break the C-O bond, which was the first kinetically relevant step (Table 4.4, step 5). The formed C* is then

hydrogenated to form CH_3* (Table 4.4, step 6~8), which then reacts with additional surface hydrogen to form adsorbed methane (Table 4.4, step 9). This is the second kinetically relevant step in methane formation. Assuming step 9 is the rate determining step, a rate law was derived as shown in equation 4.4. The derivation of equation 4.3 is shown in Table C.6.

$$r = \frac{\sqrt{\frac{\left(k_5 k_{10} K_4 K_3 K_2 K_1^{\frac{3}{2}}\right)}{2}} P_{CO_2}^{\frac{1}{2}} P_{H_2}^{\frac{3}{4}}}{\left(1+\sqrt{K_1 P_{H_2}}(1+K_3 K_2 P_{CO_2})+\sqrt{K_4 K_3 K_2 K_1^{\frac{1}{2}} P_{CO_2}^{\frac{1}{2}} P_{H_2}^{\frac{1}{4}}}\left(\sqrt{\frac{k_{10}}{2k_5}}+\sqrt{\frac{2k_5}{k_{10}}}\right)+\frac{P_{CO_2}^{\frac{1}{2}}}{k_9}\sqrt{\frac{k_5 k_{10} K_4 K_3 K_2}{2}}\left(\frac{P_{H_2}^{-\frac{5}{4}}}{K_1^{\frac{5}{4}} K_6 K_7 K_8}+\frac{P_{H_2}^{-\frac{3}{4}}}{K_1^{\frac{3}{4}} K_7 K_8}+\frac{P_{H_2}^{-\frac{1}{4}}}{K_1^{\frac{1}{4}} K_8}+K_1^{\frac{1}{4}} P_{H_2}^{\frac{1}{4}}\right)\right)\right)^2}$$

Eq. 4.4

Experimental data obtained from Figure 4.1 (a) and Figure 4.1 (b) were fit to the derived rate law (equation 4.4) for the $NaNO_3/Ru/Al_2O_3$ catalyst, as shown in Figure 4.9. Experimental data for $NaNO_3$/1% Ru/Al_2O_3 and $NaNO_3$/5% Ru/Al_2O_3 fit the derived rate law very well, showing a slope of nearly 1 for both samples with R^2 values of 0.978 and 0.987. The average error between calculated and experimental TOFs was 4.3 % for $NaNO_3$/1% Ru/Al_2O_3 and 3.4% for $NaNO_3$/5% Ru/Al_2O_3. The kinetic constants obtained from the kinetic modeling are presented in Table 4.5. Within each catalyst, among the three rate constants of k_5, k_9, and k_{10}, k_9 showed the lowest values, implying that step 9, the hydrogenation of CH_3*, may be the rate determining step on the $NaNO_3$ loaded catalysts. k_5 was still lower than k_{10}, implying that it is the second slowest step in this pathway to methane. The surface coverage of reaction intermediates calculated from the rate law are shown in Table C.7 and Table C.8. The results show that for the catalysts of similar metal loading, the surface coverage of hydrogen decreased for the $NaNO_3$ loaded catalysts. This

is conceptually consistent with experimental observations, as the much increased H_2 reaction order implies that hydrogen is consumed at a faster rate, which would lead to decreased surface coverage. Additionally, in $NaNO_3$ loaded catalysts, CH_3* showed a very high surface coverage, while the surface coverage of CO* decreased compared to the values found for the Ru/Al_2O_3 catalysts. Again, this supports the hypothesis that step 9 perhaps is the slowest step in the proposed reaction sequence.

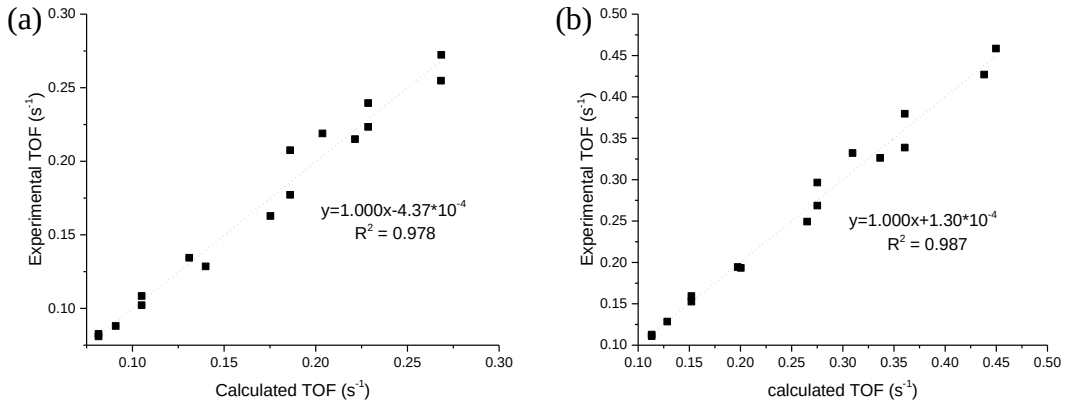

Figure 4.9. Calculated TOF vs experimental TOF for (a) $NaNO_3$/1% Ru/Al_2O_3 and (b) $NaNO_3$/5% Ru/Al_2O_3.

Table 4.5. Calculated kinetic constants for 1% Ru/Al_2O_3 and 5% Ru/Al_2O_3 catalysts at temperature of 260 °C.

Kinetic constants	$NaNO_3$/1% Ru/Al_2O_3	$NaNO_3$/5% Ru/Al_2O_3
K_1 (kPa^{-1})	0.533	0.185
K_2 K_3 (kPa^{-1})	0.00106	0.0150
K_4	2.85	2.09
k_5 (s^{-1})	34.6	27.4
K_6	0.0208	0.288
K_7	0.202	0.151
K_8	5.94	2.15
k_9 (s^{-1})	2.43	8.81
k_{10} (s^{-1})	157	120

For $NaNO_3/Ru/Al_2O_3$ catalysts, prior to finalizing reaction sequence shown in Table 4.4 as most plausible reaction pathway, different reactions sequences were considered and tested with kinetic modeling. One pathway was a sequence that involves hydrogen carbonyl intermediate (H*CO, H_2*CO), as shown in Table C.9. This sequence is similar to the reaction pathway proposed in Chapter 3, but was slightly modified, as it was found bicarbonate species are likely not reaction intermediates from SSITKA analysis. As observed in Figure C.8, the experimental TOF values fit derived rate law very well for both $NaNO_3/1\%Ru/Al_2O_3$ and $NaNO_3/5\%Ru/Al_2O_3$, showing slopes of nearly 1 and R^2 values of 0.971 and 0.984. However, it was hypothesized that this sequence is less plausible than the one in Table 4.4, due to two reasons. One is that the surface coverage of hydrogen is quite high, which is not consistent with high H_2 reaction order, implying lower surface coverage of hydrogen. For H*CO and H_2*CO species, hydrogen atoms are directly attached to Ru active sites, and surface coverage of H*, H*CO, and H_2*CO combined, ranges from approximately 0.3 to 0.47 for $NaNO_3/1\%Ru/Al_2O_3$ and 0.20 to 0.37 for $NaNO_3/5\%Ru/Al_2O_3$ in the given experimental condition, as shown in Table C.10 and Table C.11. Such higher surface coverage of hydrogen on metal surface does not align with implication from increased H_2 reaction orders, making the hydrogen carbonyl reaction pathway less likely. Another reason is that observed IR peak for carbonyl species were observed at very similar wavelengths over 5% Ru/Al_2O_3 and $NaNO_3/5\%$ Ru/Al_2O_3. Presence of hydrogen carbonyl species was hypothesized in Chapter 3, because the carbonyl species observed over $NaNO_3/1\%Ru/Al_2O_3$ was approximately 20 cm^{-1} lower than carbonyl species observed over $1\%Ru/Al_2O_3$. However, as observed in Figure 4.2 and Figure 4.3, the carbonyl species observed in 5% Ru/Al_2O_3 and $NaNO_3/5\%$ Ru/Al_2O_3 were

very similar, indicating that hydrogen carbonyl pathway is less likely at least for 5% ruthenium loading catalysts. Another pathway considered is shown in Table C.12, which is similar to the pathway shown in Table 4.4, but assumes C-O bond breaking step (step 5, Table C.12) as reversible. However, experimental TOF showed poor fitting to the rate law derived from pathway shown in Table C.12, as shown in Figure C.9. Such results show that pathway shown in Table C.12 most likely does not represent the reaction mechanism over $NaNO_3/Ru/Al_2O_3$ catalysts. While hydrogen carbonyl pathway (Table C.9) may be a possible reaction pathway, due to good fitting between experimental TOF to derived rate law, implication from calculated surface coverages, as well as spectral observation, aligns better for the reaction pathway shown in Table 4.4, therefore it is proposed that the reaction pathway which assums two irreversible step of C-O bond breaking and hydrogenation of CH3* species is the most plausible reaction pathway over $NaNO_3/Ru/Al_2O_3$ catalysts.

4.4 Conclusion

To summarize, different metal loadings (1% and 5%) of Ru/Al_2O_3 catalysts and $NaNO_3/Ru/Al_2O_3$ catalysts were synthesized, and their CO_2 methanation mechanisms were investigated. The former catalyst represents a prototypical CO_2 methanation catalyst, and the latter is a catalytic sorbent, with heavy $NaNO_3$ promotion driving high CO_2 sorption. Through DRIFT spectroscopy, along with transient isotopic experiments, it was found that bicarbonate and linear carbonyl species behave as reaction intermediates in the path to methane, while formate species are spectator species over Ru/Al_2O_3 catalysts. For $NaNO_3/Ru/Al_2O_3$ catalysts, bidentate carbonate, formate, and linear carbonyl species all appear to be reaction intermediates. Kinetic modeling showed that the C-O bond breaking of carbonyl species is likely a rate determining step for Ru/Al_2O_3, while there are likely

more kinetically relevant steps, including the hydrogenation of CH_3* species to form adsorbed methane for the $NaNO_3/Ru/Al_2O_3$ catalyst. No significant difference in reaction pathways was observed between different metal loadings. This is likely due to the fact that the different metal loading catalysts maintained similar particle sizes. The subtle differences in reaction pathways over $NaNO_3$ loaded supported ruthenium catalysts vs. the unpromoted catalysts gives insight into the kinetic consequences of catalyst designs targeting catalytic sorbents, where in situ CO_2 capture and subsequent conversion is targeted on a single solid material.

4.5 Reference

(1) Intergovernmental Panel on Climate Change. *Climate Change 2014 : Mitigation of Climate Change*; Cambridge University Press, 2014.

(2) Boden, T. A.; Marland, G.; Andres, R. J. Global, Regional, and National Fossil-Fuel CO_2 Emissions. Carbon Dioxide Information Analysis Center, Oak Ridge National Laboratory, U.S. Department of Energy. **2017**.

(3) World Energy Council. *World Energy Resources*; 2016.

(4) Wang, W.; Wang, S.; Ma, X.; Gong, J. Recent Advances in Catalytic Hydrogenation of Carbon Dioxide. *Chem. Soc. Rev.* **2011**, *40* (7), 3703–3727.

(5) Miao, B.; Ma, S. S. K.; Wang, X.; Su, H.; Chan, S. H. Catalysis Mechanisms of CO_2 and CO Methanation. *Catal. Sci. Technol.* **2016**, *6* (12), 4048–4058.

(6) Aziz, M. A. A.; Jalil, A. A.; Triwahyono, S.; Ahmad, A. CO_2 Methanation over Heterogeneous Catalysts: Recent Progress and Future Prospects. *Green Chem.* **2015**, *17* (5), 2647–2663.

(7) Wang, W.; Gong, J. Methanation of Carbon Dioxide: An Overview. *Front. Chem. Eng.* **2011**, *5* (1), 2–10.

(8) Frontera, P.; Macario, A.; Ferraro, M.; Antonucci, P. Supported Catalysts for CO_2 Methanation : A Review. **2017**, No. 1, 1–28.

(9) Lee, W. J.; Li, C.; Prajitno, H.; Yoo, J.; Patel, J.; Yang, Y.; Lim, S. Recent Trend in Thermal Catalytic Low Temperature CO_2 Methanation : A Critical Review. *Catal. Today* **2021**, *368* (February 2020), 2–19.

(10) Li, D.; Ichikuni, N.; Shimazu, S.; Uematsu, T. Hydrogenation of CO_2 over Sprayed Ru/TiO_2 Fine Particles and Strong Metal–Support Interaction. *Appl. Catal. A Gen.* **1999**, *180* (1–2), 227–235.

(11) Li, D.; Ichikuni, N.; Shimazu, S.; Uematsu, T. Catalytic Properties of Sprayed Ru/Al_2O_3 and Promoter Effects of Alkali Metals in CO_2 Hydrogenation. *Appl. Catal. A Gen.* **1998**, *172* (2), 351–358.

(12) Cimino, S.; Boccia, F.; Lisi, L. Effect of Alkali Promoters (Li, Na, K) on the Performance of Ru/Al_2O_3 Catalysts for CO_2 Capture and Hydrogenation to Methane. *J. CO_2 Util.* **2020**, *37*, 195–203.

(13) Petala, A.; Panagiotopoulou, P. Methanation of CO_2 over Alkali-Promoted Ru/TiO_2

Catalysts : I. Effect of Alkali Additives on Catalytic Activity and Selectivity. *Appl. Catal. B Environ.* **2018**, *224*, 919–927.

(14) Panagiotopoulou, P. Methanation of CO_2 over Alkali-Promoted Ru/TiO_2 Catalysts : II. Effect of Alkali Additives on the Reaction Pathway. *Appl. Catal. B Environ.* **2018**, *236*, 162–170.

(15) David, M.; Barrio, V. L.; Requies, M.; Cambra, J. F. Effect of the Addition of Alkaline Earth and Lanthanide Metals for the Modification of the Alumina Support in Ni and Ru Catalysts in CO_2 Methanation. *Catalysts* **2021**, *11*, 353.

(16) Liu, Q.; Wang, S.; Zhao, G.; Yang, H.; Yuan, M.; An, X.; Zhou, H.; Qiao, Y.; TianYuanyu. CO_2 Methanation over Ordered Mesoporous NiRu-Doped $CaO-Al_2O_3$ Nanocomposites with Enhanced Catalytic Performance. *Int. J. Hydrogen Energy* **2017**, *43* (1), 239–250.

(17) Tsiotsias, A. I.; Charisiou, N. D.; Yentekakis, I. V.; Goula, M. A. The Role of Alkali and Alkaline Earth Metals in the CO_2 Methanation Reaction and the Combined Capture and Methanation of CO_2. *Catalysits* **2020**, *10*, 812.

(18) Bermejo-López, A.; Pereda-Ayo, B.; González-Marcos, J. A.; González-Velasco, J. R. Mechanism of the CO_2 Storage and in Situ Hydrogenation to CH_4. Temperature and Adsorbent Loading Effects over $Ru-CaO/Al_2O_3$ and $Ru-Na_2CO_3/Al_2O_3$ Catalysts. *Appl. Catal. B Environ.* **2019**, *256*, 117845.

(19) Porta, A.; Visconti, C. G.; Castoldi, L.; Matarrese, R.; Jeong-Potter, C.; Farrauto, R.; Lietti, L. Ru-Ba Synergistic Effect in Dual Functioning Materials for Cyclic CO_2

Capture and Methanation. *Appl. Catal. B Environ.* **2021**, *283* (July 2020), 119654.

(20) Duyar, M. S.; Treviño, M. A. A.; Farrauto, R. J. Dual Function Materials for CO_2 Capture and Conversion Using Renewable H2. *Appl. Catal. B Environ.* **2015**, *168–169*, 370–376.

(21) Wang, S.; Farrauto, R. J.; Karp, S.; Jeon, J. H.; Schrunk, E. T. Parametric , Cyclic Aging and Characterization Studies for CO_2 Capture from Flue Gas and Catalytic Conversion to Synthetic Natural Gas Using a Dual Functional Material (DFM). *J. CO_2 Util.* **2018**, *27*, 390–397.

(22) Duyar, M. S.; Ramachandran, A.; Wang, C.; Farrauto, R. J. Kinetics of CO_2 Methanation over Ru/γ-Al_2O_3 and Implications for Renewable Energy Storage Applications. *J. CO_2 Util.* **2015**, *12*, 27–33.

(23) Proaño, L.; Tello, E.; Arellano-Trevino, M. A.; Wang, S.; Farrauto, R. J.; Cobo, M. In-Situ DRIFTS Study of Two-Step CO_2 Capture and Catalytic Methanation over Ru, "Na_2O"/Al_2O_3 Dual Functional Material. *Appl. Surf. Sci.* **2019**, *479*, 25–30.

(24) Park, S. J.; Bukhovko, M. P.; Jones, C. W. Integrated Capture and Conversion of CO2 into Methane Using $NaNO_3$ /MgO + Ru/Al_2O_3 as a Catalytic Sorbent. *Chem. Eng. J.* **2021**, *420* (P3), 130369.

(25) Duyar, M. S.; Wang, S.; Arellano-Treviño, M. A.; Farrauto, R. J. CO_2 Utilization with a Novel Dual Function Material (DFM) for Capture and Catalytic Conversion to Synthetic Natural Gas: An Update. *J. CO_2 Util.* **2016**, *15*, 65–71.

(26) Porta, A.; Matarrese, R.; Visconti, C. G.; Castoldi, L.; Lietti, L. Storage Material Effects on the Performance of Ru-Based CO_2 Capture and Methanation Dual Functioning Materials. *Ind. Eng. Chem. Res.* **2021**, *60*, 6706–6718.

(27) Jeong-potter, C.; Farrauto, R. Feasibility Study of Combining Direct Air Capture of CO_2 and Methanation at Isothermal Conditions with Dual Function Materials. *Appl. Catal. B Environ.* **2021**, *282*, 119416.

(28) Kowalczyk, Z.; Stolecki, K.; Rarog-Pilecka, W.; Miskiewicz, E.; Wilczkowska, E.; Karpinski, Z. Supported Ruthenium Catalysts for Selective Methanation of Carbon Oxides at Very Low CO_x/H_2 Ratios. *Appl. Catal. A Gen.* **2008**, *342*, 35–39.

(29) Truszkiewicz, E.; Zegadło, K.; Wojda, D.; Mierzwa, B.; Kepinski, L. The Effect of the Ruthenium Crystallite Size on the Activity of Ru/Carbon Systems in CO Methanation. *Top. Catal.* **2017**, *60* (17), 1299–1305.

(30) Wang, X.; Hong, Y.; Shi, H.; Szanyi, J. Kinetic Modeling and Transient DRIFTS–MS Studies of CO2 Methanation over Ru/Al_2O_3 Catalysts. *J. Catal.* **2016**, *343*, 185–195.

(31) Chukanov, N. V.; Chervonnyi, A. D. *IR Spectra of Minerals and Related Compounds, and Reference Samples ' Data*; Springer, 2016.

(32) Harada, T.; Hatton, T. A. Colloidal Nanoclusters of MgO Coated with Alkali Metal Nitrates/Nitrites for Rapid, High Capacity CO_2 Capture at Moderate Temperature. *Chem. Mater.* **2015**, *27*, 8153–8161.

(33) Zhang, K.; Li, X. S.; Li, W.; Rohatgi, A.; Duan, Y.; Singh, P.; Li, L.; King, D. L. Phase Transfer-Catalyzed Fast CO_2 Absorption by MgO-Based Absorbents with High Cycling Capacity. *Adv. Mater. Interfaces* **2014**, *1*, 1400030.

(34) Park, S. J.; Kim, Y.; Jones, C. W. $NaNO_3$-Promoted Mesoporous MgO for High-Capacity CO_2 Capture from Simulated Flue Gas with Isothermal Regeneration. *ChemSusChem* **2020**, *13* (11), 2988–2995.

(35) Marwood, M.; Ralf, D.; Prairie, M.; Renken, A. Transient Drift Spectroscopy for the Determination of the Surface Reaction Kinetics of CO_2 Methanation. *Chem. Eng. Sci.* **1994**, *49* (24), 4801–4809.

(36) Karelovic, A.; Ruiz, P. Mechanistic Study of Low Temperature CO_2 Methanation over Rh/TiO_2 Catalysts. *J. Catal.* **2013**, *301*, 141–153.

(37) Wang, X.; Shi, H.; Kwak, J. H.; Szanyi, J. Mechanism of CO_2 Hydrogenation on Pd/Al_2O_3 Catalysts : Kinetics and Transient DRIFTS-MS Studies. *ACS Catal.* **2015**, *5*, 6337–6349.

(38) Marwood, M.; Doepper, R.; Renken, A. In-Situ Surface and Gas Phase Analysis for Kinetic Studies under Transient Conditions. The Catalytic Hydrogenation of CO_2. *Appl. Catal. A Gen.* **1997**, No. 151, 223–246.

(39) Morterra, C.; Magnacca, G. A Case Study : Surface Chemistry and Surface Structure of Catalytic Aluminas, as Studied by Vibrational Spectroscopy of Adsorbed Species. *Catal. Today* **1996**, *27*, 497–532.

(40) Solymosi, F.; Erdohelyi, A.; Kocsis, M. Methanation of CO_2, on Supported Ru Catalysts. *Faraday. Trans. 1* **1981**, *77*, 1003–1012.

(41) Gupta, N. M.; Kamble, V. S.; Iyer, R. M.; Ravindranathan, T.; Gratzel, M. The Transient Species Formed over Ru-RuO_x/TiO_2 Catalyst in the CO and CO + H_2 Interaction : FTIR Spectroscopic Study. *J. Catal.* **1992**, *486* (1992).

(42) Guo, Y.; Mei, S.; Yuan, K.; Wang, D.; Liu, H.; Yan, C.; Zhang, Y. Low-Temperature CO_2 Methanation over CeO_2-Supported Ru Single Atoms, Nanoclusters, and Nanoparticles Competitively Tuned by Strong Metal−Support Interactions and H - Spillover Effect. *ACS Catal.* **2018**, *8*, 6203–6215.

(43) Chin, S. Y.; Williams, C. T.; Amiridis, M. D. FTIR Studies of CO Adsorption on Al_2O_3- and SiO_2-Supported Ru Catalysts. *J. Phys. Chem. B* **2006**, *110*, 871–882.

(44) Erdohlyi, A.; Pasztor, M.; Solymosi, F. Catalytic Hydrogenation of CO_2 over Supported Palladium. *J. Catal.* **1986**, *98*, 166–177.

(45) Zhao, K.; Wang, L.; Calizzi, M.; Moioli, E.; Zu, A. In Situ Control of the Adsorption Species in CO_2 Hydrogenation : Determination of Intermediates and Byproducts. *J. Phys. Chem. C* **2018**, *122*, 20888–20893.

(46) Eckle, S.; Anfang, H.; Behm, R. J. Reaction Intermediates and Side Products in the Methanation of CO and CO_2 over Supported Ru Catalysts in H_2 -Rich Reformate Gases. *J. Phys. Chem. C* **2011**, *115* (4), 1361–1367.

(47) Alexeev, O. S.; Chin, S. Y.; Engelhard, M. H.; Ortiz-soto, L.; Amiridis, M. D.

Effects of Reduction Temperature and Metal-Support Interactions on the Catalytic Activity of Pt/γ-Al_2O_3 and Pt/TiO_2 for the Oxidation of CO in the Presence and Absence of H_2. *J. Phys. Chem. B* **2005**, *109*, 23430–23443.

(48) Heyl, D.; Rodemerck, U.; Bentrup, U. Mechanistic Study of Low-Temperature CO_2 Hydrogenation over Modified Rh/Al_2O_3 Catalysts. *ACS Catal.* **2016**, *6*, 6275–6284.

(49) Wijnja, H.; Schulthess, C. P. ATR – FTIR and DRIFT Spectroscopy of Carbonate Species at the Aged γ-Al_2O_3/Water Interface. *Spectrochim. Acta. Part A* **1999**, *55*, 861–872.

(50) Du, H.; Williams, C. T.; Ebner, A. D.; Ritter, J. A. In Situ FTIR Spectroscopic Analysis of Carbonate Transformations during Adsorption and Desorption of CO_2 in K-Promoted HTlc. *Chem. Mater.* **2010**, *22*, 3519–3526.

(51) Hoffmann, F. M.; Weisel, M. D.; Paul, J. The Activation of CO_2 by Potassium-Promoted Ru(001) I. FT-IRAS and TDMS Study of Oxalate and Carbonate Intermediates. *Surf. Sci.* **1994**, *316*, 277–293.

(52) Freund, H. J.; Roberts, M. W. Surface Chemistry of Carbon Dioxide. *Surf. Sci. Rep.* **1996**, *25*, 225–273.

(53) Li, C.; Sakata, Y.; Arai, T.; Domen, K.; Maruya, K.; Onishi, T. Carbon Monoxide and Carbon Dioxide Adsorption on Cerium Oxide Studied by Fourier- Transform Infrared Spectroscopy. *J. Chem. Soc., Faraday Trans. 1* **1989**, *85* (4), 929–943.

(54) Busca, G.; Lorenzelli, V. INFRARED SPECTROSCOPIC IDENTIFICATION OF

SPECIES ARISING FROM REACTIVE ADSORPTION OF CARBON OXIDES ON METAL OXIDE SURFACES. *Mater. Chem.* **1982**, *7*, 89–126.

(55) Mohan, O.; Shambhawi, S.; Xu, R.; Lapkin, A. A.; Murshrif, S. H. Investigating CO_2 Methanation on Ni and Ru : DFT Assisted Microkinetic Analysis. *ChemCatChem* **2021**, 2420–2433.

(56) Schmider, D.; Maier, L.; Deutschmann, O. Reaction Kinetics of CO and CO_2 Methanation over Nickel. *Ind. Eng. Chem. Res.* **2021**, *60*, 5792–5805.

(57) Akamaru, S.; Shimazaki, T.; Kubo, M.; Abe, T. Density Functional Theory Analysis of Methanation Reaction of CO_2 on Ru Nanoparticle Supported on TiO_2 (101). *Appl. Catal. A Gen.* **2014**, *470*, 405–411.

(58) Zhang, S.; Yan, H.; Wei, M.; Evans, D. G.; Duan, X. Hydrogenation Mechanism of Carbon Dioxide and Carbon Monoxide on Ru(0001) Surface : A Density Functional Theory Study. *RSC Adv.* **2014**, *4*, 30241–30249.

(59) Avanesian, T.; Gusmão, G. S.; Christopher, P. Mechanism of CO_2 Reduction by H_2 on Ru(0001) and General Selectivity Descriptors for Late-Transition Metal Catalysts. *J. Catal.* **2016**, *343*, 86–96.

CHAPTER 5. SUMMARY AND FUTURE DIRECTION

A summary of the thesis dissertation is presented, followed by potential future research directions.

5.1 Introduction

5.1.1 Chapter 1

A review of the current status of research into CO_2 capture at elevated temperatures as well as catalytic CO_2 methanation was carried out. Recently reported applications of combined capture and methanation were discussed and state-of-art materials in the field were introduced. The discussion evaluated the efficiency of previously reported dual function materials, and introduced the need for improvements in materials performance in both CO_2 sorption capacity and methane production capacity. The importance of improved understanding of the CO_2 sorption and methanation mechanism was also discussed.

5.1.2 Chapter 2

$NaNO_3$ promoted mesoporous MgO sorbents were synthesized and their performance as a sorbent in the temperature range between 230 °C ~ 300 °C, a range reported to be effective for CO_2 methanation, was evaluated. Sorbents with a molar ratio of $MgO:NaNO_3$ = 1:0.10 were found to give the highest CO_2 sorption capacity of 11.2 mmol CO_2/g. Through characterization by in situ XRD and in situ FTIR, it was found that the sorption of CO_2 occurs through nucleation and growth of $MgCO_3$ crystallites in the sorbent. Partially desorbed samples were found to have much improved sorption kinetics,

likely due to secondary nucleation occurring in the partially desorbed sorbent. Lastly, it was shown that $NaNO_3$ promoted MgO sorbents could be regenerated under isothermal conditions, making them suitable for combined CO_2 capture and methanation process where capture of a large quantity of CO_2 is desired, but where its facile desorption or transfer to catalytic sites is important.

5.1.3 Chapter 3

A catalytic sorbent was synthesized through physical mixing of $NaNO_3$/MgO sorbent and Ru/Al_2O_3 catalysts. The synthesized catalytic sorbent was tested for integrated capture and conversion of CO_2 to methane at a temperature of 300 °C. Maxiumum CO_2 sorption capacity of 3.24 mmol CO_2/g and methane production capacity of 2.21 mmol CH_4/g was observed for the synthesized catalytic sorbent. CO_2 methanation reaction pathways over 1% Ru/Al_2O_3 and 5% $NaNO_3$/1% Ru/Al_2O_3 were also investigated. Through kinetic studies and in situ FTIR measurements, it was hypothesized that linear carbonyl species are likely intermediates in the pathway to methane for 1% Ru/Al_2O_3, while both linear carbonyl and formate species are potential intermediates over 5% $NaNO_3$/1% Ru/Al_2O_3.

5.1.4 Chapter 4

An in-depth investigation of reaction pathway over Ru/Al_2O_3 and $NaNO_3/Ru/Al_2O_3$ catalysts was performed, building on the preliminary results of chapter 3. Kinetic measurements and steady state isotopic transient kinetic analyses (SSITKA) were performed over the family of catalysts. It was found that for Ru/Al_2O_3 catalysts, along with linear carbonyl species that were hypothesized to be reaction intermediates in the previous

chapter, bicarbonate species also behaved as reaction intermediates in the methanation reaction. For $NaNO_3/Ru/Al_2O_3$ catalysts, along with linear carbonyl and formate species, bidentate carbonyl species also appeared as reaction intermediate. Based on these observations, different reaction pathways were proposed for the two types of catalysts, and rate laws that correspond to proposed pathways were derived. Experimental kinetic data were fitted to obtained the constants within the derived rate law, and the calculated turnover frequency corresponded very well to the experimentally obtained data.

5.2 Future Directions

5.2.1 Synthesis of MgO Sorbents Using Different Promoter

Two main drawbacks of $NaNO_3$ promoted MgO were observed from Chapter 2. One was slow kinetics, taking 12 hours to reach the CO_2 sorption capacity of 11.2 mmol CO_2/g, and the other was sintering of the sorbent over multiple cycles. In recent years, there has been a rise in interest in the use of different alkali metals, including Li, Na, K, or Rb based promoters with MgO sorbents to improve sorbent performance.[1–9] While the general observations show that mixture of promoters improve both CO_2 sorption capacity and sorption kinetics, the underlying mechanism(s) of the observed improvements are not yet understood. The effects of using different promoters or a mixture of promoters on sorbent stability have also not been studied in depth. Furthermore, such sorbents synthesized with a mixture of promoters have not yet been tested for isothermal regeneration. Hence, it will be worthwhile to test different alkali promoters for further improvement of sorbents and to understand their mechanism(s) for CO_2 sorption in the presence two or more promoters.

5.2.2 Application of Catalytic Sorbent for Different CO_2 Hydrogenation Reaction

Methanation was initially studied by numerous researchers as a primary reaction for combined capture and conversion applications, mainly because the reaction is thermodynamically favorable and requires mild reaction conditions. However, there has been increasing interest in other reactions for utilization of CO_2, such as conversion of CO_2 to syngas or using CO_2 for oxidative dehydrogenation of ethane to ethylene.[10–12] To this end, studies to convert captured CO_2 to products of higher value than methane, such as higher hydrocarbons or alcohols, will be needed, as there are very few studies performed regarding application of combined capture and conversion of CO_2 to products other than methane.

5.2.3 Chemical Looping for Combined CO_2 capture and Methanation

In Chapter 3, capture and conversion cycles were performed by switching the feed gas between CO_2 and H_2, with an N_2 purge in between the capture and conversion steps. However, a more industrially applicable method would be to perform the combined capture and conversion process through chemical looping.[13,14] In such a process, catalytic sorbents would be cycled between two reactors, one with hydrogen feed and the other with CO_2 feed. Recent studies regarding combined capture and conversion processes mostly focused on synthesizing various materials, while there have been relatively fewer studies regarding chemical looping for such applications. Therefore, future studies regarding chemical looping could help to make combined capture and conversion processes more industrially applicable.

5.3 Reference

(1) Hu, Y.; Guo, Y.; Sun, J.; Li, H.; Liu, W. Progress in MgO Sorbents for Cyclic CO_2 Capture : Review. *J. Mater. Chem. A* **2019**, *7*, 20103–20120.

(2) Xiao, G.; Singh, R.; Chaffee, A.; Webley, P. Advanced Adsorbents Based on MgO and K_2CO_3 for Capture of CO_2 at Elevated Temperatures. *Int. J. Greenh. Gas Control* **2011**, *5* (4), 634–639.

(3) Harada, T.; Hatton, T. A. Colloidal Nanoclusters of MgO Coated with Alkali Metal Nitrates/Nitrites for Rapid, High Capacity CO_2 Capture at Moderate Temperature. *Chem. Mater.* **2015**, *27*, 8153–8161.

(4) Liu, M.; Vogt, C.; Chaffee, A. L.; Chang, S. L. Y. Nanoscale Structural Investigation of Cs_2CO_3-Doped MgO Sorbent for CO_2 Capture at Moderate Temperature. *J. Phys. Chem. C* **2013**, *117*, 17514–17520.

(5) Vu, A. T.; Park, Y.; Jeon, P. R.; Lee, C. H. Mesoporous MgO Sorbent Promoted with KNO_3 for CO_2 Capture at Intermediate Temperatures. *Chem. Eng. J.* **2014**, *258*, 254–264.

(6) Lee, S. C.; Cha, S. H.; Kwon, Y. M.; Park, M. G.; Hwang, B. W.; Park, Y. K.; Seo, H. M.; Kim, J. C. Effects of Alkali-Metal Carbonates and Nitrates on the CO_2 Sorption and Regeneration of MgO-Based Sorbents at Intermediate Temperatures. *Korean J. Chem. Eng.* **2016**, *33* (12), 3448–3455.

(7) Qiao, Y.; Wang, J.; Zhang, Y.; Gao, W.; Harada, T.; Huang, L.; Hatton, T. A.; Wang,

Q. Alkali Nitrates Molten Salt Modified Commercial MgO for Intermediate-Temperature CO_2 Capture : Optimization of the Li/Na/K Ratio. *Ind. Eng. Chem. Res.* **2017**, *56*, 1509–1517.

(8) Kwak, J.; Kim, K.; Yoon, J. W.; Oh, K.; Kwon, Y. Interfacial Interactions Govern the Mechanisms of CO_2 Absorption and Desorption on A_2CO_3-Promoted MgO (A=Na, K,Rb, and Cs) Absorbents. *J. Phys. Chem. C* **2018**, *122*, 20289–20300.

(9) Vu, A. T.; Ho, K.; Jin, S.; Lee, C. H. Double Sodium Salt-Promoted Mesoporous MgO Sorbent with High CO_2 Sorption Capacity at Intermediate Temperatures under Dry and Wet Conditions. *Chem. Eng. J.* **2016**, *291*, 161–173.

(10) Bobadilla, L. F.; Riesco-garcía, J. M.; Penelás-pérez, G.; Urakawa, A. Enabling Continuous Capture and Catalytic Conversion of Flue Gas CO_2 to Syngas in One Process. *Biochem. Pharmacol.* **2016**, *14*, 106–111.

(11) Al-mamoori, A.; Lawson, S.; Rownaghi, A. A.; Rezaei, F. Oxidative Dehydrogenation of Ethane to Ethylene in an Integrated CO_2 Capture-Utilization Process. *Appl. Catal. B Environ.* **2020**, *278* (July), 119329.

(12) Omodolor, I. S.; Otor, H. O.; Andonegui, J. A.; Allen, B. J.; Alba-Rubio, A. C. Dual-Function Materials for CO_2 Capture and Conversion : A Review. *Ind. Eng. Chem. Res.* **2020**, *59*, 17612–17631.

(13) Lyngfelt, A.; Leckner, B.; Mattisson, T. A Fluidized-Bed Combustion Process with Inherent CO_2 Separation; Application of Chemical-Looping Combustion. *Chem. Eng. Sci.* **2001**, *56*, 3101–3113.

(14) Hossain, M. M.; de Lasa, H. I. Chemical-Looping Combustion (CLC) for Inherent CO2 Separations—a Review. *Chem. Eng. Sci.* **2008**, *63*, 4433–4451.

(15) Weisz, P. B.; Prater, C. D. Interpretation of Measurements in Experimental Catalysis. *Adv. Catal.* **1954**, *6*, 143–196.

(16) Mondal, S.; Malviya, H.; Biswas, P. Kinetic Modelling for the Hydrogenolysis of Bio-Glycerol in the Presence of a Highly Selective Cu–Ni–Al_2O_3 Catalyst in a Slurry Reactor. *React. Chem. Eng.* **2019**, No. 3, 595–609.

(17) Mohagheghi, M.; Bakeri, G.; Saeedizad, M. Study of the Effects of External and Internal Diffusion on the Propane Dehydrogenation Reaction over Pt-Sn/Al_2O_3 Catalyst. *Chem. Eng. Technol.* **2007**, *30* (12), 1721–1725.

(18) Ellis, C. S.; Holsen, J. N. DIFFUSION COEFFICIENTS FOR HELIUM-NITROGEN AND NITROGEN-CARBON DIOXIDE AT ELEVATED TEMPERATURES. *Ind. Eng. Chem. Fundam.* **1969**, *8* (4), 787–791.

(19) Ashok, J.; Pati, S.; Hongmanorom, P.; Tianxi, Z.; Junmei, C.; Kawi, S. A Review of Recent Catalyst Advances in CO_2 Methanation Processes. *Catal. Today* **2020**, *356* (July), 471–489.

APPENDIX A. CHAPTER 2 SUPPORTING INFORMATION

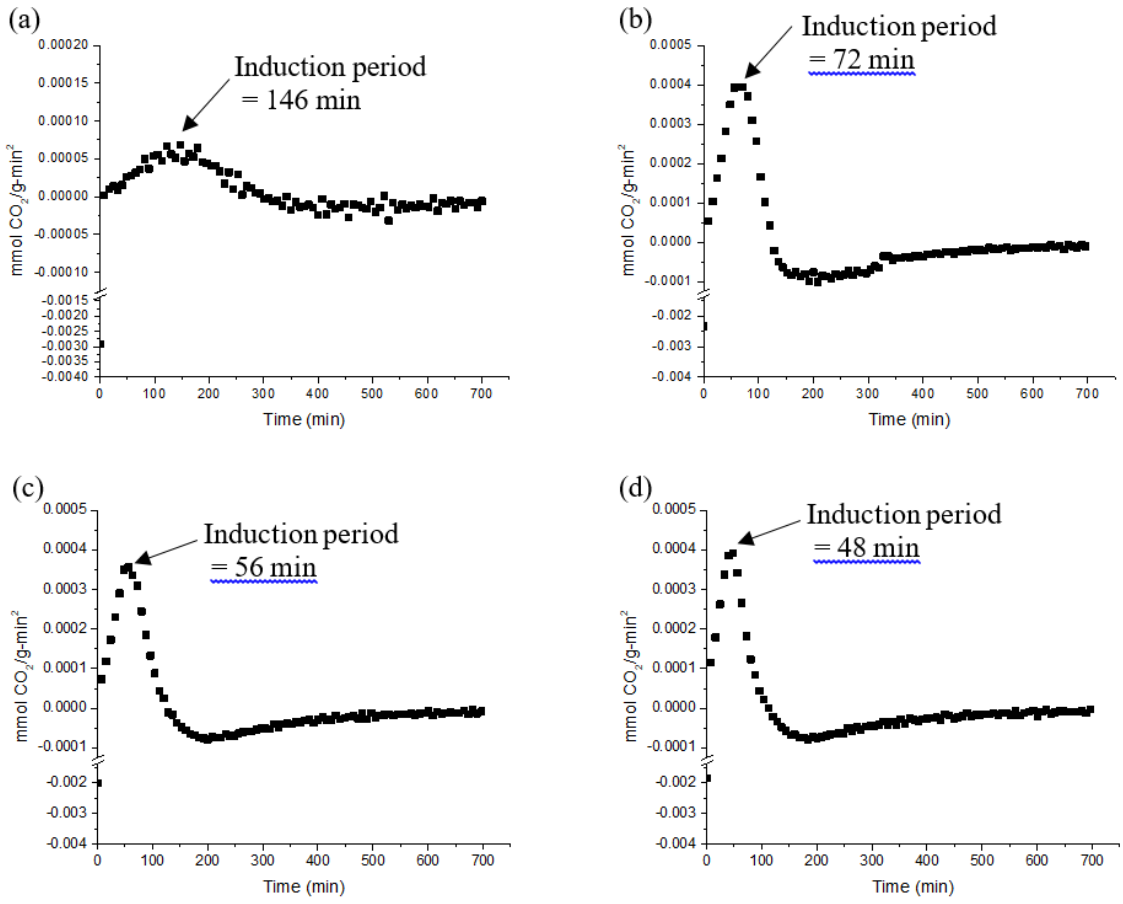

Figure A.1. Induction periods calculated based on the second derivative of the sorption capacity for samples of different $NaNO_3$ loading. (a) MgO_$NaNO_3$_0.05, (b) MgO_$NaNO_3$_0.10, (c) MgO_$NaNO_3$_0.15, (d) MgO_$NaNO_3$_0.20 at temperature of 250 °C.

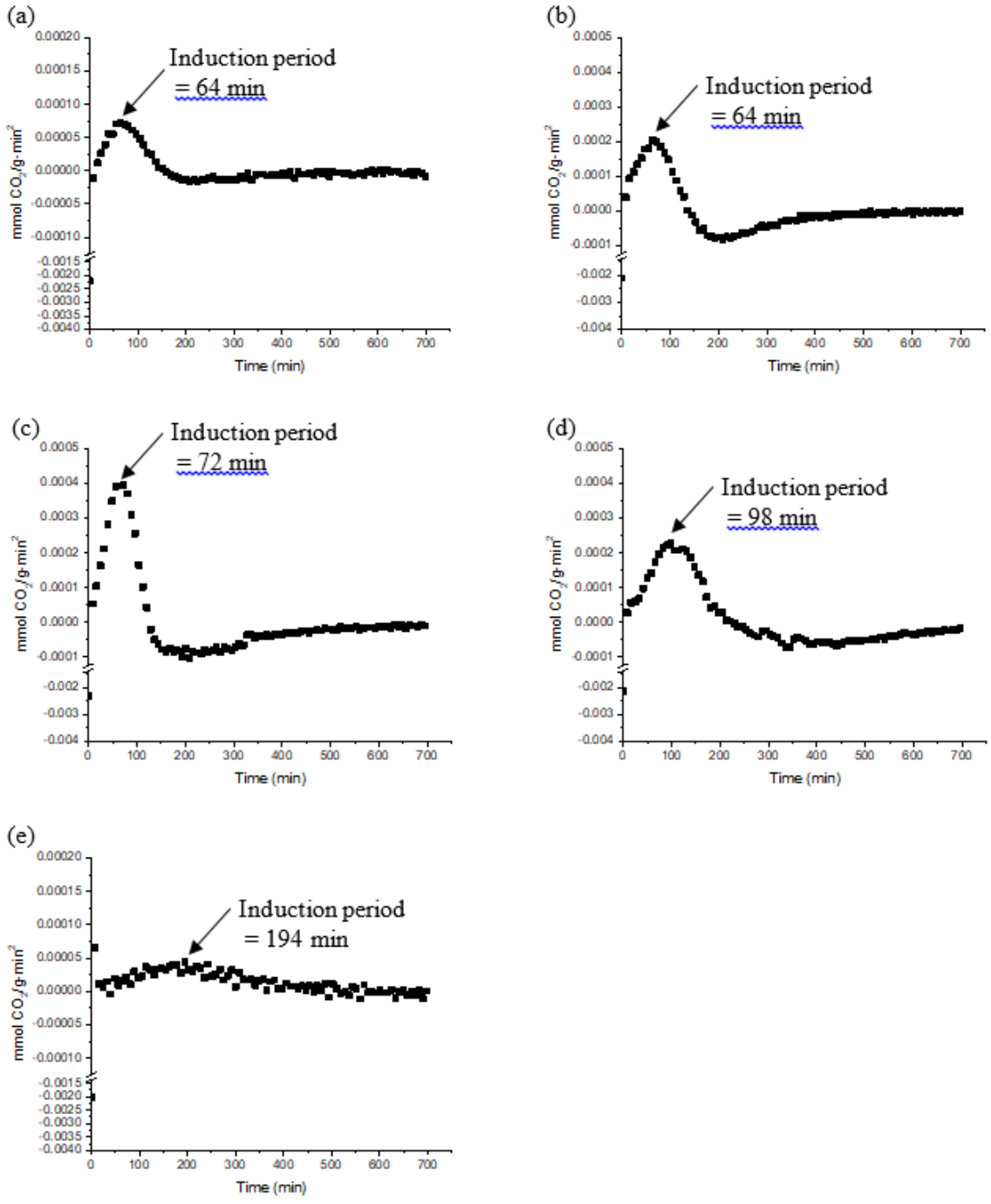

Figure A.2. Induction periods calculated based on the second derivative of the sorption capacity of MgO_$NaNO_3$_0.10 measured at different temperatures: (a) 230 °C, (b) 240 °C, (c) 250 °C, (d) 260 °C, (e) 270 °C.

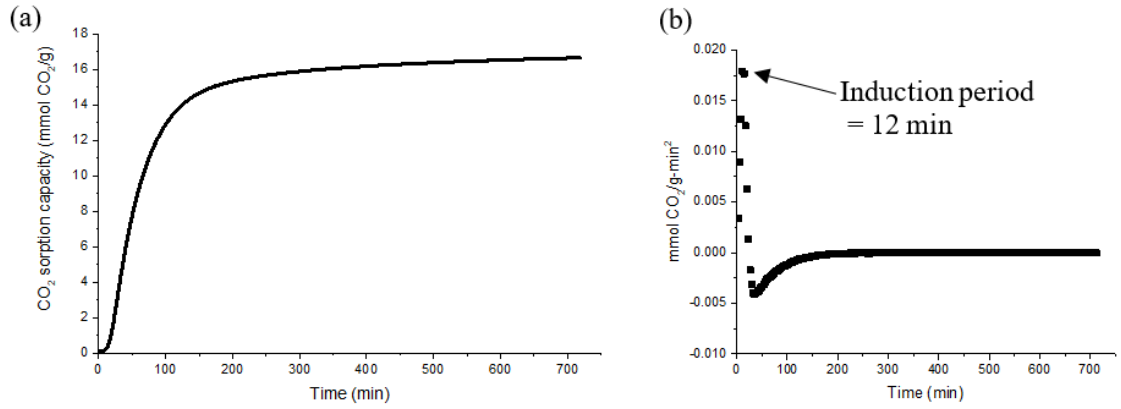

Figure A.3. (a) The sorption capacity of MgO_$NaNO_3$_0.10 under a pure CO_2 flow at 280 °C over 12 h. (b) Induction period calculated based on the second derivative of the sorption capacity from (a).

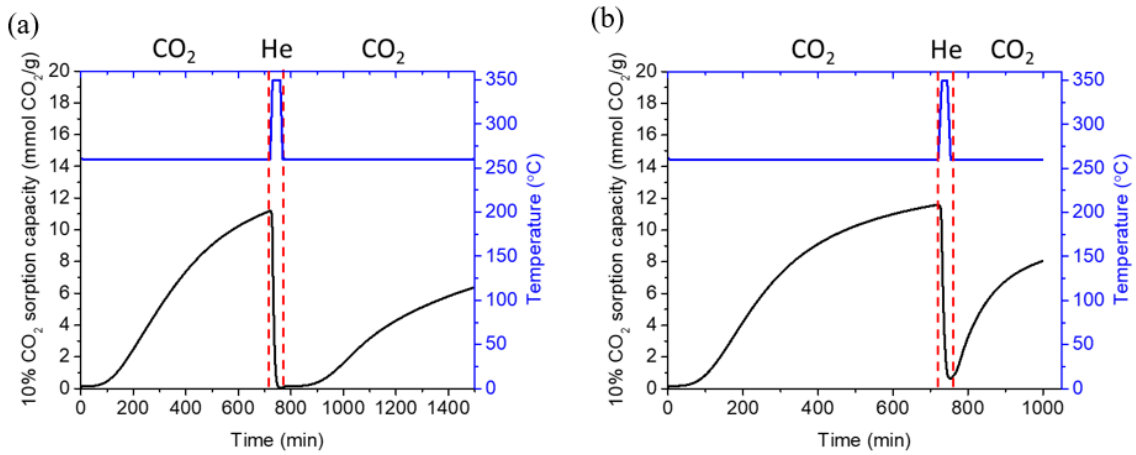

Figure A.4. The CO_2 uptake over 3 h of (a) fully desorbed MgO_$NaNO_3$_0.10 and (b) partially desorbed MgO_$NaNO_3$_0.10 after an initial 12 h sorption measured at 260 °C under 10% CO_2/He flow.

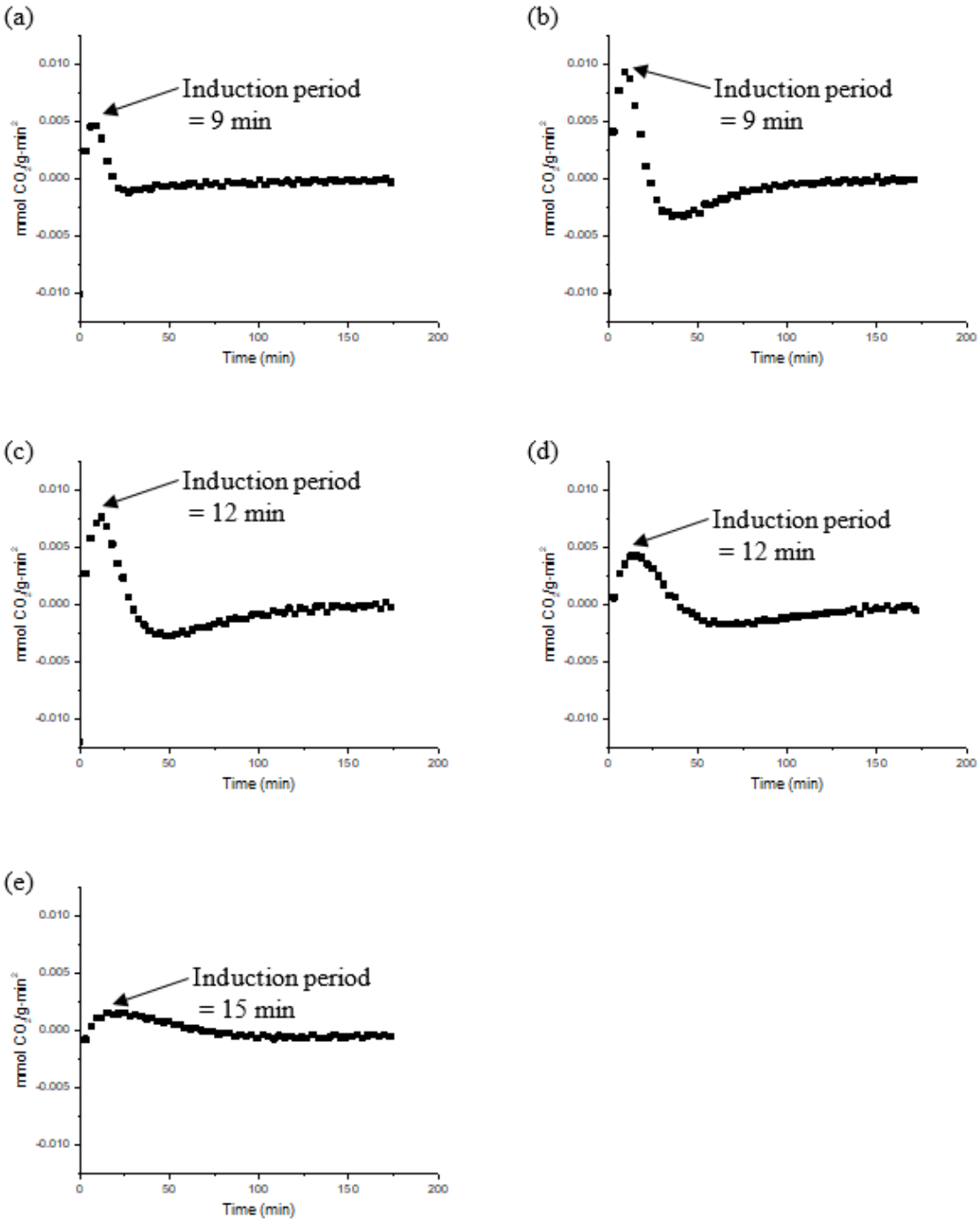

Figure A.5. Induction periods calculated based on the second derivative of the sorption capacity of partially desorbed MgO_$NaNO_3$_0.10 measured at different temperatures: (a) 260 °C, (b) 270 °C, (c) 280 °C, (d) 290 °C, (e) 300 °C.

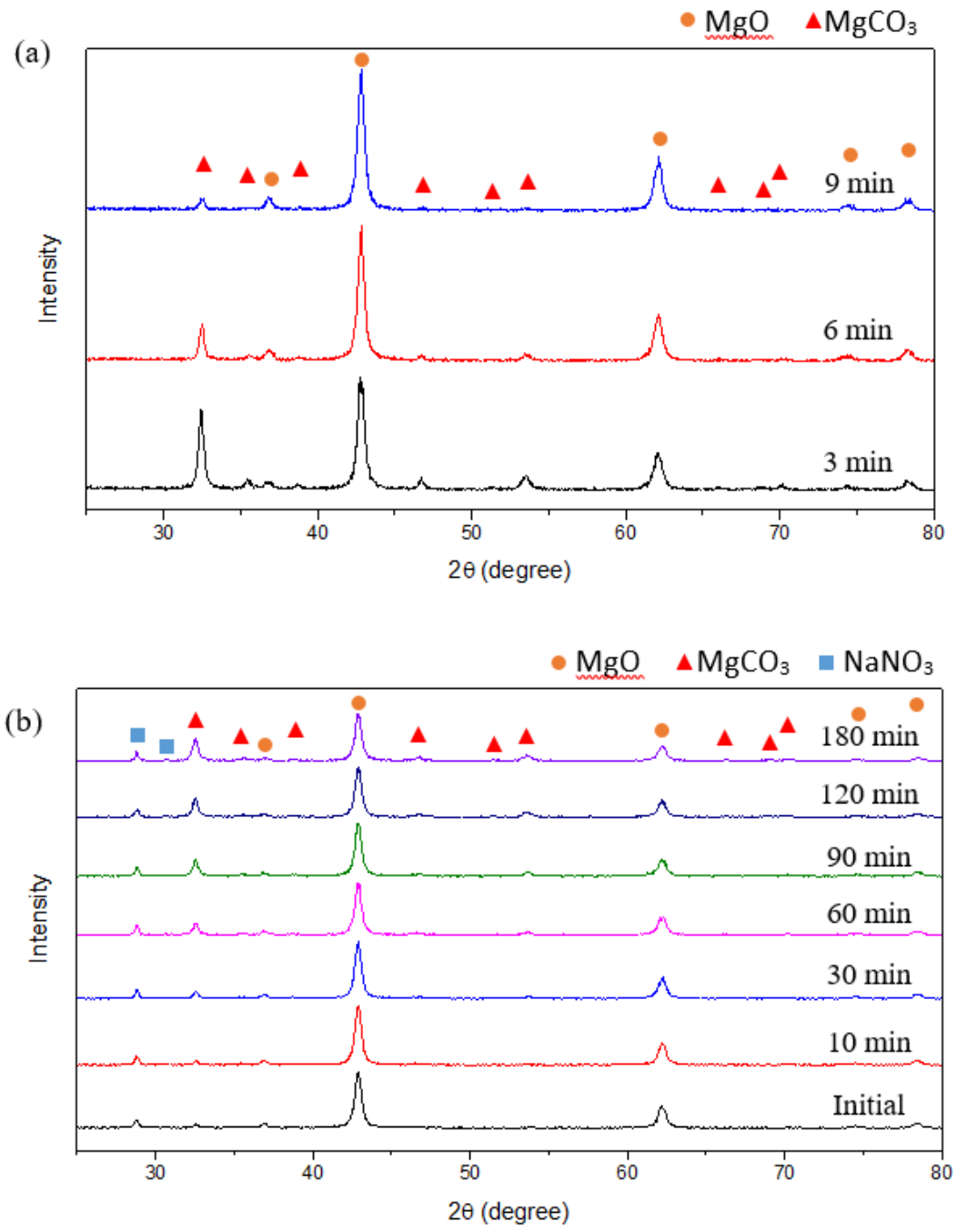

Figure A.6. In-situ XRD of MgO_$NaNO_3$_0.10 taken during (a) desorption at 350 °C under helium flow after 12 h exposure to 10% CO_2/He at 260 °C, and (b) readsorption of CO_2 after partial desorption at 260 °C.

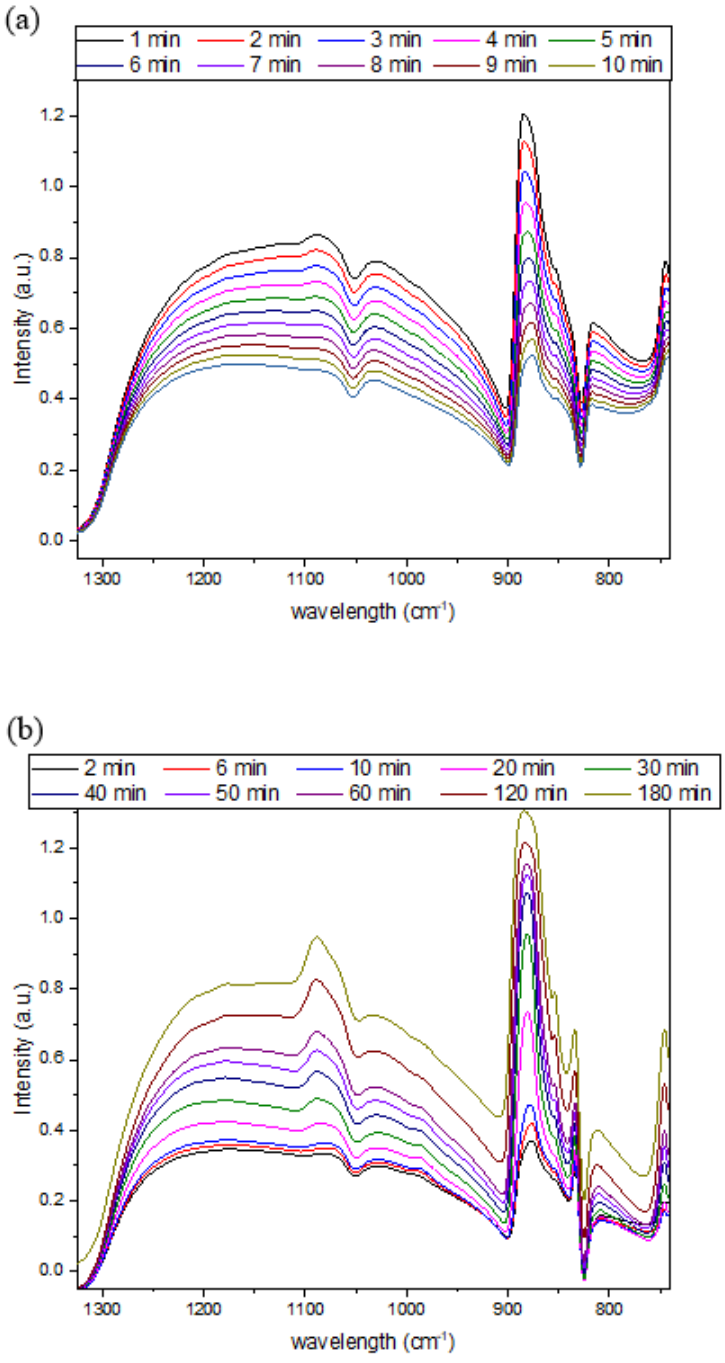

Figure A.7. In-situ FTIR spectra taken during (a) partial desorption at 350 °C under helium flow, and (b) readsorption at 260 °C after partial desorption, for the MgO_$NaNO_3$_0.10 sample.

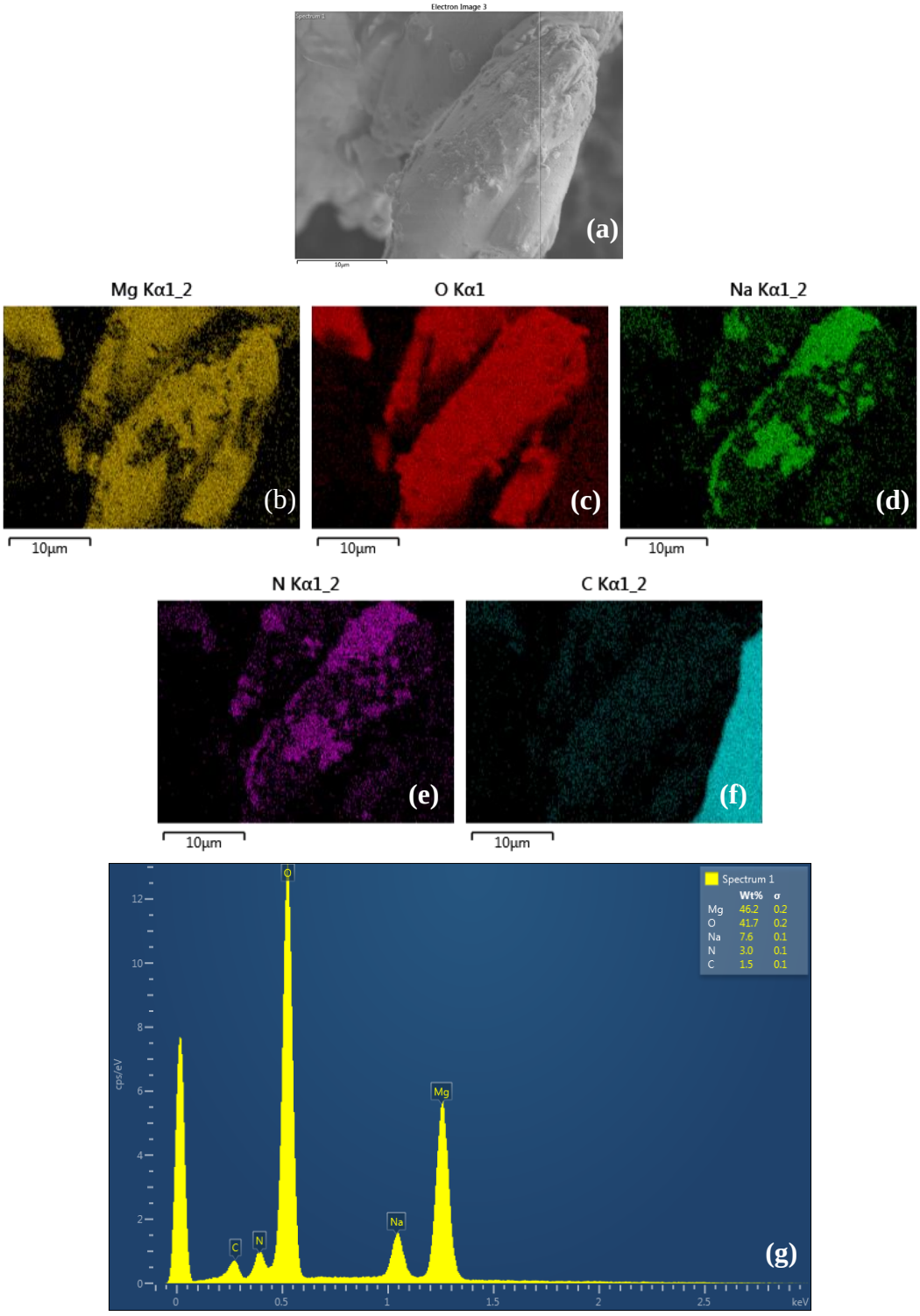

Figure A.8. (a) SEM image and elemental mapping of (b) Mg, (c) O, (d) Na, (e) N, (f) C, and (g) SEM-EDS spectrum of MgO_$NaNO_3$_0.10, as synthesized. It should be noted that a sorbent-rich portion of the image was selected for compositional analysis to minimize the carbon tape background.

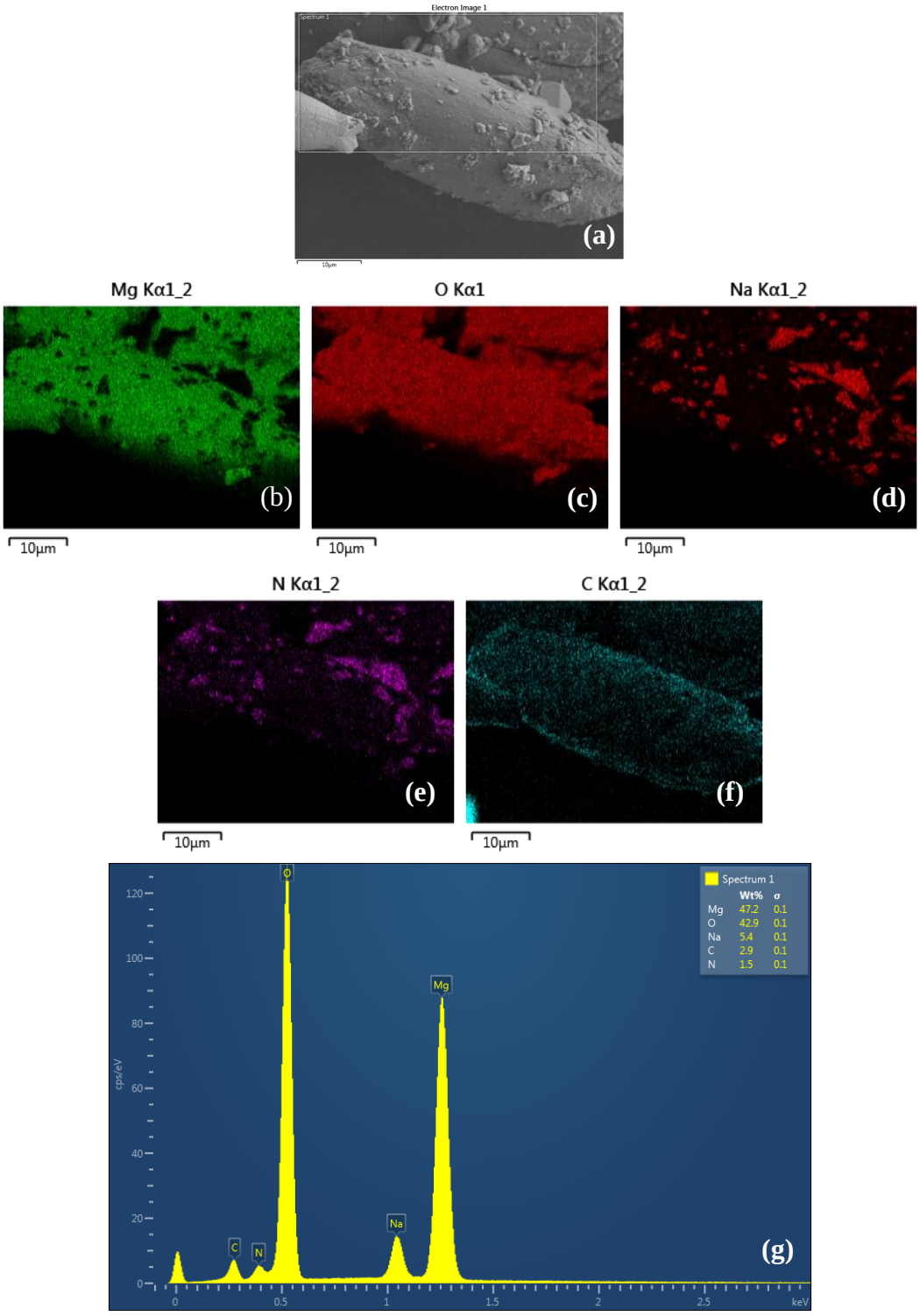

Figure A.9. (a) SEM image and elemental mapping of (b) Mg, (c) O, (d) Na, (e) N, (f) C, and (g) SEM-EDS spectrum of MgO_$NaNO_3$_0.10 after full desorption after 12 h exposure to 10% CO_2/He flow. It should be noted that a sorbent-rich portion of the image was selected for compositional analysis to minimize the carbon tape background.

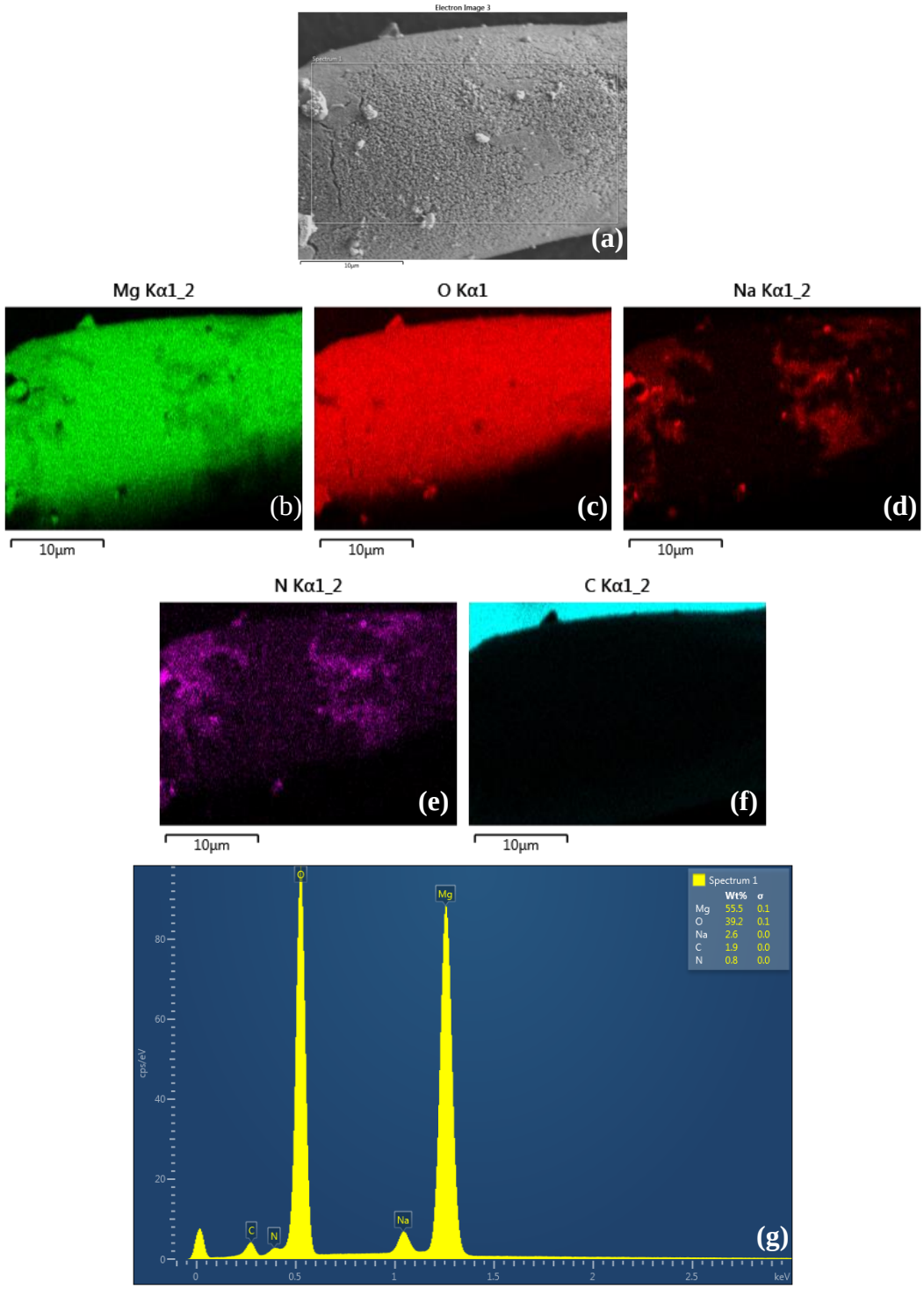

Figure A.10. (a) SEM image and elemental mapping of (b) Mg, (c) O, (d) Na, (e) N, (f) C, and (g) SEM-EDS spectrum of MgO_$NaNO_3$_0.10 after full desorption after 5 isothermal cycle. It should be noted that a sorbent-rich portion of the image was selected for com positional analysis to minimize the carbon tape background.

APPENDIX B. CHAPTER 3 SUPPORTING INFORMATION

B.1 Mass Transfer and Heat Transfer Limitation Analysis

Calculations were performed to evaluate the effects of potential mass transfer and heat transfer limitations. Internal mass transfer limitation was assessed by using the Weisz-Prater Criterion, as shown in Equation B.1.[1,2] The calculations were based on CO_2 parameters, because the CO_2 concentration ($6\% \leq C_{CO_2} \leq 14\%$) was much lower than H_2 concentration ($30\% \leq C_{H_2} \leq 50\%$) in all the runs. This specific sample calculation shows 6% CO_2 concentration over 5% $NaNO_3$/1% Ru/Al_2O_3, which gave the highest value for the Weisz-Prater parameter.

$$\varphi = -\frac{r_{obs} * \rho_p * R_p}{D_e * C_{AS}} \qquad \text{Eq. B.1}$$

The concentration of CO_2 at the external particle surface, C_{AS}, was 0.00245 mmol/mL. The radius of the catalyst particle, R_p, was 0.0138 cm. For calculation of the effective diffusivity, D_e, Knudsen diffusivity was calculated based on Equation B.2.

$$D_e = \frac{d}{3}\sqrt{\frac{8 * R * T}{\pi * M_A}} \qquad \text{Eq. B.2}$$

Pore diameter, d, was 2.50 x 10^{-8} m, which was obtained by N_2 physisorption measurement. Molecular mass, M_A, of 44.01 g/mol, temperature, T, of 573 K (300 °C), and gas constant, R, of 8.314 J/mol-K were used to obtain an effective diffusivity of 0.0438 cm^2/s. The rate observed, r_{obs} was 0.0102 mmol CO_2/s-g_{cat}. The bulk density of the catalyst, ρ_p, was 4 g/mL. The WPN parameter was calculated to be 0.072, which was much

smaller than 1. From this calculation, it was assumed that internal mass transfer limitations were negligible

External mass transfer limitation was evaluated by the Mears criterion, as shown in equation B.3. If M_{ext} is lower than 0.15, then external mass transfer limitations can be neglected.[3] It should be noted that for calculation of M_{ext}, H_2 parameters were used, because CO_2 reaction order was found to be negative for 5% $NaNO_3$/1%Ru/Al_2O_3 catalyst. To obtain the mass transfer coefficient, the Reynolds number was calculated using equation B.4.

$$M_{ext} = -\frac{r_{obs}*\rho_p*L*n}{k_c*C_{AS}} \qquad \text{Eq. B.3}$$

$$Re = \frac{2*U*L}{\nu} \qquad \text{Eq. B.4}$$

The superficial velocity, U, was 0.0202 m/s. L is particle size of the pellet, which was 0.0138 cm. Kinematic viscosity of N_2 (4.81 x 10^{-5} m^2/s) was used for conservative Re calculation, since the feed gas mixture was mostly composed of N_2 and H_2, but N_2 has lower kinematic viscosity leading to higher Re. Using such values, Re of 0.116 was obtained, which was much less than 1. This means the mass transfer coefficient could be estimated by equation B.5.

$$Sh = \frac{k_c*2*L}{D_e} = 2 \qquad \text{Eq. B.5}$$

The bulk diffusivity of H_2-N_2 was used as D_e in equation B.5, which was estimated to be 2.44 cm^2/s at 300 °C.[4] Using equation B.5, a mass transfer coefficient of 1.78 m/s was calculated. The density of the bed was 4 g/mL, and the reaction order with respect to

H_2 was 1.26. Using such values, Mears' criterion for external mass transfer limitations was calculated to be 9.75 x 10^{-4}, which is orders of magnitude smaller than 0.15, indicating external transfer limitations can be neglected. Heat transfer limitations were also evaluated by Mears' criterion, as shown in equation B.6.

$$M_{heat} = \frac{-R_{obs} * p_b * L * E_a * (-\Delta H_{rxn})}{R_g * h * T^2} \qquad \text{Eq. B.6}$$

For the heat of reaction, (ΔH_{rxn}), -165 kJ/mol was used, which corresponds to the heat of reaction for CO_2 methanation.[5] For activation energy, E_a, 78 kJ/mol was used, which was obtained in our experiment for the 5% $NaNO_3$/1% Ru/Al_2O_3 catalyst. Since Re was less than 1, the heat transfer coefficient could be calculated by equation B.7.

$$Nu = \frac{h * 2R}{k_t} = 2 \qquad \text{Eq.B.7}$$

The thermal conductivity, k_t, was estimated using the thermal conductivity of N_2 at 300 °C (43.3 mW/m*K). Using 8.314 J/mol*K as gas constant, a heat transfer coefficient of 0.315 kJ/s*m^2*K can be calculated from equation B.7. Then plugging all the obtained values into equation B.6, a Mears' criterion of 0.084 was obtained, which is smaller than 0.15, indicating heat transfer limitations can be neglected.

B.2 Calculation of absolute humidity

$$\text{Absolute Humidity}(\%) = \frac{\text{mass of dry vapor}}{\text{mass of dry gas}} * 100 = \frac{P_i * MW_i}{(P - P_i) * MW_{dry}} * 100 \qquad \text{Eq.B.8}$$

$P_i = partial\ pressure\ of\ water$

$MW_i = molecular\ weight\ of\ water$

$P = total\ pressure$

$MW_{dry} = molecular\ weight\ of\ dry\ gas$

A water bubbler is set at 54 °C, where the vapor pressure of water is 15.021 kPa. The total pressure is 101.325 kPa. Taking into account that the inlet dry gas is 10% CO_2/90% N_2, the absolute humidity is calculated as following.

$$\text{Absolute Humidity}(\%) = \frac{15.021\ kPa * 18.02 \frac{g}{mol}}{(101.325 - 15.021\ kPa) * 0.1 * 44.01 \frac{g}{mol} + (101.325 - 15.021) * 0.9 * 28.01 \frac{g}{mol}} * 100 \qquad \text{Eq. B.9}$$

B.3 Supplementary Experimental Data

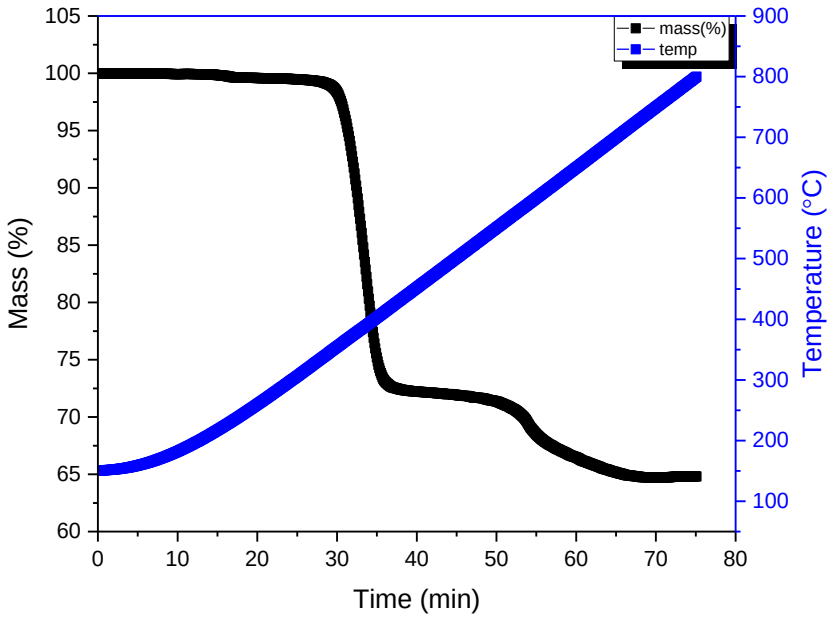

Figure B.1. TGA desorption curve for CO_2-rich 17% $NaNO_3$/MgO sample from 150 °C to 800 °C under N_2 flow. CO_2 rich 17% $NaNO_3$/MgO was obtained by exposing 17% $NaNO_3$/MgO sorbent to a flow of 15% H_2O/N2 for 2 h followed by 12 h of 10% CO_2/15%H_2O/N_2 flow for 12 h at 300

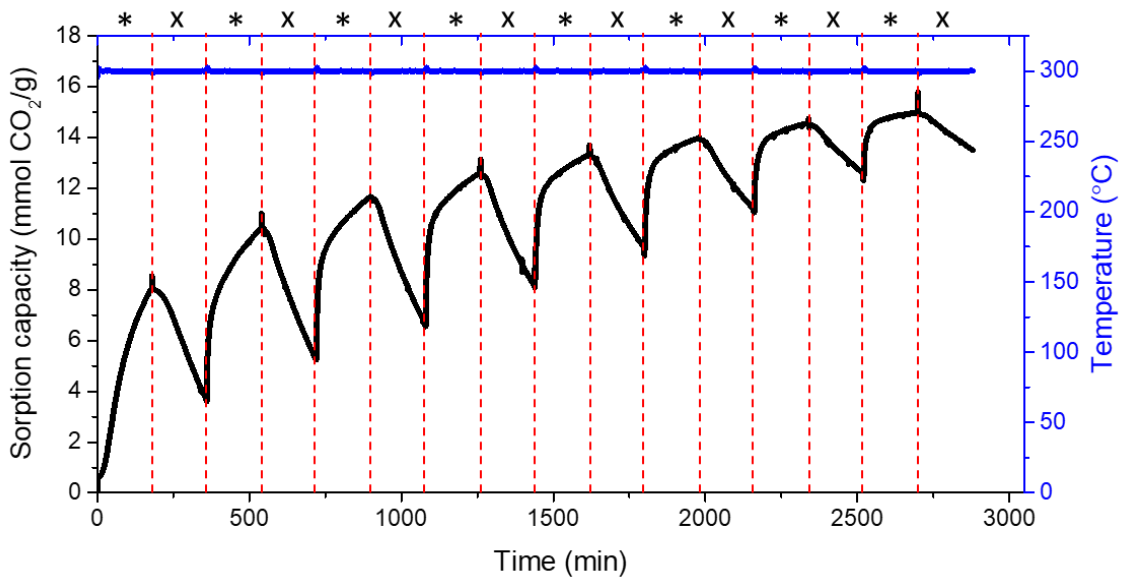

Figure B.2. Sorption and desorption of CO_2 at isothermal conditions of 300 °C by switching the feed gas between 10% CO_2/15%H_2O/N_2 flow and N_2 flow. Change in feed occurred every 3 h. Asterisk (*) notes 10% CO_2/15%H_2O/N_2 flow, and the 'x' sign notes N_2 flow.

Table B.1. Sorption and desorption capacity during each cycle over 8 cycles shown in Figure B.1.

Cycle #	1	2	3	4	5	6	7	8
Sorption capacity (mmol CO_2/g)	7.6	6.7	6.3	6.0	5.2	4.3	3.4	2.5
Desorption capacity (mmol CO_2/g)	4.3	5.1	5.1	4.5	3.7	2.8	2.1	1.5
% desorbed	57	76	81	75	71	65	62	60

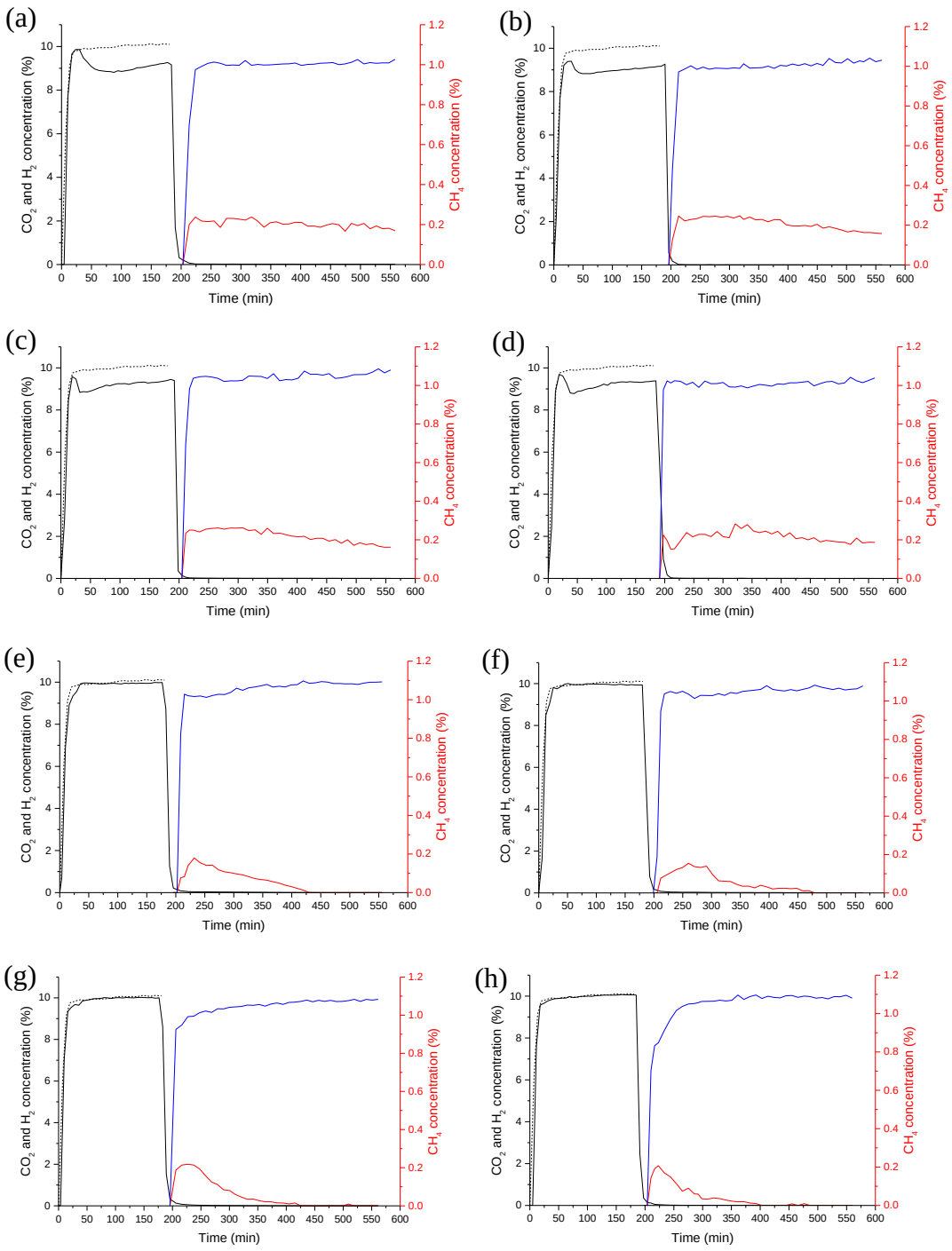

Figure B.3. Concentration of CO_2, H_2, and CH_4 in the outlet stream during 1 cycle of combined capture and methanation for (a) 0.25%Ru_2B, (b) 0.5%Ru_2B, (c) 1%Ru_2B, (d), 2%Ru_2B (e) 0.25%Ru_MP, (f) 0.5%Ru_MP, (g) 1%Ru_MP, and (h) 2%Ru_MP. Solid black line represents CO_2, blue line represents H_2, red line represents CH_4 for each run with catalytic sorbent. Dotted black line represents CO_2 at empty reactor, which was used to calculate amount of CO_2 captured.

Table B.2. Fraction of captured CO_2 that was utilized for methane production via conversion of CO_2 in the methanation step.

Sample	x% Ru/Al_2O_3_2B				x% Ru/Al_2O_3_MP			
	2%	1%	0.5%	0.25%	2%	1%	0.5%	0.25%
Fraction of captured CO_2 utilized (%)	62	62	55	56	97	119	113	96
Conversion of CO_2 in methanation step (%)	96	95	95	89	71	76	70	75

Utilization above 100% is reflective of levels of experimental uncertainty.

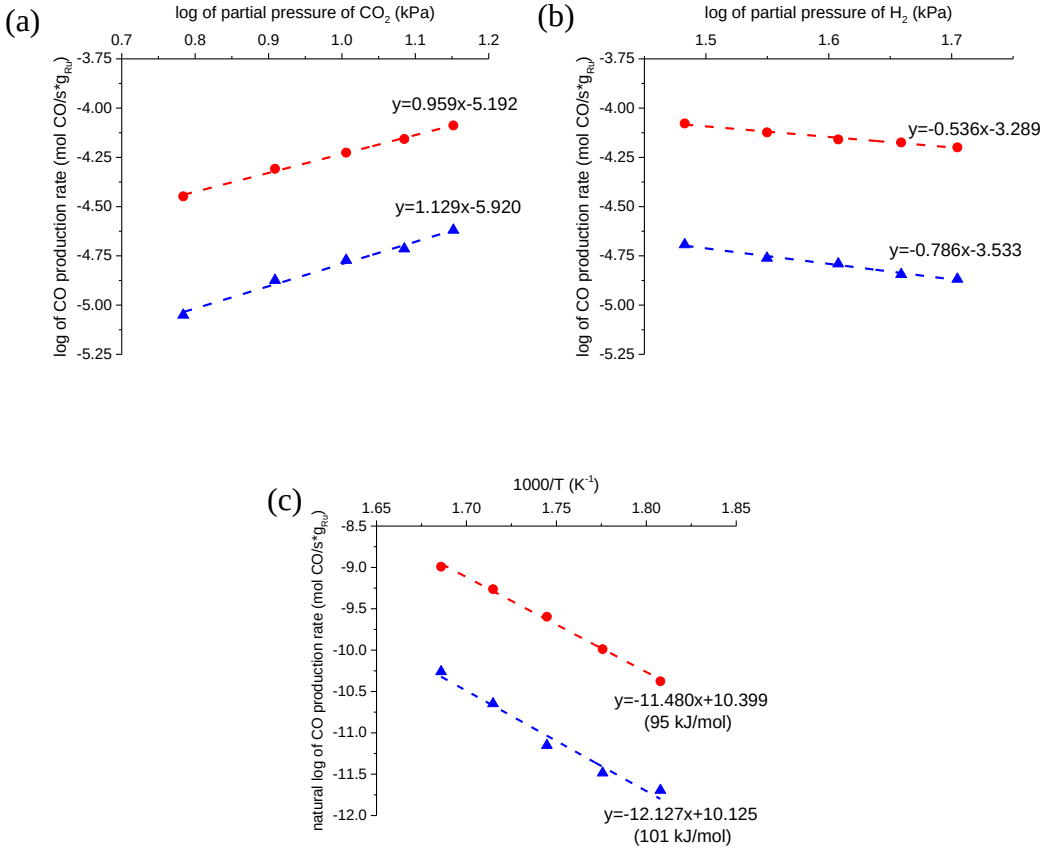

Figure B.4. (a) CO_2 reaction orders, (b) H_2 reaction orders, and (c) activation energies measured for CO formation over 1%Ru/Al_2O_3_MP (red circle) and 5% $NaNO_3$/1%Ru/Al_2O_3 (blue triangle).

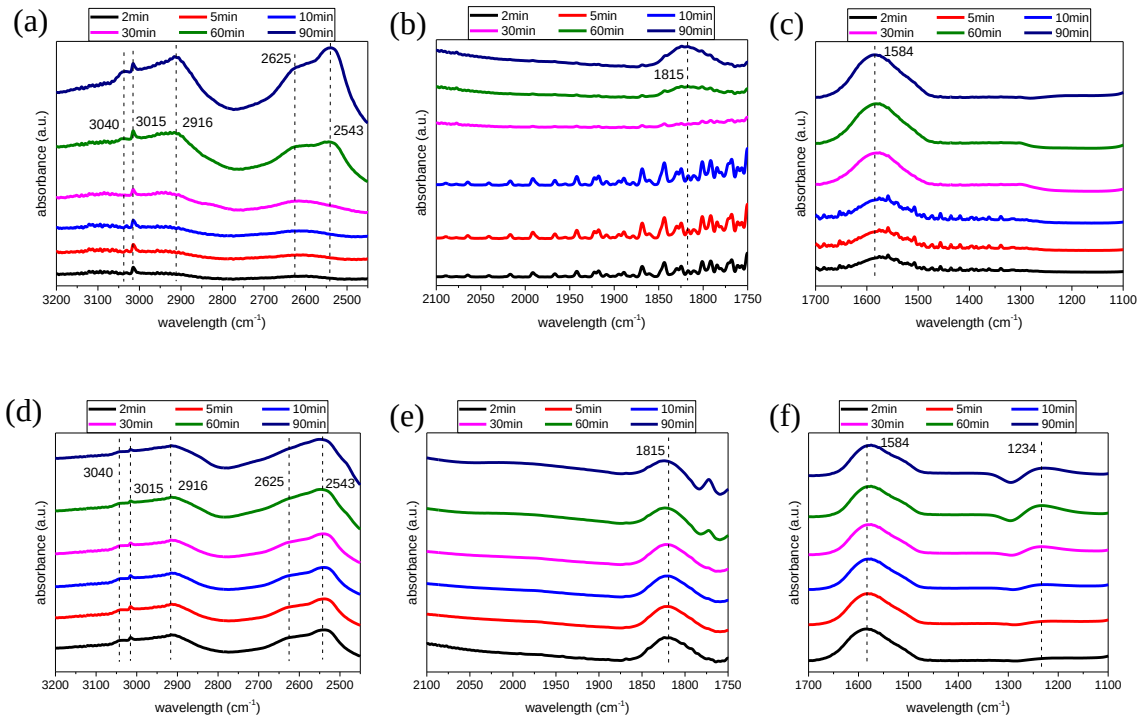

Figure B.5. FTIR spectra of 1% Ru/Al_2O_3_MP during CO_2 methanation under 10% CO_2/40% H_2/N_2 at 300 °C (a) from 2450 cm^{-1} to 3200 cm^{-1}, (b) from 1750 cm^{-1} to 2100 cm^{-1}, and (c) from 1100 cm^{-1} to 1700 cm^{-1} and after feed switch to 40% H_2/N_2 (d) from 2450 cm^{-1} to 3200 cm^{-1}, (e) from 1750 cm^{-1} to 2100 cm^{-1}, and (f) from 1100 cm^{-1} to 1700 cm^{-1}.

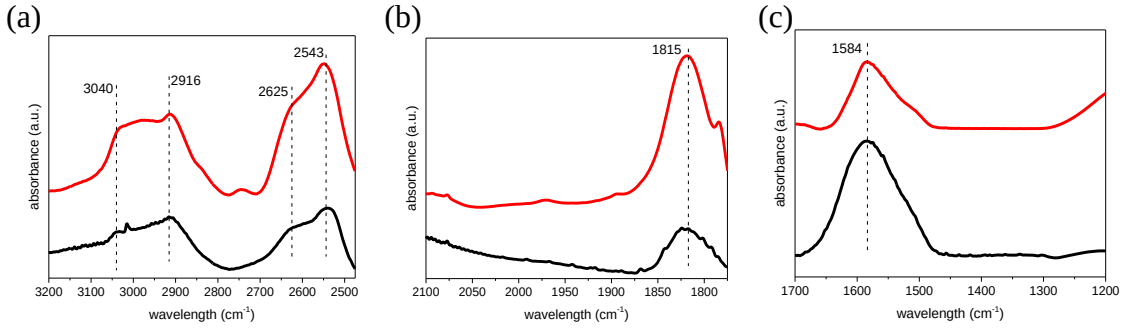

Figure B.6. FTIR spectra of 1% Ru/Al_2O_3_MP (black curve) after 90 min of exposure to 10% CO_2/40%H_2/N_2, and 17% $NaNO_3$/MgO (red curve) after 90 min of exposure to 10% CO_2/N_2 at 300 °C (a) from 2475 cm^{-1} to 3200 cm^{-1}, (b) from 1775 cm^{-1} to 2100 cm^{-1}, and (c) from 1200 cm^{-1} to 1700 cm^{-1}.

B.4 Rate Law Derivation for 1% Ru/Al_2O_3

$$[H*] = K_1^{0.5}[H_2]^{0.5}[*] \quad \text{Eq.B.4.1}$$

$$[CO_2*] = K_2[CO_2][*] \quad \text{Eq.B.4.2}$$

$$[CO*] = \frac{K_3[CO_2*][*]}{[O*]} = \frac{K_2K_3[CO_2][*]^2}{[O*]} \quad \text{Eq.B.4.3}$$

$$[O*] = \frac{[OH*][*]}{K_9[H*]} \quad \text{Eq.B.4.4}$$

$$\frac{d[O*]}{dt} = k_3[CO_2*][*] - k_{-3}[CO*][O*] + k_4[CO*][H*] - k_9[O*][H*] + k_{-9}[OH*][*] = 0 \quad \text{Eq.B.4.5}$$

$$\frac{d[OH*]}{dt} = k_9[O*][H*] - k_{-9}[OH*][*] - k_{10}[OH*][H*] = 0 \quad \text{Eq.B.4.6}$$

$$\frac{d[CO*]}{dt} = k_3[CO_2*][*] - k_{-3}[CO*][O*] - k_4[CO*][H*] = 0 \quad \text{Eq.B.4.7}$$

Plugging in Eq.B.4.6 and Eq.B.4.7 into Eq.B.4.5,

$$\frac{2k_4}{k_{10}}[CO*] = [OH*] \quad \text{Eq.B.4.8}$$

Plugging in Eq.B.4.8 into Eq.B.4.4,

$$[O*] = \frac{2k_4[CO*][*]}{k_{10}K_9[H*]} = \frac{2k_4[CO*]}{k_{10}K_1^{0.5}K_9[H_2]^{0.5}} \quad \text{Eq. B.4.9}$$

Plugging in Eq.B.4.9 to Eq.B.4.3, $[CO*]$ can be solved.

$$[CO*] = \sqrt{\frac{k_{10}{K_1}^{0.5}K_2K_3K_9}{2k_4}}[H_2]^{0.25}[CO_2]^{0.5}[*] \quad \text{Eq. B.4.10}$$

$$r_4 = k_4[CO*][H*] = \sqrt{\frac{k_4k_{10}{K_1}^{1.5}K_2K_3K_9}{2}}[H_2]^{0.75}[CO_2]^{0.5}[*]^2 \quad \text{Eq. B.4.11}$$

Assuming $[CO_2*]$ quickly dissociates, most abundant intermediates are $[H*]$ and $[CO*]$.

$$[*]_{total} = [*] + [H*] + [CO*] \quad \text{Eq. B.4.12}$$

$$[*]_{total} = [*](1 + K_1^{0.5}[H_2]^{0.5} + \sqrt{\frac{k_{10}{K_1}^{0.5}K_2K_3K_9}{2k_4}}[H_2]^{0.25}[CO_2]^{0.5}) \quad \text{Eq. B.4.13}$$

$$[*] = \frac{[*]_{total}}{1+K_1^{0.5}[H_2]^{0.5}+\sqrt{\frac{k_{10}{K_1}^{0.5}K_2K_3K_9}{2k_4}}[H_2]^{0.25}[CO_2]^{0.5}} \quad \text{Eq. B.4.14}$$

$$r_4 = \frac{\sqrt{\frac{k_4k_{10}{K_1}^{1.5}K_2K_3K_9}{2}}[H_2]^{0.75}[CO_2]^{0.5}{[*]_{total}}^2}{(1+K_1^{0.5}[H_2]^{0.5}+\sqrt{\frac{k_{10}{K_1}^{0.5}K_2K_3K_9}{2k_4}}[H_2]^{0.25}[CO_2]^{0.5})^2} \quad \text{Eq. B.4.15}$$

B.5 Rate Law Derivation for 5%$NaNO_3$/1% Ru/Al_2O_3

$$[H*] = K_1^{0.5}[H_2]^{0.5}[*] \quad \text{Eq. B.5.1}$$

$$[CO2-S] = K_2[CO2][S] \quad \text{Eq. B.5.2}$$

$$[HCO_2-S] = K_1^{0.5}K_2K_3[H_2]^{0.5}[CO2][S] \quad \text{Eq. B.5.3}$$

$$[HCO-S] = \frac{K_1K_2K_3K_4[H_2][CO2][S][*]}{[OH*]} \quad \text{Eq. B.5.4}$$

$$[CO*] = \frac{K_5[HCO-S][*]^2}{[H*][S]} \quad \text{Eq. B.5.5}$$

$$[HCO*] = \frac{K_6[CO*][H*]}{[*]} \quad \text{Eq. B.5.6}$$

$$[H_2CO*] = \frac{K_7[HCO*][H*]}{[*]} \quad \text{Eq. B.5.7}$$

$$\frac{d[OH*]}{\mathrm{dt}} = k_4[HCO_2-S][H*] - k_{-4}[HCO-S][OH*] + k_8[H_2CO*][H*] - k_{12}[OH*][H*] \quad \text{Eq. B.5.8}$$

$$\frac{d[HCO-S]}{\mathrm{dt}} = k_4[HCO_2-S][H*] - k_{-4}[HCO-S][OH*] - k_5[HCO-S][H*]^2 + k_{-5}[H*][CO*][S] \quad \text{Eq. B.5.9}$$

$$\frac{d[CO*]}{\mathrm{dt}} = k_5[HCO-S][H*]^2 - k_{-5}[H*][CO*][S] - k_6[CO*][H*] + k_{-6}[HCO*][*] \quad \text{Eq. B.5.10}$$

$$\frac{d[HCO*]}{\mathrm{dt}} = k_6[CO\ *][H\ *] - k_{-6}[HCO\ *][*] - k_7[HCO\ *][H\ *] + k_{-7}[H_2CO\ *][*]$$

Eq. B.5.11

$$\frac{d[H_2CO*]}{\mathrm{dt}} = k_7[HCO\ *][H\ *] - k_{-7}[H_2CO\ *][*] - k_8[H_2CO\ *][H\ *] \qquad \text{Eq. B.5.12}$$

Using Eq. B.5.9 - Eq. B.5.12,

$$k_4[HCO_2 - S][H\ *] - k_{-4}[HCO - S][OH\ *] = k_8[H_2CO\ *][H\ *] \qquad \text{Eq. B.5.13}$$

Plug Eq. B.5.13 into Eq. B.5.8,

$$\frac{2k_8}{k_{12}}[H_2CO\ *] = [OH\ *] \quad \text{Eq. B.5.14}$$

Plug Eq. B.5.14 into $[HCO - S]$, then $[H_2CO\ *]$ can be solved using Eq. B.5.7:

$$[HCO - S] = \frac{K_1K_2K_3K_4[H_2][CO2][S][*]}{[OH*]} = \frac{k_{12}K_1K_2K_3K_4[H_2][CO2][S][*]}{2k_8[H_2CO*]} \qquad \text{Eq. B.5.15}$$

$$[CO\ *] = \frac{K_5[HCO-S][*]^2}{[H*][S]} = \frac{k_{12}K_1K_2K_3K_4K_5[H_2][CO2][*]^3}{2k_8[H_2CO*][H*]} \qquad \text{Eq. B.5.16}$$

$$[HCO\ *] = \frac{K_6[CO*][H*]}{[*]} = \frac{k_{12}K_1K_2K_3K_4K_5K_6[H_2][CO2][*]^2}{2k_8[H_2CO*]} \qquad \text{Eq. B.5.17}$$

$$[H_2CO\ *] = \frac{K_7[HCO*][H*]}{[*]} = \frac{k_{12}{K_1}^{1.5}K_2K_3K_4K_5K_6K_7[H_2]^{1.5}[CO_2][*]^2}{2k_8[H_2CO*]} \qquad \text{Eq. B.5.18}$$

$$[H_2CO*] = \sqrt{\frac{k_{12}{K_1}^{1.5}K_2K_3K_4K_5K_6K_7}{2k_8}}[H_2]^{0.75}[CO_2]^{0.5}[*] \quad \text{Eq. B.5.19}$$

We can then solve for $[HCO*]$ and $[CO*]$

$$[HCO*] = \sqrt{\frac{k_{12}{K_1}^{0.5}K_2K_3K_4K_5K_6}{2k_8K_7}}[H_2]^{0.25}[CO_2]^{0.5}[*] \quad \text{Eq. B.5.20}$$

$$[CO*] = \sqrt{\frac{k_{12}K_2K_3K_4K_5}{2k_8{K_1}^{0.5}K_6K_7}}[H_2]^{-0.25}[CO_2]^{0.5}[*] \quad \text{Eq. B.5.21}$$

$$r_8 = k_8[H_2CO*][H*] \quad \text{Eq. B.5.22}$$

$$r_8 = \sqrt{\frac{k_8k_{12}{K_1}^{1.5}K_2K_3K_4K_5K_6K_7}{2}}[H_2]^{1.25}[CO_2]^{0.5}[*]^2 \quad \text{Eq. B.5.23}$$

$$[*]_{\text{total}} = [*] + [\text{H}*] + [\text{CO}*] + [\text{HCO}*] + [\text{H}_2\text{CO}*] \quad \text{Eq. B.5.24}$$

$$[*]_{\text{total}} = [*](1 + \text{K}_1^{0.5}[\text{H}_2]^{0.5} + \sqrt{\frac{k_{12}K_2K_3K_4K_5}{2k_8{K_1}^{0.5}K_6K_7}}[H_2]^{-0.25}[CO_2]^{0.5} +$$

$$\sqrt{\frac{k_{12}{K_1}^{0.5}K_2K_3K_4K_5K_6}{2k_8K_7}}[H_2]^{0.25}[CO_2]^{0.5} + \sqrt{\frac{k_{12}{K_1}^{1.5}K_2K_3K_4K_5K_6K_7}{2k_8}}[H_2]^{0.75}[CO_2]^{0.5})$$

Eq. B.5.25

$$[*] = \frac{[*]_{\text{total}}}{(1+\mathrm{K}_1^{0.5}[\mathrm{H}_2]^{0.5}+\sqrt{\frac{k_{12}K_2K_3K_4K_5}{2k_8{K_1}^{0.5}K_6K_7}}[H_2]^{-0.25}[CO_2]^{0.5}+ \sqrt{\frac{k_{12}{K_1}^{0.5}K_2K_3K_4K_5K_6}{2k_8K_7}}[H_2]^{0.25}[CO_2]^{0.5}+\sqrt{\frac{k_{12}{K_1}^{1.5}K_2K_3K_4K_5K_6K_7}{2k_8}}[H_2]^{0.75}[CO_2]^{0.5})}$$

Eq. B.5.26

$$r_8 = \frac{\sqrt{\frac{k_8k_{12}{K_1}^{1.5}K_2K_3K_4K_5K_6K_7}{2}}[H_2]^{1.25}[CO_2]^{0.5}{[*]_{\text{total}}}^2}{(1+\mathrm{K}_1^{0.5}[\mathrm{H}_2]^{0.5}+\sqrt{\frac{k_{12}K_2K_3K_4K_5}{2k_8{K_1}^{0.5}K_6K_7}}[H_2]^{-0.25}[CO_2]^{0.5}+ \sqrt{\frac{k_{12}{K_1}^{0.5}K_2K_3K_4K_5K_6}{2k_8K_7}}[H_2]^{0.25}[CO_2]^{0.5}+\sqrt{\frac{k_{12}{K_1}^{1.5}K_2K_3K_4K_5K_6K_7}{2k_8}}[H_2]^{0.75}[CO_2]^{0.5})^2}$$

Eq. B.5.27

B.6 Raw Data for 5 Cycles of Capture and Conversion

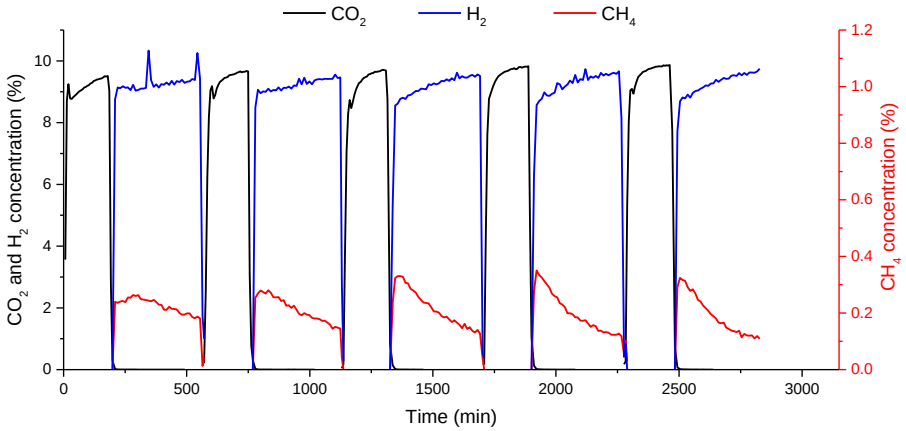

Figure B.7. Concentration of CO_2, H_2, and CH_4 in the outlet stream during 5 cycles of combined capture and methanation. CO_2 sorption step was 3 h and methanation step was 6 h. There was a 15 min N_2 purge step between switching feed gas. Temperature was isothermal at 300 °C throughout the entire 5 cycles.

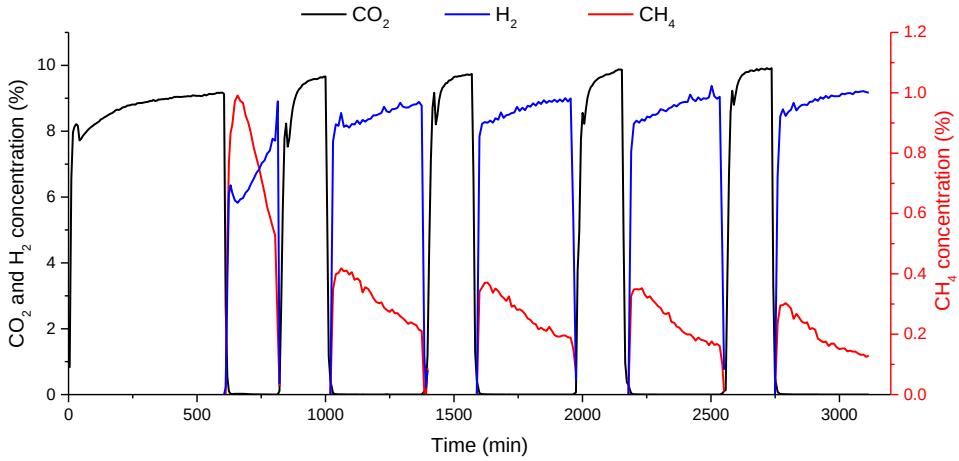

Figure B.8. Concentration of CO_2, H_2, and CH_4 in the outlet stream during 5 cycles of combined capture and methanation. In the first cycle, the CO_2 sorption step was 10 h and the methanation step was 3 h at 320 °C. For the remainder of 4 cycles, the temperature was isothermal at 300 °C, with a CO_2 sorption step of 3 h and a methanation step of 6 h. There was a 15 min N_2 purge step between switching feed gases.

B.7 Reference

(1) Weisz, P. B.; Prater, C. D. Interpretation of Measurements in Experimental Catalysis. *Adv. Catal.* **1954**, *6*, 143–196.

(2) Mondal, S.; Malviya, H.; Biswas, P. Kinetic Modelling for the Hydrogenolysis of Bio-Glycerol in the Presence of a Highly Selective Cu–Ni–Al_2O_3 Catalyst in a Slurry Reactor. *React. Chem. Eng.* **2019**, No. 3, 595–609.

(3) Mohagheghi, M.; Bakeri, G.; Saeedizad, M. Study of the Effects of External and Internal Diffusion on the Propane Dehydrogenation Reaction over Pt-Sn/Al_2O_3 Catalyst. *Chem. Eng. Technol.* **2007**, *30* (12), 1721–1725.

(4) Ellis, C. S.; Holsen, J. N. DIFFUSION COEFFICIENTS FOR HELIUM-NITROGEN AND NITROGEN-CARBON DIOXIDE AT ELEVATED TEMPERATURES. *Ind. Eng. Chem. Fundam.* **1969**, *8* (4), 787–791.

(5) Ashok, J.; Pati, S.; Hongmanorom, P.; Tianxi, Z.; Junmei, C.; Kawi, S. A Review of Recent Catalyst Advances in CO_2 Methanation Processes. *Catal. Today* **2020**, *356* (July), 471–489.

APPENDIX C. CHAPTER 4 SUPPORTING INFORMATION

C.1 TEM Images and Particle Size Distribution Analysis

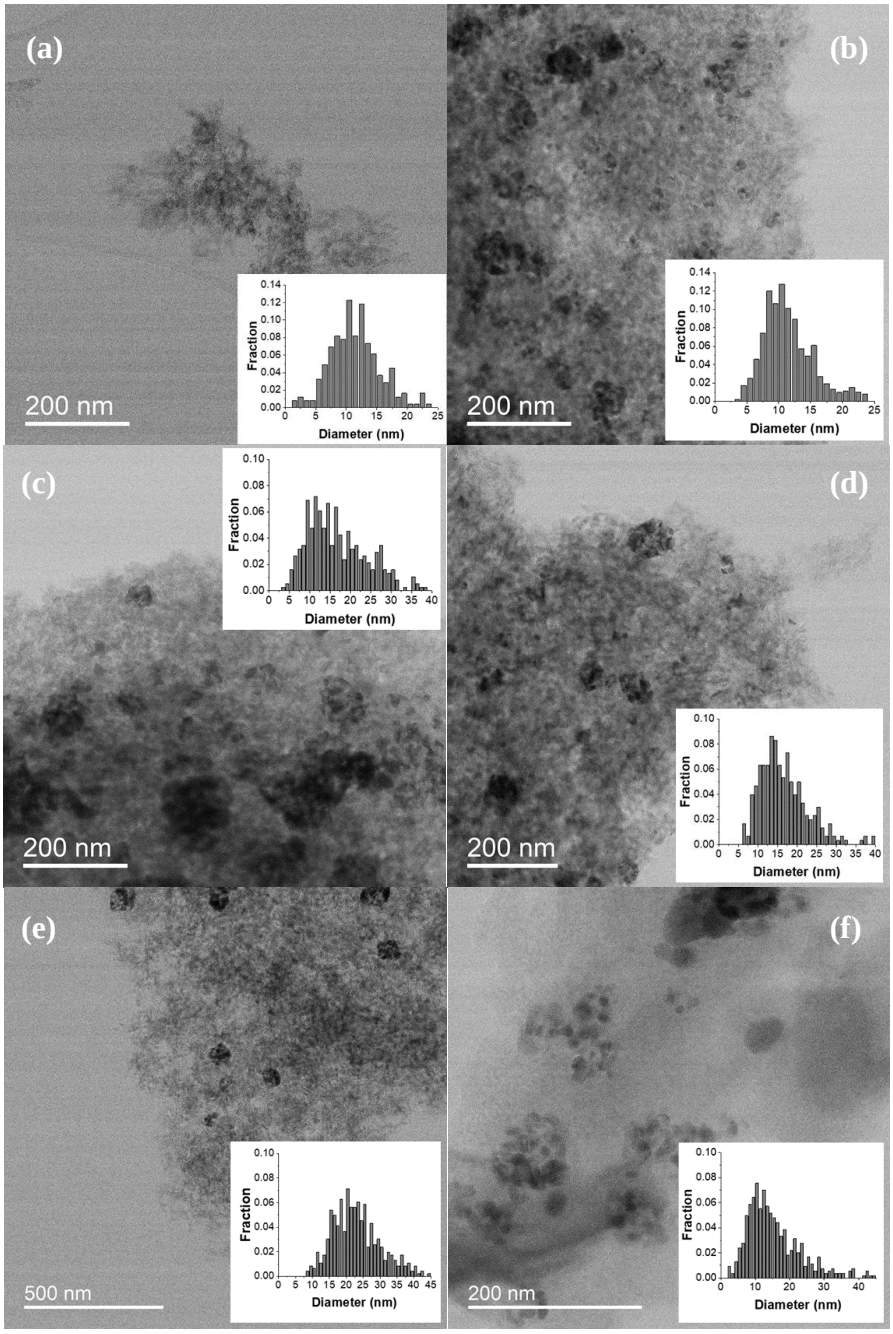

Figure C.1. TEM images of (a) 1%Ru/Al_2O_3, (b) 5%Ru/Al_2O_3, (c) $NaNO_3$/1%Ru/Al_2O_3, (d) $NaNO_3$/5%Ru/Al_2O_3, (e) 1%Ru/Al_2O_3 after additional calcination, and (f) 5%Ru/Al_2O_3 after additional calcination.

Table C.1. Metal dispersion of different catalysts measured by CO chemisorption, assuming stoichiometry of Ru/CO = 1.

	Dispersion - CO chemisorption (%)
1% Ru/Al_2O_3	9.3
5% Ru/Al_2O_3	8.6
$NaNO_3$/1% Ru/Al_2O_3	5.3
$NaNO_3$/5% Ru/Al_2O_3	4.6
1% Ru/Al_2O_3_H_2O	4.7
5% Ru/Al_2O_3_H_2O	5.0

C.2 In-situ DRIFT Measurements for Catalysts of 1% Ruthenium Loading

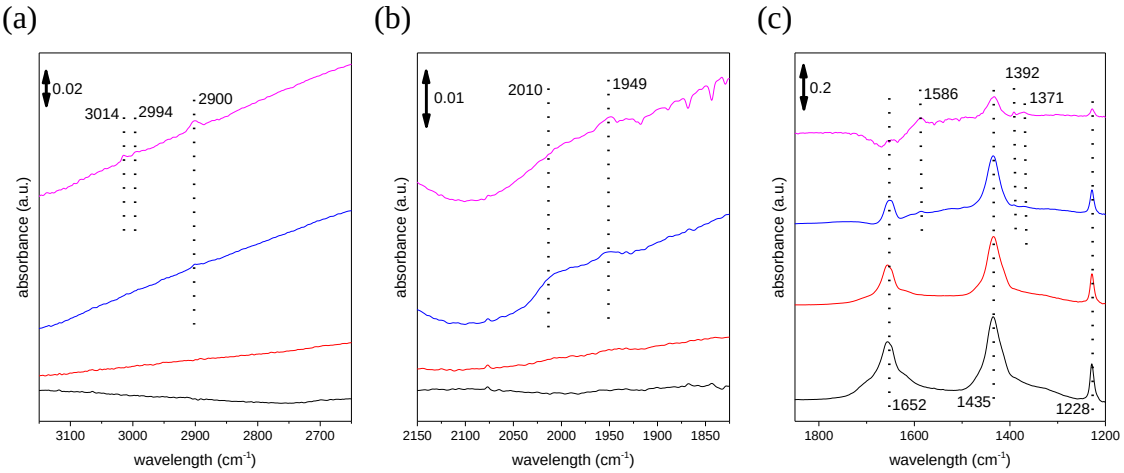

Figure C.2. DRIFT spectra taken over 1% Ru/Al_2O_3 under 5%CO_2/20%H_2/N_2 flow at 40 mL/min at temperatures of 50 °C (black), 100 °C (red), 200 °C (blue), 300 °C (pink) in the wavelength range of (a) 850 cm^{-1} to 2150 cm^{-1}, (b) 1800 cm^{-1} to 2150 cm^{-1}, and (c) 2650 cm^{-1} to 3150 cm^{-1}.

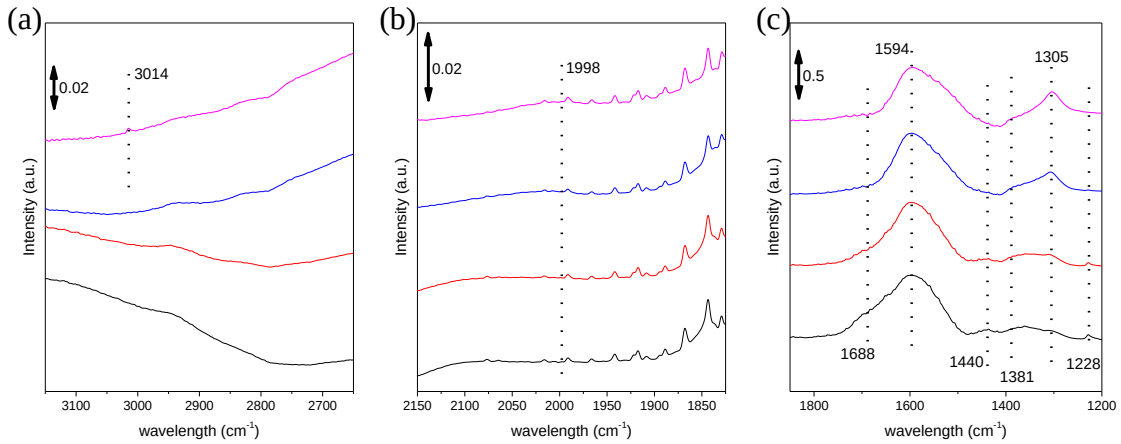

Figure C.3. DRIFT spectra taken over $NaNO_3$/1% Ru/Al_2O_3 under 5%CO_2/20%H_2/N_2 flow at 40 mL/min at temperatures of 50 °C (black), 100 °C (red), 200 °C (blue), 300 °C (pink) at a wavelength range of (a) 850 cm^{-1} to 2150 cm^{-1}, (b) 1800 cm^{-1} to 2150 cm^{-1}, and (c) 2650 cm^{-1} to 3150 cm^{-1}.

C.3 Transient Isotopic Experiment Catalysts of 1% Ruthenium Loading

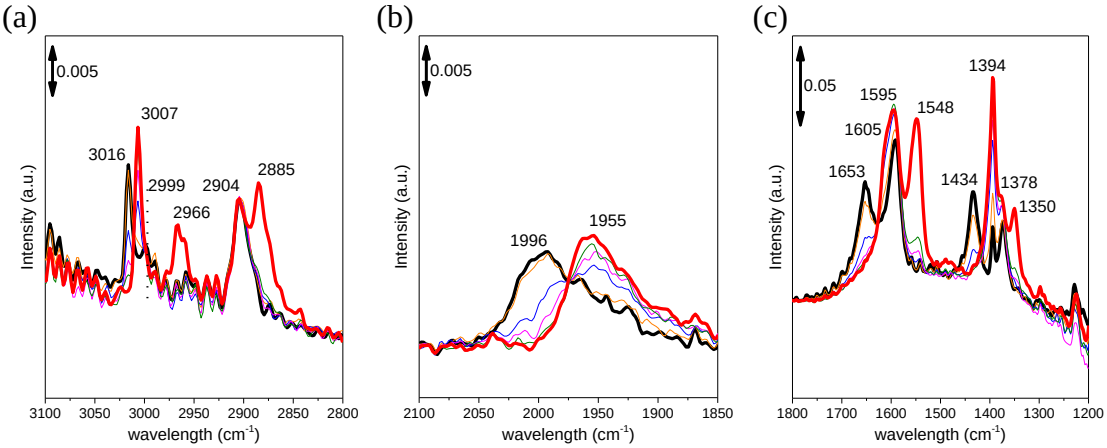

Figure C.4. In situ DRIFT spectra taken over 1% Ru/Al_2O_3 catalysts at a wavelength range of (a) 850 cm^{-1} to 2150 cm^{-1}, (b) 1800 cm^{-1} to 2150 cm^{-1}, and (c) 2650 cm^{-1} to 3150 cm^{-1} at a temperature of 260 °C under flow of 5% $^{12}CO_2$/20% H_2/N_2 (black, thickened) and after the switch to 5% $^{13}CO_2$/20% H_2/N_2 flow. (28 s (orange), 56 s (blue), 85 s (pink), 113 s (green), and 8 min (red, thickened)).

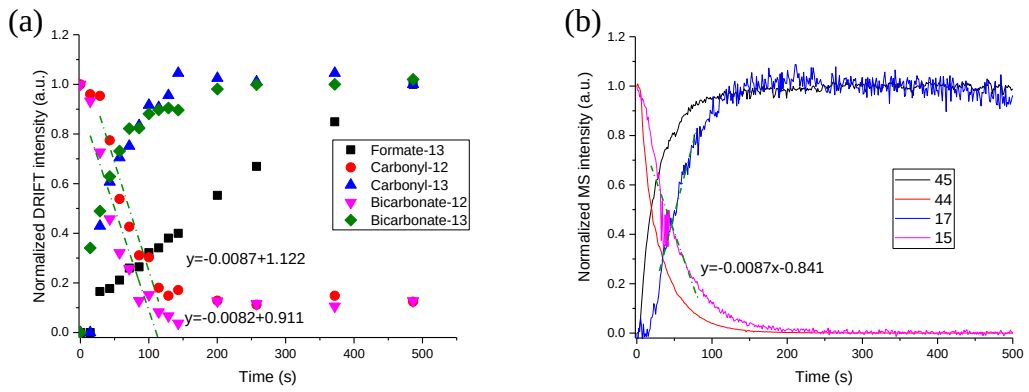

Figure C.5. (a) Change in normalized DRIFT spectral intensity of observed surface species and (b) change in normalized mass spectroscopy intensity of $^{12}CO_2$, $^{13}CO_2$, $^{12}CH_4$, and $^{13}CH_4$, after switching from 10% $^{12}CO_2$/40% H_2/He flow to 10% $^{13}CO_2$/40% H_2/He flow over 1%Ru/Al_2O_3 catalyst at a temperature of 260 °C. Total flow rate was constant at 40 mL/min.

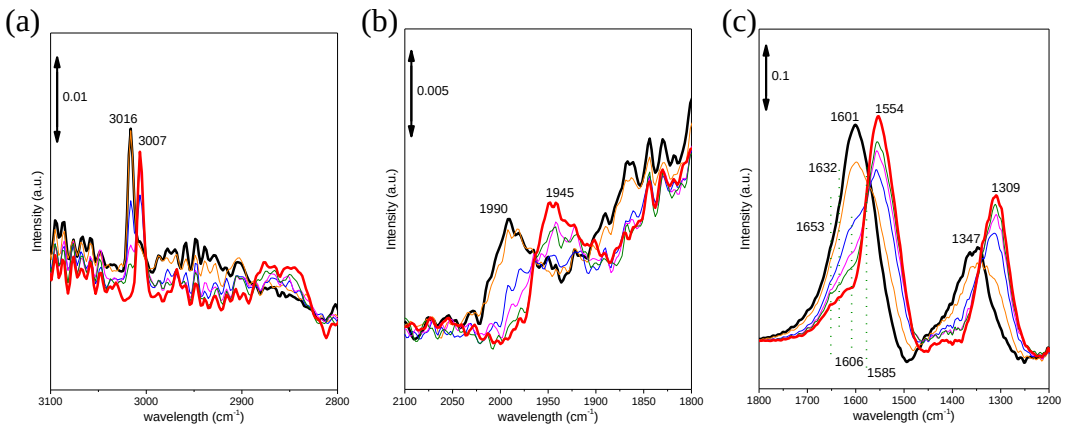

Figure C.6. In situ DRIFT spectra taken over $NaNO_3$/1% Ru/Al_2O_3 catalysts at a wavelength range of (a) 850 cm^{-1} to 2150 cm^{-1}, (b) 1800 cm^{-1} to 2150 cm^{-1}, and (c) 2650 cm^{-1} to 3150 cm^{-1} at a temperature of 260 °C under a flow of 5% $^{12}CO_2$/20% H_2/N_2 (black, thickened) and after switch to 5% $^{13}CO_2$/20% H_2/N_2 flow. (28 s (orange), 56 s (blue), 85 s (pink), 113 s (green), and 8 min (red, thickened)).

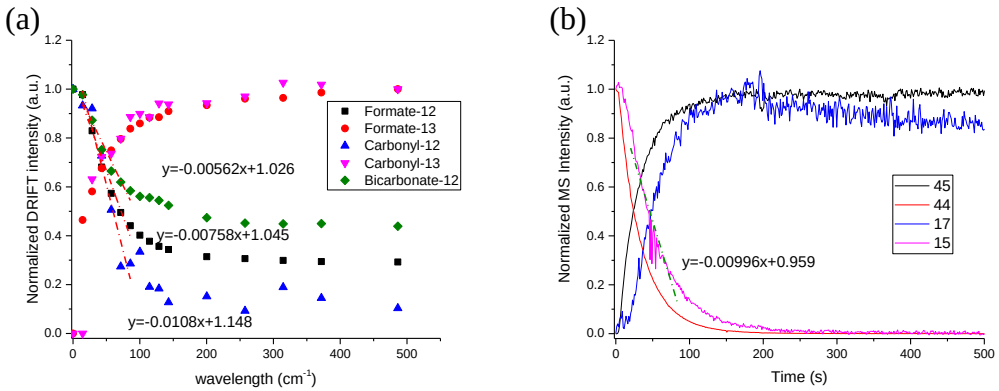

Figure C.7. (a) Change in normalized DRIFT spectral intensity of observed surface species and (b) change in normalized mass spectroscopy intensity of $^{12}CO_2$, $^{13}CO_2$, $^{12}CH_4$, and $^{13}CH_4$, after switching from 10% $^{12}CO_2$/40% H_2/He flow to 10% $^{13}CO_2$/40% H_2/He flow over $NaNO_3$/1%Ru/Al_2O_3 catalysts at a temperature of 260 °C. Total flow rate was constant at 40 mL/min.

Table C.2. Proposed elemetanry steps for CO_2 methanation over Ru/Al_2O_3 catalysts through carboxylic acid intermediate.

Step	Reaction
1	$H_2(g) + 2* \leftrightarrow 2H*$
2	$CO_2(g) + OH\text{-}S \leftrightarrow CO_3H\text{-}S$
3	$CO_3H\text{-}S + H* \leftrightarrow COOH\text{-}S + OH*$
4	$COOH\text{-}S + * \leftrightarrow CO* + OH\text{-}S$
5 (irreversible)	$CO* + H* \rightarrow C* + OH*$
6	$C* + H* \leftrightarrow CH* + *$
7	$CH* + H* \leftrightarrow CH_2* + *$
8	$CH_2+* + H* \leftrightarrow CH_3* + *$
9	$CH_3* + H* \leftrightarrow CH_4* + *$
10 (irreversibe)	$OH* + H* \rightarrow H_2O* + *$
11	$CH_4* \leftrightarrow CH_4(g) + *$
12	$H_2O* \leftrightarrow H_2O(g) + *$

C.4 Rate Law Derivation and Calculated Surface Coverage

Table C.3. Rate law derivation for the Ru/Al_2O_3 catalyst

$\frac{d\theta_{OH}}{dt} = r_4 - r_{-4} - r_5 - r_{10} = 0$	Eq.S3-1
$\frac{d\theta_{CO}}{dt} = r_4 - r_{-4} - r_5 = 0$	Eq.S3-2
$2r_5 = r_{10}$	Eq.S3-3
$\theta_{OH} = \frac{2k_5}{k_{10}}\theta_{CO}$	Eq.S3-4
$\theta_H = \theta_* \sqrt{K_1 P_{H_2}}$	Eq.S3-5
$\theta_{CO_2} = \frac{K_3[CO_3H - S]\theta_*}{[OH - S]} = \frac{K_3 K_2 P_{CO_2}[OH - S]\theta_*}{[OH - S]} = \theta_* K_3 K_2 P_{CO_2}$	Eq.S3-6
$\theta_{CO} = \frac{K_4 \theta_{CO_2} \theta_H}{\theta_{OH}} = \theta_* \sqrt{\frac{\left(k_{10} K_4 K_3 K_2 K_1^{\frac{1}{2}}\right)}{2k_5}} P_{CO_2}^{\frac{1}{2}} P_{H_2}^{\frac{1}{4}}$	Eq.S3-7
$\theta_{OH} = \theta_* \sqrt{\frac{\left(2k_5 K_4 K_3 K_2 K_1^{\frac{1}{2}}\right)}{k_{10}}} P_{CO_2}^{\frac{1}{2}} P_{H_2}^{\frac{1}{4}}$	Eq.S3-8
$1 = \theta_* + \theta_H + \theta_{CO_2} + \theta_{CO} + \theta_{OH}$	Eq.S3-9
$\theta_* = \frac{1}{1 + \sqrt{K_1 P_{H_2}} + K_3 K_2 P_{CO_2} + \sqrt{K_4 K_3 K_2 K_1^{\frac{1}{2}}} P_{CO_2}^{\frac{1}{2}} P_{H_2}^{\frac{1}{4}} \left(\sqrt{\frac{k_{10}}{2k_5}} + \sqrt{\frac{2k_5}{k_{10}}}\right)}$	Eq.S3-10
$r_5 = k_5 \theta_{CO} \theta_H$	Eq.S3-11
$r_5 = \frac{\sqrt{\frac{\left(k_5 k_{10} K_4 K_3 K_2 K_1^{\frac{3}{2}}\right)}{2}} P_{CO_2}^{\frac{1}{2}} P_{H_2}^{\frac{3}{4}}}{\left(1 + \sqrt{K_1 P_{H_2}} + K_3 K_2 P_{CO_2} + \sqrt{K_4 K_3 K_2 K_1^{\frac{1}{2}}} P_{CO_2}^{\frac{1}{2}} P_{H_2}^{\frac{1}{4}} \left(\sqrt{\frac{k_{10}}{2k_5}} + \sqrt{\frac{2k_5}{k_{10}}}\right)\right)^2}$	Eq.S3-12

Table C.4. Surface coverage of reaction intermediates over 1% Ru/Al_2O_3 catalysts calculated from kinetic modeling.

P_{CO2} (kPa)	P_{H2} (kPa)	θ_H	θ_CO2	θ_CO	θ_OH	θ*
1.01E+01	4.05E+01	3.38E-01	2.14E-05	2.50E-01	9.88E-03	4.02E-01
2.03E+01	4.05E+01	3.05E-01	3.86E-05	3.19E-01	1.26E-02	3.63E-01
3.04E+01	4.05E+01	2.84E-01	5.38E-05	3.64E-01	1.44E-02	3.38E-01
4.05E+01	4.05E+01	2.68E-01	6.78E-05	3.97E-01	1.57E-02	3.19E-01
1.01E+01	2.03E+01	2.78E-01	2.48E-05	2.44E-01	9.67E-03	4.68E-01
2.03E+01	2.03E+01	2.52E-01	4.50E-05	3.13E-01	1.24E-02	4.23E-01
3.04E+01	2.03E+01	2.35E-01	6.28E-05	3.57E-01	1.41E-02	3.94E-01
4.05E+01	2.03E+01	2.22E-01	7.92E-05	3.90E-01	1.54E-02	3.73E-01
2.03E+01	3.04E+01	2.82E-01	4.12E-05	3.17E-01	1.25E-02	3.88E-01
2.03E+01	5.07E+01	3.24E-01	3.66E-05	3.20E-01	1.26E-02	3.44E-01
4.05E+01	3.04E+01	2.49E-01	7.25E-05	3.95E-01	1.56E-02	3.41E-01
4.05E+01	5.07E+01	2.84E-01	6.43E-05	3.97E-01	1.57E-02	3.02E-01

Table C.5. Surface coverage of reaction intermediates over 5% Ru/Al_2O_3 catalysts calculated from kinetic modeling.

P_{CO2} (kPa)	P_{H2} (kPa)	θ_H	θ_CO2	θ_CO	θ_OH	θ*
1.01E+01	4.05E+01	1.78E-01	2.75E-05	2.26E-01	5.90E-03	5.90E-01
2.03E+01	4.05E+01	1.62E-01	5.02E-05	2.92E-01	7.60E-03	5.38E-01
3.04E+01	4.05E+01	1.52E-01	7.05E-05	3.35E-01	8.73E-03	5.04E-01
4.05E+01	4.05E+01	1.44E-01	8.93E-05	3.67E-01	9.57E-03	4.79E-01
1.01E+01	2.03E+01	1.38E-01	3.02E-05	2.09E-01	5.44E-03	6.47E-01
2.03E+01	2.03E+01	1.27E-01	5.55E-05	2.71E-01	7.07E-03	5.95E-01
3.04E+01	2.03E+01	1.19E-01	7.83E-05	3.13E-01	8.15E-03	5.60E-01
4.05E+01	2.03E+01	1.14E-01	9.94E-05	3.44E-01	8.96E-03	5.33E-01
2.03E+01	3.04E+01	1.47E-01	5.24E-05	2.84E-01	7.39E-03	5.62E-01
2.03E+01	5.07E+01	1.75E-01	4.84E-05	2.98E-01	7.76E-03	5.19E-01
4.05E+01	3.04E+01	1.31E-01	9.35E-05	3.58E-01	9.33E-03	5.01E-01
4.05E+01	5.07E+01	1.55E-01	8.59E-05	3.74E-01	9.74E-03	4.61E-01

Table C.6. Rate law derivation for $NaNO_3/Ru/Al_2O_3$ catalyst

$\frac{d\theta_{CO}}{dt} = r_4 - r_{-4} - r_5 = 0$	Eq.S6-1
$\frac{d\theta_{OH}}{dt} = r_4 - r_{-4} + r_5 - r_{10} = 0$	Eq.S6-2
$\theta_{OH} = \frac{2k_5}{k_{10}}\theta_{CO}$	Eq.S6-3
$\frac{d\theta_{C}}{dt} = r_5 - r_6 - r_{-6} = 0$	Eq.S6-4
$\frac{d\theta_{CH}}{dt} = r_6 - r_{-6} - r_7 + r_{-7} = 0$	Eq.S6-5
$\frac{d\theta_{CH_2}}{dt} = r_7 - r_{-7} - r_8 + r_{-8} = 0$	Eq.S6-6
$\frac{d\theta_{CH_3}}{dt} = r_8 - r_{-8} - r_9 = 0$	Eq.S6-7
$\theta_{CO} = \frac{k_9}{k_5}\theta_{CH_3}$	Eq.S6-8
$\theta_H = \theta_* \sqrt{K_1 P_{H_2}}$	Eq.S6-9
$\theta_{HCOO} = \frac{K_3[CO_3 - S]\theta_H}{[O-S]} = \frac{K_3K_2P_{CO_2}[O-S]\theta_H}{[O-S]} = \theta_* K_3K_2K_1^{\frac{1}{2}}P_{CO_2}P_{H_2}^{\frac{1}{2}}$	Eq.S6-10
$\theta_{CO} = \frac{K_4\theta_{HCOO}\theta_*}{\theta_{OH}} = \theta_* \sqrt{\frac{\left(k_{10}K_4K_3K_2K_1^{\frac{1}{2}}\right)}{2k_5}} P_{CO_2}^{\frac{1}{2}}P_{H_2}^{\frac{1}{4}}$	Eq.S6-11
$\theta_{CH_3} = \frac{\theta_*}{k_9} \sqrt{\frac{\left(k_5k_{10}K_4K_3K_2K_1^{\frac{1}{2}}\right)}{2}} P_{CO_2}^{\frac{1}{2}}P_{H_2}^{\frac{1}{4}}$	Eq.S6-12
$\theta_{OH} = \theta_* \sqrt{\frac{\left(2k_5K_4K_3K_2K_1^{\frac{1}{2}}\right)}{k_{10}}} P_{CO_2}^{\frac{1}{2}}P_{H_2}^{\frac{1}{4}}$	Eq.S6-13

$$\theta_{CH_2} = \frac{\theta_{CH_3}\theta_*}{K_8\theta_H} = \frac{\theta_*}{k_9K_8}\sqrt{\frac{(k_5k_{10}K_4K_3K_2)}{2K_1^{\frac{1}{2}}}}P_{CO_2}^{\frac{1}{2}}P_{H_2}^{-\frac{1}{4}}$$	Eq.S6 -14
$$\theta_{CH} = \frac{\theta_{CH_2}\theta_*}{K_7\theta_H} = \frac{\theta_*}{k_9K_7K_8}\sqrt{\frac{(k_5k_{10}K_4K_3K_2)}{2K_1^{\frac{3}{2}}}}P_{CO_2}^{\frac{1}{2}}P_{H_2}^{-\frac{3}{4}}$$	Eq.S6 -15
$$\theta_C = \frac{\theta_{CH}\theta_*}{K_6\theta_H} = \frac{\theta_*}{k_9K_6K_7K_8}\sqrt{\frac{(k_5k_{10}K_4K_3K_2)}{2K_1^{\frac{5}{2}}}}P_{CO_2}^{\frac{1}{2}}P_{H_2}^{-\frac{5}{4}}$$	Eq.S6 -16
$$1 = \theta_* + \theta_H + \theta_{HCOO} + \theta_{CO} + \theta_{OH} + \theta_C + \theta_{CH} + \theta_{CH_2} + \theta_{CH_3}$$	Eq.S6 -17
$$\theta_* = \frac{1}{1+\sqrt{K_1P_{H_2}}+K_3K_2K_1^{\frac{1}{2}}P_{CO_2}P_{H_2}^{\frac{1}{2}}+\sqrt{K_4K_3K_2K_1^{\frac{1}{2}}P_{CO_2}^{\frac{1}{2}}P_{H_2}^{\frac{1}{4}}\left(\sqrt{\frac{k_{10}}{2k_5}}+\sqrt{\frac{2k_5}{k_{10}}}\right)}+\frac{P_{CO_2}^{\frac{1}{2}}}{k_9}\sqrt{\frac{k_5k_{10}K_4K_3K_2}{2}}\left(\frac{P_{H_2}^{-\frac{5}{4}}}{K_1^{\frac{5}{4}}K_6K_7K_8}+\frac{P_{H_2}^{-\frac{3}{4}}}{K_1^{\frac{3}{4}}K_7K_8}+\frac{P_{H_2}^{-\frac{1}{4}}}{K_1^{\frac{1}{4}}K_8}+K_1^{\frac{1}{4}}P_{H_2}^{\frac{1}{4}}\right)}}$$	Eq.S6 -18
$$r_9 = k_5\theta_{CH_3}\theta_H$$	Eq.S6 -19
$$r_5 = \frac{\sqrt{\frac{\left(k_5k_{10}K_4K_3K_2K_1^{\frac{3}{2}}\right)}{2}}P_{CO_2}^{\frac{1}{2}}P_{H_2}^{\frac{3}{4}}}{\left(1+\sqrt{K_1P_{H_2}}+K_3K_2K_1^{\frac{1}{2}}P_{CO_2}P_{H_2}^{\frac{1}{2}}+\sqrt{K_4K_3K_2K_1^{\frac{1}{2}}P_{CO_2}^{\frac{1}{2}}P_{H_2}^{\frac{1}{4}}\left(\sqrt{\frac{k_{10}}{2k_5}}+\sqrt{\frac{2k_5}{k_{10}}}\right)}+\frac{P_{CO_2}^{\frac{1}{2}}}{k_9}\sqrt{\frac{k_5k_{10}K_4K_3K_2}{2}}\left(\frac{P_{H_2}^{-\frac{5}{4}}}{K_1^{\frac{5}{4}}K_6K_7K_8}+\frac{P_{H_2}^{-\frac{3}{4}}}{K_1^{\frac{3}{4}}K_7K_8}+\frac{P_{H_2}^{-\frac{1}{4}}}{K_1^{\frac{1}{4}}K_8}+K_1^{\frac{1}{4}}P_{H_2}^{\frac{1}{4}}\right)}\right)}$$	Eq.S6 -20

Table C.7. Surface coverage of reaction intermediates over $NaNO_3$/1% Ru/Al_2O_3 catalysts calculated from kinetic modeling.

P_CO2	P_H2	θ_H	θ_HCOO	θ_CO	θ_C	θ_CH	θ_CH2	θ_CH3	θ_OH	θ*
1.01E+01	4.05E+01	2.52E-01	2.70E-03	3.08E-02	1.75E-01	1.69E-02	1.59E-02	4.39E-01	1.36E-02	5.43E-02
2.03E+01	4.05E+01	1.96E-01	4.19E-03	3.38E-02	1.92E-01	1.85E-02	1.74E-02	4.81E-01	1.49E-02	4.21E-02
3.04E+01	4.05E+01	1.67E-01	5.36E-03	3.53E-02	2.00E-01	1.94E-02	1.82E-02	5.03E-01	1.56E-02	3.59E-02
4.05E+01	4.05E+01	1.49E-01	6.36E-03	3.62E-02	2.06E-01	1.99E-02	1.87E-02	5.17E-01	1.60E-02	3.19E-02
1.01E+01	2.03E+01	1.62E-01	1.73E-03	2.34E-02	3.77E-01	2.57E-02	1.71E-02	3.34E-01	1.03E-02	4.92E-02
2.03E+01	2.03E+01	1.22E-01	2.60E-03	2.50E-02	4.01E-01	2.74E-02	1.82E-02	3.56E-01	1.10E-02	3.70E-02
3.04E+01	2.03E+01	1.02E-01	3.28E-03	2.57E-02	4.13E-01	2.82E-02	1.88E-02	3.66E-01	1.13E-02	3.11E-02
4.05E+01	2.03E+01	9.01E-02	3.86E-03	2.61E-02	4.20E-01	2.87E-02	1.91E-02	3.73E-01	1.15E-02	2.74E-02
2.03E+01	3.04E+01	1.65E-01	3.54E-03	3.06E-02	2.68E-01	2.24E-02	1.83E-02	4.37E-01	1.35E-02	4.11E-02
2.03E+01	5.07E+01	2.18E-01	4.67E-03	3.56E-02	1.45E-01	1.56E-02	1.64E-02	5.07E-01	1.57E-02	4.20E-02
4.05E+01	3.04E+01	1.24E-01	5.32E-03	3.26E-02	2.85E-01	2.38E-02	1.94E-02	4.64E-01	1.44E-02	3.09E-02
4.05E+01	5.07E+01	1.67E-01	7.13E-03	3.84E-02	1.56E-01	1.69E-02	1.77E-02	5.48E-01	1.70E-02	3.20E-02

Table C.8. Surface coverage of reaction intermediates over $NaNO_3$/5% Ru/Al_2O_3 catalysts calculated from kinetic modeling.

P_CO2	P_H2	θ_H	θ_HCOO	θ_CO	θ_C	θ_CH	θ_CH2	θ_CH3	θ_OH	θ*
1.01E+01	4.05E+01	1.80E-01	2.74E-02	9.10E-02	1.47E-01	1.16E-01	4.80E-02	2.83E-01	4.15E-02	6.60E-02
2.03E+01	4.05E+01	1.36E-01	4.12E-02	9.69E-02	1.57E-01	1.23E-01	5.11E-02	3.01E-01	4.42E-02	4.97E-02
3.04E+01	4.05E+01	1.14E-01	5.17E-02	9.93E-02	1.61E-01	1.27E-01	5.24E-02	3.09E-01	4.53E-02	4.16E-02
4.05E+01	4.05E+01	9.98E-02	6.05E-02	1.01E-01	1.63E-01	1.28E-01	5.31E-02	3.13E-01	4.59E-02	3.65E-02
1.01E+01	2.03E+01	1.10E-01	1.66E-02	6.57E-02	3.01E-01	1.67E-01	4.90E-02	2.04E-01	3.00E-02	5.67E-02
2.03E+01	2.03E+01	8.09E-02	2.45E-02	6.86E-02	3.14E-01	1.75E-01	5.12E-02	2.13E-01	3.13E-02	4.18E-02
3.04E+01	2.03E+01	6.72E-02	3.06E-02	6.98E-02	3.19E-01	1.78E-01	5.20E-02	2.17E-01	3.18E-02	3.47E-02
4.05E+01	2.03E+01	5.87E-02	3.56E-02	7.04E-02	3.22E-01	1.79E-01	5.25E-02	2.19E-01	3.21E-02	3.03E-02
2.03E+01	3.04E+01	1.12E-01	3.41E-02	8.61E-02	2.14E-01	1.46E-01	5.24E-02	2.68E-01	3.93E-02	4.74E-02
2.03E+01	5.07E+01	1.54E-01	4.67E-02	1.04E-01	1.20E-01	1.06E-01	4.90E-02	3.23E-01	4.73E-02	5.03E-02
4.05E+01	3.04E+01	8.22E-02	4.98E-02	8.90E-02	2.22E-01	1.51E-01	5.42E-02	2.77E-01	4.06E-02	3.47E-02
4.05E+01	5.07E+01	1.13E-01	6.88E-02	1.08E-01	1.25E-01	1.10E-01	5.10E-02	3.36E-01	4.93E-02	3.71E-02

C.5 Results for Different Reaction Pathway Models

Table C.9. Proposed elementary step for CO_2 methanation over $NaNO_3/Ru/Al_2O_3$ catalysts, using hydrogen carbonyl species as reaction intermediate.

Step	Reaction
1	$H_2(g) + 2* \leftrightarrow 2H*$
2	$CO_2(g) + O\text{-}S \leftrightarrow CO_3\text{-}S$
3	$CO_3\text{-}S + H* \leftrightarrow HCOO* + O\text{-}S$
4	$HCOO* + * \leftrightarrow CO* + OH*$
5	$CO* + H* \leftrightarrow H*CO + *$
6	$H*CO + H* \leftrightarrow H_2*CO + *$
7 (RDS)	$H_2*CO + H* \rightarrow CH_2* + OH*$
8	$CH_2{+}* + H* \leftrightarrow CH_3* + *$
9	$CH_3* + H* \leftrightarrow CH_4* + *$
10	$CH_4* \leftrightarrow CH_4(g) + *$
11 (irreversible)	$OH* + H* \rightarrow H_2O* + *$
12	$H_2O* \leftrightarrow H_2O(g) + *$

Table C.10. Rate law derivation for pathway shown in Table C.9.

$\frac{d\theta_{CO}}{dt} = r_4 - r_{-4} - r_5 + r_{-5} = 0$	Eq. S10-1
$\frac{d\theta_{H*CO}}{dt} = r_5 - r_{-5} - r_6 + r_{-6} = 0$	Eq. S10-2
$\frac{d\theta_{H_2*CO}}{dt} = r_6 - r_{-6} - r_7 = 0$	Eq. S10-3
$\frac{d\theta_{OH}}{dt} = r_4 - r_{-4} + r_7 - r_{11} = 0$	Eq. S10-4
$\theta_{OH} = \frac{2k_7}{k_{11}}\theta_{H_2*CO}$	Eq. S10-5
$\theta_H = \theta_* \sqrt{K_1 P_{H_2}}$	Eq. S10-6
$\theta_{HCOO} = \frac{K_3[CO_3 - S]\theta_H}{[O-S]} = \frac{K_3K_2P_{CO_2}[O-S]\theta_H}{[O-S]} = \theta_* K_3 K_2 K_1^{\frac{1}{2}} P_{CO_2} P_{H_2}^{\frac{1}{2}}$	Eq. S10-7
$\theta_{CO} = \frac{K_4\theta_{HCOO}\theta_*}{\theta_{OH}} = \theta_* \sqrt{\frac{(k_{11}K_4K_3K_2)}{2k_7K_6K_5K_1^{\frac{1}{2}}}} P_{CO_2}^{\frac{1}{2}} P_{H_2}^{-\frac{1}{4}}$	Eq. S10-8

$$\theta_{H*CO} = \frac{K_5\theta_{CO}\theta_H}{\theta_*} = \theta_* \sqrt{\frac{\left(k_{11}K_5K_4K_3K_2K_1^{\frac{1}{2}}\right)}{2k_7K_6}} P_{CO_2}^{\frac{1}{2}} P_{H_2}^{\frac{1}{4}}$$	Eq. S10-9
$$\theta_{H_2*CO} = \frac{K_6\theta_{H*CO}\theta_H}{\theta_*} = \theta_* \sqrt{\frac{\left(k_{11}K_6K_5K_4K_3K_2K_1^{\frac{3}{2}}\right)}{2k_7}} P_{CO_2}^{\frac{1}{2}} P_{H_2}^{\frac{3}{4}}$$	Eq. S10-10
$$\theta_{OH} = \theta_* \sqrt{\frac{\left(2k_7K_6K_5K_4K_3K_2K_1^{\frac{3}{2}}\right)}{k_{11}}} P_{CO_2}^{\frac{1}{2}} P_{H_2}^{\frac{3}{4}}$$	Eq. S10-11
$$1 = \theta_* + \theta_H + \theta_{HCOO} + \theta_{CO} + \theta_{H*CO} + \theta_{H_2*CO} + \theta_{OH}$$	Eq. S10-12
$$\theta_* = \frac{1}{1+\sqrt{K_1P_{H_2}}\left(1+K_3K_2P_{CO_2}\right)+\sqrt{K_4K_3K_2}P_{CO_2}^{\frac{1}{2}}\left(\sqrt{\frac{k_{11}}{2k_7K_6K_5K_1^{\frac{1}{2}}}}P_{H_2}^{-\frac{1}{4}}+\sqrt{\frac{k_{11}K_5K_1^{\frac{1}{2}}}{2k_7K_6}}P_{H_2}^{\frac{1}{4}}+\sqrt{K_6K_5K_1^{\frac{3}{2}}}P_{H_2}^{\frac{3}{4}}\left(\sqrt{\frac{k_{11}}{2k_7}}+\sqrt{\frac{2k_7}{k_{11}}}\right)\right)}$$	Eq. S10-13
$$r_7 = k_7\theta_{H_2*CO}\theta_H$$	Eq. S10-14
$$r = \frac{\sqrt{\frac{\left(k_7K_{11}K_6K_5K_4K_3K_2K_1^{\frac{5}{2}}\right)}{2}}P_{CO_2}^{\frac{1}{2}}P_{H_2}^{\frac{5}{4}}}{\left(1+\sqrt{K_1P_{H_2}}\left(1+K_3K_2P_{CO_2}\right)+\sqrt{K_4K_3K_2}P_{CO_2}^{\frac{1}{2}}\left(\sqrt{\frac{k_{11}}{2k_7K_6K_5K_1^{\frac{1}{2}}}}P_{H_2}^{-\frac{1}{4}}+\sqrt{\frac{k_{11}K_5K_1^{\frac{1}{2}}}{2k_7K_6}}P_{H_2}^{\frac{1}{4}}+\sqrt{K_6K_5K_1^{\frac{3}{2}}}P_{H_2}^{\frac{3}{4}}\left(\sqrt{\frac{k_{11}}{2k_7}}+\sqrt{\frac{2k_7}{k_{11}}}\right)\right)\right)^2}$$	Eq. S10-15

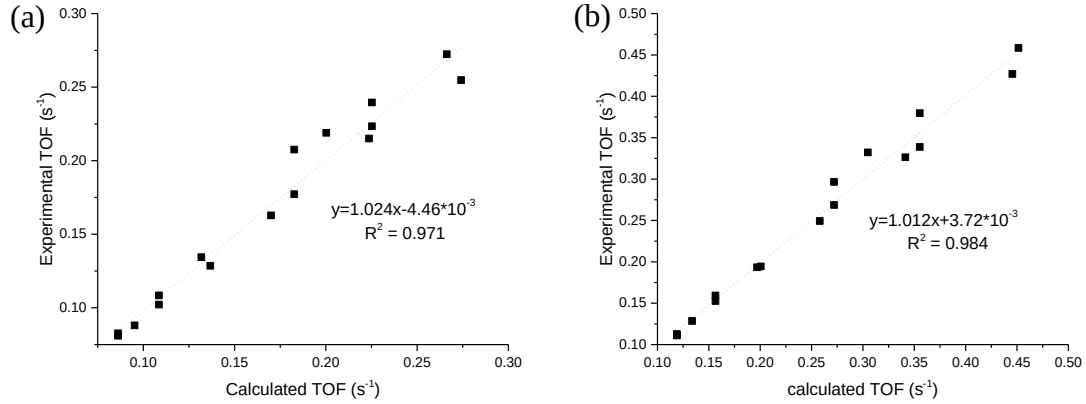

Figure C.8. Calculated TOF vs experimental TOF for (a) $NaNO_3$/1% Ru/Al_2O_3 and (b) $NaNO_3$/5% Ru/Al_2O_3 using rate law derived from proposed pathway shown in Table C.9.

Table C.11. Surface coverage of reaction intermediates over $NaNO_3$/1% Ru/Al_2O_3 catalysts calculated from kinetic modeling, using rate law derived from proposed pathway shown in Table C.9.

P_CO2	P_H2	θ_H	θ_HCOO	θ_CO	θ_H*CO	θ_H2*CO	θ_OH	θ*
10.1325	40.53	2.10E-01	1.16E-04	4.46E-01	1.95E-02	2.37E-01	4.28E-03	8.27E-02
20.265	40.53	1.63E-01	1.79E-04	4.87E-01	2.14E-02	2.60E-01	4.69E-03	6.39E-02
30.3975	40.53	1.39E-01	2.29E-04	5.09E-01	2.23E-02	2.71E-01	4.89E-03	5.45E-02
40.53	40.53	1.23E-01	2.71E-04	5.22E-01	2.29E-02	2.78E-01	5.02E-03	4.84E-02
10.1325	20.265	1.61E-01	8.88E-05	5.75E-01	1.78E-02	1.53E-01	2.76E-03	8.97E-02
20.265	20.265	1.23E-01	1.36E-04	6.21E-01	1.92E-02	1.65E-01	2.98E-03	6.85E-02
30.3975	20.265	1.04E-01	1.72E-04	6.43E-01	1.99E-02	1.71E-01	3.09E-03	5.79E-02
40.53	20.265	9.23E-02	2.03E-04	6.58E-01	2.04E-02	1.75E-01	3.16E-03	5.13E-02
20.265	30.3975	1.46E-01	1.61E-04	5.45E-01	2.07E-02	2.18E-01	3.93E-03	6.65E-02
20.265	50.6625	1.75E-01	1.92E-04	4.42E-01	2.17E-02	2.95E-01	5.32E-03	6.14E-02
40.53	30.3975	1.10E-01	2.43E-04	5.81E-01	2.21E-02	2.32E-01	4.19E-03	5.01E-02
40.53	50.6625	1.33E-01	2.92E-04	4.75E-01	2.33E-02	3.16E-01	5.71E-03	4.66E-02

Table C.12. Surface coverage of reaction intermediates over $NaNO_3$/5% Ru/Al_2O_3 catalysts calculated from kinetic modeling, using rate law derived from proposed pathway shown in Table C.9.

P_CO2	P_H2	θ_H	θ_HCOO	θ_CO	θ_H*CO	θ_H2*CO	θ_OH	θ*
10.1325	40.53	6.57E-02	5.40E-04	5.37E-01	2.27E-02	2.38E-01	2.30E-02	1.13E-01
20.265	40.53	4.90E-02	8.06E-04	5.66E-01	2.40E-02	2.51E-01	2.43E-02	8.44E-02
30.3975	40.53	4.10E-02	1.01E-03	5.80E-01	2.46E-02	2.58E-01	2.49E-02	7.07E-02
40.53	40.53	3.61E-02	1.19E-03	5.89E-01	2.49E-02	2.61E-01	2.53E-02	6.21E-02
10.1325	20.265	4.78E-02	3.93E-04	6.56E-01	1.96E-02	1.46E-01	1.41E-02	1.16E-01
20.265	20.265	3.55E-02	5.83E-04	6.89E-01	2.06E-02	1.53E-01	1.48E-02	8.64E-02
30.3975	20.265	2.96E-02	7.31E-04	7.05E-01	2.11E-02	1.56E-01	1.51E-02	7.22E-02
40.53	20.265	2.60E-02	8.55E-04	7.14E-01	2.14E-02	1.59E-01	1.53E-02	6.34E-02
20.265	30.3975	4.33E-02	7.12E-04	6.21E-01	2.28E-02	2.07E-01	2.00E-02	8.61E-02
20.265	50.6625	5.34E-02	8.78E-04	5.22E-01	2.47E-02	2.89E-01	2.79E-02	8.22E-02
40.53	30.3975	3.18E-02	1.05E-03	6.45E-01	2.36E-02	2.15E-01	2.07E-02	6.33E-02
40.53	50.6625	3.93E-02	1.29E-03	5.43E-01	2.57E-02	3.01E-01	2.91E-02	6.05E-02

Table C.13. Proposed elementary step for CO_2 methanation over $NaNO_3/Ru/Al_2O_3$ catalysts, assuming reversible reaction for step 5 from sequence from Table 4.5.

Step	Reaction
1	$H_2(g) + 2* \leftrightarrow 2H*$
2	$CO_2(g) + O\text{-}S \leftrightarrow CO_3\text{-}S$
3	$CO_3\text{-}S + H* \leftrightarrow HCOO* + O\text{-}S$
4	$HCOO* + * \leftrightarrow CO* + OH*$
5	$CO* + H* \leftrightarrow C* + OH*$
6	$C* + H* \leftrightarrow CH* + *$
7	$CH* + H* \leftrightarrow CH_2* + *$
8	$CH_2{+}* + H* \leftrightarrow CH_3* + *$
9 (RDS)	$CH_3* + H* \rightarrow CH_4* + *$
10 (irreversible)	$OH* + H* \rightarrow H_2O* + *$
11	$CH_4* \leftrightarrow CH_4(g) + *$
12	$H_2O* \leftrightarrow H_2O(g) + *$

Table C. 14. Rate law derivation for pathway shown in Table C.13.

$\frac{d\theta_{OH}}{dt} = r_4 - r_{-4} + r_5 - r_{-5} - r_{10} = 0$	Eq. S14-1
$\frac{d\theta_{CO}}{dt} = r_4 - r_{-4} - r_5 + r_{-5} = 0$	Eq. S14-2
$\frac{d\theta_{C}}{dt} = r_5 - r_{-5} - r_6 + r_{-6} = 0$	Eq. S14-3
$\frac{d\theta_{CH}}{dt} = r_6 - r_{-6} - r_7 + r_{-7} = 0$	Eq. S14-4
$\frac{d\theta_{CH_2}}{dt} = r_7 - r_{-7} - r_8 + r_{-8} = 0$	Eq. S14-5
$\frac{d\theta_{CH_3}}{dt} = r_8 - r_{-8} - r_9 = 0$	Eq. S14-6
$\theta_{OH} = \frac{2k_9}{k_{10}}\theta_{CH_3}$	Eq. S14-7
$\theta_H = \theta_* \sqrt{K_1 P_{H_2}}$	Eq. S14-8
$\theta_{HCOO} = \frac{K_3[CO_3 - S]\theta_H}{[O-S]} = \frac{K_3 K_2 P_{CO_2}[O-S]\theta_H}{[O-S]} = \theta_* K_3 K_2 K_1^{\frac{1}{2}} P_{CO_2} P_{H_2}^{\frac{1}{2}}$	Eq. S14-9
$\theta_{CO} = \frac{K_4\theta_{HCOO}\theta_*}{\theta_{OH}} = \frac{\sqrt[3]{4}\theta_* k_{10}^{\frac{1}{3}}(K_4K_3K_2)^{\frac{2}{3}}}{2(k_9K_1K_5K_6K_7K_8)^{\frac{1}{3}}} P_{CO_2}^{\frac{2}{3}} P_{H_2}^{-\frac{1}{3}}$	Eq. S14-10
$\theta_C = \frac{K_5\theta_{CO}\theta_H}{\theta_{OH}} = \frac{\theta_* k_{10}^{\frac{2}{3}}(K_5K_4K_3K_2)^{\frac{1}{3}}}{\sqrt[3]{4}(k_9K_1K_6K_7K_8)^{\frac{2}{3}}} P_{CO_2}^{\frac{1}{3}} P_{H_2}^{-\frac{2}{3}}$	Eq. S14-11
$\theta_{CH} = \frac{K_6\theta_C\theta_H}{\theta_*} = \frac{\theta_* k_{10}^{\frac{2}{3}}(K_6K_5K_4K_3K_2)^{\frac{1}{3}}}{\sqrt[3]{4}(k_9K_7K_8)^{\frac{2}{3}}K_1^{\frac{1}{6}}} P_{CO_2}^{\frac{1}{3}} P_{H_2}^{-\frac{1}{6}}$	Eq. S14-12
$\theta_{CH_2} = \frac{K_7\theta_{CH}\theta_H}{\theta_*} = \frac{\theta_* k_{10}^{\frac{2}{3}}(K_7K_6K_5K_4K_3K_2K_1)^{\frac{1}{3}}}{\sqrt[3]{4}(k_9K_8)^{\frac{2}{3}}} P_{CO_2}^{\frac{1}{3}} P_{H_2}^{\frac{1}{3}}$	Eq. S14-13

$$\theta_{CH_3} = \frac{K_8\theta_{CH_2}\theta_H}{\theta_*} = \frac{\theta_* k_{10}^{\frac{2}{3}}(K_8K_7K_6K_5K_4K_3K_2)^{\frac{1}{3}}K_1^{\frac{5}{6}}}{\sqrt[3]{4}k_9^{\frac{2}{3}}}P_{CO_2}^{\frac{1}{3}}P_{H_2}^{\frac{5}{6}}$$	Eq. S14-14
$$\theta_{OH} = \frac{2\theta_* k_9^{\frac{1}{3}}(K_8K_7K_6K_5K_4K_3K_2)^{\frac{1}{3}}K_1^{\frac{5}{6}}}{\sqrt[3]{4}k_{10}^{\frac{1}{3}}}P_{CO_2}^{\frac{1}{3}}P_{H_2}^{\frac{5}{6}}$$	Eq. S14-15
$$1 = \theta_* + \theta_H + \theta_{HCOO} + \theta_{CO} + \theta_{OH} + \theta_C + \theta_{CH} + \theta_{CH_2} + \theta_{CH_3}$$	Eq. S14-16
$$\theta_* = \frac{1}{1+\sqrt{K_1P_{H_2}}\left(1+K_3K_2P_{CO_2}\right)+\frac{\sqrt[3]{4}k_{10}^{\frac{1}{3}}(K_4K_3K_2)^{\frac{2}{3}}}{2(k_9K_1K_5K_6K_7K_8)^{\frac{1}{3}}}P_{CO_2}^{\frac{2}{3}}P_{H_2}^{-\frac{1}{3}}+\frac{k_{10}^{\frac{2}{3}}(K_5K_4K_3K_2)^{\frac{1}{3}}}{\sqrt[3]{4}(k_9)^{\frac{2}{3}}}P_{CO_2}^{\frac{1}{3}}\left(\frac{P_{H_2}^{-\frac{2}{3}}}{(K_1K_6K_7K_8)^{\frac{2}{3}}}+\frac{K_6^{\frac{1}{3}}P_{H_2}^{-\frac{1}{6}}}{K_1^{\frac{1}{6}}(K_7K_8)^{\frac{2}{3}}}+\frac{(K_1K_7K_8)^{\frac{1}{3}}P_{H_2}^{\frac{1}{3}}}{K_8^{\frac{2}{3}}}+(K_8K_7K_6)^{\frac{1}{3}}K_1^{\frac{5}{6}}P_{H_2}^{\frac{5}{6}}\left(1+\frac{2k_9}{k_{10}}\right)\right)}$$	Eq. S14-17
$$r_9 = k_5\theta_{CH_3}\theta_H$$	Eq. S14-18
$$r = \frac{\frac{k_5k_{10}^{\frac{2}{3}}(K_8K_7K_6K_5K_4K_3K_2)^{\frac{1}{3}}K_1^{\frac{4}{3}}}{\sqrt[3]{4}k_9^{\frac{2}{3}}}P_{CO_2}^{\frac{1}{3}}P_{H_2}^{\frac{4}{3}}}{\left(1+\sqrt{K_1P_{H_2}}\left(1+K_3K_2P_{CO_2}\right)+\frac{\sqrt[3]{4}k_{10}^{\frac{1}{3}}(K_4K_3K_2)^{\frac{2}{3}}}{2(k_9K_1K_5K_6K_7K_8)^{\frac{1}{3}}}P_{CO_2}^{\frac{2}{3}}P_{H_2}^{-\frac{1}{3}}+\frac{k_{10}^{\frac{2}{3}}(K_5K_4K_3K_2)^{\frac{1}{3}}}{\sqrt[3]{4}(k_9)^{\frac{2}{3}}}P_{CO_2}^{\frac{1}{3}}\left(\frac{P_{H_2}^{-\frac{2}{3}}}{(K_1K_6K_7K_8)^{\frac{2}{3}}}+\frac{K_6^{\frac{1}{3}}P_{H_2}^{-\frac{1}{6}}}{K_1^{\frac{1}{6}}(K_7K_8)^{\frac{2}{3}}}+\frac{(K_1K_7K_8)^{\frac{1}{3}}P_{H_2}^{\frac{1}{3}}}{K_8^{\frac{2}{3}}}+(K_8K_7K_6)^{\frac{1}{3}}K_1^{\frac{5}{6}}P_{H_2}^{\frac{5}{6}}\left(1+\frac{2k_9}{k_{10}}\right)\right)\right)^2}$$	Eq. S14-19

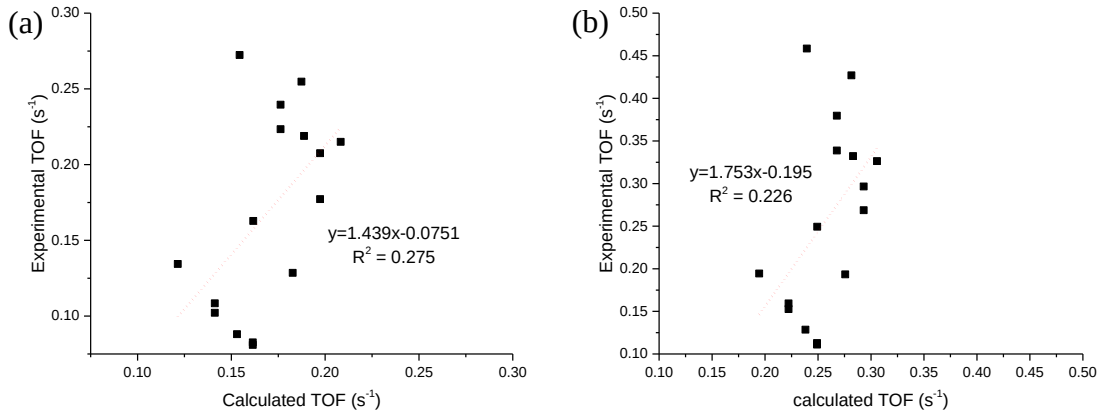

Figure C.9. Calculated TOF vs experimental TOF for (a) $NaNO_3$/1% Ru/Al_2O_3 and (b) $NaNO_3$/5% Ru/Al_2O_3 using rate law derived from proposed pathway shown in Table C.13.

Table C.15. Surface coverage of reaction intermediates over $NaNO_3$/1% Ru/Al_2O_3 catalysts calculated from kinetic modeling, using rate law derived from proposed pathway shown in Table C.13.

P_CO2	P_H2	θ_H	θ_HCOO	θ_CO	θ_C	θ_CH	θ_CH2	θ_CH3	θ_OH	θ*
10.1325	40.53	0.706518	3.53361E-05	2.88747E-05	0.000171699	0.001177045	0.00820925	0.071273565	0.113881739	0.098704356
20.265	40.53	0.67245	6.72645E-05	4.36256E-05	0.000205896	0.001411475	0.009844273	0.085469002	0.136563375	0.093944884
30.3975	40.53	0.650441	9.75945E-05	5.52947E-05	0.000227978	0.001562853	0.010900054	0.094635398	0.15120955	0.090870105
40.53	40.53	0.633919	0.000126821	6.52832E-05	0.000244549	0.001676448	0.011692314	0.101513886	0.162200079	0.088561839
10.1325	20.265	0.703269	3.51736E-05	5.12123E-05	0.000383679	0.00185985	0.009172194	0.056309699	0.089972298	0.138947064
20.265	20.265	0.675535	6.75731E-05	7.80886E-05	0.000464342	0.002250857	0.011100517	0.068148012	0.108887694	0.133467654
30.3975	20.265	0.657342	9.86299E-05	9.95692E-05	0.000517224	0.002507196	0.012364703	0.075909069	0.121288402	0.129873162
40.53	20.265	0.643539	0.000128745	0.000118087	0.000557325	0.00270158	0.013323342	0.081794322	0.130691929	0.127145988
20.265	30.3975	0.675757	6.75953E-05	5.57169E-05	0.000289428	0.001718289	0.010378562	0.078035602	0.124686201	0.109011647
20.265	50.6625	0.668029	6.68223E-05	3.59847E-05	0.00015766	0.001208376	0.009422528	0.091463419	0.146141325	0.083474455
40.53	30.3975	0.639914	0.00012802	8.3754E-05	0.000345315	0.00205008	0.012382601	0.093103818	0.148762374	0.103229608
40.53	50.6625	0.627464	0.000125529	5.36535E-05	0.000186577	0.001430007	0.01115074	0.108238972	0.1729455	0.078405492

Table C.16. Surface coverage of reaction intermediates over $NaNO_3$/1% Ru/Al_2O_3 catalysts calculated from kinetic modeling, using rate law derived from proposed pathway shown in Table C.131.

P_CO2	P_H2	θ_H	θ_HCOO	θ_CO	θ_C	θ_CH	θ_CH2	θ_CH3	θ_OH	θ*
10.1325	40.53	0.682285	4.09201E-05	2.23538E-05	0.000104115	0.000840163	0.007190194	0.08728799	0.140475254	0.081753759
20.265	40.53	0.642835	7.71082E-05	3.34328E-05	0.000123592	0.000997334	0.008535277	0.103617115	0.166754218	0.077026719
30.3975	40.53	0.61777	0.000111153	4.21012E-05	0.000135961	0.001097147	0.009389494	0.113987196	0.183443109	0.074023375
40.53	40.53	0.599167	0.00014374	4.94661E-05	0.000145138	0.001171202	0.010023262	0.12168105	0.195825067	0.071794226
10.1325	20.265	0.690295	4.14005E-05	4.02976E-05	0.000236473	0.001349331	0.008165462	0.070093808	0.112804126	0.116974505
20.265	20.265	0.657337	7.88477E-05	6.09143E-05	0.000283713	0.001618882	0.009796647	0.084096194	0.135338598	0.111389581
30.3975	20.265	0.636025	0.000114437	7.72325E-05	0.000314241	0.001793077	0.010850787	0.093145123	0.14990132	0.107778285
40.53	20.265	0.620017	0.000148742	9.12056E-05	0.000337162	0.001923864	0.011642241	0.099939107	0.160835087	0.105065556
20.265	30.3975	0.650721	7.80541E-05	4.30114E-05	0.000175003	0.001223004	0.009064331	0.095297227	0.153364766	0.090033841
20.265	50.6625	0.635048	7.61742E-05	2.74234E-05	9.41098E-05	0.000849065	0.008124058	0.110266074	0.177454594	0.068060239
40.53	30.3975	0.6096	0.000146243	6.39617E-05	0.000206557	0.001443516	0.010698661	0.112479646	0.181016963	0.084344375
40.53	50.6625	0.589518	0.000141426	4.04109E-05	0.00011007	0.000993057	0.009501812	0.128966024	0.207549	0.06318057